COMMUNICATIONS

COMMUNICATIONS

Peter Bury - Taketoshi Matsumoto - Stefan Hardon - Ivan Bellan - Marian Janek - Hikaru Kobayashi *

INVESTIGATION OF INTERFACE STATES IN Si/NAOS-SiO_2/HFO_2 STRUCTURES USING COMPLETE ACOUSTIC SPECTROSCOPY

The set of MOS structures formed on n-type Si substrate with (NAOS)-SiO_2/HfO_2 gate dielectric layers was prepared and annealed in N_2 atmosphere at various temperatures to stabilize the structure and to decrease the interface states density. Two Acoustic DLTS techniques using both surface (SAW) and longitudinal (LAW) acoustic waves including acoustoelectric response signal versus gate voltage dependence (U_{ac}-U_g characteristics) were used to characterize the interface states and the role of annealing treatment. The main interface deep centers with activation energies about 0.30 and 0.20 eV, typical for dangling bonds were observed as well as a particular influence of annealing treatment on the interface states. The obtained results are analyzed, discussed and mutually compared.

Keywords: *Acoustic DLTS, MOS structures, NAOS SiO_2/HfO_2 oxide layer, interface states.*

1. Introduction

High permittivity (high-κ) dielectrics are subject of great study in order to replace SiO_2 as gate dielectric in metal-oxide-semiconductor field-effect (MOS-FET) transistors in the future scales of integration [1]. HfO_2 is among the most promising high-κ dielectrics, but before these materials can replace SiO_2 as gate dielectric, the nature and formation of electrically active defects existing in these materials should be known because they play an important role in device operation. Moreover, HfO_2, as most of the high-k materials, when deposited in direct contact with Si an interfacial oxide layer few nanometers thick is formed [2]. One of the possible procedures to avoid reaction on Si surface is to grow a controlled free-defect SiO_2 barrier layer between substrate and high-κ dielectric. However, this barrier layer can lead to a reduction of the dielectric constant and, hence, to the effective capacitance of the gate dielectric stack, impeding to reach the necessary equivalent oxide thickness values [3 and 4].

Two basic modifications of acoustic (acoustoelectric) deep-level transient spectroscopy (A-DLTS) were introduced after the acoustoelectric effect (AE) in semiconductor structures has been shown to be one of a useful tool for the experimental study of interface states. The surface acoustic wave (SAW) technique uses a nonlinear acoustoelectric interaction between the SAW electric field and the free carriers in an interface region which generates a transverse acoustoelectric signal (TAS) across the structure [5 and 6]. The longitudinal acoustic wave (LAW) technique uses an acoustoelectric response signal (ARS) observed at the interface of the semiconductor structure when a longitudinal acoustic wave propagates through the structure [7 and 8]. Because both TAS and ARS are very sensitive to any changes in the space charge distribution in the interface region their time development after an injection pulse has been applied to the structure (A-DLTS) and their dependence on external voltage (U_{ac}-U_g curves) can be used to study the interface states properties including their activation energy, cross-section and concentration and interface states distribution [8 - 10].

In this contribution the MOS structures prepared on n-type Si substrate with SiO_2/HfO_2 gate dielectric layers formed by HfO_2 oxide deposited by atomic layer deposition on SiO_2 oxide film prepared with nitric acid oxidation of Si (NAOS) are investigated by the SAW and LAW A-DLTS techniques including the ARS – gate voltage (U_{ac}-U_g) dependences to characterize the interface states and the role of annealing treatment. The obtained results are analyzed, discussed and mutually compared.

2. Theoretical principles

The basic principle of an ARS creation can be explained using the idea of an acoustic wave passing through the MOS structure characterized by the particular space charge region at the interface. The acoustic wave, following the modulation of charge density by acoustic pressure $p = p_0 \cos(\omega t - kx)$ evokes

* [1]Peter Bury, [2]Taketoshi Matsumoto, [1]Stefan Hardon, [1]Ivan Bellan, [1]Marian Janek, [2]Hikaru Kobayashi
[1]Department of Physics, Faculty of Electrical Engineering, University of Zilina, Slovakia
E-mail: peter.bury@fel.uniza.sk
[2]Institute of Scientific and Industrial Research, Osaka University, CREST, Japan Science and Technology Organization, Osaka, Japan

the change of the potential difference that manifests as an ARS signal. The ARS produced by a MOS structure propagating by longitudinal acoustic wave can be then expressed by the relation [10 and 11]

$$U_{ac} = \varphi_s \frac{p}{K_s} - \frac{Q(\varphi_s)}{C_{ox}} \frac{p}{K_i} - \frac{Q_{it}(\varphi_s)}{C_{ox}} \frac{p}{K_i} = \\ = U_{ac}^{o} \cos(\omega t - kx) \quad , \qquad (1)$$

where φ_s is the surface potential, Q_s is the semiconductor charge, Q_{it} is the trapped charge at the interface state, C_{ox} is the oxide capacitance, K_s and K_i are the elastic moduli of the semiconductor and insulator, respectively and p_0 is the acoustic pressure amplitude.

The non-destructive SAW A-DLTS technique is based on the fact that the electric field accompanying the SAW on a piezoelectric substrate can generate the TAS that reflects any changes in the space charge distribution in the interface regions. The resulting electric field across the structure calculates dc AE effect and hf wave propagation properties and can be expressed by the relation [12]

$$E = E_0 + E_1 e^{-i(\omega t - kx)} \, , \qquad (2)$$

where E_0 is dc part and E_1 is the amplitude of hf part of TAS, respectively. The corresponding carrier density follows the relation

$$n = n^0 + n_0 + n_1 e^{j(\omega t - kx)} , \qquad (3)$$

where n^0 is the carrier concentration with no applied field and n_0, n_1 are the AE term and term proportional to the amplitude of exciting wave, respectively. The transversal hf acoustoelectric signal can be then given by the relation

$$U_{ac} = \int_0^d E_{1y} \sin(\omega t - kx) dx \, . \qquad (4)$$

Here d is the selected window width. Choosing the interaction space of the λ/2 length [or (2n+1) λ/2] in x direction, where n is the natural number, the average value is not zero any more and reaches its maximum.

The principle of A-DLTS technique [6, 8 and 10] is based on the fact that the change of the amplitude of the measured ARS, δU_{ac}^0 and/or TAS after an injection pulse has been applied is proportional to the nonequilibrium charge at the interface and the decay time constant associated with the relaxation of the ARS or TAS amplitude is then a direct measure of the time constant associated with the relaxation processes of injected carriers. Therefore, the ARS amplitude time dependence can be written as

$$U_{ac}^0(t) = U_0 + U_1 \exp(-t/\tau) \, , \qquad (5)$$

where U_0 is the original ARS (TAS) due to the acoustoelectric interaction of acoustic wave and charge at the interface of MOS structure and U_1 represents the increase of the ARS (TAS) due to the injection pulse. The time constant characterizing the relaxation processes after applied injection pulse can be expressed for electrons by the relation

$$\tau^{-1} = \gamma_n \sigma_n T^2 \exp\left[-\frac{E_a}{k_B T}\right], \qquad (6)$$

where σ_n is the capture cross section, γ_n is constant, E_a is the interface state activation energy related to the bottom of conduction band, k_B is the Boltzmann's constant and T is the thermodynamic temperature. The analysis of the time dependence of the ARS or TAS at different temperatures then allows to construct the A-DLTS spectra and following to determine the activation energy of interference states E_a and corresponding cross section σ_n [6 - 11].

If the ARS in the MOS structure without any interface states (Q_{it} = 0) is indexed as "ideal" then the ARS amplitude can be expressed [10 - 11] in the form

$$U_{ac}^0(ideal) = \left| \frac{p_0}{K_s} \right| (U_g - U_{fb}) \Big| + \frac{Q_s}{C_{ox}} \frac{K_i - K_s}{K_s K_i} p_0 \Bigg| \, , \qquad (7)$$

where U_{fb} is the flatband voltage. As it can be seen from Eq. (7) the ARS of ideal MOS structure is the superposition of linear term with zero at flatband voltage and term representing the contribution from the semiconductor charge Q_s. Comparing Eq.(1) and Eq.(7) the interface trapped charge can be expressed through the deviation of the ARS of real and ideal structures as

$$Q_{it} = S(U_{ac}^0 - U_{ac}^0(ideal)) \, , \qquad (8)$$

where $S = C_{ox} K_s / p_o$. To determine the energy distribution of interface states, it is necessary to know the dependence of the semiconductor charge on the surface potential for an ideal MOS structure. This dependence can be obtained using Terman's model [13]. The physical meaning of the absolute values is that the ARS cannot differentiate the total charge or potential polarity.

The interface state density D_{it} can be then expressed, appearing from the U_{ac}-U_g curves for ideal and real MOS structures, by the relation

$$D_{it}(E_t) = \frac{1}{q} \left| \frac{dQ_{it}}{d\varphi_s} \right| = \frac{1}{q} \left| S \frac{d(U_{ac}^0 - U_{ac}^0(ideal))}{d\varphi_s} \right| \, , \qquad (9)$$

Eq. (5) allows to determine the modeling of the distribution of interface states from the measured ARS.

However, the leakage current represented by tunneling transport in the case of very thin oxide layers (< 10 nm) becomes a significant problem. The tunneling current for very thin oxide layers influences the division of the applied voltage U_g between the semiconductor and insulator layer and for the oxide layer thickness < 2 nm the whole applied voltage practically spreads

across the semiconductor, especially in the range of inversion [14]. Concerning the tunneling process the transport of free charge curriers through the thin oxide layer caused by applied electric field has to be taken into account where the tunneling current following the Fowler-Nordheim mechanism [15] induces additional change of the ARS

$$\Delta U_{ac} = A\left(U_g^2 + B\right)e^{-\frac{C}{U_g}}, \tag{10}$$

where A, B and C are constants. The tunneling current is supposed to be dependent only on the applied voltage. The simulation of the "ideal" ARS inclusive the calculation of tunnel current contribution gives a new ideal ARS, $U_{ac}^0(tunnel)$. The interface charge can be then expressed using the new ideal and real ARS-voltage curves for MOS structure by the relation

$$Q_{it} = S\left|\left(U_{ac}^0 - U_{ac}^0\left(tunnel\right)\right)\right|. \tag{11}$$

The calculation procedure for determination of interface states density is ~~is~~ then given by Eq. (9). Except the leakage current the Schottky contact on the metal-semiconductor interface can be the reason of some deviation of the measured U_{ac}-U_g dependence, especially near the flatband. To eliminate this influence, the added capacitance of Schottky contact was included into the calculation procedure.

3. Experimental

The MOS structure prepared on n-type Si substrate wafers with NAOS-SiO_2/HfO_2 gate dielectric layer was formed by 5nm HfO_2 oxide deposited by atomic layer deposition on 0.6 nm NAOS-SiO_2 oxide film prepared in ~100% HNO_3 vapor [16]. The set of investigated MOS capacitors contained ~~such~~ original MOS structures (A1, A2) and structures ~~was~~ annealed in N_2 atmosphere at 200 (A3, A4), 300 (A5, A6) and 400 °C (A7, A8) for 10 min to stabilize the structure and decrease the leakage current density. After annealing procedure, aluminum dot electrodes were evaporated. The samples size was 2x2 cm^2 and electrodes were evaporated with diameter 2.5, 1.5 and 1.0 mm. The investigated samples list and obtained experimental results are summarized in Table 1. It should be noted that couples of samples A1-A2, A3-A4, A5-A6 and A7-A8 represent the same structures but prepared for LAW or SAW techniques, respectively.

The block diagram of the experimental setup for A-DLTS is illustrated in Fig. 1. The computer was used to trigger the apparatus, to generate excitation bias pulses as well as to record and evaluate the isothermal transients of the ARS and/or TAS. The LAW of frequency 13.2 MHz and SAW of frequency 10 MHz were generated using $LiNbO_3$ transducer and interdigital transducer evaporated on $LiNbO_3$ delay line, respectively in the arrangement illustrated in the A- and B-detail of Fig. 1. The acoustoelectric signals produced by MOS structure were after detection in the Box-car Averager recorded and stored by computer. The quiescent bias voltage pulses of 200 ms with filling traps completely were applied to the MOS structures. The ARS and TAS were monitored as a function of temperature and peaks with maxima of the temperature for which the emission rate was the same as the adjusted sample rate were observed in A-DLTS spectra [8 - 10]. The A-DLTS experimental results were at temperatures varying between 400 and 77 K, with the samples cooled in nitrogen cryostat.

To determine the interface states density the U_{ac}-U_g measurements were performed using the same acoustic equipment as for A-DLTS with the difference of bias source. Whereas for the A-DLTS the voltage source provided with bias voltage pulses, for the measurement of U_{ac}-U_g curves the voltage source provided with both the linear increase (decrease) of gate bias and the variation of increasing (decreasing) rate. Current voltage (*I-V*) and capacitance voltage (*C-V*) characteristics were observed using FLUKE PM 6306, programmable automatic RLC meter.

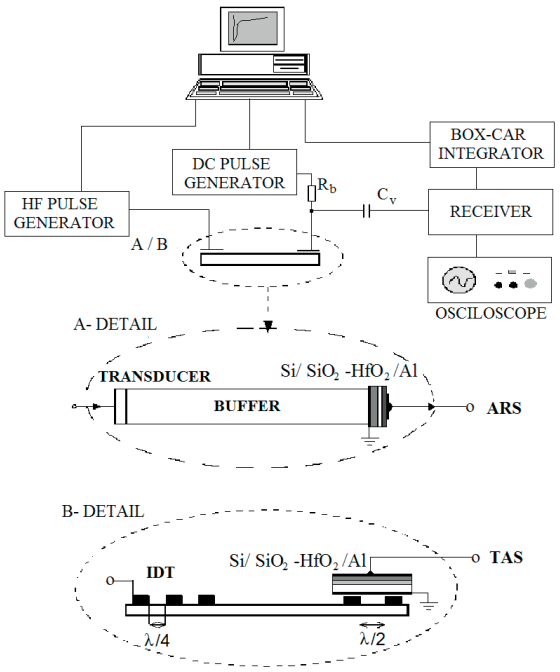

Fig. 1 Block diagram of the experimental setup for A-DLTS. The sample configuration for LAW technique is in A- detail and For SAW in B-detail

4. Results and discussion

Figure 2 shows the representative SAW A-DLTS spectrum of original Si/SiO_2/HfO_2 structure and calculated Arrhenius plot inside. The illustrated spectrum that was observed with pulse voltage ΔUg = +4.0 V (Ug = -1 V), similarly as other samples,

contains one evident peak with some lateral structure that gradually decreases from the original structure A2 to the sample A8 annealed at 400°C. Except for this "cleaning process" there was observed also some shift of the activation energy in regard to the original structure.

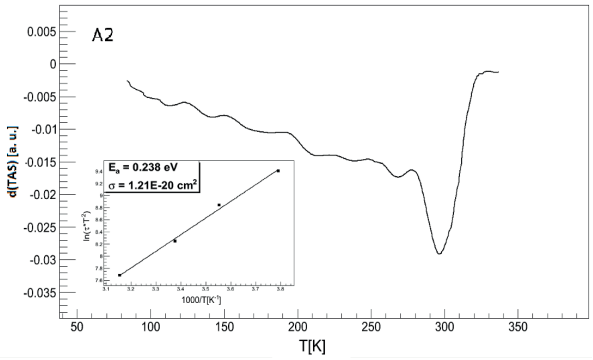

Fig. 2 SAW A-DLTS spectrum of Si/SiO$_2$/HfO$_2$ structure (A2) and calculated Arrhenius plot (inside)

Figure 3 presents a representative A-DLTS spectrum of original structure A1 obtained using LAW technique and calculated Arrhenius plot (inside). The illustrated spectrum that was observed with pulse voltage ΔU_g = +3.0 V (Ug = 0 V) contains one evident peak with some lateral structure that also gradually decreases from the original structure A1 to the sample A7 annealed at 400°C [11]. Except for this reducing process there was observed also some shift of the activation energy in regard of the original structure. Therefore, the interface quality using the interfacial SiO_2 layer seems not to be influenced by the annealing process markedly.

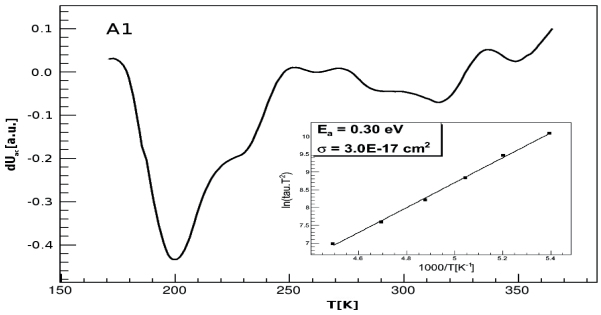

Fig. 3 LAW A-DLTS spectrum of Si/SiO$_2$/HfO$_2$ structure (A1 sample) and calculated Arrhenius plot (inside)

The results of both TAW and SAW A-DLTS are summarized in Table 1. The activation energies and corresponding cross sections of interface states were determined from the A-DLTS spectra, observed from the ARS and/or TAS amplitude transients measured at different temperatures.

The Electron Spin Resonance data [2] indicated that the basic defects observed at the Si/HfO_2 interface were identical to those found in conventional thermally oxidized silicon. However, the tunneling process from inner layer interface states is possible, too. Both kinds of interface states detected by SAW and/or LAW technique were already observed [3 and 17]. Interface states observed on Si/SiO_2/HfO_2 structures are usually attributed to isolated Si dangling bonds with which no atoms in the oxide layer interact and/or attributed to Si dangling bonds interacting weakly with an oxygen or Si atom in the oxide layer, respectively. The difference between SAW and LAW A-DLTS results can be caused by the different mechanism of SAW and LAW interaction with charge at the interface region, as well as the shift of applied voltage U_g in the case of SAW technique due to the dc transversal acoustoelectric voltage (TAV) produced by structure [5 and 12].

Summarization of the investigated Al/NAOS-SiO_2-HfO_2/Si MOS structures, activation energies and cross-sections provided by LAW and SAW A-DLTS

Table 1

	Annealing process	E_a [eV]		σ [cm^2]	
		LAW	SAW	LAW	SAW
A1	Without annealing	0.30		3.0×10^{-17}	
A2	Without annealing		0.23		1.2×10^{-20}
A3	N_2 at 200°C for 10 min	0.28		8.4×10^{-17}	
A4	N_2 at 200°C for 10 min		0.17		6.6×10^{-22}
A5	N_2 at 300°C for 10 min	0.37		4.0×10^{-16}	
A6	N_2 at 300°C for 10 min		0.20		9.8×10^{-21}
A7	N_2 at 400°C for 10 min	0.33		6.1×10^{-17}	
A8	N_2 at 400°C for 10 min		0.19		1.2×10^{-21}

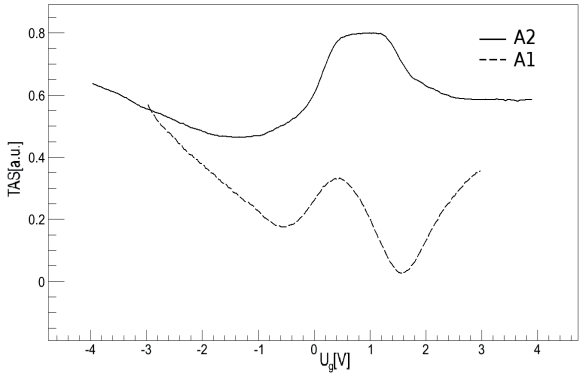

Fig. 4 Dependence of the TAS and ARS on gate voltage Ug for original structures, A1 and A2

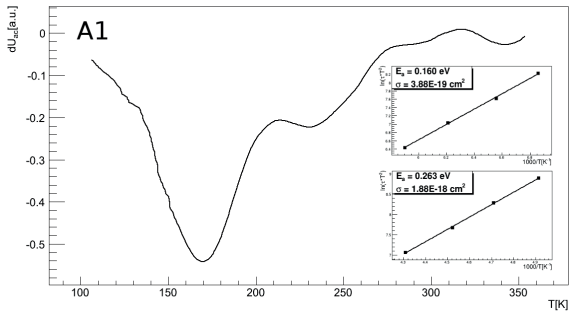

Fig. 5 LAW A-DLTS spectrum of Si/SiO_2/HfO_2 structure (A1 sample) and calculated Arrhenius plots (inside) obtained for ΔU_g = +5.0 V, U_g = -2.0 V

Figure 4 presents the dependences of the ARS as well as TAS on the gate voltage for original structures A1 and A2, respectively. Besides, the LAW technique can identify the role of interfacial SiO_2 layer (interface SiO_2/HfO_2) and corresponding tunneling, the SAW technique is not so sensitive.

However, using pulse voltage ΔU_g =+5.0 V (U_g= -2.0 V), similar as in the case of SAW spectra we found as a certain shift of A-DLTS spectra obtained for only positive voltage (ΔU_g = +3.0 V, U_g= 0 V) [11] as also some highlighting of another peak at lower temperatures (˜170 K) corresponding to the interface state with activation energy ˜0.12-0.16 eV (see Fig. 5). This fact indicates as the typical feature of interface states moreover the role of HfO_2/ SiO_2/ interlayer (IL).

The energy diagrams of the MOS structures under accumulation and inversion are illustrated in Fig. 6. We also assume that defects exist also at the HfO_2/SiO_2 IL as well as at Si/SiO_2 interface. A-DLTS measurements consist of applying accumulation pulses to fill the interface states in the upper half of the semiconductor band gap followed after reverse voltage in which the interface states emit electrons to the conduction band yielding the ARS or TAS transients that are conveniently recorded and processed to obtain the A-DLTS spectra. If the SiO_2 film is thin enough, tunneling between the semiconductor and the IL may occur. At accumulation,

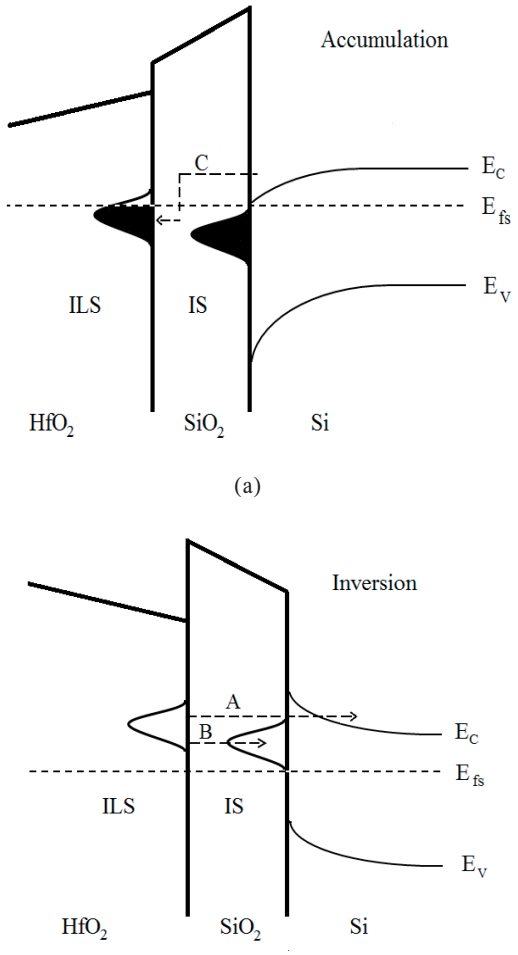

Fig. 6 Energy band diagram of Si/ SiO_2/HfO_2 structure at accumulation (a) and inversion (b)

capturing electrons coming from the semiconductor band by direct tunneling fills IL states. When the reverse pulse is applied, these defects emit the captured electrons to the semiconductor band. The emission process may occur in two different ways: IL states with energies above the silicon conduction band emit electrons by direct tunneling (A). On the other hand, for energies ranging from the Fermi level to the semiconductor conduction band tunneling between the IL states and the interface states (B) and following to the conduction band can occur. Electrons emitted according the (B) sequence increase the acoustoelectric transient, obtaining an

apparent increase in the measured interfacial state densities. Since all these mechanisms are tunneling assisted the thinner the silicon dioxide films the higher their probability. In our experiment, the SiO_2 layer thickness was 0.6 nm.

Moreover, an increase in the filling electric field in Fig. 6(a) (higher bias in the accumulation regime) causes a larger number of IL filled traps (C). Then, when biasing the sample in the inversion regime, a higher number of IL traps can contribute to the ARS or TAS transients by direct tunneling. This result agrees with results shown in [3]. On the contrary, variations in the inversion bias should not change the total filled traps, and the emitted charge from the IL traps does not change - significantly.

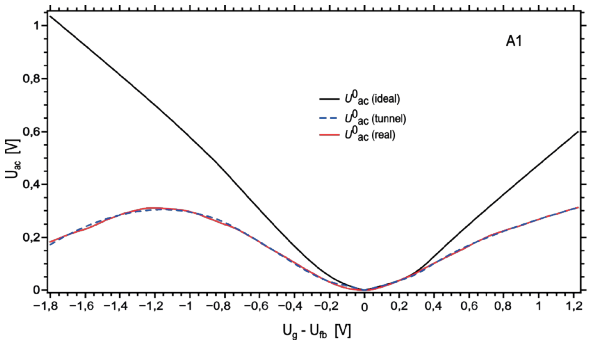

Fig. 7 Theoretical U_{ac}- U_g characteristics of "ideal" $Si/SiO_2/HfO_2$ structure without any interface states (thick line) and "ideal" structure with tunneling process (dashed line) compared with real U_{ac}-U_g curve (red line)

Figure 7 shows the measured ARS dependence on gate voltage, U_{ac}-U_g curve for sample A1 (Fig. 4) including the theoretical (ideal) U_{ac}-U_g characteristics for the $Si/SiO_2/HfO_2/Al$ MOS structure without any interface states as well as simulated characteristics for the same structure comprehensive of tunneling process. Using these real and theoretical characteristics the density of interface states could be determined (Fig. 8). We can see, in the first place, that our theoretical calculation of ideal U_{ac}-U_g curve very well coincides with real one and, secondly, that the density of interface states course corresponds to the presence of interface states with energies around ~ 0.2 – 0.3 eV detected also by A-DLTS (Table 1). The average values of density of interface states calculated using the correct value of donor concentration, N_D=4.7×10^{21} m^{-3} and considering the Schottky contact, changed from 2.64$_x$10^{12} eV^{-1}cm^{-2} (A1) up to 1.05$_x$10^{12} eV^{-1}cm^{-2} (A7).

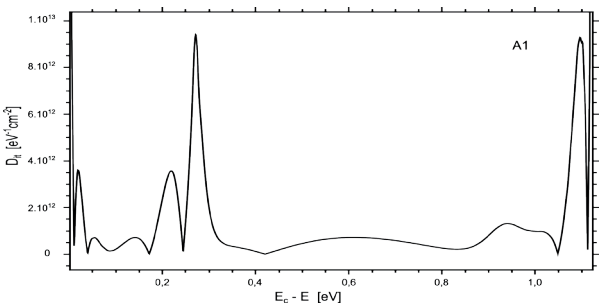

Fig. 8 Distribution of interface states calculated from U^0_{ac} - U_g characteristics for original structure (A1)

The reduction of the leakage current densities for annealed structures is evident only for the gate voltage close to zero (from –0.3 V to +0.3 V) decreasing from sample A1 gradually to sample A7 [11]. The behavior of *I-V* curves corresponds to theoretical predictions for such structures [14] but except for the mentioned interval it is almost identical for both untreated and treated structures, although there were significant differences in *C-V* characteristics. The reason of such behavior could be caused by two kinds of interface states, at both SiO_2/Si and HfO_2/SiO_2 interfaces. Then the tunneling process through the SiO_2 interfacial layer at accumulation and/or depletion can lower the influence of the annealing treatment [3 and 11]

5. Conclusion

MOS structures with HfO_2 oxide layer formed on n-type silicon with interfacial SiO_2 layer prepared by NAOS method and annealed in N_2 at various temperatures were studied by LAW and SAW acoustic spectroscopy. The main interface states with activation energy of 0.17 – 0.23 eV, observed by SAW A-DLTS are quite different from those found by LAW A-DLTS (0.27-0.37 eV) typical for dangling bonds type defects and identical to those in Si/SiO_2 interface. These differences can be caused by both the different mechanism of SAW and LAW interaction with charge at the interface region and due to the dc transversal acoustoelectric voltage produced by structure. Except for this, a post-deposition annealing at 200, 300, and mainly at 400°C leads to the reduction of interface state density, hysteresis effect as well, but only insignificantly leakage current density. The lowering influence on the characteristics of annealed MOS structures with NAOS-SiO_2/HfO_2 gate dielectric layers can indicate the stabilization role of the NAOS-SiO_2 interfacial layer. However, the next reduction should be realized by appropriate modification of structure processing steps. An observed shift of the interface state activation energies and some "cleaning" process observed in annealed structures can be explained by reduction of weak Si dangling bonds with surrounding atoms.

Acknowledgements

The authors would like to thank to Mr. F. Černobila for technical assistance and Assoc. prof. I. Jamnický for some remarks. This work was financially supported by the R&D operational program Centrum of excellence of power electronics systems and materials for their components II. No. OPVaV-2009/2.1/02-SORO, ITMS 26220120046 funded by the European Community.

References

[1] LOCQUET, J.-P., MARCHIORI, C., SOUSA, M., FOMPEYRINE, J., SEO, J. W.: *J. App. Phys.* 100, 2006, 051610
[2] STESMANS, A., AFANAS`EV, V. V.: *Appl. Phys. Lett.* 82, 2003, 4074
[3] CASTAN, H., DUENAS, S., GARCIA, H., GOMEZ, A., BAILON, L., TOLEDANO-LUQUE, M., DEL PRADO, A., MARTIL, I., GONZALEZ-DIAZ, G.: *J. Appl. Phys.* 107, 2010, 114104
[4] HEE-WOOK YOU, WON-JU CHO: *Appl. Phys. Lett.* 96, (2010) 093506
[5] ABATE, A., MAN, K. J., OSTROVSKIJ, I. V., DAS, P.: *Solid State Electronics* 36 1993, 697
[6] BURY, P., JAMNICKY, I., RAMPTON, V. W.: *Phys.* B 94, 1999, 263
[7] BURY, P., JAMNICKY, DURCEK, J.: *Phys. Stat. Sol.* A 151, 1991, 126
[8] BURY, P., JAMNICKY: *Acta Phys. Slovaca* 46, 1996, 693
[9] HOCKICKO, P., BURY, P., SIDOR, P., JURECKA, S., JAMNICKY, I.: *Communications - Scientific Letters of the University of Zilina,* 12, 2010, 44
[10] HOCKICKO , P., BURY, P., SIDOR, P., KOBAYASHI, H., TAKAHASHI, M., YANASE, T.: Cent. *Eur. J. Phys.* 9, 2011, 242
[11] BURY, P., MATSUMOTO, T., BELLAN, I., JANEŕK, M., KOBAYASHI, H.: *Applied Surface Sciences* 269, 2013, 50
[12] FRITZ, I. J.: *J. Appl. Phys.* 52, 1981, 6749
[13] NICOLLIAN, E. M., BREWS, J. R.: MOS (Metal Oxide Semiconductor), Physics and Technology, New York : Wiley, 1982.
[14] RACKO, J., VALENT, P., BENKO, P., DONOVAL, D., HARMATHA, L., PINTES, P., BREZA, J.: *Solid State Electronics* 52, 2008, 1755.
[15] WEINBERG, Z. A.: *Solid State Electronics* 20, 1977, 11.
[16] ASUHA, A., YUSA. T., MAIDA, O ., KOBAYASHI, H.: *Appl. Phys. Lett.* 80, 2002, 4175.
[17] MASSON, P., AUTRAN, J.-L., HOUSSA, M.: *App. Phys. Lett.* 81, 2002, 3392.

Jakub Rybar - Lubica Stuchlikova - Ladislav Harmatha - Juraj Jakus - Jaroslav Kovac
Beata Sciana - Damian Radziewicz - Damian Pucicki - Wojciech Dawidowski - Marek Tlaczala *

DLTS STUDY OF InGaAsN/GaAs p-i-n DIODE

The paper presents an in-depth DLTS characterization of the p-i-n structure based on the InGaAsN/GaAs triple quantum well. Three DLTS evaluation methods were used for evaluation of the measured DLTS spectra. The results of all evaluation methods are compared and discussed. One of the evaluation methods that were used is a novel numerical algorithm that was recently developed. Several material and growth defects were identified. Emission from the quantum well was also observed and identified. The parameters of the energy levels were calculated and compared. The studied InGaAsN/GaAs structure is promising candidate for the solar cell applications and the further refinement of the growth process and technology is encouraged.

Keywords: *DLTS, deep energy level, InGaAsN, p-i-n, multijunction solar cells.*

1. Introduction

One of the very promising materials in optoelectronics is a new class of semiconductors known as dilute nitrides. These dilute nitrides with nitrogen concentrations less than 5%, are opening the door for several key technologies in the near-infrared, particularly for optical fiber communication and solar cells applications. Dilute nitrides such as GaInNAs can be grown directly on gallium arsenide, which allows well-established processing techniques [1]. Unusual properties of the $In_yGa_{1-y}As_{1-x}N_x$ semiconductor alloys such as a huge and negative band gap bowing coefficient and a large conduction band offset make this semiconductor very promising for applications in high efficient multijunction solar cells [2].

DLTS (Deep Level Transient Spectroscopy) study of the p-i-n structure based on the triple quantum well InGaAsN/GaAs heterostructure is introduced in the paper. The structure was grown by atmospheric pressure metalorganic vapor phase epitaxy. In order to determine the origin of the traps detected in this sample, we had to use several evaluation methods of measured DLTS spectra and compare the evaluated results of all used methods. The measured data were compared with other similar structures [3] and thus it was possible to determine, whether the deep energy levels are caused by emission from quantum well or by presence of material defects in the structure. This paper summarizes the results of the in-depth study of this very interesting p-i-n structure with QW (quantum well), which is promising candidate for the solar cell applications.

2. Experiment

The p-i-n diode labeled NI71n based on InGaAsN/GaAs multi-quantum well structure was investigated in this experiment (Table 1 and Fig. 1 list the parameters of the sample). The investigated sample was manufactured at Wroclaw University

The parameters of the p-i-n diode structure labeled NI71n — Table 1

Sample	Substrate	Buffer	Buffer	3xUD $In_yGa_{1-y}As_{1-x}N_x$ quantum wells			UD GaAs barrier	UD GaAs	p-GaAs: Zn	p^+-GaAs: Zn
				thickness (nm)	y (%)	x (%)				
NI71n	n-GaAs:Si (100)	n^+-GaAs:Si 0.30 µm	UD-GaAs 0.45 µm	8.8 nm 8.8 nm	8.0 17.0	0.47 0.10	22.5 nm	0.45 µm	0.25 µm	„cap“ 50 nm

* [1]Jakub Rybar, [1]Lubica Stuchlikova, [1]Ladislav Harmatha, [1]Juraj Jakus, [1]Jaroslav Kovac,
[2]Beata Sciana, [2]Damian Radziewicz, [2]Damian Pucicki, [2]Wojciech Dawidowski, [2]Marek Tlaczala
[1]Institute of Electronics and Photonics, Faculty of Electrical Engineering and Information Technology,
Slovak University of Technology, Bratislava, Slovakia
E-mail: jakub.rybar@stuba.sk
[2]Wrocław University of Technology, Faculty of Microsystem Electronics and Photonics, Wroclaw, Poland

of Technology using APMOVPE with AIX200 R&D AIXTRON horizontal reactor on (100)-oriented Si-doped n-type GaAs substrate at specific growth conditions [4]. 3 × $In_yGa_{1-y}As_{1-x}N_x$ quantum wells consist of two sub wells (Table 1). The top ohmic contact (area of 2 × 10^{-2} cm^2) was prepared by AuMn evaporation on p^+GaAs:Zn "cap" layer. The bottom ohmic contact was created by AuGeNi evaporation.

p^+- GaAs:Zn	"cap"	50.0 nm
p - GaAs:Zn		0.25 µm
UD GaAs		0.45 µm
UD InGaAsN	QW	17.6 nm
UD GaAs	barrier	22.5 nm
UD InGaAsN	QW	17.6 nm
UD GaAs	barrier	22.5 nm
UD InGaAsN	QW	17.6 nm
UD GaAs	buffer	0.45 µm
n^+- GaAs:Si	buffer	0.30 µm
n- GaAs:Si (100)	substrate	

Fig. 1 Schematic description of the investigated structure

BIORAD DL8000 measurement system was used for measurement of the DLTS spectra in the temperature range from 80 to 550 K. Apart from the standard DLTS maximum evaluation analysis, this measurement system is equipped with the Fourier transform analysis for the evaluation of the measured capacitance transients (Direct auto Arrhenius Single and Multilevel evaluation). An evaluation method that uses numerical algorithm and least square method for calculation of the deep energy level parameters (LSQ method) has been recently developed at our institute [5] and is suitable for evaluation of the studied structure. The obtained DLTS spectra were evaluated using all available DLTS evaluation methods.

3. Results and discussion

The evaluation of the measured DLTS spectra had resulted in the identification of several deep energy levels in the measured structure. Several sets of measurement conditions were used during the study of the sample. Fig. 2 depicts one of the measured DLTS spectra with the measurement conditions. The Arrhenius plot in Fig. 3 shows all the evaluated deep energy levels with their activation energies.

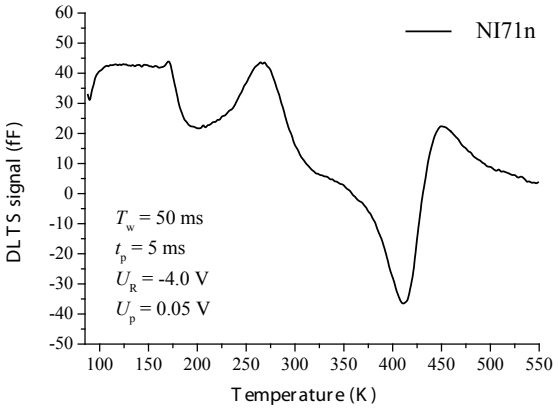

Fig. 2 Measured DLTS spectra with the measurement conditions

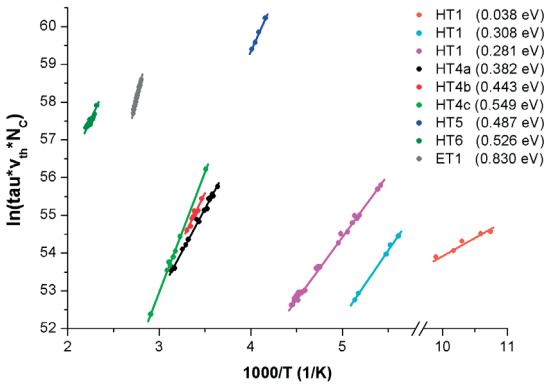

Fig. 3 Arrhenius plot of the evaluated and identified deep energy levels HT1-HT6 and ET1

Table 2 lists the evaluated deep energy levels with their parameters (activation energy ΔE_T, capture cross-section σ_T, and trap concentration N_T), the evaluation method type by which it was evaluated, and the probable origin of the deep energy level. The deep energy level HT1 (Table 2) was identified by evaluation with "min. class for evaluation" 40 and it's very interesting for a brief discussion. This hole-like level with rather small activation energy has a very small value of the capture cross-section. If we consider the fact that one of the most valuable properties of dilute nitride alloys is a discontinuity of the valence band equal to 150 meV we may assume that the level HT1 (0.038 eV) is related with this discontinuity and corresponds with the emission of the holes from the quantum well in the valence band.

List of parameters and evaluation conditions for all identified deep energy levels Table 2

Energy level	Evaluation method used	Activation energy ΔE_T (eV)	Capture cross-section prierez σ_T (cm^2)	Trap concentration N_T (cm^{-3})	Probable origin
HT1	MultiLevel	0.038	1.1E-20	3.4E+13	Emission from QW
	LSQ	0.080	1.7E-20	9.0E+13	
HT2	MultiLevel	0.308	1.2E-15	6.5E+13	HL7 0.35 eV [6]
	LSQ	0.309	6.0E-15	6.2E+13	
HT3	MultiLevel	0.281	2.7E-17	3.0E+13	HL12 0.27 eV [6]
	LSQ	0.289	2.2E-16	5.0E+13	
HT4	Single level	0.200	4.7E-21	1.1E+14	Summary signal
HT4a HT4b HT4c	MultiLevel	0.382 0.443 0.549	6.1E-18 4.6E-17 2.0E-15	1.0E+14 8.3E+13 2.4E+14	HL8 0.519 eV [6] HM1 0.55 eV [7], [8]
	LSQ	0.385 0.439 0.549	2.8E-17 2.6E-17 6.2E-15	5.5E+13 6.2E+13 2.5E+13	
HT5	Single level	0.487	1.1E-16	8.2E+12	HL8 0.519 eV [6]
	LSQ	0.480	1.0E-17	1.9E+13	
HT6	Single level	0.526	1.0E-19	4.7E+13	Fe 0.54 eV [9]
	LSQ	0.529	8.0E-20	4.0E+13	
ET1	Single level	0.830	1.9E-14	1.2E+13	EL2 0.831 eV [10], [11]
	LSQ	0.815	9.5E-15	7.4E+13	

Most of the energy levels that were evaluated were identified as well-known material defects of GaAs (HT2, HT3, HT4a, HT4b, HT4c, HT5, and ET1). Energy level HT2 was identified as HL7 with activation energy ΔE_T = 0.35 eV [6], HT3 as HL12 with activation energy ΔE_T = 0.27 eV [6]. Energy level HT3 is related to the contamination by zinc [6], which in case of the investigated sample is used as p-type doping in the upper GaAs layer. Energy level HT4 is in most measured DLTS spectra represented by single wide peak. In fact it consists of three peaks representing three energy levels HT4a, HT4b a HT4c. This information was obtained by Multi level Auto Arrhenius evaluation method. This evaluation method uses Fourier transformation and allows detailed analysis of the measured DLTS spectra, which can lead to identification of the component energy levels of the summary

signal. The component energy levels HT4a, HT4b and HT4c were confirmed by the LSQ algorithm as well. Energy levels HT4a, HT4b and HT4c were identified as defects related to the growth of GaAs (HL8 with activation energy ΔE_T = 0.519 eV [6] and HM1 with activation energy ΔE_T = 0.55 eV, representing AsGa antisite [7] and [8]). Energy level HT5 corresponds with HL8 (activation energy ΔE_T = 0.519 eV) [6]. Energy level HT6 is related to iron contamination and has an activation energy ΔE_T = 0.54 eV [9]. Energy level EL2 represents a well-known material defect of GaAs EL2 often found in bulk GaAs (activation energy of EL2: ΔE_T = 0.831 eV [10], [11]). The results of the evaluation of the measured DLTS spectra by LSQ algorithm is depicted in Fig. 4.

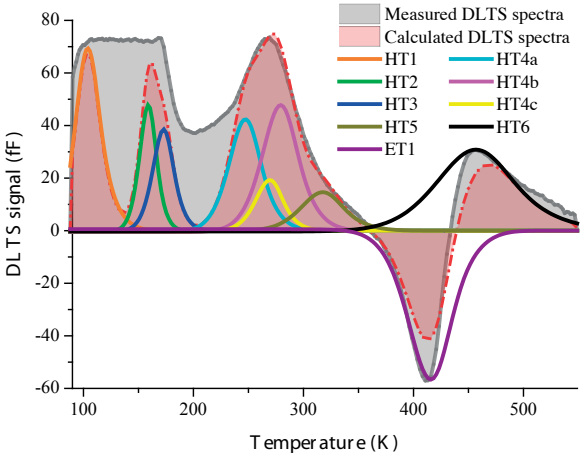

Fig. 4 Arrhenius plot of the evaluated and identified deep energy levels HT1-HT6 and ET1

Deep energy level parameters that were calculated by LSQ algorithm are listed in Table 2 and it is possible to compare them with the results of other evaluation methods. All deep energy levels were confirmed by LSQ algorithm evaluation and the existence of other deep energy levels in the grey areas of Fig. 4 is suggested. Small differences in the values of the deep energy level parameters obtained by different evaluation methods don't refer to the calculation error, but rather confirm the use of different physical models in the evaluation analysis.

4. Conclusion

DLTS study of p-i-n structure (NI71n) based on the triple quantum well (MQW) InGaAsN/GaAs heterostructure with the application of the numerical algorithm evaluation is presented in this paper. Several electrically active deep energy levels were confirmed. The parameters of the identified deep energy levels were calculated by three methods of evaluation with high level of precision. The assignment to the previously known defects of the evaluated deep energy levels was suggested. Emission of the charge carriers from the quantum well was observed and identified as an energy level HT1 (0.038 eV). Seven more hole energy levels and one electron energy level were identified and related to known material and growth defects of GaAs. Out of them two energy levels (HT3 and HT6) were identified as contaminations.

Acknowledgement

This work has been supported by the Scientific Grant Agency of the Ministry of Education of the Slovak Republic (Projects VEGA 1/0377/13 and VEGA 1/0439/13). This work was co-financed by the Polish Ministry of Science and Higher Education under the grant No. N N515 607539, by the European Union within European Regional Development Fund, through grant Innovative Economy (POIG.01.01.02-00-008/08-05), by Wrocław University of Technology statutory grant and Slovak-Polish International Cooperation Program No. SK-PL-0005-12.

References

[1] WISTEY, M. A.: *Growth of 1.5 um GaInNAsSb Vertical Cavity Surface Emitting Lasers by Molecular Beam Epitaxy*, Stanford University Thesis, 2005.

[2] MILANOVA, A. M. et al.: *J. Optoelectronics and Advanced Materials*, vol. 11, No. 10, pp. 1471-1474, 2009.

[3] STUCHLIKOVA, L. et al.: DLTFS Study of p-i-n Diode Based on InGaAsN/GaAs Multi-Quantum Well Structure, *APCOM 2013. Applied Physics of Condensed Matter : Proceedings of the 19th Intern. Conference*, Strbske Pleso, 2013.

[4] PUCICKI,. D. et. al: XIV European Workshop on Metalorganic Vapor Phase Epitaxy, Wroclaw, Poland, 2011, p. 287.

[5] RYBAR, J., KOSA, A., STUCHLIKOVA, L.: *Deep Level Parameters Calculation Using Fitting Evaluation Analysis in Digital DLTS MeasurementsS*," Proc. of ADEPT, High Tatras, 2013, pp. 262-265.

[6] MITONNEAU, A., MARTIN, G. M., MIRCEA, A.: Hole Traps in Bulk and Epitaxial GaAs Crystals, *Electronics Letters*, vol. 13, No. 22, pp. 666-668, 1977.

[7] DEENAPANRAY, P. N. K., PETRAVIC, M., JAGADISH, C., KRISPIN, M., AURET, F. D.: Electrical Characterization of p-GaAs Epilayers Disordered by Doped spin-on-Glass, *J. of Applied Physics*, vol. 97, No. 3, 2005.

[8] LAGOWSKI, J., LIN, D. C., CHEN, F., SKOWRONSKI, M., GATOS, H. C.: Native Hole Trap in Bulk GaAs and its Association with the Double-charge state of the arsenic antisite defect, *Applied Physics Letters*, vol. 47, No. 9, p. 929, 1985.

[9] KLEVERMAN, M., OMLING, P., LEDEBO, L. A., GRIMMEISS, H. G.: Electrical Properties of Fe in GaAs, *J. of Applied Physics*, vol. 54, No. 2, 1983.

[10] YU, P. W., REYNOLDS, D. C., STUTZ, C. E.: Sharp-line Photoluminescence of GaAs Grown by Low-temperature Molecular Beam Epitaxy, *Applied Physics Letters*, vol. 61, No. 12, p. 1432, 1992.

[11] BOURGOIN, J. C., NEFFATI, T.: The Energy Level of the EL2 Defect in GaAs, *Solid-State Electronics*, vol. 43, No. 1, p. 153-158, 1999.

Dusan Pudis - Daniel Jandura - Peter Gaso - Lubos Suslik - Pavol Hronec
Ivan Martincek - Jaroslav Kovac - Sofia Berezina *

PDMS-BASED NANOIMPRINT LITHOGRAPHY FOR PHOTONICS

Implementation of planar surface photonic crystal (PhC) structures leads to improvement of optical properties of optoelectronic devices. Application of such structures can be attractive for overall and local enhancement of light from patterned areas of the light emitting diode surface and for lightwave-guiding devices. We present techniques useful for PhC patterning and for patterning of different optic structures in surface of new promising material polydimethylsiloxane (PDMS). Paper proposes nanoimprint technology for fabrication of PhC in the surface of thin PDMS membranes for possible application in light emitting diodes. By PDMS patterning and its positioning on the device surface one can achieve original optical properties of optoelectronic devices. We also present new technique for fabrication of surface-relief fiber Bragg grating (SR FBG) based on PDMS waveguide.

Keywords: *Polydimethysiloxane, nanoimprint lithography, photonic crystal.*

1. Introduction

Photonics has recently become an intensively evolving area where the possibilities of photonic structures or crystals (PhC) for integrated optoelectronics were found. PhCs have a periodic change of refractive index at the interface of two materials, which causes the creation of photonic band gap in the crystal [1 and 2]. These features of PhCs cause the effects that are not possible to obtain by means of conventional optical and optoelectronic devices. From the application point of view, there is a wide range of PhCs applications with perspective of significant improvement of features of optoelectronic devices as light emitting diodes, lasers and optical waveguides with photonic structure [3 - 5]. Typically, a photonic light emitting diode (LED) shows enhancement of light extraction efficiency due to the improvement of total internal reflection on the semiconductor-air interface diffraction light on surface roughness or photonic band gap [6]. Also PhC in lightwave-guiding applications increased the transmission of sharp bended waveguides and Y-splitters [7].

There are different ways how to fabricate optical elements and devices with patterned surface for application in optics and optoelectronics. This paper summarizes few techniques useful for PhC patterning and for patterning of different optic structures using new promising material polydimethylsiloxane (PDMS), with significant optic and elastic properties. In visible range of spectrum, PDMS shows high transparency and is well formable by imprinting techniques. By PDMS patterning and its positioning on the device surface one can achieve original optical properties of optoelectronic devices [8]. The paper proposes technology for fabrication of PDMS membranes which were patterned by PhC in the surface. Such PhC PDMS membranes can be attractive for application in optoelectronic devices. Using direct laser writing (DLW) technique, Fresnel zone plate (FZP) was prepared in the surface of thin PDMS membrane. We also present a new technique for fabrication of surface-relief fiber Bragg grating (SR FBG) embedded in PDMS waveguide.

2. PDMS membranes with PHC

Typically, PhC are prepared on different metal and semiconductor surfaces. Here, we present a technique for surface patterning of thin PDMS membranes. In this experiment we used interference lithography in combination with PDMS imprinting to prepare planar two-dimensional (2D) PhC at the PDMS membrane surface.

2.1 Experimental

The patterned PDMS membranes are fabricated using interference lithography in patterning process of a thin photoresist layer and followed by imprinting of liquid PDMS. First, 2-3 μm thin layer of positive photoresist AZ 5214E was

* [1]Dusan Pudis, [1]Daniel Jandura, [1]Peter Gaso, [1]Lubos Suslik, [2]Pavol Hronec, [1]Ivan Martincek, [2]Jaroslav Kovac, [1]Sofia Berezina
[1] Dept. of Physics, University of Zilina, Slovakia
[2] Inst. of Electronics and Photonics, Slovak University of Technology, Bratislava, Slovakia
E mail: pudis@fyzika.uniza.sk

spin coated on GaAs (100) substrate using SPIN 150 coater. The photoresist layer was patterned by interference lithography in Mach-Zehnder configuration using multiple exposure process [9]. The interference optical field is formed by the interference of two coherent beams of Toptica laser operating at wavelength of 403 nm. Interference optical field exposed the thin photoresists layer. Its period can be simply adjusted by anlge of incident beams. For this experiment the angle was 48 degree, corresponding to wavelength of 495 nm. The 10x expander was used for exposure homogeneity improving in the exposed area with diameter of 5 mm and exposure intensity of 25 mW/cm^2 in both laser beams.

2D PhC structure of square symmetry was achieved by double exposure process, with a sample perpendicular rotation between exposures [10]. After exposure, the sample was developed in AZ 400K developer for 10 s and rinsed in deionized water. Using the interference lithography process we obtained patterned surface in thin photoresist layer in area of 5x5 mm^2.

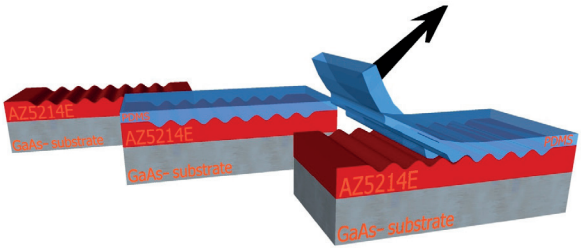

Fig. 1 PDMS membrane fabrication process using imprinting process with patterned positive photoresist AZ5214E deposited on GaAs substrate

In the next process, polydimethylsiloxane layer was deposited. Liquid PDMS was prepared from components of Sylgard 184 elastomer and curing agent at ratio 10:1. For a uniform surface, the 30 µm thin PDMS layer was spin coated at 4000 rpm on the patterned photoresist layer. Subsequently, the sample was cured for 45 min at 75°C. After PDMS curing, the PDMS membrane was mechanically removed from the sample (Fig. 1). The original patterned photoresist structures and imprinted PDMS membranes were finally investigated in optical microscope and atomic force microscope (AFM).

2.2 Results and discussion

Quality of imprinted PDMS membranes as well as original structures prepared in the photoresist layer was analyzed in AFM microscope as is shown in Fig. 2. In Fig. 2a, AFM image of original photoresist master prepared in the thin photoresist layer is shown. Fig. 2b shows surface of imprinted PDMS membrane. Period of the photoresist structure is 495 nm and imprinted structure in PDMS preserves the photoresist pattern with the same period. Thickness of prepared PDMS membranes is app. 30 µm. Membrane thickness can be controlled by PDMS viscosity and speed of coating process. Much thinner membranes could be prepared, however, manipulation of thin PDMS membrane is then complicated. More detailed in-depth analysis was investigated from line profiles of AFM analysis taken at diagonal direction of 2D structure (Figs. 2c and 2d). Depth of app. 140 nm was observed from AFM line profile for the patterned photoresist layer (Fig. 2c) and nearly 100 nm for imprinted PDMS membrane surface (Fig. 2d).

Such patterned PDMS membrane can be directly applied on optoelectronic devices, e.g. on top of a LED chip or other elements. Such PhC structures have capability to significantly improve their optoelectronic properties as light extraction efficiency and far-field radiation pattern [10].

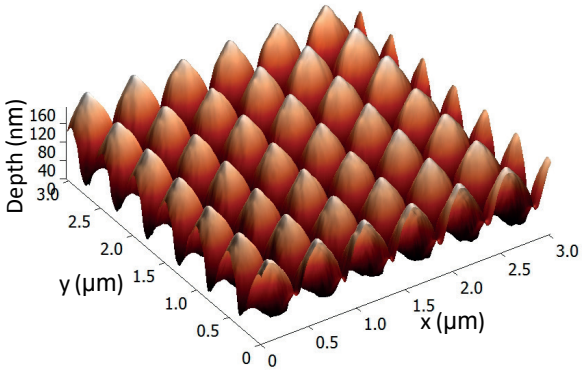

a)

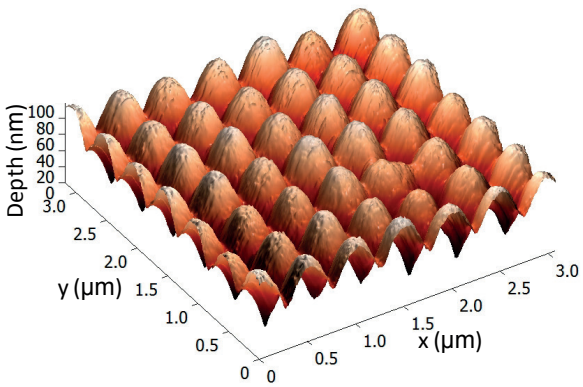

b)

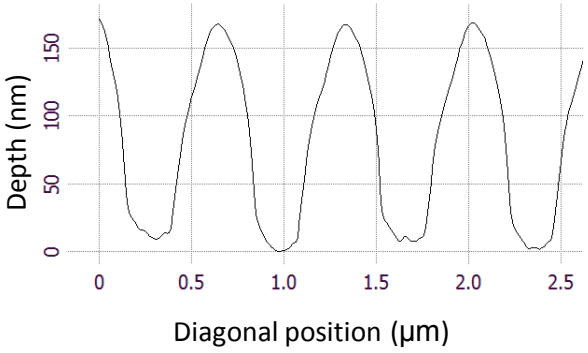

c)

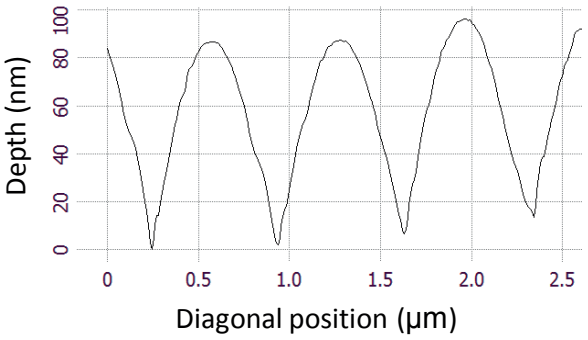

d)

Fig. 2 AFM images of surfaces: a) original patterned photoresist layer and b) imprinted PDMS surface. Line profile of patterned c) photoresist layer and d) imprinted PDMS membrane taken at diagonal direction

3. PDMS membranes for microptics

Improving of light divergence from small light emitting sources motivates to fabrication of micro-optic devices. The main idea of this part is to fabricate Fresnel zone plate for improvement of beam divergence from a LED chip using experimental experiences with PDMS membrane fabrication. PDMS is appropriate material on which FZP can be prepared and directly applied in a LED surface. For the FZP fabrication we used direct laser writing (DLW) method for a thin photoresist layer patterning and followed by Al etching process on PDMS membrane surface [11].

FZP is a structure where alternate transparent and opaque zones. These zones are defined by concentric circles with defined radius. Appropriate radius is given so, that the incident light constructively interferes at the focus of FZP. It follows that the arrangement of zones depends on the collimated light wavelength and desired focus distance. Radius of individual circles is then given by following equation

$$R_n = \sqrt{n\lambda f + \frac{n^2\lambda^2}{4}} \qquad (1)$$

where n is integer describing order of circle, λ is wavelength and f is focus distance. With respect to this equation and desired focal length, we prepared FZP on glass and PDMS substrate.

3.1. Experimental

Patterning of a thin photoresist layer was achieved by scanning of a focused laser beam on a sample surface. High resolution dual-axes galvanometer mirror system GVSM002 controlled by computer was used for DLW technique. To control scanning system, the LabView program automatically calculates desired radius of FZP circles and applies them to control scanning process of galvanometer mirrors. In arrangement with 10 x objective the scanning range of the system is few hundreds of micrometers and the focused laser spot in the photoresist layer achieves resolution better than 3 μm [12].

For resolution optimization and focusing capability, the glass substrate with a thin deposited Al layer was used. In order to create opaque zones on glass, a 50 nm Al layer was evaporated on the glass surface using K975X turbo-pumped thermal evaporator. Positive photoresist was used as a mask for Al layer patterning (Fig. 3a).

Using 405 nm laser beam, the sample was irradiated through the objective at desired positions. After exposure, the sample was developed and subsequently wet etched in solution of H_3PO_4 and ethanol at the ratio 1:10 at 50°C, where uncovered Al parts were etched (Fig. 3b). Finally, the remaining photoresist was removed in solvent (Fig 3c).

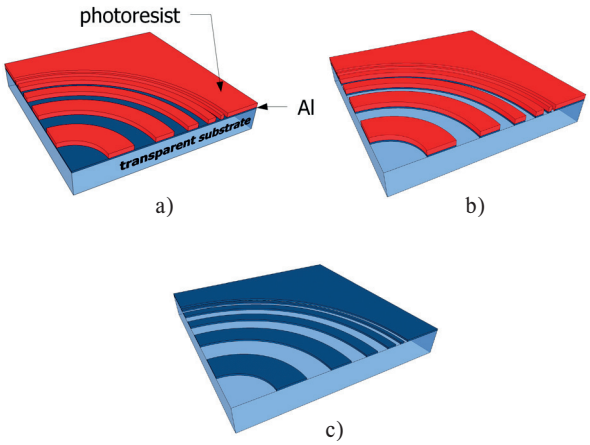

Fig. 3 FZP fabrication process: a) exposition and developing process of thin photoresist layer deposited on Al layer b) Al layer wet etching c) photoresist removing

Transparent parts of created FZP are shown in optical microscope image in Fig. 4a. Fabricated FZP structure was

designed for wavelength λ = 600 nm and for focal length *f* = 10 mm. In order to apply FZP directly on LED chip we prepared FZP on a thin PDMS layer. For uniform surface, the 30 μm thin PDMS layer was spin coated at 4000 rpm on a glass substrate. Subsequently, the sample was cured for 45 min at 75°C. FZP based on PDMS layer was patterned by the same lithography process using thin positive photoresist layer (3μm) followed by exposure using DLW technique. The FZP prepared on PDMS membrane is shown in Fig. 4b.

a)

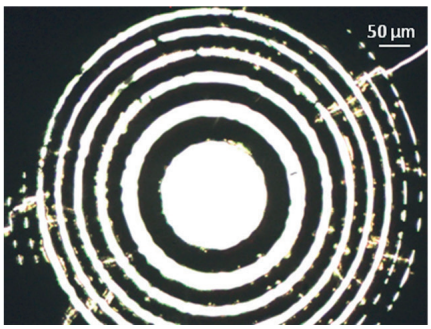

b)

Fig. 4 Optical microscope image of FZP structure prepared on a) glass and b) PDMS surface

The focal length of prepared FZP was measured in simple experimental arrangement LED source-FZP-CCD camera and calculated using standard lens equation. The measured focal length was approximately 9.5 mm, which nearly corresponds to the designed FZP with *f* = 10 mm. The real image of orange LED source with central wavelength λ = 612 nm using prepared FZP is shown in Fig. 5. Due to a wide spectral range of LED source the real image is not perfectly contrasted, because the FZP focal length shows dependence on the used wavelength. The orientation of the image is reversed in comparison with original object as is shown in inset figure in Fig. 5, which fulfils the basic optical imaging principle and lens equation. We conclude that FZP based on PDMS can be directly applied on the LED surface and can lead to modification of beam shape.

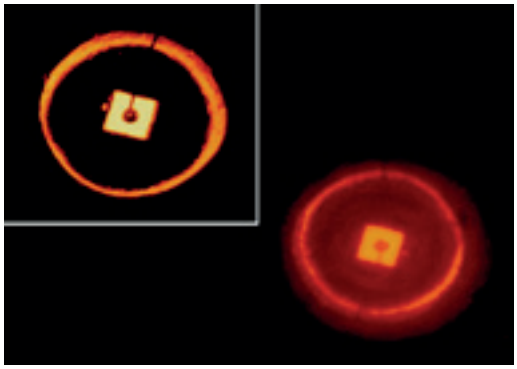

Fig. 5 Real LED image after imaging using FZP and original object (inset figure)

4. Surface-relief fiber bragg grating in PDMS

In this part, we describe a new fabrication method for SR FBG based on PDMS waveguide fabricated by combination of interference lithography process and imprinting technique. PDMS shows unique elastic properties allowing elongation for more than 100%, which may be attractive in tunable optic devices based on FBG [13 and 14].

4.1 Experimental

For the fabrication of SR FBG in the PDMS layer, the combination of interference lithography and imprinting technique with liquid PDMS was used. Individual steps of the whole process are described in Fig. 6. The first step is hand made fiber drawing process from positive photoresist AZ5214E that will finally form a core of waveguide (Fig. 6a). It was necessary to achieve appropriate fiber diameter in the range 10-100 μm. In the next step, the prepared fiber was placed on a PDMS layer (Fig. 6b). For fabrication of the PDMS layer, we used PDMS Sylgard 184. It was prepared in the same way as described in PDMS membrane fabrication. It is necessary to achieve partial curing of the PDMS at temperature of 60 °C for about 20 minutes which ensures appropriate viscosity. If a photoresist fiber is placed on such a PDMS layer, the fiber is slightly immersed. Subsequently, the photoresist fiber is exposed by one dimensional interference optical field (Fig. 6c). Interference workplace based on Mach-Zehnder configuration was used to create one-dimensional interference pattern. Exposed structure photoresist fiber - PDMS layer was developed in AZ400 K developer to remove exposing parts of photoresist and rinsed in deionised water. One-dimensional periodic surface structure with length of app. 1 mm was patterned on the photoresist fiber surface with normal orientation to the fiber axis (Fig. 6d).

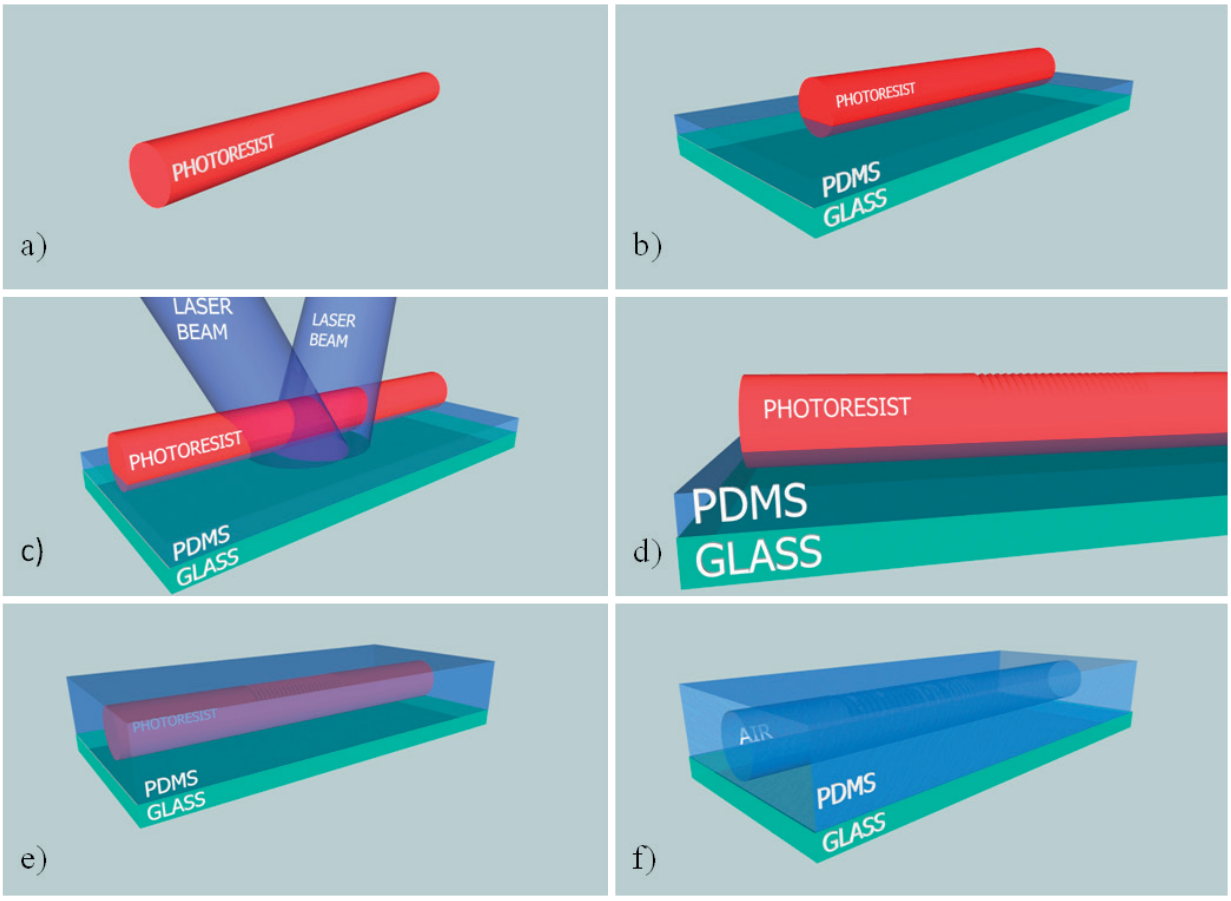

Fig. 6 Schema of SR-FBG fabrication process in PDMS layer

The patterned photoresist fiber was covered with an additional layer of PDMS in order to form a waveguide core (Fig. 6e). One-dimensional structure from the photoresist fiber was imprinted into the covered PDMS layer. After curing PDMS in the next step, photoresist was removed in Microposit Solvent EC 11 in a long time process (app. 24 hours) (Fig. 6f). By this process, the SR-FBG is obtained in the PDMS material.

4.2 Results and discussion

After removing the photoresist from PDMS waveguide, we obtained air core waveguide structure in PDMS material with SR-FBG. Fig. 7 shows microscope image of SR-FBG patterned in thin photoresist fiber placed on PDMS layer.

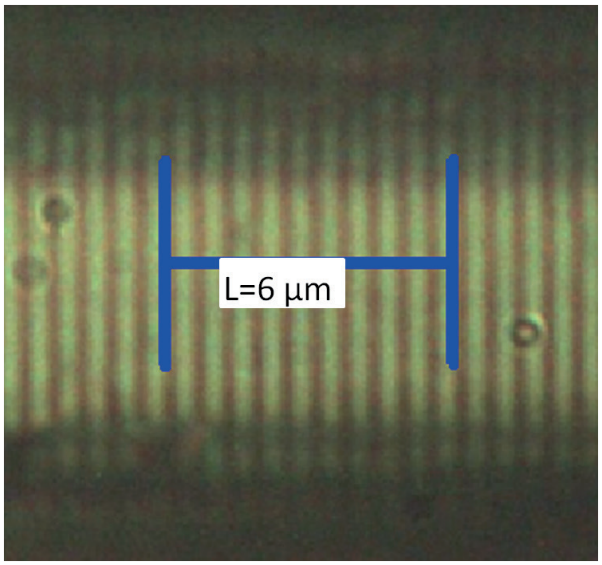

Fig.7 Optical microscope image of prepared SR-FBG on surface of photoresist fiber

The prepared air core waveguide is not appropriate for further low-loss guiding application. Then the core was filled with material which refractive index greater than PDMS cladding ($n > 1.45$). For this purpose, a different mixture of PDMS was used. Such prepared PDMS structure can be used in waveguide applications for light filtration in specified region.

5. Conclusion

We presented few patterning techniques leading to fabrication of PDMS based micro- and photonic structures. We prepared PDMS membranes with 2D PhC patterned surface of period 495 nm and depth of 100 nm using interference lithography and imprinting technique. Such membranes can be simply applied on different optoelectronic device surfaces and could modify final optical properties.

We also described fabrication of PDMS membranes for micro-optics. We presented fabrication of Fresnel zone plate structure prepared on PDMS substrates using direct laser writing technique. We favor this FZP prepared on PDMS substrate for direct application on LED chips, which may be attractive for output beam collimation.

We presented new fabrication method of SR-FBG waveguide prepared in PDMS layer. Waveguide structure with SR-FBG was prepared in PDMS with period of 600 nm. For patterning of Bragg grating in fiber surface, the interference lithography was used in combination with imprinting technique. Fabricated SR-FBG in PDMS can be used for application in waveguide optics and optoelectronics.

Mechanical and optical properties of PDMS favor this material for application in optic and optoelectronic devices. Variability of presented techniques opens wide possibilities to form submicrometer periodic structures in PDMS based devices.

Acknowledgement

This work was supported by the Slovak National Grant Agency under the projects No. VEGA 1/1058/11 and 1/0528/12 and the Slovak Research and Development Agency under the project No. APVV 0395 12. The authors wish to thank for the support to the R&D operational program Centre of excellence of power electronics systems and materials for their components II. No. OPVaV-2009/2.1/02-SORO, ITMS 26220120046 funded by European regional development fund (ERDF).

References

[1] JOANNOPOULOS, J. D., MEADE, R. D., WINN, J. N.: *Photonic Crystals - Molding the Flow of Light*, Princeton University Press, Princeton 1995.
[2] LOURTIOZ, J. M.: *Photonic Crystals - Towards Nanoscale Photonic Devices*, Springer-Verlag Berlin Heidelberg, Berlin 2008.
[3] KIM, S. H., LEE, K. D., KIM, J. Y., KWON, M. K., PARK, S. J.: *Nanotechnology* 18, 2007, p. 055306.
[4] ALTUG, H., VUCKOVIC, J.: *Opt. Express* 13, 2005, pp. 8819-8828.
[5] LONCAR, M., NEDELJKOVIC, D., DOLL, T., VUCKOVIC, J., SCHERER, A., PEARSALL, T. P.: *Appl. Phys. Lett.* 77, 2000, pp. 1937-1939.
[6] FUJII, T., GAO, Y., SHARMA, R., HU, E. L., DENBAARS, S. P., NAKAMURA, S.: *Appl. Phys. Lett.* 84, 2004, pp. 855–7.
[7] KRAUSS, T. F.: *Phys. Stat. Sol.* 197, 2003, pp. 688-702.
[8] VALOUCH, S., SIEBER, H., KETTLITZ, S., ESCHENBAUM, C., HOLLENBACH, U., LEMMER, U.: *Opt. Express* 20, 2012, pp. 28855-28861.
[9] SKRINIAROVA, J., PUDIS, D., MARTINCEK, I., KOVAC, J., TARJANYI, N., VESELY, M., TUREK, I.: *Microelectron. J.* 38, 2007, pp. 746-749.
[10] PUDIS, D., SUSLIK, L., SKRINIAROVA, J., KOVAC, J., MARTINCEK, I., KOVAC JR., J., HASCIK, S., KUBICOVA, I., NOVAK, J., VESELY, M.: *Optics and Laser Technol.* 43, 2011, pp. 917-921.
[11] YANG, R., TANG, W., HAO, Y.: *Opt. Express* 19, 2011, pp. 12348-12355.
[12] PUDIS, D., KUBICOVA, I., GASO, P., JANDURA D.: *Technolog* 1, 2012, pp. 13-15.
[13] MELTZ, G., MOREY, W. W., GLENN, W. H.: *Opt. Lett.*, Vol. 14, 1989, pp. 823–825.
[14] OTHONOS, A., KALLI, K.: *Fiber Bragg Gratings: Fundamentals and Applications in Telecommunications and Sensing*, Artech House, Boston, 1999.

Ivana Lettrichova - Dusan Pudis - Agata Laurencikova - Stanislav Hasenohrl
Jozef Novak - Jaroslava Skriniarova - Peter Gaso *

NSOM LITHOGRAPHY FOR ORGANIZED GROWTH OF GAP NANOWIRES

In this contribution, near field scanning optical microscope (NSOM) lithography is presented as a tool for organized growth of nanowires. Non contact mode of NSOM lithography was used to pattern planar structures in photoresist deposited on GaP substrate. In combination with lift-off technique, metal-catalyst particles on GaP substrate for subsequent growth of GaP nanowires were prepared. Different periodic and predefined arrangements of GaP nanowires were achieved.

Keywords: *NSOM lithography, predefined structure, organized nanowire growth.*

1. Introduction

Preparation of semiconductor nanowires (NWs) has been studied intensively due to their unique structural and physical properties that offer big potential for technological applications. Standard technique for one-dimensional growth of NWs is vapor-liquid-solid (VLS) mechanism invented in 1960 by Wagner [1]. VLS process starts with formation of a small liquid droplet followed by alloying, nucleation and growth of NW [2]. Growth is started on a clean semiconductor surface. First, metal particles with diameter below 100 nm are deposited on the substrate surface. Such substrate is heated in reaction chamber until particles melt and form liquid droplets. The semiconductor material is dissolved and forms an alloy which has lower melting point in comparison with pure metal. In this phase, a gas containing growth material flows through the reaction chamber and incorporation of precursor atoms into the alloy leads to supersaturation of semiconductor component. It precipitates at solid-liquid interface which starts growth of NW with diameter determined by size of the droplet [2].

Various technologies have also been used for spatial positioning or organized growth of NWs [2 and 3]. Very convenient is combination of VLS NW growth mechanism with nanopatterning techniques. Patterned metal arrays function as a template; grown NWs have the same pattern, diameter of NWs is correlated to the size of metal particles. Various methods can be applied for controlled preparation of metal template: photolithography [4], e-beam [5], interference [6] or nanosphere lithography [7], as well as manipulation of single gold nanodots [8].

One of optical technologies for planar structure fabrication is near-field scanning optical microscope (NSOM) lithography [9 and 10]. It employs NSOM in illumination mode, where patterning of structures is done through a maskless exposure process performed by the optical near field produced at the tip of scanning fiber probe. Since it is a scanning technique, NSOM lithography is a time-consuming process. On the other hand, this allows wide design flexibility and besides periodic patterns, it allows fabrication of 2D structures with predefined arrangement. When comparing to different scanning techniques, e. g. e-beam lithography, this technique is low-cost and it doesn't require vacuum environment. In non-demanding experimental setup, exposure of defined regions directly on the device on chip can be achieved. Moreover, due to the exploitation of the near field properties, the spatial resolution limit known from far-field microscopy as a diffraction barrier is overcome; it is no more a function of the wavelength but rather of the fiber tip aperture diameter [11].

We demonstrate NSOM lithography as a tool for organized growth of nanowires. The non-contact mode of NSOM lithography was used to pattern planar structures in photoresist layer deposited in GaP substrate in different two dimensional (2D) grids with pitch step 1.5 – 2.5 μm. In this way, predefined metallic nanostructures on GaP surface which are used for organized GaP nanowire growth were prepared. GaP nanowires were grown

* [1]Ivana Lettrichova, [1]Dusan Pudis, [2]Agata Laurencikova, [2]Stanislav Hasenohrl, [2]Jozef Novak, [3]Jaroslava Skriniarova, [1]Peter Gaso
[1]Div. of Optics and Photonics, Dept. of Physics, University of Zilina, Slovakia
[2]Inst. of Electrical Engineering, Slovak Academy of Sciences, Bratislava, Slovakia
[3]Inst. of Electronics and Photonics, Slovak University of Technology, Bratislava, Slovakia
E-mail: lettrichova@fyzika.uniza.sk

by VLS technique using Au seeds defined by photoresist layer patterning followed by metal evaporation and lift-off technique. Both periodic and predefined 2D arrangements of GaP nanowires were achieved and analyzed.

2. Experimental setup

Schematically is the NSOM lithography process shown in Fig. 1. Experimental stage for NSOM lithography requires high resolution 3D nanoposition system controlled by computer. Because of the photoresist sensitivity in the violet-blue wavelength range, a modulated 473 nm diode-pumped solid state laser was used as a light source. The laser beam was focused by micro objective into conventional optical fiber, which was coupled to the fiber probe fixed on the 3D axis nanoposition piezosystem. Scanning range of the nanoposition system is 20 x 20 μm^2 and a movement resolution is less than 5 nm. The non-contact mode of NSOM lithography was performed in this experiment, where the fiber tip realized the in-plane movement over the sample without touching the sample surface.

As a fiber probe, a home-made metal coated apertureless fiber tip was used. It was prepared by pulling of conventional optical fiber in small flame followed by coating by Al evaporation.

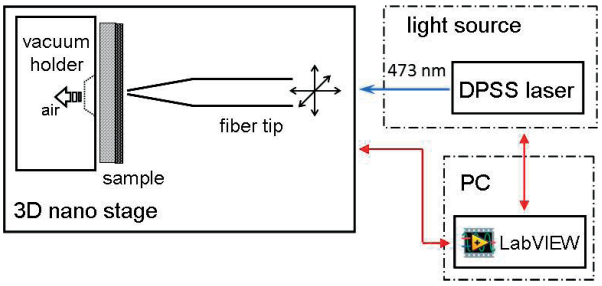

Fig. 1 Experimental set-up for NSOM lithography

GaP NWs were grown on GaP(111)B substrate by VLS technique using Au seeds. For organized growth of NWs, it is necessary to prepare highly ordered and spatially separated metal-catalyst particles. It was achieved using NSOM lithography process in combination with lift-off technique. Schematically, the process is shown in Fig. 2.

First, 500 nm thin photoresist AZ 5214E was spin-coated on the GaP substrate with post-baking at 65 °C for 2 minutes and at 103 °C for 3 minutes. Photoresist layer was subsequently exposed by NSOM lithography in experimental set-up shown in Fig. 1. After exposure, photoresist was developed in AZ 400K developer for 30 s and rinsed in deionized water (Fig. 2a). Different periodic and predefined planar structures in grid with pitch step of 1.5 – 2.5 μm were created in photoresist layer.

In the next step, 2 nm thick Au layer was evaporated on the top of the sample (Fig. 2b). Lift-off technique was used to remove residual photoresist so that the spatially organized Au seeds were formed on the GaP substrate (Fig. 2c).

NWs were grown in palladium purified H_2 carrier gas from phosphine (PH_3) and trimethylgallium (TMGa) used as the phosphorus and gallium sources, respectively. The doping source was diethylzinc (DEZn). For NWs growth, the GaP substrate with Au seeds was heated at 20 mbar to 650 °C for 10 minutes under a H_2 + PH_3 flow with PH_3 molar fraction of 1.67 x 10^{-2}. Within the next 10 minutes, the pressure was increased to 100 mbar and the temperature was lowered to 500 °C and stabilized. The TMGa and DEZn flows were finally switched into reactor and the growth of NWs proceeded in VLS mode (Fig. 2d). The molar fractions of PH_3 and TMGa in the carrier gas during the growth were 7.5 x 10^{-3} and 1.25 x 10^{-5}, respectively (V/III ratio of 600). After 4 min growth, app. 3 μm long GaP NWs were grown.

3. Results and discussion

First, 2D structures with periodic and predefined arrangement were prepared in photoresist layer deposited on GaAs substrate. For preparation of 2D structures in GaAs using NSOM lithography, (001) oriented GaAs substrate was used. Exposure

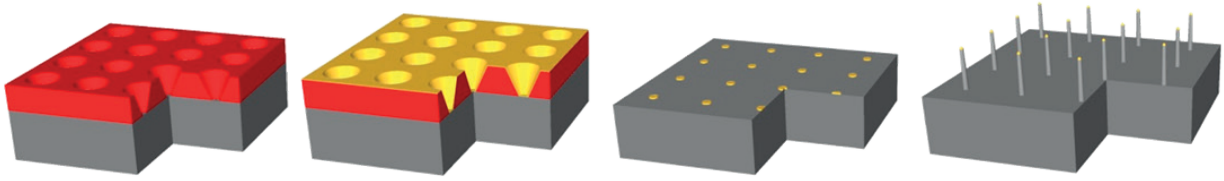

a) b) c) d)

Fig. 2. Fabrication process for organized growth of NWs using NSOM lithography: a) structure patterning in photoresist layer, b) Au coating by evaporation, c) lift-off, creation of organized Au seeds and d) NWs growth by VLS technique.

by the near field of the fiber tip controlled by PC leads to formation of 2D patterns with desired arrangement.

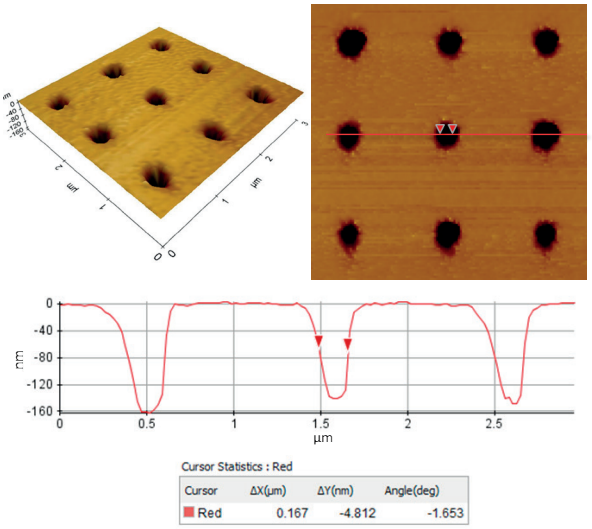

Fig. 3 AFM image and line profile analysis of prepared periodic structure with 1 µmm period in both directions and air hole FWHM app. 170 nm

Example of prepared 2D periodic structure is shown in Fig. 3. Air holes were arranged in square lattice with period 1 µm in two perpendicular directions. Detail morphology of prepared structure was examined using atomic force microscope (AFM). Line profile analysis documents that full width at half maximum (FWHM) of patterned air holes is app. 170 nm and the depth is about 160 nm. Due to the nearly Gaussian shape of the exposing optical field irradiated from the fiber probe, air hole edges are oblique, which is in good agreement with published results on NSOM lithography [10]. This characteristic appears inconvenient for etch step, nevertheless, it may be interesting for patterning of metal-catalyst arrays for NWs growth.

NSOM lithography followed by Au evaporation and lift-off technique was used to pattern Au seeds on GaP substrate for further organized NW growth. After 4 min growth, groups of app. 3 µm long GaP NWs were grown from each Au seed. Different Au seed arrangements were patterned in the GaP surface. In Fig. 4, there is shown scanning electron microscope (SEM) image of periodic arrangement that was designed in square lattice with pitch step of 2.5 µm. Due to big Au particle diameter (about 400 nm), GaP NWs were grown radial from the seed and they form a hedgehog-like structure (detail in SEM image in Fig. 4b).

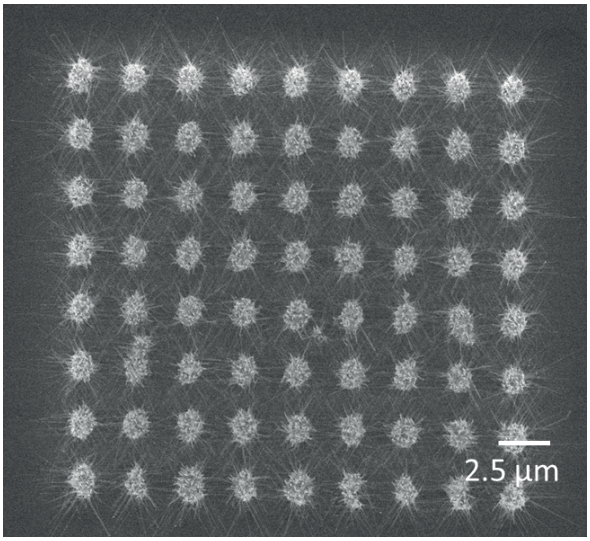

a)

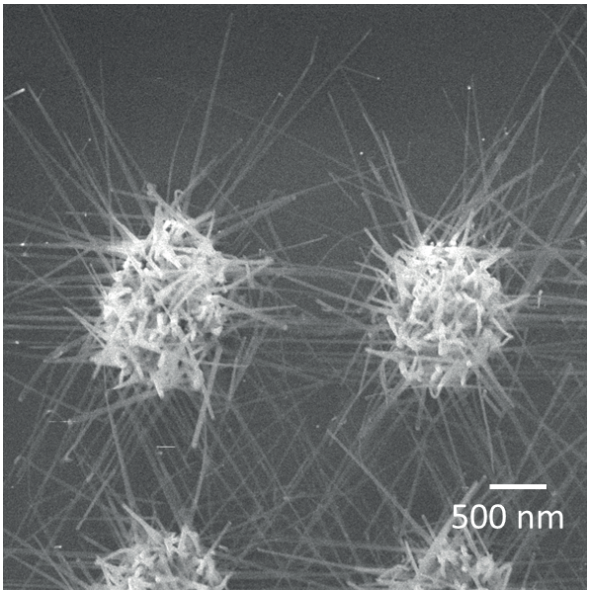

b)

Fig. 4 a) Top-view of prepared organized GaP NWs in regular arrangement and b) detail, SEM images

One of NSOM lithography advantages as scanning technique is possibility to prepare any predefined arrangement of patterned structure. In this way, Au seeds were arranged in different predefined patterns. Example of GaP NWs grown in predefined arrangement is shown in Fig. 5. Heart-shaped structure was designed in grid with 2.5 µm pitch step. Due to Au remains in middle part of heart-shaped structure after lift-off technique, GaP NWs were also grown in central unpatterned area.

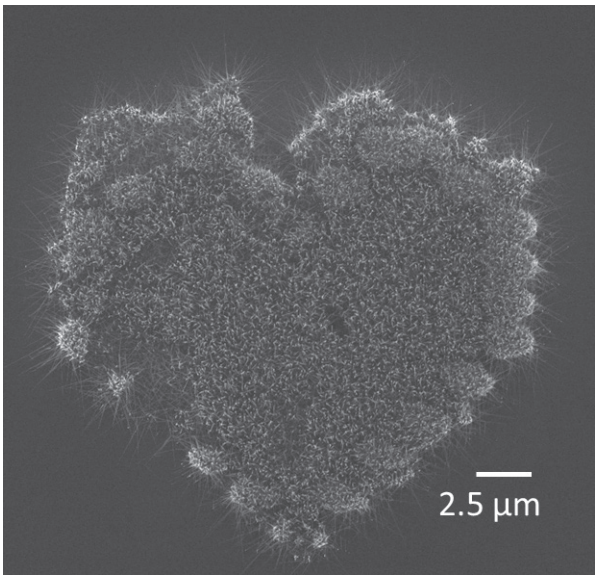

Fig. 5 Top-view of prepared organized GaP NWs in predefined arrangement, SEM image

Diameter and number of metal particles relates to thickness of evaporated Au layer, as well as to dimensions of photoresist holes formed by lithography process. For NSOM lithography, Gaussian shape of patterned air hole is typical and resolution limits depend on fiber probe apex dimensions [10]. We assume that by fine-tuning of the exposure process, it is possible to reduce photoresist hole diameter down to tens of nanometers in order to decrease number of Au seeds per hole.

4. Conclusion

This contribution presents possibilities of non-contact NSOM lithography for organized growth of NWs. In our experimental setup, planar 2D structures with periodic and predefined arrangement with pitch step 1.5 – 2.5 µm were patterned in photoresist layer deposited on GaAs substrate. AFM line profiles document air hole FWHM down to 170 nm.

NSOM lithography was successfully applied as lithography technique for preparation of predefined metallic nanostructures on GaP surface which were used for organized GaP nanowire growth. Both periodic and predefined 2D structures were prepared and GaP NWs were grown radial from the seed to form a hedgehog-like structure.

Acknowledgement

This work was supported by the Slovak National Grant Agency under the projects No. VEGA 1/1058/11 and 1/0528/12 and the Slovak Research and Development Agency under the project No. APVV 0395 12. Authors wish to thank for the support to the R&D operational program Centre of excellence of power electronics systems and materials for their components II. No. OPVaV-2009/2.1/02-SORO, ITMS 26220120046 funded by European regional development fund (ERDF).

References

[1] WAGNER, R. S., ELLIS, W. C.: The Vapor-liquid-solid Mechanism of Crystal Growth and its Application to Silicon, *Trans. Metall. Soc.* AIME 233, 1053-1064, 1965.

[2] FAN, H. J., WERNER, P., ZACHARIAS, M.: Semiconductor Nanowires: From Self-organization to Patterned Growth, *Small* 2(6), 700-717, 2006.

[3] BARTH, S., HERNANDEZ-RAMIREZ, F., HOLMES, J. D., ROMANO-RODRIGUEZ, A.: Synthesis and Application of One-dimensional Semiconductors, *Prog. Mater. Sci.* 55, 563-627, 2010.

[4] GREYSON, E. C., BABAYAN, Y. AND ODOM, T. W.: Direct Growth of Ordered Arrays of Small-diameter ZnO Nanowires, *Adv. Mater.* 16, 1348-1352, 2004.

[5] JENSEN, L. E., BJORK, M. T., JEPPESEN, S., PERSSON, A. I., OHLSSON, B. J., SAMUELSON, L.: Role of Surface Diffusion in Chemical Beam Epitaxy of InAs Nanowires, *Nano Lett.* 4(10), 1961–1964, 2004.

[6] WEI, Y., WU, W., GUO, R., YUAN, D., DAS, S. AND WANG, Z. L.: Wafer-scale High-throughput Ordered Growth of Vertically Aligned ZnO Nanowire Arrays, *Nano Lett.* 10(9), 3414 – 3419, 2010.

[7] KOSIOREK, A., KANDULSKI, W., CHUDZINSKI, P., KEMPA, K., GIERSIG, M.: Shadow Nanosphere Lithography: Simulation and Experiment, *Nano Lett.* 4(7), 1359-1363, 2004.

[8] OHLSSON, B. J., BJORK, M. T., MAGNUSSON, M. H., DEPPERT, K. SAMUELSON, L., WALLENBERG, L. R.: Size-, shape-, and Position-controlled GaAs Nano-whiskers, *Appl. Phys. Lett.* 79(20), 3335-3337, 2001.

[9] WEGSCHEIDER, S., KIRSCH, A., MLYNEK, J., KRAUSCH, G.: Scanning Near-field Optical Lithography, *Thin Solid Films* 264, 264–267, 1995.

[10] KRAUSCH, G., MLYNEK, J.: Surface Modification in the Optical Near Field, *Microelectron. Eng.* 32, 219-228, 1996.

[11] BETZIG, E., TRAUTMAN, J. K.: Near-field Optics: Microscopy, Spectroscopy, and Surface Modification Beyond the Diffraction Limit, *Science* 257, 189-195, 1992.

Matus Molcan - Anezka Hashim - Jozef Kovac - Hubert Gojzewski - Andrzej Skumiel - Francois Royer
Damien Jamon - Peter Kopcansky - Milan Timko *

MAGNETOSOMES – BACTERIAL MAGNETIC NANOPARTICLES

The magnetic properties, magneto-optical effects and hyperthermia effect were studied in solution of magnetosomes extracted from cultivated bacteria Magnetospirillum sp. AMB-1. The properties of magnetosomes were changed using different conditions during synthesis and by modification of particles after synthesis by using sonication and ultracentrifugation methods. It was shown that adding a higher amount of Wolfe's vitamin solution (WVS) or ferric quinate (FQ) cause increase of the mean diameter from 47 nm (normal condition) up to 52 nm and 58 nm respectively. Hyperthermic measurements were performed for three types of magnetosome samples: (I) M - not influenced by separation method (long - chains magnetosomes), (II) UM - after centrifugation procedure, and (III) SM - after centrifugation procedure including sonication. The Specific Absorption Rate (SAR) decreased depending on chains shortening and decrease in hysteresis too. The SAR values were 1083, 934 or 463 W/g for the sample M, UM and SM, respectively.

Keywords: *Nanoscale materials and structures, hysteresis, ultrasound effects on biological systems, electron microscopy.*
PACS numbers: 81.07.-b, 75.60.-d, 87.50.Y-, 68.37.-d

1. Introduction

Magnetotactic bacteria are microorganisms which belong to heterogeneous group of Gram-negative bacteria with diverse morphologies and habitats. They are a diverse group of aquatic prokaryotes [1]. They create in their body the chains of magnetic crystals called magnetosomes [2].

Bacterial magnetic particles - magnetosomes can be distinguished by the regular morphology and the presence of a thin organic membrane enveloping crystals from biologically formed magnetite. Magnetosome formation is achieved by a mineralization process with biological control over the accumulation of iron and the deposition of the mineral particle with specific size and orientation within a membrane vesicle at specific locations in the cell [3].

2. General background

Magnetic bacteria have an unfathomable amount of potential value for various biomedical and biotechnological applications not only scientific interests. One of potential application areas of magnetosomes is hyperthermia. Research has shown that high temperatures can damage and kill cancer cells, usually with minimal injury to normal tissues [4]. Numerous clinical trials have studied hyperthermia in combination with radiation therapy and/or chemotherapy [5].

Since the pioneer work of Rosenblatt [6], few works have been led on the magneto-optical properties of magnetosomes. In this paper, we propose to explore some physical and magneto-optical properties of such particles in order to provide a better understanding of their behavior.

The aim of this work was isolation of magnetosomes from MTB and characterization of magnetosomes in terms of morphological, magnetically, magneto-optical and also hyperthermical properties with a view of bio-applications.

Magneto-optical effects in magnetic suspensions

Numerous materials exhibit linear or circular optical anisotropy under the influence of a magnetic field. These anisotropic media generate two effects: the magneto-optical birefringence and dichroism which introduce respectively a phase shift Δ and a difference of absorption (related to an angular parameter Ψ) between optical waves polarized along Eigen

* [1]Matus Molcan, [1]Anezka Hashim, [1]Jozef Kovac, [2,3]Hubert Gojzewski, [4]Andrzej Skumiel, [5,6]Francois Royer, [5,6]Damien Jamon, [1]Peter Kopcansky, [1]Milan Timko
[1]Institute of Experimental Physics, Slovak Academy of Sciences, Kosice, Slovakia
[2] Institute of Physics, Poznan University of Technology, Poznan, Poland
[3] Max Planck Institute of Colloids and Interfaces, Potsdam, Germany
[4] Faculty of Physics, Adam Mickiewicz University, Poznan, Poland
[5] Universite de Lyon, Saint Etienne, France
[6] DIOM EA 3523, Universite de Saint Etienne, Saint Etienne, France
E-mail: molcan@saske.sk

polarizations of the material. These Eigen polarizations are linear (along orthogonal axis x and y) or circular (along opposite circular senses + and -) for linear or circular anisotropic media, respectively. In the case of a suspension of magnetic nanoparticles in a carrier liquid, an anisotropic linear effect is obtained with a magnetic field direction perpendicular to the light beam (Oz), whereas circular effect needs a longitudinal magnetic field.

Both anisotropic media may be fully characterized by the two ellipsometric angles Δ and Ψ linked to the ratio of eigenvalues:

$$\frac{t_x}{t_y}\left(or\frac{t_+}{t_-}\right) = \tan\psi\,\exp(i\Delta),$$

where $t_{x,y}$ and $t_{+,-}$ are transmission coefficients of linear or circular Eigen polarizations. For linear effect, one often uses the expression:

$$\Delta n = \frac{\lambda}{2\pi e}\Delta$$
$$\Delta k = \frac{\lambda}{\pi e}\left(\psi - \frac{\pi}{4}\right)$$

where e is the sample thickness, λ the wavelength, $\Delta n = n_x - n_y$ the linear birefringence and $\Delta k = k_x - k_y$ the linear dichroism.

The anisotropic circular effect is the well-known Faraday effect: a Faraday Rotation γ_F associated to a Faraday Ellipticity ε_F:

$$\Delta = 2\gamma_F$$
$$\tan\psi = 1 + 2\varepsilon_F$$

As these anisotropic media play a role on the behavior of polarized light, the study of the modification of the state of polarization of a linearly polarized light is a way to measure this effect. A full description of these measurements is given by Jamon [7].

Suspensions of magnetic nanoparticles are able to produce these two different effects depending on the orientation of the applied magnetic field. When the magnetic field H is parallel to the laser beam direction, the magnetic moments μ of the particles align along the beam producing the Faraday Effect [8].

A suspension of magnetic nanoparticles can also produce a linear anisotropy when it is submitted to a magnetic field whose direction is perpendicular to the laser beam. This linear anisotropy originates from the alignment of the optical axes of the nanoparticles with the field direction through a rotation of the core body of the particles. This rotation is due to the external magnetic field through an orientation of the magnetic moments of the particles. Indeed, the optical axis of a particle is linked to the magnetic moment through anisotropy energy [7 and 9].

Magnetic Fluid Hyperthermia

The body maintains a normal temperature of 37 °C. Healthy cells, however, can survive temperatures up to 42°C. According to the National Cancer Institute, hyperthermia cancer treatment kills cancerous cells by elevating their temperatures to the therapeutic temperature range, 42-45°C. This approach can destroy tumors with minimal damage to healthy tissues and, therefore, limit negative side effects [10].

For the case of placing a magnetic fluid into an external alternating magnetic field, the magnetic vector ***M*** in that sample undergoes reorientation in space following the magnetic field intensity vector ***H***. As a result of the phase delay of the magnetic vector ***M*** in relation to the vector ***H***, a part of the magnetic field energy undergoes irreversible conversion into thermal energy [11].

Magnetic losses in an alternating magnetic field to be utilized for heating arise due to different processes of magnetization reversal in the particle system: (1) hysteresis, (2) Nèel or Brown relaxation, and (3) frictional losses in viscous suspensions [12].

For multidomain ferro- or ferrimagnetic materials, heating is due to hysteresis losses. Indeed, large particles of such materials contain several sub-domains, each of them having a definite magnetization direction. When exposed to a magnetic field, the domain with magnetization direction along the magnetic field axis grows and the other ones shrink. This phenomenon is called ''domain wall displacements''. As this phenomenon is not reversible, i.e. magnetization curves for increasing and decreasing magnetic field amplitudes do not coincide, the material is said to exhibit a ''hysteresis behavior'' and produces heat under AC magnetic field. In sub-domain particles (superparamagnetic particles) no heating due to hysteresis losses can occur because there is no domain wall. In this case, an external AC magnetic field supplies energy and assists magnetic moments to rotate in overcoming the energy barrier E = KV, where K is the anisotropy constant and V is the volume of the magnetic core. This energy is dissipated when the particle moment relaxes to its equilibrium orientation (Nèel relaxation). For both types of particles, heating can also be due to the rotational Brownian motion within a carrier liquid, i.e. the rotation of the magnetic particle as a whole because of the torque exerted on the magnetic moment by the external AC magnetic field. In this case, the energy barrier for reorientation of a particle is determined by rotational friction within the surrounding liquid [13].

The experimental setup is shown in Fig. 1. This figure presents the experimental setup used for recording temperature changes in the ferrofluid that is subjected to the alternating magnetic field. The ferrofluid sample placed in a glass vial is mounted inside the solenoid and represents an element of the RLC series circuit. The circuit is supplied by the sinusoidal signal generator with a signal of frequency f and voltage U [14].

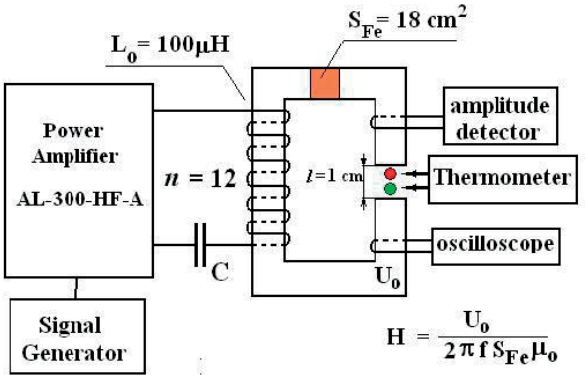

Fig. 1 Scheme of the measuring device for studying the effect of heating

3. Material and methods

Bacterial magnetosomes were synthesized by biomineralization process of magnetotactic bacteria Magnetospirillum strain AMB-1. Magnetospirillum Magnetotacticum sp. AMB-1 was grown microaerobically at 25 °C in grown medium for a period of 10-14 days. A microaerobic condition was establishing nitrogen, using copper as a reducing agent, and was subsequently dispersed into culture tubes for a period of 1 h. The detailed description of the cultivation process of the bacteria is given in our previous contribution [15].

For the isolation of the magnetosome particles from bacterial body, we used the modified method described by Karen Grünberg et al. [16]. For the isolation of magnetosomes approximately 100 ml cell culture of Magnetotacticum Magnetospirillum suspended in 100 ml of 20 mM HEPES-4 mM EDTA, pH 7.4, was split up (disrupted) by signification. The unbroken cells and the cell debris were removed from the sample by centrifugation (30 min, 9000 rpm). The cell extract was placed on magnet (NdFeB-magnets, 1h). The black magnetosomes sediment at the bottom of the tube and the residual contaminating cellular material was retained in the upper part of the tube. The residual contaminating cellular material was decanted. To eliminate the electrostatically bound contamination, the magnetic particles were rinsed first with 50 ml of 10 mM HEPES-200 mM NaCl, pH 7.4, and subsequently with 100 ml of 10 mM HEPES, pH 7.4. After removal of the cell extract from the magnets, the magnetic particles were flushed with 10 mM HEPES buffer. The magnetosome suspension (black sediment) was centrifuged (18000 rpm, 30 min). After centrifugation the cell extract was placed on the magnet for 30 minutes. The magnetic particles were sediment at the bottom of the tube, whereas residual contaminating cellular material was retained in the upper part of the tube. The last procedure was repeated ten-times to obtain well purified magnetosomes.

In order to improve cultivation process the culture medium was changed by adding higher FQ amount and higher WVS amount comparing to normal culture medium (NP).

To obtain the individual magnetosomes, the isolated magnetosome chains (sample M) were ultracentrifuged at the speed of 100 000 rpm for 4 hours at 4°C (sample UM) and ultracentrifugated at 100 000 rpm for 3h and sonicated at power of 120 W for 3 hours (sample SM), respectively.

The morphological properties and size of magnetosomes were estimated from scanning electron microscopy (SEM) and transmission electron microscopy (TEM). The micrographs of magnetosomes were obtained by low-voltage scanning electron microscope (LEO 1530 Gemini, Carl Zeiss NTS, Oberkochen, Germany) and TEM using JEOL1200EX microscope working at 120 kV. The samples for TEM experiments were prepared on amorphous carbon foil by micropipette of diluted aqueous solution of magnetosomes. The solution (solvent) was left to dry completely at room temperature. Samples for SEM were prepared by spin coating (Süss MicroTec, model Delta 80 BM) and drop coating deposition on polished silicon wafers (Grinm Semiconductor Materials Co., Ltd.). The particle size and its distribution were analyzed by Ellipse 2.08 image processing program supplied with segmentation modules. The whole process of analysis consists of three steps: calibration, segmentation and calculation of size (more details [17]).

The micrographs of magnetosomes were obtained by Transmission Electron Microscopy (TEM) FEI Tecnai F20 S-TWIN Philips. TEM was operated using the accelerating voltage of 200 kV in a bright field mode.

For Atomic Force Microscopy (AFM) the samples were prepared by spin coating. Magnetosomes diluted in HEPES solution (1 mM HEPES solution in double purified MilliQ water) were deposited on polished silicon wafers at rotation time of 60 s and rotation speed of 1500 rpm. Prior the depositions silicon wafers were chemically treated by Piranha solution later flushed by pure water and dried under a nitrogen stream. After deposition the layer of magnetosomes was left to dry completely at room temperature. AFM experiments were performed by NanoWizard II JPK. The AFM images were obtained in the tapping mode with a standard AFM tip (Olympus, model OMCLAC 160 TS, nominal tip radius < 10 nm). All measurements were done in air (relative humidity in the range of 25-40%) at room temperature, in a low-noise acoustic chamber.

Magnetization measurements of the prepared magnetosomes suspension were carried out by SQUID magnetometer of Quantum Design at room temperature.

The magnetosome suspension within HEPES buffer was heated in the alternating magnetic field which was generated with the help of ferrite core (with cross intersection $S_{Fe} \cong 18$ cm^2) in the C-shape. The coil is made of 12 copper (wire with intersection S_{Cu} = 2.5 mm^2.) winds, which makes the inductance of the setup around L ≅ 100 mH. The glass phial

with sample in it was placed in magnetic gap with a diameter of l_g = 10 mm. The determination of magnetic field intensity amplitude was carried out on the basis of voltage measurement which was induced in the one turn placed in magnetic gap. Used sample volume for the experiment was 0.5 ml. The ferrofluid sample placed in a glass vial is mounted in a gap of magnetic system. This sensor is not sensitive on AC magnetic field, but on temperature only. In order to test the achieved thermal equilibrium the temperature had been recorded for 20 seconds before magnetic field was switched on. Magnetic field *H* was switched on for 4 minutes and the temperature had been registered.

4. Experimental results

Typical electron micrograph of magnetosomes on surface obtained by SEM technique for prepared samples NP, FQ and WVS are shown in Fig. 2. For evaluation of different preparation conditions the size distributions of magnetosomes (from 100 particles) according to SEM photographs were prepared. The diameter of magnetosomes was estimated from TEM photographs.

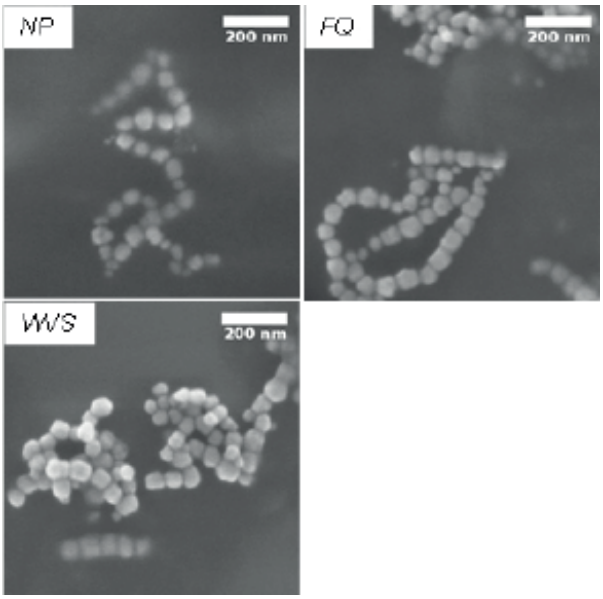

Fig. 2 Scanning electron micrograph of magnetosomes NP, FQ and WVS

The mean diameter of magnetosomes d, coercive force Hc and saturation magnetization Ms of magnetosomes suspensions prepared at various conditions Table1

	NP	WVS	FQ
d [nm]	47	52	58
H_C [Oe]	0	6.5	20
M_S [emu/g]	0.2	0.21	0.23

The size distribution of magnetosomes obtained by cultivation at normal culture (NP), containing higher FQ amount and higher WVS amount are given in Fig. 3a-c, respectively. The mean diameter of magnetosomes isolated from new bacterial tin at normal culture medium is 47 nm (Fig. 3a). On the opposite side after adding more FQ or WVS the value of mean diameter is shifted to higher values 52 nm for WVS (Fig. 3b) and 58 nm for FQ (Fig. 3c).

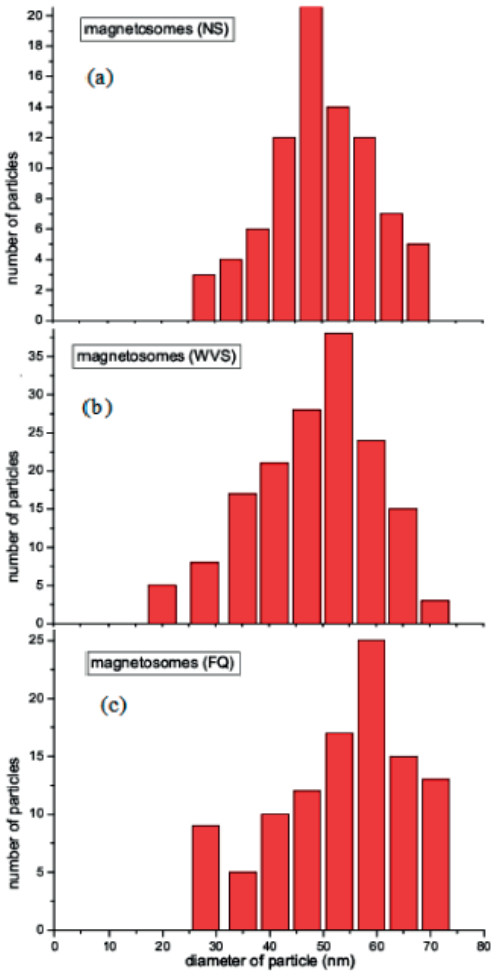

Fig. 3 Size distribution of magnetosomes obtained from different culture medium: normal (a), higher amount of WVS (b), and higher amount of FQ (c)

The curves of field dependence of magnetization at 293 K are reported in Fig. 4. These curves show that zero hysteresis loop (H_C = 0 Oe) exists at room temperature on suspension of magnetosomes prepared at normal condition (NP) and this suspension behaves superparamagnetically. Small increase of hysteresis is observed for sample WVS (H_C = 6.5 Oe) and for sample FQ (H_C = 20 Oe) which means that these samples show ferromagnetic behavior. The reason may be caused by higher shape anisotropy, resulting in a higher coercivity for samples with higher mean diameter. The larger H_C value reveals stronger magnetic correlations between particles of magnetite chains. The data obtained from magnetization measurements are collected in Table 1.

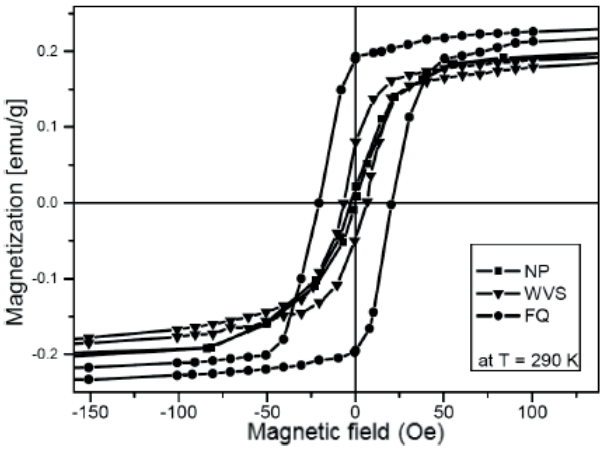

Fig. 4 Magnetization of magnetosomes suspension versus magnetic field at 293 K obtained under normal conditions (NP), with higher amount WVS and FQ

Figure 5 shows electron micrographs (TEM and AFM) of three samples of magnetosomes: (I) not influenced by separation method (standard magnetosomes sample, i.e. long - chains magnetosomes), (II) after centrifugation procedure (100 000 rpm, 8h), and (III) after centrifugation procedure (100 000 rpm, 12h) including sonication (120 W, 3h).

Sample I shows characteristic features for magnetosomes, i.e. long chains. Due to centrifugation at high rotation speed of 100 000 rpm the magnetosomes' chains (sample II) are shorter than in the case of sample I. Individual, single magnetosomes are also visible, but rare. Sample III presents almost no long chains (see inset also), but small groups of a few magnetosomes (not ordered) and certain amount of single magnetosomes. This result indicates that the desired separation force was greatly exceeded after sonication.

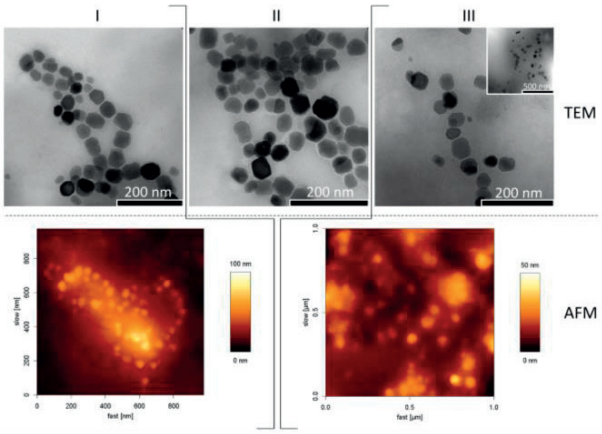

Fig. 5 TEM and AFM images of magnetosomes deposited on solid surfaces (TEM - drop coating on carbon-coated copper grid, AFM - spin coating on Si wafer): I (MP), II (UM) and III (SM), (inset shows a large scan area of the same sample - the result indicates a strong impact of the separation procedure that uses sonication treatment)

We also observed that the centrifugation at the same rotation speed, but different procedure time (e.g. 4h vs. 12h), has minor effect on separation of magnetosomes' chains, whereas time of sonication has a significant impact on separation.

The M–H hysteresis loops (Fig. 6) measured at room temperature show a ferromagnetic property of all samples with the same saturation magnetization M_S = 2.1 emu.g^{-1} and coercive field 41 Oe, 12 Oe and 7 Oe for samples M, UM and SM, respectively. These results correspond to the results obtained from microscopy measurements.

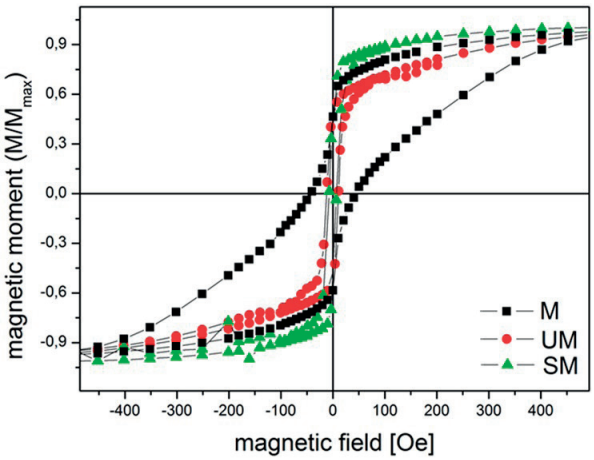

Fig. 6 Hysteresis loops for sample M, UM and SM

Hyperthermic measurements were performed at a frequency of *f* = 508 kHz vs. the AC- field amplitude in the range 0–5 kA/m. One of the most important parameters of hyperthermia – the

SAR values were evaluated (Fig. 7). SAR - (Specific Absorption Rate) is defined as the amount of heat released by a weight unit of the material per time unit during exposure to an oscillating magnetic field [18]. It is important to have these values for the material as high as possible. The slope of the curve informs about the dynamics of temperature rise of the sample and it also informs about the power release in a unit of volume at a given magnetic field strength. The dynamics of the increase was more visible in samples M and UM, so the heating is more effective in the samples with unbroken chains, which have higher coercivity, where hysteresis losses contribute much more significantly (Fig. 8). On the other hand, in sonicated samples, which have a significant presence of individual magnetosomes, the dominant mechanisms of heating are relaxation processes; hysteresis does not contribute too much. Our SAR values were 1083, 934 or 463 W/g for the sample of magnetosomes.

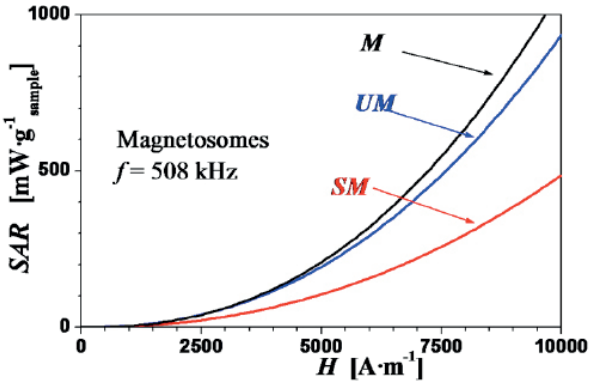

Fig. 7 Specific absorption rate

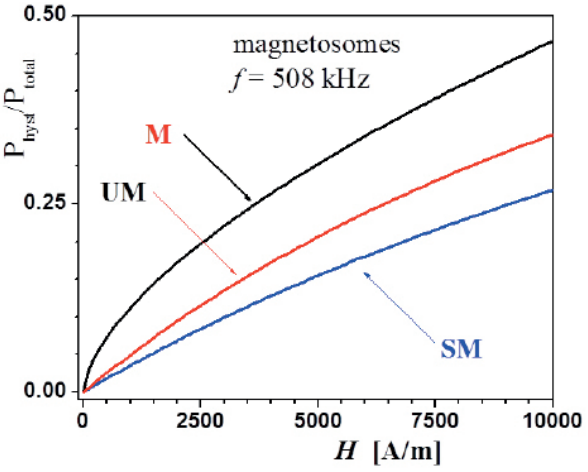

Fig. 8 Proportion of hysteresis processes to total losses

The magneto-optical properties of prepared magnetosomes were studied and described in the work [15]. Magneto-induced linear and circular anisotropy confirmed the important role played by the chains in the orientation mechanism of such magnetic dipoles. Numerical adjustments of the linear anisotropy curves using a classical Langevin orientation model gave the average number of magnetosomes per chain, about 12. Magnetic and magneto-optical measurements confirmed the large sensitivity of these magnetosomes to the magnetic field. This large sensitivity is really interesting for optical applications because a very low field is required to obtain the effect, which should make the technologic realization of devices easier.

5. Conclusion

The present result provides a synthesis method of magnetosome chains at various cultivation conditions. The sizes of biological magnetite nanoparticles (magnetosome) was increased from 47 nm (NP) up to 52 nm (WVS) and 58 nm (FQ) as a consequence of cultivation at higher amount of Wolfe's vitamin solution or ferric quinate. The chains of magnetite behave superparamagnetically for a sample cultivated at normal condition and display ferromagnetic properties at room temperature for samples WVS and FQ. The increase of coercivity for samples WVS and FQ is connected with higher shape anisotropy for samples with higher mean size diameter. The application ultracentrifugation and sonication process on isolated magnetosomes arranged in chains allowed us to prepare shorter chains and partly individual magnetosomes which was confirmed by TEM and AFM microscopy measurements and by obtained values of the coercive force. SAR values showed that bacterial nanoparticles are promising material for hyperthermia.

Acknowledgement

This work was supported by the Ministry of Education Agency for the Structural Funds No. 26220120021, 26220120033, 26110230061 and by the Slovak Research and Development Agency under the contract No. APVV-0171-10, APVV SK-FR 0012-11 and by the grant VEGA 2/0045/12, by a Polish National Science Centre grant, no DEC-2011/03/B/ST7/00194 and partially financed by the Human Capital Operational Program, Grant No. UDA-POKL.04.01.01-00-133/09-00.

References

[1] MATSUNAGA, T., SAKAGUCHI, T.: Molecular Mechanism of Magnet Formation in Bacteria, *J. of Bioscience and Bioengineering,* vol. 90, No. 1, 2000, pp. 1-13, ISSN 1389-1723

[2] MUXWORTHY, A. R., WILLIAMS. W.: *Critical Superparamagnetic/single-domain Grain Sizes in Interacting Magnetite Particles: Implications for Magnetosome Crystals*. Royal Society Interface, 2009 December 6; 6(41): 1207–1212

[3] SCHULER, D., FRANKEL, R. B.: Bacterial Magnetosomes: Microbiology, Biomineralization and Biotechnological Applications. Appl Microbiol Biotechnol. 1999 Oct; 52(4): 464-73

[4] RUBIO, M. F. J. C., HERNANDEZ, A. V., SALAS, L. L., AVILA-NAVARRO, E., NAVARRO, E. A.: *The Open Nanomedicine J.*, 2011, 3, 2-9

[5] WUST, P., HILDEBRANDT, B., SREENIVASA, G., RAU B., GELLERMANN, J., RIESS, H., FELIX, R., SCHLAG, P. M.: Hyperthermia in Combined Treatment of Cancer. *Lancet Oncol*., 2002 Aug; 3(8): 487-97

[6] ROSENBLATT, CH., TORRES DE ARAUJO, F. F., FRANKEL, R. B.: Birefringence Determination of Magnetic Moments of Magnetotactic Bacteria, *Biophysical J*, vol. 40, No. 1, 1982, pp. 83-85, ISSN 0006-3495

[7] JAMON, D., DONATINI, F., SIBLINI, A., ROYER, F., PERZYNSKI, R.,CABUIL, V., NEVEU, S.: Experimental Investigation on the Magneto-optic Effects of Ferrofluids Via Synamic Measurements, *J. of Magnetism and Magnetic Materials*, vol. 321, No. 9, 2009, pp. 1148-1154, ISSN 0304-8853

[8] ROYER, F., JAMON, D., ROUSSEAU, J. J., CABUIL, V., ZINS, D., ROUX, H., BOVIER, C.: Experimental Investigation on Gamma-Fe_2O_3 Nanoparticles Faraday Rotation: Particles Size Dependence, *European Physical J. Applied Physics*, 22 (2), 83-87, 2003

[9] HASMONAY, E., DUBOIS, E., BACRI, J. C., PERZYNSKI, R., RAIKHER, Y. L., STEPANOV, V. I.: Static Magneto-optical Birefringence of Size-sorted γ-Fe_2O_3 Nanoparticles. *European Phys. J.* B 5(3): 859–867 1998.

[10] PHILLIPS, J. L.: *A Topical Review of Magnetic Fluid Hyperthermia,* American Society of Chemical Engineers, 2005

[11] SKUMIEL, A., KACZMAREK-KLINOWSKA, M., TIMKO, M., MOLCAN, M., RAJNAK, M.: Evaluation of Power Heat Losses in Multidomain Iron Particles under the Influence of AC Magnetic Field in RF Range**,** *Intern. J. of Thermophysics*, 2013, DOI: 10.1007/s10765-012-1380-0

[12] HERGT, R., DUTZ, S., MULLER, R., ZEISBERGER, M.: Magnetic Particle Hyperthermia: Nanoparticle Magnetism and Materials Development for Cancer Therapy, *J. Phys.: Condens. Matter* 18, 2006, S2919–S2934

[13] MORNET, S., VASSEUR, S., GRASSET, F., VEVERKA, P., GOGLIO, G., DEMOURGUES, A., PORTIER, J., POLLERT, E., DUGUET, E.: Magnetic Nanoparticle Design for Medical Applications, *Progress in Solid State Chemistry*, vol. 34, No. 2-4, 2006, pp. 237-247, ISSN 0079-6786

[14] SKUMIEL, A., JOZEFCZAK A., TIMKO M., KOPCANSKY, P., HERCHL F., KONERACKA, M., TOMASOVICOVA, N.: The Heating Effect in Biocompatible Magnetic Fluid, *Intern. J. of Thermophysics*, 28, No. 5, 2007, 1461-1469

[15] DZAROVA, A., ROYER, F., TIMKO, M., JAMON, D., KOPCANSKY, P., KOVAC, J., CHOUEIKANI, F., GOJZEWSKI, H., ROUSSEAU, J. J.: Magneto-optical Study of Magnetite Nanoparticles Prepared by Chemical and Biomineralization Process. *J. of Magnetism and Magnetic Materials*, 2011, vol. 323, No. 11, p. 1453 – 1459, ISSN 0304 - 8853

[16] GRUNBERG, K., WAWER, C., BRADLEY, M. T., SCHULER, D.: A Large Gene Cluster Encoding Several Magnetosome Proteins is Conserved in Different Species of Magnetotactic Bacteria, *App. Environ. Microbiol*. 2001, 67(10), 4573-4582

[17] GOJZEWSKI, H., MAKOWSKI, M., HASHIM, A., KOPCANSKY, P., TOMORI, Z., TIMKO, M.: Magnetosomes on Surface: An Imaging Study Approach. *Scanning*, 2012 May-Jun; 34(3): 159-69

[18] HASHIM, A., MOLCAN, M., KOPCANSKY, P., KOVAC, J., GOJZEWSKI, H., MAKOWSKI, M., SKUMIEL, A., JOZEFCZAK, A., TIMKO, M.: *Bacterial Magnetite Nanoparticles - Magnetospirillum Magnetotacticum sp. AMB-1 Magnetosomes*, Proc. Nanocon 2011, 3rd Intern. Conference, Brno.

Jozef Kudelcik - Peter Bury - Peter Kopcansky - Milan Timko *

TEMPERATURE EFFECT ON ANISOTROPY OF ACOUSTIC ATTENUATION IN MAGNETIC FLUIDS BASED ON TRANSFORMER OIL

Magnetic nanoparticles in magnetic fluids under the effect of magnetic field create structures, which are not arranged uniformly. These structures have various shapes dependent on the intensity and duration of applied magnetic field. In the case of such structures the anisotropy of acoustic attenuation can be observed. The effect of temperature on this process was studied by acoustic spectroscopy in transformer oil-based magnetic fluids. Taketomi theory that assumes existence of spherical clusters was used. These clusters form long chains, aligned in magnetic field direction. The cluster radius, the number density of the colloidal nanoparticles as well as other parameters of magnetic nanoparticles were determined from experimental results. These data allowed to draw conclusions about the changes in the parameters describing the structures of magnetic nanoparticles in the investigated magnetic fluid caused by different temperatures.

Keywords: *Magnetic fluid, transformer oil MOGUL, anisotropy of acoustic attenuation.*

1. Introduction

Nanotechnology is very progressive research area and their results can be found in many parts of our daily life. Nanoparticles are used in chemistry, biology, technology and other areas to improve the properties of various materials. One of the technological applications is utilization of magnetic nanoparticles in the magnetic fluids based on transformer oil [1 and 2]. These types of the transformer oils should have better insulating and thermal properties. The dielectric breakdown strength of these liquids is influenced by the concentration of magnetic nanoparticles and can have the positive influence on electric breakdown [3, 4 and 5].

One of the methods to study changes in the magnetic fluid structure is based on the measurement of the acoustic wave attenuation changes Δa under the external magnetic field at various conditions [6, 7 and 8]. The investigation of the attenuation changes of the acoustic wave propagating through suspensions, in which magnetic nanoparticles representing one phase are dispersed in carried liquid representing a continuous second phase, can indicate characteristic properties and structure of magnetic liquids. The interaction between the acoustic waves and the magnetic nanoparticles or clusters leads to the additional attenuation of acoustic wave compared to that in the carried liquid.

Several authors studied the arrangement of magnetic nanoparticles in magnetic fluid under the effect of an external magnetic field both theoretically and experimentally [2, 8 and 9]. There are also computer simulations [10 and 11] that investigated aggregation phenomena in a polydisperse colloidal dispersion of ferromagnetic nanoparticles. All these works suppose that chainlike clusters with various shapes are formed along magnetic field direction. These shapes are influenced by the magnitude of both particle-particle and particle-field interactions, which is characterized by the coupling constant. Large values of coupling constant mean agglomeration of particles in larger structures – clusters, chains. In this paper the authors study the influence of temperature on the anisotropy of the acoustic attenuation in magnetic fluids based on transformer oil MOGUL. The observed results are analyzed and discussed.

2. Experimental details

The subject of the study was magnetic fluid based on transformer oil MOGUL. The structure of magnetic fluid was investigated by acoustic spectroscopy. The magnetic fluid used in experiments consisted of magnetite nanoparticles ($FeO.Fe_2O_3$) with the mean diameter d = 9.8 nm (σ = 0.28 nm), coated with oleic acid as a surfactant dispersed in transformer oil MOGUL. The basic properties of this magnetic fluid, such as the density,

* [1]Jozef Kudelcik, [1]Peter Bury, [2]Peter Kopcansky, [2]Milan Timko
[1]Department of Physics, Faculty of Electrical Engineering, University of Zilina, Slovakia
E-mail: kudelcik@fyzika.uniza.sk
[2]Department of Magnetism, IEP SAS, Kosice, Slovakia

saturation magnetization and volume fraction were equal to 0.89 g/cm^3 and 3.39 mT for 1% magnetic fluid and 0.95 g/cm^3 and 6.17 mT for 2% magnetic fluid.

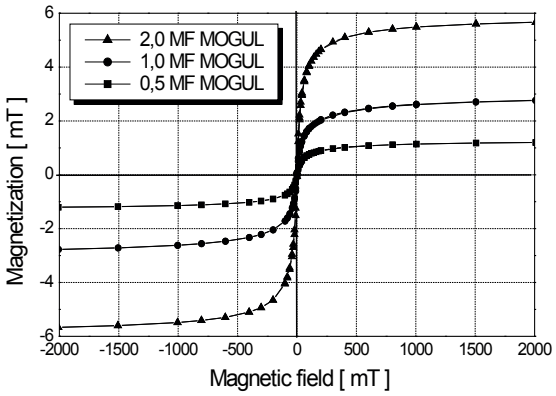

Fig. 1 Magnetization curves for various concentrations of magnetic nanoparticles in magnetic fluid based on transformer oil MOGUL

Volume concentrations, average diameter and standard deviation of magnetic particles were determined from vibrating sample magnetometer measurements. The dependences of magnetic moment of samples on magnetic field were measured in the range of -2T to 2T at room temperature (25 ^0C) (Fig. 1). The acoustic wave attenuation was measured at the frequency 12.65 MHz as a function of magnetic field and for different temperature. The experimental arrangement of acoustic spectrometer has been already described [12 and 13]. The acoustic velocity was measured using the double distance between transducers (18 mm) and time between the first two selected adjacent echoes.

3. Results and discussion

The attenuation of acoustic wave in magnetic fluid depends on the magnetic field intensity, the rate of its changes and the temperature [13]. The initial increase of acoustic attenuation with increasing magnetic field is connected with the aggregation of magnetic nanoparticles and following clusters creation due to the presence of magnetic field and particle-field interaction. This process can continue also at decreasing magnetic field and the development of attenuation shows then hysteresis which strongly depends also on the temperature. At lower temperature the creation of clusters is more effective because Brown thermal motion is not so effective to destroy the clusters [6 and 10]. The thermal motion increases with increasing temperature that results in decrease of number of clusters and their size and, subsequently, also in decrease of acoustic attenuation.

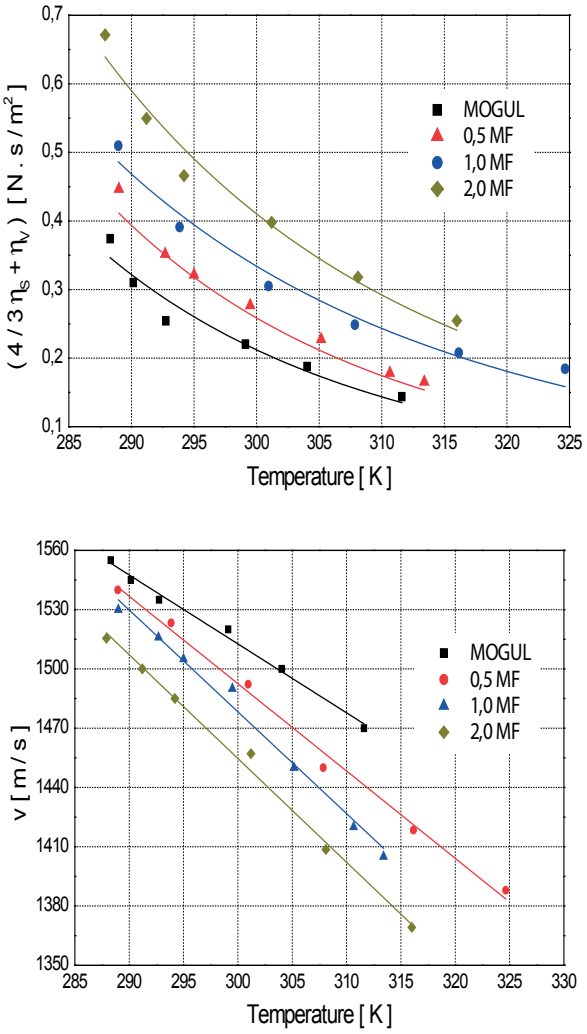

Fig. 2 The temperature dependences of term (4/3 η_S+η_V) (a) and velocity (b) for various concentrations of magnetic nanoparticles in magnetic fluid based on MOGUL

More information about existence, size and density of cluster can be obtained from the analysis of the dependence of the acoustic attenuation on the angle ϕ between wave vector $\boldsymbol{k}$ and direction of magnetic field $\boldsymbol{B}$ (anisotropy). These parameters can be calculated using Taketomi theory [14] that unlike another, Shliomis and Mond theory [15] often used to describe the anisotropy of acoustic attenuation, is able to explain measured dependences in magnetic fluids based on transformer oil [13].

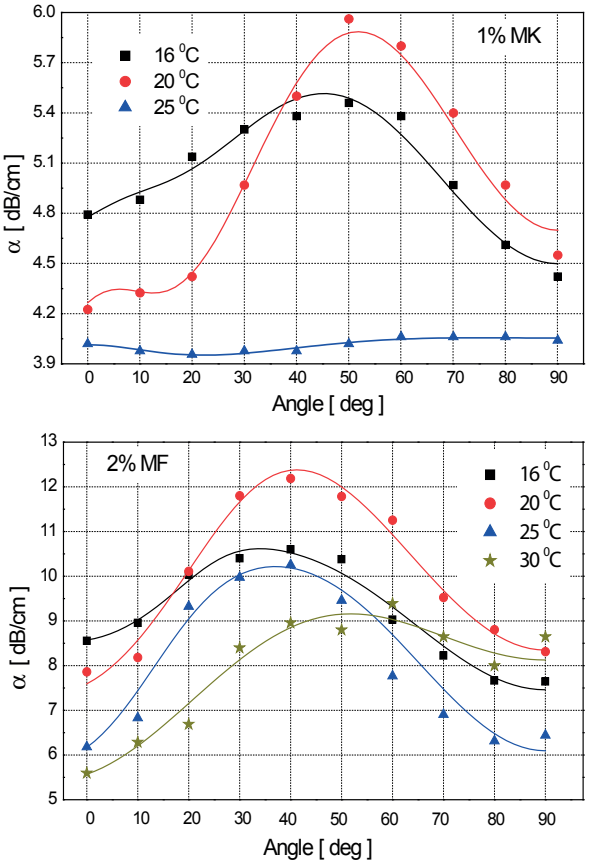

Fig. 3 Anisotropy measurement of the acoustic attenuation (B = 200 mT) in the 1% (a) and 2% (b) MF based on MOGUL measured at various temperatures (■ 16 °C, ● 20 °C, ▲ 25 °C) including the sum of the components α_{rot} + α_{tr} of the Taketomi functions [14] (full lines)

Magnetic fluid in the presence of external magnetic field consists of individual magnetic nanoparticles, long chains, clusters and their various combinations which in interaction with acoustic wave cause its additional absorption. In general, the acoustic attenuation is the sum of rotation and translation part [14]

$$\alpha = \alpha_{rot} + \alpha_{tr}. \tag{1}$$

The rotating mechanism affecting the part of acoustic attenuation is described as

$$\alpha_{rot} = \frac{2\pi^2 f}{\rho_0 c^3}\left(\left(\frac{4}{3}\eta_S + \eta_V\right) + 2\alpha_5 \cos^2\varphi + \alpha_1 \cos^4\varphi\right), \tag{2}$$

where ρ_0 is the density of the carrier fluid, c is the velocity of the acoustic wave of the frequency f, (4/3 η_S + η_V) is viscosity, α_1, α_5 are the Leslie coefficients appearing in the theory of liquid crystals. Three types of forces are assumed in his theory. The first one is a recovering force that acts on the cluster toward to original point and makes then periodic motion. The second force is the frictional force, that decelerates the moving cluster and particles in viscose liquid. From the acoustic theory of fluids, the last force is derived - the force of the pressure. From the solution of the equation of motion for a cluster and expression of the dissipative energy the translational acoustic attenuation was derived in the form

$$\alpha_{tr} = \frac{3\pi\eta_0 a\omega^3 \rho_0 V\ N(6\pi\eta_0 a + \rho_0 V\omega)/(kc^2)}{(\sin\varphi - \rho_m V\omega^2/k)^2 + (6\pi\eta_0 a\omega/k)^2}, \tag{3}$$

where k is the constant of recovering force, a is the radius of clusters and N is the density of clusters.

The second and the third terms in Eq. 2 are non zero only in presence of external magnetic field. In a magnetic fluid not subjected to an external magnetic field, the acoustic attenuation, α_{rot}, is firstly related to the dynamic viscosity, η_S, and volume viscosity, η_V [9]. The temperature dependence of the term (4/3 η_S+η_V) enables the fit with the Arrhenius function

$$\left(\frac{4}{3}\eta_S + \eta_V\right) = f(T) = A\exp\left\{\frac{B}{T}\right\}, \tag{4}$$

where A and B are coefficients dependent on the properties of magnetic fluids. These coefficients are summarized in Table 1. As follows from Fig. 2a illustrating the temperature dependence of this term, the coefficient of viscosity decreases with increasing temperature. The coefficient increases also with the concentration of magnetic nanoparticles in magnetic fluid. From Fig. 2b it can be seen that the velocity of acoustic wave decreases with increasing temperature that corresponds to the increasing density of magnetic fluid. In this case the velocity is smaller for higher concentration of magnetic nanoparticles in magnetic liquid. The velocity of acoustic wave in investigated magnetic fluid based on transformer oil can be fitted by function

$$c = c_0(1 - \beta\Delta T), \tag{5}$$

where c_0 is the velocity at temperature 273K and β is the coefficient of the temperature change of the velocity. Calculated values are also summarized in Table 1.

Parameters of the temperature dependences of term (4/3 η_S+η_V) and velocity for various concentrations of magnetic nanoparticles in magnetic fluid based on MOGUL Table 1

X% MF	c_0 [m/s]	β [mK^{-1}]	A [10^{-6}]	B[K]
MOGUL	1607	2.2	1.2	3628
0.5%	1612	2.7	1.3	3658
1.0%	1617	3.2	1.0	2944
2.0%	1596	3.3	1.0	3160

Type values of parameters described 1% and 2% magnetic fluids based on the MOGUL obtained from the fit of measured anisotropy data using Taketomi functions

Table 2

X% MF MOGUL	1%			2%			
Temperature	16 °C	20 °C	25 °C	15 °C	20 °C	25 °C	30 °C
$4/3\eta_S+\eta_V$[N.s.m^{-2}]	0.38	0.35	0.32	0.58	0.45	0.39	0.36
α_5[N.s.m^{-2}]	0.18	0.25	0.00022	0.33	0.40	0.48	0.16
α_1[N.s.m^{-2}]	-0.39	-0.73	-0.02249	-0.56	-0.76	-1.03	-0.6
k[N.m^{-1}]	11.73	7.88	2.52	66	42	37	10
a[nm]	93	62	19	290	265	217	135
10^{-17} N[m^{-3}]	9.8	102	313	0.5	2	3.1	17.3
V×N [10^{-3}]	0.42	1.27	0.11	0.64	1.95	1.66	2.22

The anisotropy of acoustic attenuation measured at magnetic field 200 mT for two different concentrations of magnetic nanoparticles in magnetic fluid is shown in Fig. 3. The solid lines represent the theoretical fit of experimental data using Taketomi functions (Eqs. 2, 3). The measured anisotropy shows curves with the maximum value whose position depends on the concentration and temperature: for 1% MF MOGUL: 16 °C - 45°, 20 °C - 50°, 25 °C – no evident maximum; for 2% MF MOGUL: 15 °C - 40°, 20 °C - 40°, 25 °C - 40°, 30 °C - 55°. Using rotation $\alpha_{rot}(\phi)$ and translational $\alpha_{tr}(\phi)$ part of Taketomi function next parameters can be determined: $(4/3\ \eta_S + \eta_V)$ (viscosity), α_5, α_1, k (constant of recovering force), a (radius of clusters) and N (density of clusters). These parameters obtained from the fit of measured data in Microcal Origin are summarized in Table 2.

Figure 4 shows both anisotropy of the acoustic wave absorption in 1% and 2% magnetic fluid measured at 20 °C as well as the individual components a_{rot}, a_{tr} obtained from Taketomi functions (Eqs. 1, 3). As follows from the dependence $\alpha_{rot}(\phi)$, the curve has a maximum value whose position depends on concentration: 1% - 55°, 2% - 50° and temperature, too. On the other hand, the second component of the acoustic attenuation, $\alpha_{tr}(\phi)$, decreases monotonously with increasing angle ϕ for lower concentration (1% MF), but at higher concentration (2% MF) reaches the maximum value around 40°.

The volume concentration of all clusters (V×N) can be determined also from the parameters of a and N. This value implies which part of the magnetic grains (domains) is included in the clusters, while other part is free in the carrier fluid. As it can be seen from the volume (V×N) more than 4,2% of all magnetite particles are in clusters.

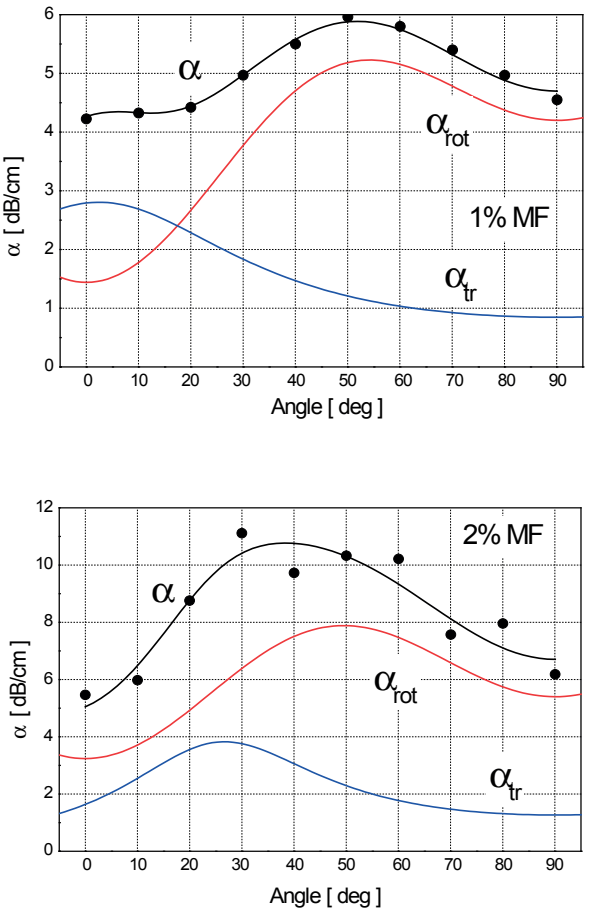

Fig. 4 Development of rotation and translation part of acoustic attenuation and their sum measured in the 1% and 2% MF based on MOGUL for temperature 20 °C

The measurement of the acoustic attenuation as a function of the angle φ between the direction of propagation represented by $\boldsymbol{k}$ and that of the magnetic field $\boldsymbol{B}$ (anisotropy) for magnetic fields when the majority of the particles are involved in the cluster structures, confirmed the contribution of two components of the acoustic attenuation α_{rot}, α_{tr} related to the rotational and translational degrees of freedom, respectively. The translational and rotation parts of acoustic attenuation express also what part of acoustic wave energy losses is due to the translation and/or rotational movement of the clusters. So that it is possible also to estimate the percentage contribution of acoustic attenuation to the individual kinds of cluster motion.

It is known that the interaction between the external magnetic field and the magnetic moment of nanoparticles in magnetic fluids leads to the aggregation of nanoparticles to new structures. These structures enlarge with the increasing magnetic field and this process has the influence on the value of the acoustic attenuation, so that the acoustic attenuation increases, too. The acoustic attenuation initially increases with increasing magnetic field due to the starting process of aggregation of magnetic particles to the cluster and later to chains (structures as long as tens of nanometers, see Table 2). However, following progress at higher magnetic field can be different depending on the structure changes caused by developing of cluster shape in individual cases.

The complex viscosity as a function of temperature was determined from the measurement of acoustic attenuation for various concentrations and temperature. It can be seen that viscosity decreases with temperature and increases with concentration. The similar results were observed from the velocity measurements. The velocity decrease with the concentration is caused by higher numbers of nanoparticles in magnetic fluid and consequently its higher density.

The important feature of studied magnetic liquid is the anisotropy of acoustic attenuation, which was investigated in the temperature range of 16 – 30 ^{0}C. The obtained results indicate the significant effect of temperature on the acoustic attenuation. The measurements of the anisotropy of acoustic attenuation in the case of 1% MF MOGUL at temperatures 16 and 20 ^{0}C show large changes connected with the process of chains orientation and its rotation in the direction of magnetic field. At higher temperature (>24 ^{0}C) the acoustic attenuation is almost independent on magnetic field. There are also other parameters discovered by acoustic attenuation: the radius of clusters and the length of their chains. These parameters are strong function of temperature. Its mean value changes from 93 nm to 19 nm corresponding to the temperature increase from 16 ^{0}C to 25 ^{0}C.

The measurement of the anisotropy of acoustic attenuation for 2% MF MOGUL even indicates stronger effect as that for 1% concentration, when the radius of clusters at the same magnetic field and temperature is much higher. For this concentration the anisotropy of acoustic attenuation also at temperature 25 ^{0}C shows large changes connected with the process of chains orientation and its rotation concerning the direction of magnetic field. The anisotropy measured at 30 ^{0}C still has maximum although less expressive. Very important fact is that the values of cluster radius at lower temperature (16 ^{0}C) can be larger than 250 nm, comparing with the value 93 nm for 1% MF. This is explanation also for dominant effect of rotation part on acoustic attenuation relative to transaction part. This big difference in cluster radius indicates also that clusters in this type of MF look like separate spheres and they do not create long chains.

At higher temperature the thermal motion increases resulting in decrease of numbers of clusters and mainly their radius and volume concentration. The both smaller numbers of clusters and their smaller size induce the smaller influence on the acoustic attenuation. The changes in the clusters size affect also the magnitude of the rotation and translation components of the acoustic attenuation.

4. Conclusions

The influence of both magnetic field and temperature on the structures of investigated magnetic fluids based on the transformer oil MOGUL was observed using acoustic spectroscopy. The anisotropy of the acoustic attenuation in the presence of external magnetic field of the value 200 mT for two different concentrations was measured and analyzed. The effect of temperature on the cluster radius and their configuration considering the direction of magnetic field was confirmed. The study of the anisotropy showed also the important role of rotational and translational motion of the clusters on the acoustic attenuation and the fact that the concentration of magnetic nanoparticles in transformer oil MOGUL has influence on the size of clusters and their arrangement. Using Taketomi theory the radius of clusters, their density and viscous term as a function of temperature were determined.

Acknowledgement

This work was supported by VEGA projects 1/0624/13 and 2/0045/13. The authors wish to thank also for the support to the R&D operational program Centrum of excellence of power electronics systems and materials for their components, No. OPVaV-2008/2.1/01-SORO, ITMS 2622012046 funded by European Community.

References

[1] SEGAL, V., RAJ, K.: An Investigation of Power Transformer Cooling with Magnetic Fluids**,** *Indian J. Eng. Mater.* Sci. 5 (6), 1998, 416.

[2] ODENBACH, S.: Ferrofluids - magnetically Controlled Suspensions, Colloids and Surfaces A: *Phys. Eng. Aspects,* 217, 2003, 171.

[3] KUDELCIK, J., BURY, P., ZAVISOVA, V., TIMKO, M., KOPCANSKY, P.: The Dielectric Breakdown Of Magnetic Fluids, *Communications - Scientific Letters of the University of Zilina, vol.* 12, Nr. 2. 2010, 34-37.

[4] KUDELCIK, J., BURY, P., KOPCANSKY, P., TIMKO, M.: Dielectric Breakdown in Mineral Oil ITO 100 Based Magnetic Fluid, *Physics Procedia* 9, 2010, 78-81.

[5] YUE-FAN, DU, YU-ZHEN, LV., JIAN-QUAN, Z. XIAO-XIN, LI, CHENG-RONG, LI: *Breakdown Properties of Transformer Oil-based TiO2 Nanofluid Electrical Insulation and Dielectric Phenomena (CEIDP),* 2010 Annual Report Conference on Electrical Insulation and Dielectric Phenomena 2010 http://dx.doi.org/10.1109/CEIDP.2010.5724082.

[6] MENDELEV, V. S., IVANOV, A. O.: Ferrofluid Aggregation in Chains under the Influence of a Magnetic Field, *Phys. Rev.* 70, 2004, 051502

[7] ROZYNEK, Z. et al: Structuring from Nanoparticles in Oil-based Ferrofluids, *Eur. Phys. J. E* 2011, 34: 28 DOI 10.1140/epje/i2011-11028-5

[8] SINGH, V., BANERJEE, V., SHARMA, M.: *Dynamics of Magnetic Nanoparticle Suspensions, J. Phys. D: Appl. Phys.* 42, 2009, 245006

[9] SKUMIEL, A.: The Effect of Temperature on the Anisotropy of Ultrasound Attenuation in a Ferrofluid, *J. Phys. D: Appl. Phys.* 37, 2004, 3073.

[10] AOSHIMA, M., SATOH, A.: Two-dimensional Monte Carlo Simulations of a Colloidal Dispersion Composed of Polydisperse Ferromagnetic Particles in an Applied Magnetic Field, *J. of Colloid and Interface Science* 288, 2005, 475-488.

[11] SATOH, A., COVERDALE, G. N., CHANTRELL, R. W.: Stokesian Dynamics Simulations of Ferromagnetic Colloidal Dispersions Subjected to a Sinusoidal Shear Flow, *J. of Colloid and Interface Science* 231, vol. 2, 2000, 238-246

[12] KUDELCIK, J., BURY, P., DRGA, J., KOPCANSKY, P., ZAVISOVA, V., TIMKO, M.: Temperature Effect on The Structure of Transformer Oil Based Magnetic Fluids Using Acoustic Spectroscopy, *Acta Physica Polonica A*, 2012, vol. 121, No. 5-6, ISSN 0587-4246 1169-1171

[13] KUDELCIK, J., BURY, P., DRGA, J., KOPCANSKY, P., ZAVISOVA, V., TIMKO, M.: Structure of Transformer Oil-based Magnetic Fluids Studied using Acoustic Spectroscopy, *J. of Magnetism and Magnetic Materials* 326, 2013, 75-80.

[14] TAKETOMI, S.: The Anisotropy of the Sound Attenuation in Magnetic Fluid under an External Magnetic Field, *J. Phys. Soc. Japan* 55, 1986, 838.

[15] SHLIOMIS, M., MOND, M.: Ultrasound Attenuation in Ferrofluids, *Phys. Rev. Lett.* 101, 2008, 074505.

Daniel Kacik - Peter Tatar - David Liachovicky *

NANO-MANAGEMENT OF LINEAR PROPERTIES OF PHOTONIC CRYSTAL FIBERS

The array of nanometer air holes positioned in the core can significantly modify the properties of guided mode in photonic crystal fiber. Changing geometrical properties of nanometer holes enables tuning of fiber dispersion and the effective mode area. This is related to losses of mode. In this paper, a rigorous analysis of dispersion and losses has been carried out for photonic crystal fiber with special arrangement of nanometer air holes in the core.

Keywords: *Photonic crystal fiber, nanometer air holes ring, dispersion, losses.*

1. Introduction

The ability of controlling wave propagation has always been a challenge in huge number of applications. Development in this area experienced great progress by revealing the principles of light behavior in photonic crystals [1]. These principles were also applied on waveguides [2 and 3]. Unique properties of these waveguides called photonic crystal fibers (PCFs), are achieved by different methods, but mostly by changing geometrical arrangement (for example modifying the elliptical shape of holes, gradually changing size of holes) or chemical composition of fibers [4 - 6]. Special way of controlling fiber properties is the inclusion and the modification of cylindrical defects with cross-sectional dimensions of tens to hundreds of nanometers within the core. So far this method addressed several groups [7 - 9]. The implementation of one central circular hole with a diameter of approximately 500 nm the ultra-flat behavior of dispersion with the variation of 2 ps.nm^{-1}. km^{-1}, in the wavelength range of light 700 nm [8] was verified with simulation methods. Produced fiber with such a structure can be found in [9]. Also influence of hexagonal structure of nanometer air holes in core was shown in [10] to be effective for fine tuning of dispersion, nonlinearity and gain. Effective mode area, in relation to fiber dimension, describes degree of localization of mode in core of fiber. While fibers with large mode area (LMA) are designed for linear performance, in those with small mode area one can expect strong effects of nonlinearities. Combining strong mode confinement within a very small area and the appropriate value of dispersion at wavelength of emitting light source can create conditions for supercontinuum generation [11].

The aim of this paper is to provide deep analysis of the effects of changing geometric parameters of air nanostructures within the core of pure-silica PCF, a focus on linear properties of such PCFs, namely the dispersion and losses.

2. Geometry of the studied structure and modal analysis

We use the five-ring-hexagonal-lattice structure of photonic crystal fiber shown in Fig. 1a. The pitch Λ of the fiber is 2 mm, d/Λ is 0.6, where d is the diameter of cladding hole, and the effective mode area is 5.7678 mm^2. To the area of the solid core formed by omission of the single central hole we add the ring of air nanostructure holes (Fig. 1d, Fig. 1e). The arrangement of ring holes is defined by its radius L_n and nanohole diameter d_n.

As it can be seen from Fig. 1 the area of fundamental mode in fiber with nanostructure (e) is slightly compressed (94.58%) compared to the fiber without nanostructure, but still more than in (d) structure (the effective mode area compressed to 98.79%). With both enlargement and the proximity to the innermost cladding ring the nanoholes take over the mode-confining function. Further, to see only the influence of the position we kept the nanohole diameter constant. The mode power distributions with different L_n swept for multiple wavelengths help us visualize the wavelength-selective localization of mode power within the nanostructure (Fig. 2).

* **Daniel Kacik, Peter Tatar, David Liachovicky**
Department of Physics, University of Zilina, Slovakia
E-mail: daniel.kacik@fel.uniza.sk

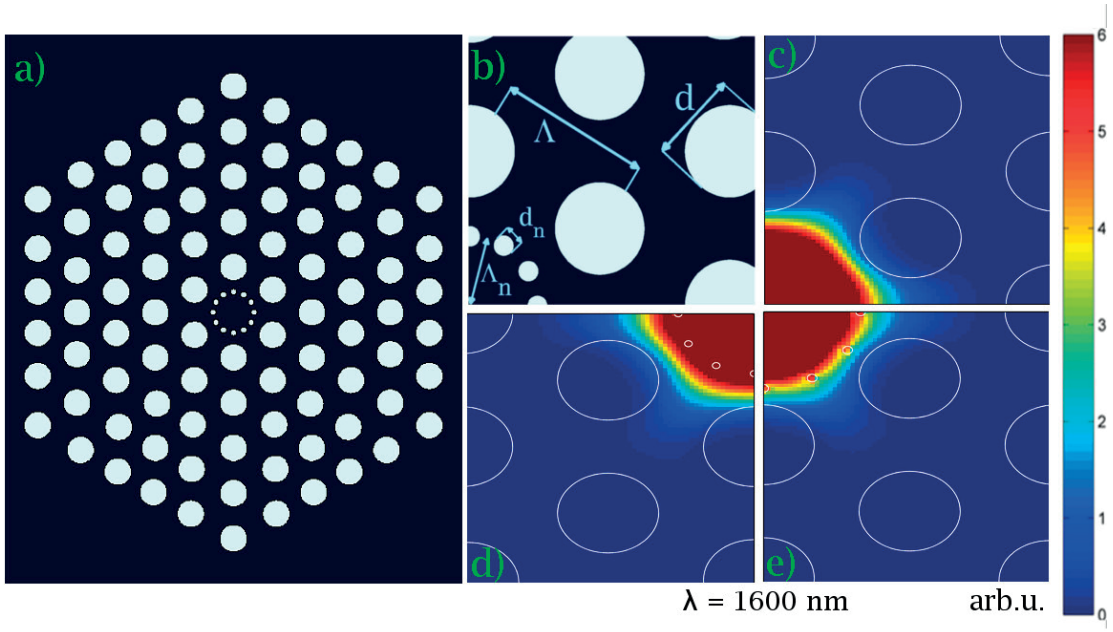

Fig. 1 Structure of the modeled PCF with solid core (a) and details of the structure (b) and of mode distributions of z - component of Poynting vector for PCF (shown π/2 quadrant) with Λ=2mm and d/Λ=0.6: (c) without nanostructure, (d) with nanostructure where L_n = 900nm, d_n = 90nm, (e) with nanostructure where L_n = 1150nm, d_n = 115nm

λ	without nanostructure	Λ_n = 1000 nm, d_n = 200 nm	Λ_n = 900 nm, d_n = 200nm
420 nm	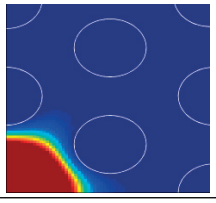	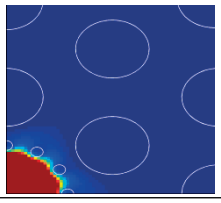	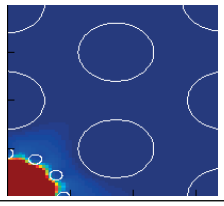
660 nm	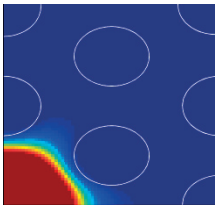	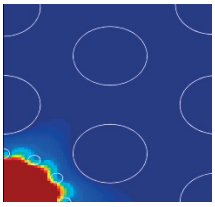	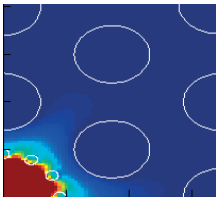
920 nm	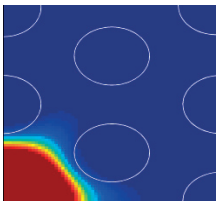	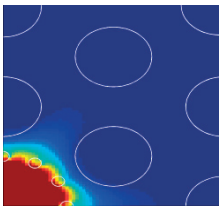	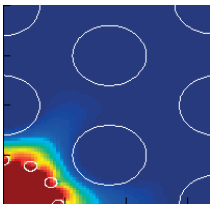
1140 nm	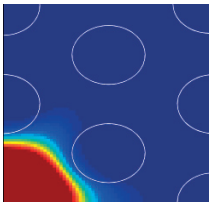	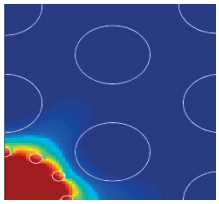	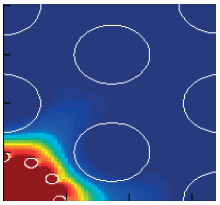

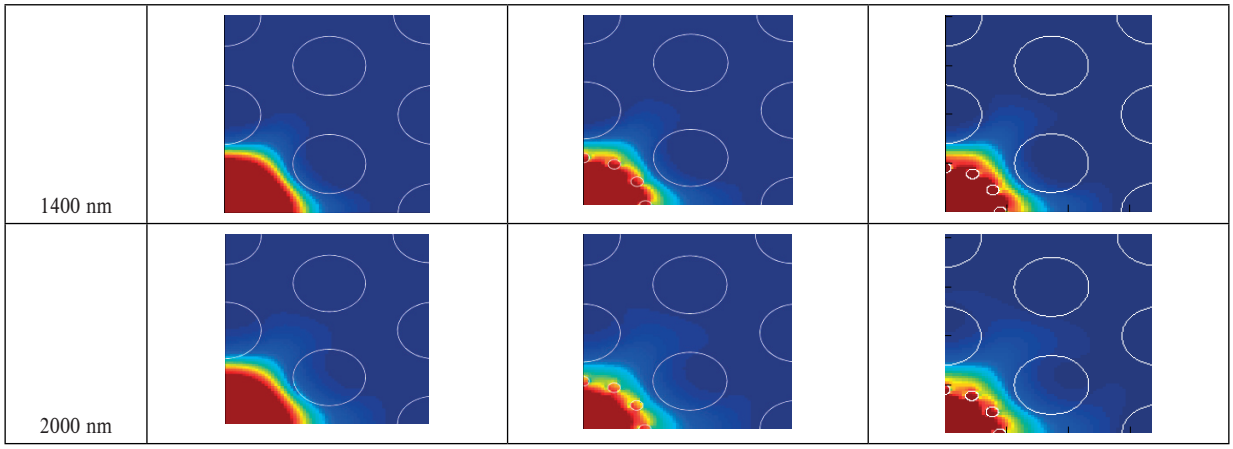

Fig. 2 Mode distributions of z-component of Poynting vector for PCFs with constant d_n = 200 nm, but radius of rings L_n = 1000 nm and 900 nm for different wavelengths of light.

3. Propagation characteristic: Results and discussion

To investigate the sensitivity of linear properties of PCF to the nanostructure with respect to the position in the core area (at different distance from the center) the nanostructure ring was scaled with constant ratio d_n/L_n = 0.1 which is small relative to the wavelength. In Fig. 3 we observe only slight changes in dispersion values that retain the shape of the dispersion curve of fiber without nanostructure ring in core. The small holes can be perceived as elements that lower the overall refractive index of the homogeneous core. In accordance with this conception is the greatest decrease of dispersion curve associated with the largest change in the waveguide geometry (structure given at Fig. 1e: d_n = 115 nm). For this configuration of holes, which are nearly adjacent to the innermost cladding ring, the loss curve does not obey monotonic increase with nanohole diameter coupled with increased radius of the ring nanostructure.

In Fig. 4 we see that concentrating the ring by changing L_n with 100 nm step causes significant red-shift (200 nm) of lower zero dispersion wavelength (ZDW) and smaller blue-shift (100 nm) of higher ZDW. Although such change does not yield any profile that would not be achievable by cladding modification, it is manifestation of sensitivity to the density and thickness of the formed ring. If we continue to decrease L_n with constant hole diameter, ring closure is stronger and also mode power distribution slowly transforms into a shape resembling more an annulus. Nanoholes touch at d_n/L_n = 0.515, which is certainly not a manufacturable case of fiber.

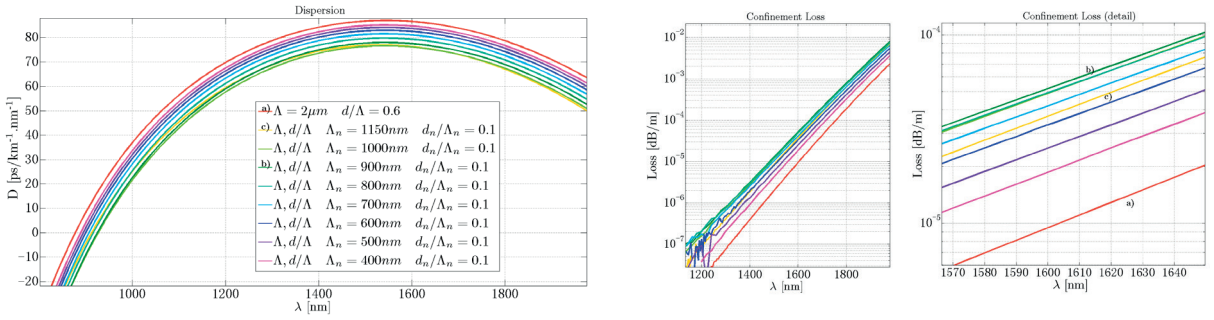

a) b)

Fig. 3 Dispersion (a) and confinement losses (b) for different radii of ring nanostructures and constant relative nanohole size (structures from Fig. 1b)

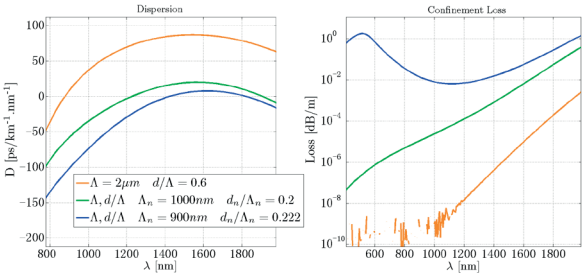

Fig. 4 Dispersion and confinement losses for different radii of ring nanostructures and the same diameter of nanoholes (200 nm) (structures from Fig. 2cde)

Noteworthy is the loss plot of the structure L_n = 900 nm and d_n/L_n = 0.222 (Fig. 4): such fiber experiences region of stronger confinement in near-infrared while the losses at the blue-green part of the studied spectrum exceed 1dB/m.

Such behavior corresponds with mode power distributions illustrated in Fig. 2. The fundamental mode of the structure (L_n = 900 nm, d_n = 200 nm) propagates partially in the cladding more than in the other structure (L_n = 1000 nm, d_n = 200 nm). At wavelength 420 nm the power surrounds the nanoholes without penetrating inside. We can surmise that nanoring enhances the light confinement in the way similar to PCF rings. With increasing wavelength the power expands through the nanoring and at λ≈1200 nm resembles the mode of the structure with L_n = 1000 nm. Towards longer wavelengths both structures leak the power into the cladding which corresponds to the loss curves in Fig. 4 running in quasi-parallel manner at that spectral region.

Simulations were carried out for smaller L_n and large relative hole size d_n/L_n = 0.48±0.05, too. Qualitatively, in Fig. 5 for small nanoholes arranged in the vicinity of the center the scenario is similar to that in Fig. 3. With the expansion of the nanoring the dispersion curve submerges and the structure allows more leakage. The window of anomalous dispersion is being contracted and shifted more to the shorter wavelengths region.

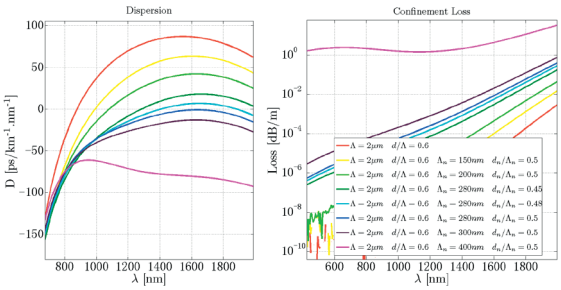

Fig. 5 Dispersion (a) and confinement losses (b) for smaller radii of ring nanostructures and constant relative nanohole size

Quantitatively, the level of dispersion drops very rapidly. A particular structure around (L_n ≈ 280 nm and d_n/L_n ≈ 0.5) exhibits only one ZDW. Further increasing of the nanoring radius yields all-normal dispersion profiles.

λ	540 nm	920 nm	1540 nm
L_n = 200 nm, d_n/L_n = 0.5	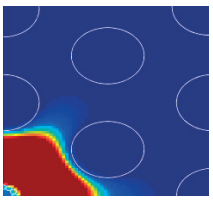	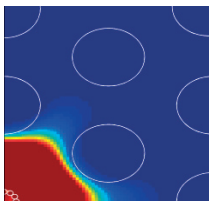	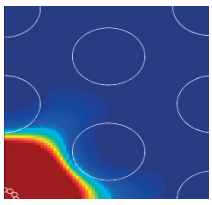
L_n = 400 nm, d_n/L_n = 0.5	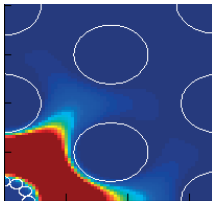	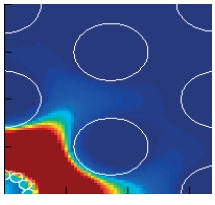	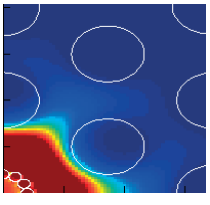

Fig. 6 Mode distributions of z-component of Poynting vector for PCF with constant d_n/L_n = 0.5, but for different radii of ring nanostructure; penetration of light through the ring occurs for different structures at different wavelength

For the design of fiber having only one ZDW we separate the influence of holes' size. The difference between structures with L_n = 280 nm is in the hole size: 140 nm, 134 nm and 126 nm (see legend in Fig. 5). For example, at 1650 nm the change of the hole diameter as small as 6 nm will induce relatively strong dispersion change 6.8 ps.nm^{-1}.km^{-1} and if we again diminish the diameter (8 nm) this change will result in 11.2 ps.nm^{-1}.km^{-1}.

With increasing L_n the sensitivity of dispersion does not rise dramatically, rather we notice significant changes in loss curves. Positioning larger nanoholes roughly to the half way from fiber center to first cladding ring prevents the fundamental mode from the low-loss guidance around the middle of the studied spectrum where can be also substantial mode leakage (see Fig. 6).

For power distribution of modes, the ring is closed and at short wavelengths prevents the power to be localized within such small area. With increasing wavelength the power starts to penetrate into the area encircled by nanoholes and finally at longer wavelengths the power of mode is comparable inside and outside the nanoring. The wavelength at which the light starts to disobey the nanoring as an obstacle depends on its radius. The smaller the ring, the shorter is this wavelength, which is illustrated in Fig. 6.

So far the effects of nanostructure were examined in terms of its distance from center and first inner ring of cladding. Last modification taken into account is how it behaves with holes having same position, but difference size.

Fig. 7 illustrates the nanostructures within core and one can see that, in fact, they form the core, becoming the innermost ring, since their effective mode areas are smaller than those of the core without nanostructure (data not shown). For larger hole size (Figs. 7c, 7d) at longer wavelengths they release the strong mode confinement thus extending the effective mode areas over those of structures with smaller nanoholes (Figs. 7a, 7b).

Concerning the dispersion, the red shift of ZDW is characteristic for the small holes whilst for the large ones strong waveguide contribution to anomalous dispersion shifts the ZDW towards blue: ZDW is 817 nm and 738 nm for the fibers given by Figs. 7c and 7d, respectively. In this case, the large holes of diameter $d_n > \lambda/2$ provoke strong oscillations of the dispersion curve. At near infrared wavelengths the slope of the strong anomalous dispersion is crossing zero and the curve falls to the

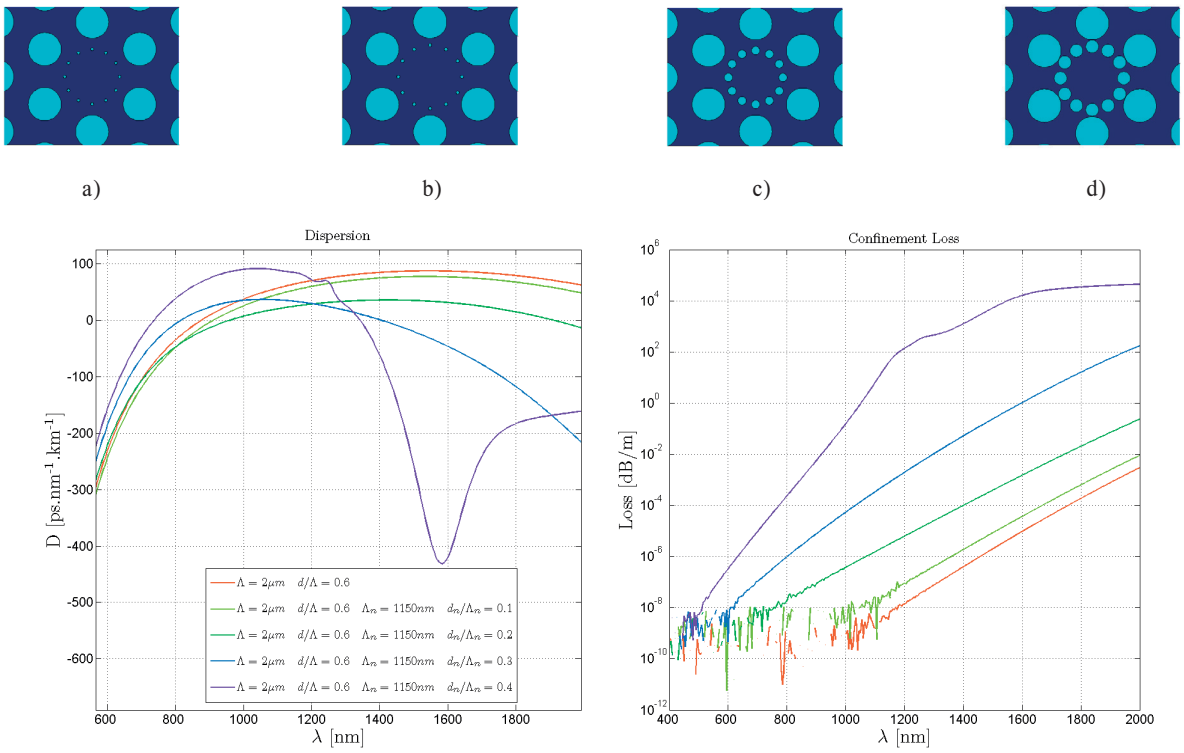

Fig. 7 Ring nanostructure with holes (a) 115 nm, (b) 174 nm, (c) 261 nm, (d) 348 nm, all 1150 nm far from the center, (e) dispersion and losses as a function of wavelength for the structures (a)(b)(c)(d)

normal dispersion half plane, which is connected with steep grow of loss.

Finally, the large normal dispersion region in mid infrared band with remarkable dip corresponds to the modes with effective mode area larger than 8 mm^2 which visually means radius of the circle circumscribing such effective mode area is app. 300 nm^2 greater than that in case of core without nanostructure. At $\lambda \approx 1900$ nm the mode power, however, leaks strongly into the cladding.

4. Conclusion

We carried out detailed analysis of the dispersion, losses and cross-sectional mode power distribution of photonic crystal fibers with nanohole ring structure placed in the core. The simulations revealed a great sensitivity of these properties to changes of geometrical parameters of nanostructure involving position and size of arrayed nanoholes. With proper adjustment of the available parameters the desired dispersion characteristic could be achieved. Strong ties between wild dispersion profiles and high losses were manifested in critically leaky structures.

Furthermore, due to their circular arrangement the nanoholes do not perfectly fit the pattern of cladding holes and thus not serve as an extension of periodical cladding, which significantly affects the mode shape (for nanoholes' size further above homogenization limit).

Besides, it should be noted that whether the structure is producible or not is questionable since the holes can be too small and close to each other to not collapse. Supposedly, the silica-air combination would make the fabrication of such fibers even more challenging issue.

Acknowledgements:

The authors would like to express their thanks to Dr. Peter Tvarožek for his idea and helpfull discussion. This work was partly supported by the Slovak National Grant Agency No. VEGA 1/1058/11 and No. VEGA 1/0528/12.

References:

[1] JOANNOPOULOS, J. D., JOHNSON, S. G., WINN, J. N., MEADE, R. D.: *Photonic Crystals: Molding the Flow of Light,* Princeton University Press, 2008.

[2] KNIGHT, J. C.: Photonic Crystal Fibers, *Nature* 424, 8471, 2003.

[3] RUSSEL, P. St. J.: Photonic Crystal Fibers, *J. of Lightwave Technology* 24, 4729, 2006.

[4] TARTARINI, G., PANSERA, M., ALKESKJOLD, T. T., BJARKLEV, A., BASSI, P.: Polarization Properties of Elliptical-Hole Liquid Crystal Photonic Bandgap Fibers, *J. Lightwave Technol.* 25, pp. 2522-2530, 2007.

[5] RENVERSEZ, G., KUHLMEY, B., MCPHEDRAN, R.: Dispersion Management with Microstructured Optical Fibers: Ultraflattened Chromatic Dispersion with Low Losses, *Opt. Lett.* 28, pp. 989-991, 2003.

[6] KANKA, J.: Design of Photonic Crystal Fibers with Highly Nonlinear Glasses for Four-wave-mixing Based Telecom Applications, *Opt. Express* 16, pp. 20395-20408, 2008.

[7] WIEDERHECKER, G. S., CONDEIRO, C. M. B., COUNY, F., BENABID, F., MAIER, S. A., KNIGHT, J. C., CRUZ, C. H. B., FRAGNITO, H. L.: Field Enhancement within an Optical Fibre with a Subwavelength Air Core, *Nature Photonics*, 1, pp. 115 – 118, 2007.

[8] SAITOH, K., FLOROUS, N., KOSHIBA, M.: Ultra-flattened Chromatic Dispersion Controllability Using a Defected-core Photonic Crystal Fiber with Low Confinement Losses, *Opt. Express,* vol. 13, pp. 8365-8371, 2005.

[9] RUAN, Y., EBENDORFF-HEIDEPRIEM, H., AFSHAR, S.,MONRO, T. M.: Light Confinement within Nanoholes in Nanostructured Optical Fibers, *Opt. Express*, vol. 18, pp. 26018-26026, 2010.

[10] SEREBRYANNIKOV E. E., ZHELTIKOV, A. M.,: Nanomanagement of Dispersion, Nonlinearity, and Gain of Photonic-crystal Fibers: Qualitative Arguments of the Gaussian-mode Theory and Nonperturbative Numerical Analysis, *J. Opt. Soc. Am. B*, vol. 23, pp. 1700-1707, 2006.

[11] SHAVRIN, I., TVAROZEK, P., KOYS, M., SCHUSTER, K., NOVOTNY, S., LUDVIGSEN, H.: EXTREMELY WHITE SUPERCONTINUUM GENERATION IN THREE-HOLE SUSPENDED-CORE FIBER, *Conference on Lasers and Electro-Optics Europe and 12th European Quantum Electronics Conference, CLEO EUROPE/EQEC 2011*, art. No. 5943001, 2011.

Peter Hockicko - Peter Bury - Francisco Munoz - Laura Munoz-Senovilla *

INVESTIGATION OF ACOUSTIC AND ELECTRICAL PROPERTIES OF A $LiPO_3$ METAPHOSPHATE GLASS

The acoustic attenuation spectroscopy in connection with conductivity and dielectric relaxation spectroscopy can be useful techniques for the study of relaxation processes and transport mechanisms in Li^+ ion conducting glasses. A theoretical model and mathematical fit of acoustic and conductivity measurements are used for characterization of the ionic hopping motion, relaxation processes and transport mechanisms connected with the mobility of conducting Li^+ ions. Results from acoustic measurements are compared with results obtained from electrical conductivity measurements.

Keywords: *Acoustic spectroscopy, conductivity spectroscopy, dielectric spectroscopy, Li phosphate glasses, relaxation and transport processes.*

1. Introduction

The research of lithium conducting glasses has recently seen an increase due to their potential application mainly as solid-state amorphous electrolytes in secondary batteries and the advantages they may offer [1]. In a secondary lithium ion battery, Li metal can be used as the anode material allowing higher energy and power densities than when graphitized anodes are used as anode materials, and one of the most important requirements of the electrolyte material in such a system is to have a high ionic conductivity and being compatible with the electrode materials. The use of solid electrolytes in rechargeable batteries can provide numerous advantages such as the possibility of miniaturization through thin-film production, longer active life, high reliability, thermal, chemical and mechanical stability. Most of the works have been focused on the ionic conductivity of LiPON thin-films, which is generally given around 2×10^{-6} S/cm at 25°C [2] and average activation energy of E_a = (0.55 ± 0.02) eV [3]. LiPON thin-film electrolytes have been recently studied and their properties and structure compared to those found in lithium phosphate glasses and their oxynitride counterparts [4 and 5]. The structure of a $LiPO_3$ metaphosphate glass is known to be built of long chains or rings of PO_4 tetrahedra [6]. Two of the oxygens in each PO_4 are bridging oxygens that link together neighbouring groups while the other two are non-bridging oxygens bonded to the modifier cations Li^+. On the other hand, the structure of an oxynitride glass will be formed by PO_4 and also by new groups, PO_3N and PO_2N_2 tetrahedra, having nitrogen in two different bonding states, as dicoordinated –N= (N_d) or tricoordinated –N< (N_t) nitrogen species. The study of the relaxation processes taking place in these glasses can be important for the future development of all solid-state electrolytes.

The acoustic attenuation measurements seem to be a useful technique for investigation of transport mechanisms in conducting glasses and compared to the electrical one it has even some advantages as high sensitivity, the absence of contact phenomena and several others [7]. Acoustical measurements made over a wide range of frequencies and temperatures can characterize different relaxation processes according to corresponding transport mechanisms due to the strong acousto-ionic interaction and it can discover also different kinds of sites and/or ionic hopping motions associated with the charge mobility [8]. The dielectric spectroscopy in principle derived from the same experimental data as electrical conductivity spectroscopy (i.e., real and imaginary components of the sample impedance) is another powerful technique for the study of ion relaxation and transport mechanisms [9 and 10]. The shape of the loss tangent angle tan $\delta(\omega)$ is actually sensitive to the imaginary part of the permittivity $\varepsilon_r''(\omega)$ passes through a maximum at a frequency which is temperature dependent and whose inverse is commonly associated with the characteristic time required for dipoles to reorient.

In this contribution we present first results of combined acoustic and electrical investigation of $LiPO_3$ metaphosphate

* [1]Peter Hockicko, [1]Peter Bury, [2]Francisco Munoz, [2]Laura Munoz-Senovilla
[1]Department of Physics, Faculty of Electrical Engineering, University of Zilina, Slovakia
[2]Instituto de Ceramica y Vidrio (CSIC), Madrid, Spain
E-mail:hockicko@fyzika.uniza.sk

glasses. Double Power Law (DPL) model is used for description of experimental results obtained from acoustic spectra of the glasses with the purpose to study ion relaxation processes and transport mechanisms. Electrical measurements characterizing the ion relaxation processes and possible transport mechanisms in investigated ion conducting glasses are presented. The results obtained by different methods are then summarized and compared.

2. Theoretical principles

The acoustic attenuation will exhibit a maximum when the condition ωτ is equal to 1 and

$$\tau = \tau_0 \exp\left(\frac{E_a}{k_B T_{peak}}\right), \quad (1)$$

is the most probable relaxation time, T thermodynamic temperature, k_B the Boltzmann constant, $\omega = 2\pi\nu$ and ν is frequency of applied acoustic waves. The relaxation processes, described by an Arrhenius equation (1), are characterized by activation energy E_a for jumps over the barrier between two potential minima and typical relaxation frequency of ion hopping $1/\tau_0 \approx 10^{13} - 10^{14}$ s^{-1}. An Arrhenius - type relaxation between the temperature of peak maximum T_{peak} and the applied frequency ν of acoustic waves can be then expressed as

$$\nu = \nu_0 \exp\left(-\frac{E_a}{k_B T_{peak}}\right), \quad (2)$$

where ν_0 is the preexponential factor [11].

Double Power Law (DPL) function (3) has been mainly used to fit mechanical loss data in investigated glassy materials [11 and 12]

$$\alpha(\omega, T) \propto \frac{1}{(\omega\tau)^{-n} + (\omega\tau)^{m}} . \quad (3)$$

Using this function, we can fit also the acoustic attenuation spectrum of the lithium metaphosphate glass.

Determination of the imaginary part of the complex dielectric constant (ε'') compared to the real part (ε') play a crucial role in the study of fundamental properties of investigated materials [13], where $\varepsilon'(\omega)$ and $\varepsilon''(\omega)$ characterize the *refractive* and *absorptive* properties of the material, respectively. The *loss tangent* defined by the relation

$$\tan\delta(\omega) = \frac{\varepsilon''(\omega)}{\varepsilon'(\omega)}, \quad (4)$$

can be also used for the relaxation spectroscopy that reflects the basic features of the relaxation processes of mobile ions. This quantity is related to the attenuation constant (or absorption coefficient) of an electromagnetic wave propagating in a material. The activation energies of the relaxation processes can be estimated from the plots of log f vs. $1/T_{max}$ were T_{max} can be found using the isochronal peaks of tan $\delta(\omega,T)$. These plots are straight lines in accordance with Arrhenius equation

$$f = f_0 \exp\left(-\frac{E_a^{tg\delta}}{k_B T_{peak}}\right), \quad (5)$$

where f is the frequency of the applied electrical field, f_0 is the pre-exponential factor. $E_a^{tg\delta}$ is the activation energy associated to the dielectric loss [14].

The electrical conductivity σ of many solids, including glasses, polymers and crystals, has been shown to consist of a frequency independent and a strongly frequency dependent component [15]. Experimental data in a limited frequency region revealed that the overall frequency dependence of σ or the so called "universal dynamic response" (UDR) of ionic conductivity can be approximated by the following simple relation

$$\sigma(\omega) = \sigma_{DC} + A\omega^s = \sigma_0 \exp\left(-\frac{E_a^{DC}}{k_B T}\right) + A\omega^s , \quad (6)$$

where ω (=2πf) is the angular frequency of measurement. Both σ_{DC} and A follow Arrhenius type strong temperature dependencies. In Eq. 6 σ_0 is the pre-exponential factor, E_a^{DC} is the activation energy of the ion transport through hopping processes which can be determined from the DC measurements.

3. Experimental

A lithium metaphosphate glass with composition $50Li_2O.50P_2O_5$ was prepared by conventional melt-quenching procedure. Reagent grade raw materials analytically pure Li_2CO_3 and $(NH_4)_2HPO_4$ were mixed in stoichiometric amounts and the batch was calcined in a porcelain crucible up to 450 ºC, in an electric furnace, then melted during 2 h at 800 ºC. The melt was poured onto a brass mould and annealed slightly above its glass transition temperature, previously determined through Differential Thermal Analysis.

Experimental arrangement for acoustic attenuation measurement has been already described in [16]. The longitudinal acoustic waves of frequency 13 MHz were generated by the Pulse Modulator and Receiver - MATEC 7700 and a $LiNbO_3$ transducer acoustically bonded to a quartz rod buffer. The computer system was used to trigger the apparatus, to record the attenuation changes and to evaluate obtained acoustic spectra. We performed acoustic measurements of the signal going only through the rod buffer without studied sample. So that for the sample investigation we have used only acoustic attenuation on investigated sample. The electrical conductivity measurements were performed by the FLUKE PM 6306 RCL impedance analyzer at frequencies in the range 50 Hz to 1 MHz. The acoustic and electrical measurements

were carried out at temperatures ranging from 290 K to 560 K (to 640 K for acoustic measurements) at a heating rate of 0.5 K/min.

The sample for acoustic and electrical measurements was square in shape (thickness≈1.82 mm and area = 10.1 x 10.1 mm^2) and end faces were polished to be flat and parallel.

4. Experimental results and discussion

The acoustic attenuation spectrum (Fig. 1) indicates one broad attenuation peak with a maximum at a temperature about 530 K. Applying DPL function (3) we could simulate acoustic attenuation spectra at constant frequency as a superposition of individual peaks and determined the values of activation energies of the individual relaxation processes connected with ion hopping. The other peak occurring at the temperature higher than 590 K are connected with the processes appearance above the glass transition temperature, T_g (for investigated sample T_g = *587 K*).

The whole temperature dependence of acoustic attenuation has been analyzed assuming the existence of a thermally activated relaxation process associate to Li^+ ions. Using the theoretical double power law (DPL) model (Eq. 3), and Arrhenius equation (Eq. 2), we calculated the energy of the main relaxation process, E_{a1} = *0.73 eV* from acoustic attenuation measurement. This value is very close to the activation energy for conduction found from DC measurements E_a^{DC} = *0.735 eV* (Fig. 2). Using AC measurements the activation energy of the dielectric losses $E_a^{tg\delta}$ = *0.79 eV* was obtained (Fig. 3).

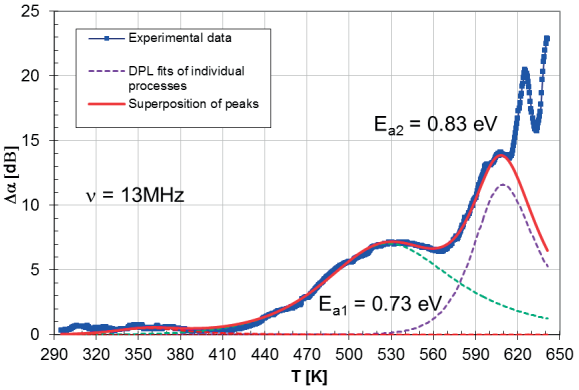

Fig 1. The acoustic attenuation spectra of investigated lithium metaphosphate glass measured at frequency ν = 13MHz (full blue line) and the DPL fits of the supposed relaxation processes (dashed lines) including their superposition (full red line)

We have found that activation energy for conduction E_a^{DC} is very close to activation energy E_{a1} of the main relaxation process calculated from acoustic measurement which can be connected with the same microscopic process. However, the acoustic spectra detected also a second process, which could be related to the appearance of the glass transition with activation energy E_{a2} = *0.83 eV*. It is known that the conductivity of glasses shows a change in activation energy when passing over the glass transition [17]. Therefore, the second thermally activated process that has been seen through the acoustic measurements, with E_{a2}=*0.83 eV*, could correspond to movement of Li^+ ions above T_g.

Complex impedance $(Z^* = Z' - jZ'')$ plots at the temperatures from T = 330 - 390 K are illustrated in the insert of Fig. 2. The Nyquist plot consists of a depressed semicircle. The σ_{DC} was calculated using the relation $\sigma_{DC} = d/(RA)$, where d is the thickness of the bulk glass piece and A is the area of cross section of the glass piece, resistance R was calculated from the Nyquist plot. The DC conductivity was observed above 310 K and is ranged from $6.5x10^{-9}$ S/cm at 330 K to $2.1x10^{-4}$ S/cm at 550 K. The increase of DC conductivity with the temperature indicates a thermally activated conduction mechanism. The representative

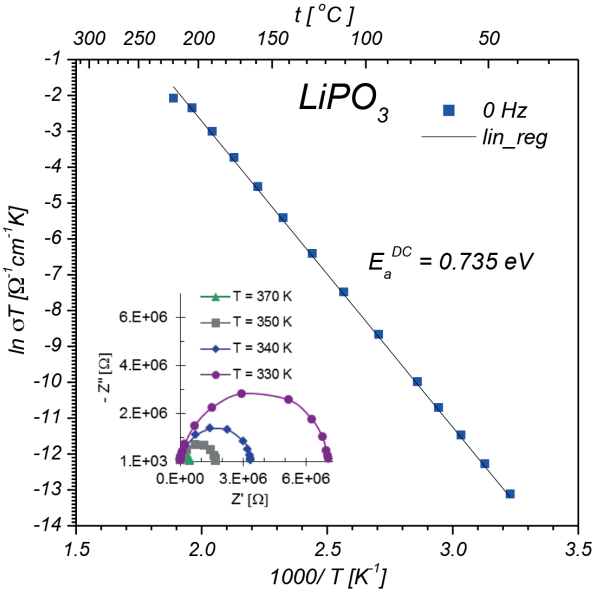

Arrhenius plot for investigated sample is illustrated in Fig. 2.

Fig. 2 Arrhenius plot constructed from temperature dependences of DC conductivity calculated from Nyquist diagram (inside)

Plotting the frequency of AC electric field in logarithmic scale as a function of corresponding inverse temperature of maximum of loss tangent angle (Arrhenius plot), the activation energy of the dielectric losses have been obtained.

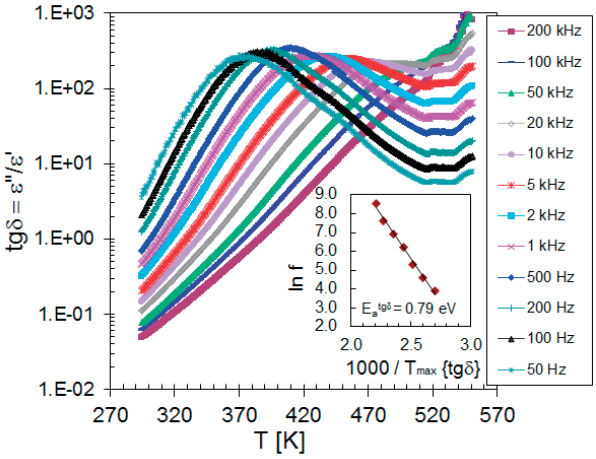

Fig. 3 Temperature dependence of loss tangent and Arrhenius plot of dielectric loss angle tangent maxima and applied frequency

The set of the frequency dependencies of AC conductivity measured at various temperatures (conductivity spectra) is illustrated for the glass in Fig. 4. The obtained AC conductivity measurements correspond to the complete conductivity spectra of glassy samples. However, because of the limited frequency range only two regimes (II and III) of the whole conductivity spectra represented by a different slope of individual curves could be recognized, moreover the regime II only at low temperatures. The low frequency part in regime III and the dispersive regime II are due to the hopping motion of the mobile ions. Adopting the Eq. 6, slopes can be derived at the higher frequencies with parameter $s = 0.68$ for temperature 310 K (Fig. 4).

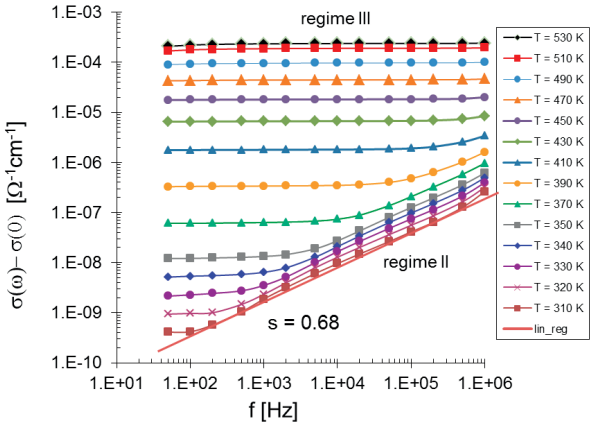

Fig. 4 Results obtained from AC electrical conductivity measurements

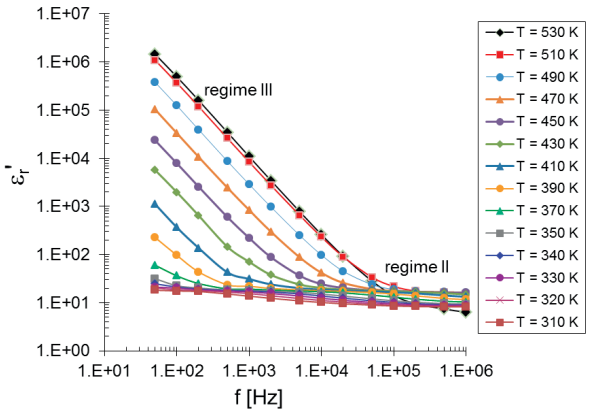

Fig. 5 Frequency dependences of the real part of complex relative permittivity

The real part of the complex relative permittivity versus frequency has been reported in Fig. 5. The behaviour of conductivity and permittivity is divided in two regimes: regime II can be observed only at low temperatures (310 K – 350 K). The conductivity at low temperatures and high frequencies is increased dramatically with the frequency and the permittivity is almost the same in anyway of the frequency and the temperature. Regime III is appeared at higher temperatures. The conductivity is almost constant and corresponds to the σ_{DC}. The permittivity curve shows a slope. In this frequency range, ions jump from site to site through the bulk of the electrolyte. This corresponds to the random diffusion of Li ions in a disorder matrix [18]. In some materials [18 and 19] regime I can be observed: at low frequencies and high temperatures the ionic conductivity decreases drastically. The permittivity is very high and much constant for the lowest frequencies but decreases quickly when the frequency increases. This low-frequency part is influenced by the electrode polarization effect and the Li^+ ions are piled up on the blocking metal electrode.

5. Conclusion

Acoustical and conductivity measurements and dielectric relaxation behaviour have been examined over a wide temperature range in the glass with metaphosphate composition $LiPO_3$. Using the theoretical model of Double Power Law function for the simulation of acoustic spectra we have determined the main relaxation process. Comparison the activation energies obtained from acoustic and electric DC measurements showed that the same microscopic phenomena can be responsible for the acoustic and electrical relaxation processes.

Acknowledgements

The authors would like to thank to Mr. F. Cernobila for technical assistance. This study was supported by R&D operational program Centre of excellence of power electronics systems and materials for their components II. No. OPVaV-2009/2.1/02-SORO, ITMS 26220120046 funded by European regional development fund (ERDF) and by project KEGA No. 035ZU-4/2012 and VEGA No. 1/0853/13. Funding from project MAT2010-20459 of MINECO (Spain) is acknowledged and L. Munoz-Senovilla also thanks the MINECO for her PhD scholarship (BES-2011-044130).

References

[1] DUCLOT, M., SOUQUET, J.-L.: *J. Power Sources*, 97-98, 2001, 610-615.
[2] BATES, J. B., DUDNEY, N. J., GRUZALSKI, G. R., ZUHR, R. A., CHOUDHURY, A., LUCK, C. F., ROBERTSON, J. D.: *Solid State Ionics* 53-56, 1992, 647-654.
[3] YU, X., BATES, J. B., JELLISON JR., G.E., HART, F. X.: *J. Electrochem. Soc.* 144 (2) 1997, 524.
[4] MUNOZ, F., DURAN, A., PASCUAL, L., MONTAGNE, L., REVEL, B., RODRIGUES, A. C. M.: *Solid State Ionics* 179 (15-16), 2008, 574-579.
[5] MASCARAQUE, N., FIERRO, J. L. G., DURAN, A., MUNOZ, F.: *Solid State Ionics* 233(0), 2013, 73-79.
[6] BROW, R. K.: Review: The Structure of Simple Phosphate Glasses, *J. Non-Cryst. Solids* 263&264, 2000, 1-28.
[7] ROLING, B., HAPPE, A., INGRAM M. D., FUNKE, K.: *J. Phys. Chem.* B 103, 1999, 4122.
[8] FUNKE, K.: *Sol. State Ionics* 94, 1997, 27.
[9] ALMOND, D. P., WEST, A. R.: *Solid State Ionics* 26, 1988, 265.
[10] KUDELCIK, J., BURY, P., ZAVISOVA, V., TIMKO, M., KOPCANSKY, P.: *Communications - Scientific Letters of the University of Zilina* 12 (2), 2010, 34-37.
[11] ROLING, B., INGRAM, M. D.: *Physical Review B* 57 (22), 1998, 14 192 – 14 199.
[12] BURY, P., HOCKICKO, P., JAMNICKY, M.: *Advanced Materials Research* 39-40, 2008, 111.
[13] VENKATESH, J., SIVASUBRAMANIAN, V., SUBRAMANIAN, V., MURTHYA, V. R. K.: *Materials Research Bulletin* 35 (8), 2000, 1325-1332.
[14] PEVZNER, B., HEBARD, A. F., DRESSELHAUS, M. S.: *Physical Review B* 55 (24), 1997, 16 439 – 16 449.
[15] JONSCHER, A. K.: *Nature* 267, 1977, 673-679.
[16] HOCKICKO, P., BURY, P., MUNOZ, F.: *J. Non-Crystalline Solids*, 363 (1), 2013, 140-146.
[17] HALL, A. , SWENSON, J., BOWRON, D. T., ADAMS, S.: *J. Phys.: Condens. Matter* 21, 2009, 245106 (7pp).
[18] LE VAN-JODIN, L., DUCROQUET, F., SABARY, F., CHEVALIER, I.: *Solid State Ionics* 253, 2013, 151-156.
[19] HOCKICKO, P., BURY, P., MUNOZ, F.: *Communications - Scientific Letters of the University of Zilina* 15 (2a), 2013, 33-39.

Mikulas Gintner - Josef Juran *

HIDING THE VECTOR RESONANCE SIGNAL

We investigate how the interplay of the direct and mixing-induced couplings of the hypothetical $SU(2)_{L+R}$ vector triplet resonance to the third quark generation can hide the resonance signal in $\bar{t}t$, $\bar{b}b$, and $\bar{b}t/\bar{t}b$ channels. The vector resonances are assumed to represent bound states of hypothetical strongly-interacting new physics, the extension of the Standard model.

Keywords: *Electroweak symmetry breaking, effective Lagrangian, vector resonances, new strong interactions.*

1. Introduction

Even though the ATLAS and CMS announcements of the 125 GeV boson discovery [1] have not settled the question about the mechanism of electroweak symmetry breaking yet they did provide major hints pointing to its solution. At the moment, it is clear that the observed properties of the discovered boson are compatible with the Standard model Higgs boson hypothesis [2 and 3]. At the same time they are compatible with many alternative extensions of the Standard model (SM). From a theoretical point of view, the extensions get some preference over the SM Higgs due to the naturalness argument. They include supersymmetry theories as well as theories where electroweak symmetry is broken by new strong interactions, like in Technicolor [4 - 7].

Following theoretical arguments, as well as the example of QCD, it seems reasonable to expect that beside the composite scalar the new strong interactions would also produce bound states of higher spins. The vector $SU(2)$ triplet resonance is a natural candidate to look for. From other point of view, in strongly interacting theories new resonances are required to tame the unitarity. If, as expected, the composite Higgs couplings differ from the SM ones the Higgs alone will fail to unitarize the VV (V=$W^{\pm}$, Z) scattering amplitudes and other resonances are necessary to do the job.

Recently, we studied the effective Lagrangian where beside the 125-GeV scalar resonance – an $SU(2)_{L+R}$ singlet complementing the non-linear triplet of the Nambu-Goldstone bosons, the $SU(2)_{L+R}$ triplet of vector resonances is explicitly present. It fits the situation when the global $SU(2)_L \times SU(2)_R$ symmetry is broken down to $SU(2)_{L+R}$. As far as the vector resonance sector is concerned the vector triplet is introduced as a gauge field via the hidden local symmetry approach [8]. Because of this, the vector resonance mixes with the EW gauge bosons which result in appearance of indirect couplings of the vector resonance with all SM fermions. Besides, the direct couplings of the vector resonance triplet to the SM fermions are also allowed by the Lagrangian symmetry. Regarding the direct couplings we opt for a special setup inspired by the speculations about an extraordinary role of the top quark (or the third quark generation) in new strong physics: we admit direct couplings of the new triplet to no other SM fermions but the top and bottom quarks only. Finally, the symmetry allowed interaction terms between the scalar and vector resonances are also present. We nicknamed the effective Lagrangian as the tBESS model.

In the paper [9], we had introduced the so-called Death Valley (DV) effect. The DV is a region in the (b_L, b_R) parameter space where the interplay of the direct and indirect couplings of the vector triplet with fermions can diminish or even zero a particular top/bottom quark channel decay width of the vector resonance.

In this paper, we analyze the DV effect in the light of the updated low-energy limits for the parameters of the tBESS Lagrangian. The Higgsless tBESS model considered in [9] was made obsolete by the LHC discovery of the 125 GeV boson. Following this development we augmented our effective Lagrangian with the scalar resonance representing the discovered boson and recalculated the low-energy limits [10 and 11]. In this paper we calculate the relevant DV regions and superimpose them over the regions allowed by the low-energy data.

In Section 2 we briefly explain the structure of the tBESS effective Lagrangian. In Section 3 we outline the structure of the low-energy limit of the tBESS Lagrangian and how the low-energy fits and confidence level limits on its free parameters were obtained. The fits and limits are briefly summarized. Eventually, we present the obtained Death Valley regions in the superposition with the low-energy limits for the free parameters. In Section 4 we discuss our findings and conclusions.

* [1,2]**Mikulas Gintner,** [2,3]**Josef Juran**

[1]Physics Department, University of Zilina, Zilina, Slovakia, E-mail: gintner@fyzika.uniza.sk

[2]Institute of Experimental and Applied Physics, Czech Technical University in Prague, Prague, Czech Republic, E-mail: josef.juran@utef.cvut.cz

[3]Institute of Physics, Silesian University in Opava, Opava, Czech Republic

2. The effective Lagrangian

We introduced the $SU(2)_{L+R}$ triplet vector resonance to the usual $SU(2)_L \times SU(2)_R \to SU(2)_{L+R}$ effective Lagrangian with the non-linearly transforming $SU(2)_{L+R}$ triplet of the would-be Nambu-Goldstone bosons augmented with the $SU(2)_{L+R}$ singlet scalar resonance. For simplicity, we assumed the SM couplings of the scalar resonance only in our analysis. Recall that the current LHC measurements admit about 10% deviations from the SM for the 125 GeV boson couplings.

The vector triplet is brought in as a gauge field via the hidden local symmetry (HLS) approach [8]. The effective Lagrangian is built to respect the global $SU(2)_L \times SU(2)_R \times U(1)_{B-L} \times SU(2)_{HLS}$ symmetry of which the $SU(2)_L \times U(1)_Y \times SU(2)_{HLS}$ subgroup is also a local symmetry. The $SU(2)_{HLS}$ symmetry is an auxiliary gauge symmetry invoked to accommodate the $SU(2)$ triplet of vector resonances. Beside the scalar singlet and the vector triplet, the effective Lagrangian is built out of the SM fields only.

Our effective Lagrangian can be split in three terms

$$\mathcal{L} = \mathcal{L}_{GB} + \mathcal{L}_{ESB} + \mathcal{L}_{ferm} , \qquad (1)$$

where $\mathcal{L}_{GB}$ describes the gauge boson sector including the $SU(2)_{HLS}$ triplet, $\mathcal{L}_{ESB}$ is the scalar sector responsible for spontaneous breaking of the electroweak and hidden local symmetries, and $\mathcal{L}_{ferm}$ is the fermion Lagrangian of the model. We will not show full Lagrangian (1) here. All details regarding the Lagrangian can be found in [10 and 11]. Out of its three terms we will briefly discuss the third term, $\mathcal{L}_{ferm}$. The fermion part of the Lagrangian is directly related to the effects analyzed in this paper.

As far as the fermion sector is concerned no new fermions beyond the SM were introduced in our Lagrangian. The fermion sector of the Lagrangian can be divided into three parts

$$\mathcal{L}_{ferm} = \mathcal{L}^{SM}_{ferm} + \mathcal{L}^{scalar}_{ferm} + \mathcal{L}^{tBESS}_{(t,b)} , \qquad (2)$$

where $\mathcal{L}^{SM}_{ferm}$ contains the SM interactions of fermions with the electroweak gauge bosons, $\mathcal{L}^{scalar}_{ferm}$ is about the interactions of the fermions with scalar fields and includes the fermion masses, and $\mathcal{L}^{tBESS}_{(t,b)}$ describes the third quark generation direct interactions with the vector resonance. In addition, it contains symmetry allowed non-SM interactions of the third quark generation with the EW gauge bosons.

The vector resonance couples directly to the third quark generation only. The interactions of the left and right fields are proportional to b_L and b_R, respectively. In addition, there is a free parameter p which disentangles the right bottom coupling from the right top coupling. The assumption that the vector resonance interaction with the right bottom quark is weaker than the interaction with the right top quark corresponds to the expectation that $0 \le p \le 1$. While p=1 leaves the interactions equal, the p=0 turns off the right bottom quark interaction completely and maximally breaks the $SU(2)_R$ part of the Lagrangian symmetry down to $U(1)_{R3}$. In addition the symmetry of the Lagrangian admits non-SM interaction of the fermions with the EW gauge bosons that we also include in $\mathcal{L}^{tBESS}_{(t,b)}$ under the assumption that they apply to the third quark generation only. These interactions are proportional to the free parameters λ_L and λ_R. In the unitary (physical) gauge where all six unphysical scalar fields are gauged away the new physics part of the (t,b) Lagrangian assumes the form

$$\mathcal{L}^{tBESS}_{(t,b)} = ib_L \bar{\psi}_L (\not{V} - \not{W}) \psi_L + ib_R \bar{\psi}_R P (\not{V} - \not{B}^{R3}) \times P\psi_R + i\lambda_L \bar{\psi}_L (\not{W} - \not{B}^{R3}) \psi_L + i\lambda_R \bar{\psi}_R P (\not{W} - \not{B}^{R3}) P\psi_R \qquad (3)$$

where $\not{W}_\mu = ig \not{W}^a_\mu \tau^a, \not{B}^{R3} = ig' \not{B} \tau^3, \not{V}_\mu = i\frac{g''}{2} \not{V}^a_\mu \tau^a$ and the matrix P=diag(1,p) disentangles the direct interaction of the vector triplet with the right top quark from the interaction with the right bottom quark.

The masses of the vector triplet are set by the scale v and depend on the three gauge couplings g,g',g'', and the free parameter α. In the limit when g and g' are negligible compared to g'' the masses of the neutral and charged resonances are degenerate, $M_V = \sqrt{\alpha}\, g'' v/2$. If higher order corrections in g/g'' are admitted a tiny mass splitting occurs such that $M_{V^0} > M_{V^\pm}$ [9].

Once the gauge boson fields are expressed in the gauge boson mass basis the mixing generated interactions of the vector triplet with all fermions will emerge from the fermion Lagrangian $\mathcal{L}^{SM}_{ferm}$. However, these indirect interactions of the vector resonance with the light fermions will be suppressed by the mixing matrix elements proportional to $1/g$''.

3. The low-energy limits vs the Death Valley effect

If there is the tBESS vector resonance triplet we can learn about its parameters even before its discovery by measuring deviations of the known particle couplings from their SM values. For example, due to the mixing between the vector resonance and the EW gauge bosons the deviations from the SM values would be present in the couplings of the EW gauge bosons to the SM fermions. In this sense, in the case of our effective Lagrangian the most interesting vertices should be those of the top and bottom quarks: *Wtb*, *Zbb*, and *Ztt*.

Unfortunately, the measurements of the *Wtb* and *Ztt* vertices have been rather coarse so far [12]. On the other hand, the couplings of the light fermion vertices including *Zbb* were measured at previous colliders, sometimes to a very high precision. We refer to these measurement as the low-energy measurements. While the LHC is capable to refine these measurements, and it has done so already, the existing improvement are not sufficient

to compete with the low-energy restrictions on the tBESS parameters.

To confront the tBESS free parameters with the low-energy measurements performed at $O(10^2)GeV$ we derive the low-energy (LE) Lagrangian by integrating out the vector resonance triplet the assumed mass of which is $O(10^3)GeV$. It proceeds by taking the limit $M_{triplet} \to \infty$, while g'' is finite and fixed, and by substituting the vector resonance equation of motion (EofM) obtained under these conditions.

Beside other Lagrangian terms the EofM also modifies the $\mathcal{L}^{tBESS}_{(t,b)}$ term in (2). Thus

$$\mathcal{L}^{LE}_{ferm} \equiv \mathcal{L}^{SM}_{ferm} + \mathcal{L}^{LE-tBESS}_{(t,b)} + \mathcal{L}^{scalar}_{ferm}. \tag{4}$$

In the EW gauge boson mass eigenstate basis and after the proper renormalization the relevant parts of the $\mathcal{L}^{LE}_{ferm}$ can be expressed as

$$\mathcal{L}^{SM}_{ferm} + \mathcal{L}^{LE-tBESS}_{(t,b)} = i\overline{\psi}\not{\partial}\psi - e\overline{\psi}\not{A}Q\psi - \frac{G_{LE}}{2}\overline{\psi}\not{Z}\left(C_L P_L + C_R P_R\right)\psi - \frac{g_{LE}}{\sqrt{2}}\overline{\psi}\left(\not{W}^{+}\tau^{+} + \not{W}^{-}\tau^{-}\right)\left(D_L P_L + D_R P_R\right)\psi, \tag{5}$$

where $\tau^{\pm} = \tau^1 \pm i\tau^2$, $P_{L,R} = \left(1 \mp \gamma_5\right)/2$. For the light fermions (all SM fermions except the top and bottom quarks) $D_L=1$, $D_R=0$, and

$$C_L = 2T^3_L - 2\kappa s^2_\theta Q,\ CR = -2\kappa s^2_\theta Q, \tag{6}$$

where

$$\kappa = \frac{1+2x^2}{1+4s^2_\theta x^2}, \tag{7}$$

and

$$g^2_{LE} = \frac{1+4s^2_\theta x^2}{1+x^2}\frac{e^2}{s^2_\theta},\ G^2_{LE} = \frac{\left(1+4s^2_\theta x^2\right)^2}{c^2_\theta + x^2}\frac{e^2}{s^2_\theta} \tag{8}$$

$$e = \frac{gg'/G}{\sqrt{1+\left(\frac{gg'}{Gg''/2}\right)^2}},\ s_\theta = g'/G,\ x = g/g'', \tag{9}$$

where $G = \left(g^2 + g'^2\right)^{1/2}$ and $c_\theta = \left(1 - s^2_\theta\right)^{1/2}$. In the case of the top and bottom quarks

$$C_L = 2\left(1 - \Delta L/2\right)T^3_L - 2\kappa s^2_\theta Q, \tag{10}$$

$$C_R = 2\left(P_f \Delta R/2\right)T^3_R - 2\kappa s^2_\theta Q, \tag{11}$$

where $P_t=1$, $P_b=p^2$, and

$$D_L = 1 - \Delta L/2,\ D_R = p\Delta R/2, \tag{12}$$

where

$$\Delta L = b_L - 2\lambda_L,\ \Delta R = b_R - 2\lambda_R. \tag{13}$$

Hence, the number of free parameters was reduced also in the fermion sector of the low-energy Lagrangian. The low-energy observables will depend on the combinations (13) of b and λ parameters only. Therefore, no limits derived from the low-energy measurements can apply to b's and λ's individually.

The deviations of the LE Lagrangian from its SM counterpart modify predictions for the low-energy observables. Thus we can use their measured values to derive the preferences and restrictions on the LE free parameters.

In particular, the experimental limits for the LE-tBESS parameters were derived by fitting the low-energy (pseudo) observables $\varepsilon_1, \varepsilon_2, \varepsilon_3, \Gamma_b\left(Z \to b\overline{b}\right)$, and $BR\left(B \to X_s\gamma\right)$. The epsilons are related to the *basic observables* [13]: the ratio of the electroweak gauge boson masses, $r_M \equiv M_W/M_Z$; the inclusive partial decay width of Z to the charged leptons, $\Gamma_l\left(Z \to l\overline{l} + photons\right)$; the forward-backward asymmetry of charged leptons at the Z-pole, $A^{FB,l}(M_Z)$; and the inclusive partial decay width of Z to bottom quarks, $\Gamma_b\left(Z \to b\overline{b} + X\right)$.

The full-scale analysis along with its results can be found in [11]. By fitting the five observables mentioned above with the four free parameters – x, ΔL, ΔR, and p – we found the best values

$$g''(x)=29,\quad \Delta L=-0.004,\quad p\,\Delta R=0.003, \tag{14}$$

with $x^2_{min}(chi)=2.40$. Since $d.o.f.=5-4=1$ the obtained value of x^2_{min} corresponds to the backing of 12%. Within the rounding errors these values hold for the cut-off scale between $0.3TeV \le \Lambda \le 10^3 TeV$, at least. The best values of p and ΔR depend on Λ, separately; in particular,

$$\Lambda=1\ TeV:\quad \Delta R=0.016\quad p=0.209 \tag{15}$$

$$\Lambda=2\ TeV:\quad \Delta R=0.011\quad p=0.289 \tag{16}$$

In Fig. 1 the x^2_{min} values for various combinations of fixed g'' and p are shown. We can see that the best backing for the fits is getting less pronounced as g'' approaches 30 from below. More specifically, while backings of the fits with different p's can differ by several orders of magnitude when $g''<20$, the backing for $g''=30$ changes between 10% and 50% as p crawls along the $\langle 0;1\rangle$ interval.

Recall that beside the direct interactions the new vector triplet couples to the third quark generation via mixing with the electroweak gauge bosons. In certain regions of the parameter space the negative interference between the two kinds of interactions takes place. Thus, it might happen that even though the direct couplings of the vector resonance to the top and/

or bottom quark are non-trivial the resonance will not decay through the given quark channel. Or, the particular decay will be suppressed below the value that would be implied by the indirect couplings alone. If this occurred the resonance peak in a process where V decays to top and/or bottom quarks could disappear even though the resonance exists and couples directly to the third quark generation.

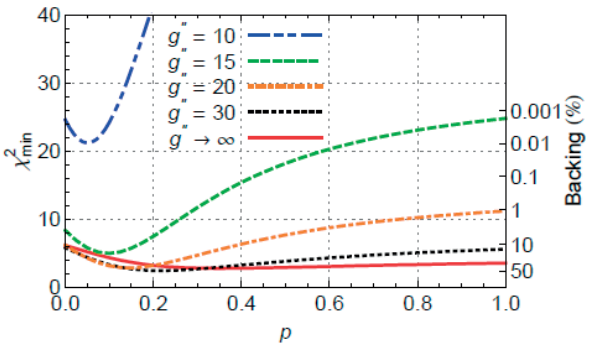

Fig. 1 x^2_{min} of the fit by ΔL and ΔR as a function of the fixed parameters g'' and p for Λ=1 TeV; The labels on the r.h.s. axis indicate the backings for d.o.f.=3

We calculated the DV regions for M_V=1*TeV* and for the parameter values g''=15 (30) and p=0.10 (22). For each case, the DV's in three decay channels of the vector resonance triplet were found. The channels are $V^{\pm} \to t\bar{b}/\bar{t}b$, $V^0 \to b\bar{b}$, and $V^0 \to t\bar{t}$.

In Fig. 2, the DV regions of the three decay channels at g''=15 and p=0.1 are depicted. In each of the three graphs, there are the 95% C.L. electroweak precision data (EWPD) contours for Λ=1 TeV superimposed. The low-energy limits apply to the combination of b's and λ's (ΔL and ΔR) rather than to the parameters alone. The low-energy limits depicted in the b_R-b_L

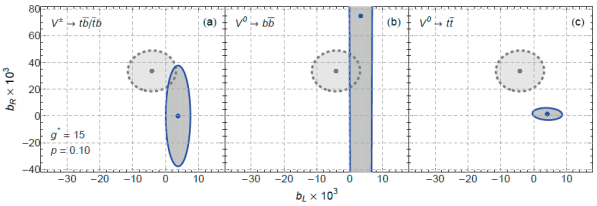

Fig. 2 The DV regions (dark-shaded areas with the blue solid boundary) of the V vector resonance for three decay channels: (a) $V^{\pm} \to t\bar{b}/\bar{t}b$, (b) $V^0 \to b\bar{b}$, and (c) $V^0 \to t\bar{t}$. The blue dots inside the DV's indicate the point of no decay for the particular channels. The DV regions are calculated for g''=15 and p=0.10. The corresponding 95% C.L. EWPD contours for Λ=1 TeV and $\lambda_L = \lambda_R$=0 are superimposed to the graphs as the regions with the gray dashed boundaries. The gray dots inside the EWPD regions indicate the point with the highest backing. Note that the DV for the $V^0 \to b\bar{b}$ channel exceeds the displayed range of the b_R axis. The complete DV region has an oval shape centered at the blue dot. Its lower and upper ends are found at b_R= -0.272 and b_R= 0.422, respectively.

graphs correspond to $\lambda_L = \lambda_R$=0. Nevertheless, by choosing non-zero values for $\lambda_{L,R}$ the low-energy contours get shifted around the (b_L, b_R) parameter space. Various values of λ's can result either in no overlap of the low-energy regions with the DV's or in maximal overlap of the two areas.

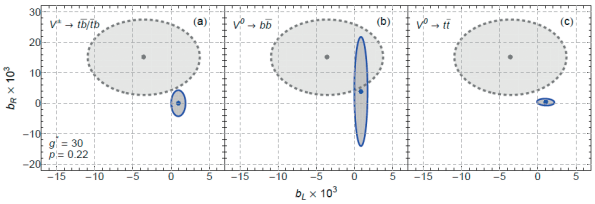

Fig. 3 The same as in Fig. 2 except for different values of g'' and p. In this case, g''=30 and p=0.22

Figure 3 displays the same contents as Fig. 2, except for different values of the parameters g'' and p. Here, the values of the parameters correspond to g''=30 and p=0.22. There are also the 95% C.L. electroweak precision data contours for Λ=1 *TeV* and $\lambda_L = \lambda_R$=0 superimposed in Fig. 3.

As we can see in Figs. 2 and 3 the DV areas are more or less comparable in size with the EWPD regions. In addition, both structures are located not far away from each other when $\lambda_L = \lambda_R$=0. Hence, there are reasonable values of the λ parameters for which the significant part of an EPWD region falls inside the DV.

There might be new physics materialized through the existence of the new vector resonances as well as non-zero values of the b parameters, yet it does not have to reveal itself in an experiment. If the actual values of the b parameters fell in the DV it would make the detection and study of the new vector resonance more difficult. In particular, thanks to the indirect mixing-induced coupling the vector resonance can be produced and studied in the Drell-Yan processes at the LHC or in the s-channel at a future electron-positron collider [14 and 15]. As we demonstrated in [9] the signal of the vector resonance in the top and bottom decay channels can be diminished or hidden by the negative interference between the direct and indirect couplings.

4 Conclusions

We formulated and studied the effective Lagrangian for description of phenomenology of new scalar and vector resonances which might result from new strong physics beyond the SM. Following the often used and studied approach, the ESB sector of the effective Lagrangian was based on the $SU(2)_L \times SU(2)_R \to SU(2)_{L+R}$ non-linear sigma model while the scalar resonance was introduced as the $SU(2)_{L+R}$ singlet and identified with the newly discovered 125-GeV boson. The vector resonance was built in as the $L+R$ triplet employing the hidden local symmetry approach. Throughout the paper we assumed the

vector resonance mass at the bottom of the TeV scale. No other non-SM fields were considered in our effective Lagrangian.

There might be new physics materialized through the existence of the new vector resonances as well as non-zero values of the *b* parameters, yet it does not have to reveal itself in an experiment. Even though there are no direct interactions of the vector resonance triplet to the light fermions the resonance does couple to the light fermions thanks to the mixing with the electroweak gauge bosons. This enables processes with a direct production of the vector resonance at the LHC and future electron-positron colliders. However, in the top and bottom decay channels the signal of the vector resonance can be diminished or hidden by the negative interference between the direct and indirect couplings. We calculated the regions of the negative interference for the studied values of the top-BESS parameters and found that they are often comparable in size and close in position with the 95% C.L. regions. As a general tendency, the relative size of the DV's with respect to the low-energy allowed areas shrinks as the value of *g*'' grows.

Acknowledgments

We would like to thank Ivan Melo for useful discussions. The work of M.G. and J.J. was supported by the Research Program MSM6840770029 and by the project International Cooperation ATLAS-CERN of the Ministry of Education, Youth and Sports of the Czech Republic. M.G. was supported by the Slovak CERN Fund. J.J. was supported by the NSP grant of the Slovak Republic.

References

[1] AAD, G. et al.: (ATLAS Collaboration), *Phys. Lett.* B 716, 1, 2012; Chatrchyan, S. et al. (CMS Collaboration), *ibid.* 30, 2012.
[2] ELLIS, J., You, T.: *J. High Energy Phys.* 09, 2012, 123.
[3] GIARDINO, P. P. , KANNIKE, K., RAIDAL, M., STRUMIA, A.: *Phys. Lett*. B 718, 469, 2012; Carmi, D., Falkowski, A., Kuflik, E., Volansky, T., Zupan, J.: *J. High Energy Phys.* 10, 2012, 196; Montull, M., Riva, F. *ibid.* 11, 2012, 018; Plehn, T., Rauch, M.: *Europhys. Lett.* 100, 11002, 2012; Corbett, T., Eboli, O. J. P., Gonzalez-Fraile, J., Gonzalez-Garcia, M. C.: *Phys. Rev.* D 86, 075013, 2012; arXiv:1211.4580; Peskin, M. E. arXiv:1208.5152.
[4] WEINBERG, S.: *Phys. Rev.* D 19, 1277, 1979; Susskind, L. *ibid.* 20, 2619, 1979; Farhi, E., Susskind, L.: *Phys. Rept.* 74, 277, 1981.
[5] DIMOPOULOS, S., SUSSKIND, L.: *Nucl. Phys.* B155, 237, 1979; Eichten, E., Lane, K. D.: *Phys. Lett.* B90, 125, 1980.
[6] HOLDOM, B.: *Phys. Rev.* D 24, 1441, 1981; *Phys. Lett.* B150, 301, 1985; Yamawaki, K., Bando, M., Matumoto, K.-i.: *Phys. Rev. Lett.* 56, 1335, 1986; Appelquist, T., Karabali, D., Wijewardhana, L. C. R.: *ibid.* 57, 957, 1986; Akiba, T., Yanagida, T.: *Phys. Lett.* B169, 432, 1986; Appelquist, T., Wijewardhana, L. C. R.: *Phys. Rev.* D 36, 568, 1987; Lane, K., Eichten, E.: *Phys. Lett.* B222, 274 1989.
[7] HILL, C. T.: *Phys. Lett.* B266, 419, 1991; B345, 483, 1995.
[8] BANDO, M., KUGO, T., YAMAWAKI, K.: *Phys. Rep.* K. 217, 1988.
[9] GINTNER, M., JURAN, J., MELO, I.: *Phys. Rev.* D 84, 035013, 2011.
[10] GINTNER, M., Juran, J.: arXiv:1301.2124.
[11] GINTNER, M., JURAN, J.: *Europ. Phys. J.* C73 (2013) 2577.
[12] The D0 Collaboration, *Phys. Lett.* B713, 2012, 165-171.
[13] ALTARELLI, G., BARBIERI, R., CARAVAGLIOS, F.: *Nucl. Phys.* B405, 3, 1993; *Int. J. Mod. Phys*. A13, 1031, 1998.
[14] ACCOMANDO, E., BECCIOLINI, D., DE CURTIS, S., DOMINICI, D., FEDELI, L.: *Phys. Rev.* D 83, 115021, 2011.
[15] ACCOMANDO, E., DE CURTIS, S., DOMINICI, D., FEDELI, L.: *Phys. Rev.* D 79, 055020, 2009; Gintner, M., Melo, I., Trpisova, B.: arXiv:0903.1981; Barducci, D., Belyaev, A., De Curtis, S., Moretti, S., Pruna, G. M.: arXiv:1210.2927.

Ivan Melo - Boris Tomasik *

TEMPERATURE AND TRANSVERSE EXPANSION OF FIREBALLS IN Pb+Pb COLLISIONS AT THE LHC

We analyze hadron transverse momentum spectra from Pb+Pb Collisions recorded by the LHC detector ALICE. As the theoretical model we use a Monte Carlo model which includes production and decays of resonances. The transverse expansion of the fireball is shown to be stronger and the freeze-out temperature higher than in similar collisions at RHIC, where collision energy is more than ten times lower.

Keywords: *Heavy ion collisions, quark-gluon plasma, transverse expansion, freeze-out temperature, particle spectra.*

1. Introduction

Heavy atomic nuclei at room temperatures behave as liquids. If we collide two nuclei at moderate energies in a particle accelerator, the nuclei will be compressed and heated and as a result the nuclear liquid will turn into a hadron gas – a gas of pions, protons, neutrons and other hadron species. Hadrons include baryons (such as protons and neutrons) composed of three quarks, and mesons (such as pions and kaons) composed of one quark and one antiquark. The quarks are bound inside hadrons by the strong interaction which is mediated by gluons. Under normal conditions it is impossible to knock a single quark or gluon out of a hadron - the more we pull it, the stronger is the binding force which keeps it inside. This phenomenon is called confinement.

There is, however, a special state of nuclear matter, the so-called quark-gluon plasma (QGP), in which the quarks and gluons are not confined. Quantum chromodynamics (QCD) predicts that if the nuclei are heated above the critical temperature, the density of particles becomes so high that quarks are no longer bound to particular hadrons. Thus hadrons are dissolved into individual quarks and gluons. There is no confinement and quarks as well as gluons move freely within the whole QGP volume. Simulations of QCD on the lattice predict [1] that the (deconfinement) phase transition from the hadron gas phase to the QGP phase occurs at the critical temperature around $T_c \approx 170$ MeV and very high energy density. (In this paper we shall use energy units for the temperature. This should be understood as the energy equivalent which is obtained from the temperature by multiplying with the Boltzmann constant.) Such conditions are presently achieved in collisions of heavy nuclei at ultrarelativistic energies at two operating colliders: at the Relativistic Heavy Ion Collider (RHIC) of the Brookhaven National Laboratory gold nuclei are accelerated to the center of mass energies up to 200 GeV per nucleon pair, and at the Large Hadron Collider (LHC) at CERN the QGP is formed in lead-lead collisions at the energy of 2760 GeV per nucleon pair. The quark-gluon plasma is also believed to be the state of the Universe around 1μs after the Big Bang.

Properties of the QGP and of the deconfinement phase transition are under intense theoretical and experimental scrutiny. The challenge of the program is the complicated nature of heavy ion collisions. The hot nuclear matter created in the collision (the fireball) expands and cools down very quickly and the QGP phase (if present) changes back into the hadron gas phase within $\sim 10^{-23}$ s. The remaining hadronic fireball then continues its rapid expansion during which hadrons interact with each other and create new hadrons until the point of chemical freeze-out when the chemical composition of hadron species is fixed. After that the hadrons keep scattering elastically until the fireball disintegrates at the point of kinetic freeze-out after $\sim 10^{-22}$ s. The initial information present in the QGP phase is thus heavily distorted by the phase transition into the hadron phase, expansion and hadron interactions. Fortunately some signals of QGP remain in the bulk properties of the collisions such as particle rates, transverse flow, chemical freeze-out temperature T_{ch} and kinetic freeze-out temperature T_{kin}. These quantities can be studied via hadron spectra measured by the detectors. In this paper we will study transverse momentum (p_T) spectra of several hadron species measured by the ALICE detector at the LHC [2]

* [1,2]**Ivan Melo, [2]Boris Tomasik**
[1]Department of Physics, University of Zilina, Slovakia,
[2]Department of Physics, Matej Bel University Banska Bystrica, Slovakia
E-mail: melo@fyzika.uniza.sk

and extract the transverse flow and T_{kin} by fitting the experimental spectra with the predictions based on the Blast Wave model [3] which also includes the production of final state hadrons (e.g. pions) from the decays of short-lived resonances. The model is implemented as a Monte Carlo generator published under the title DRAGON [4].

2. Transverse flow

The fireball in the QGP phase exhibits collective flow/expansion in the local thermal equilibrium which can be reasonably well described hydrodynamically. Expansion of the fireball results from strong pressure gradients in the hot nuclear matter. The fireball expands both longitudinally (along the direction of heavy ion beams, the z-axis) and transversely (perpendicularly to the beams).

The transverse flow is particularly interesting since it is entirely generated from the pressure of the hot matter unlike the longitudinal flow which is present also in the initial conditions (incident nucleons tend to continue in the beam direction after the collision). The transverse flow is described in terms of the transverse expansion velocity v_t which depends on the radial distance r from the centre of the fireball. The outer layers of the fireball move with the largest velocity while the central part is at rest in the laboratory system.

In the Blast Wave model [3] one parametrizes the final freeze-out state of the fireball. It is motivated by the assumption that the hydrodynamic relativistic expansion continues up to the point when the temperature of the fluid falls below T_{kin} and the freeze-out from a thermalized fluid into non-interacting free-streaming hadrons occurs suddenly. Within the model this happens at the same longitudinal proper time[1] $\tau = \sqrt{t^2 - z^2}$ for each part of the fireball. Further assumptions include parametrization of v_t as

$$v_t = \tanh\left(\sqrt{2}\,\eta_f \frac{r}{R}\right)$$

where η_f is the transverse flow parameter and R is the radius of the cylindrical fireball at the freeze-out. Hadron number density is assumed to be constant within the cylinder and zero for $r > R$. The Blast Wave model gives a prescription to calculate transverse momentum (p_T) spectra of different species of hadrons as a function of T_{kin}, η_f, hadron masses and several other parameters. For more details about the model we refer the reader to the original works [3]. The calculated spectra can then be used to fit the experimental data and extract T_{kin} and η_f [2].

3. DRAGON calculations and results

We calculate the p_T spectra with the DRAGON tool based on the Blast Wave model to which a careful treatment of all 277

1 We work in units where the speed of light c=1

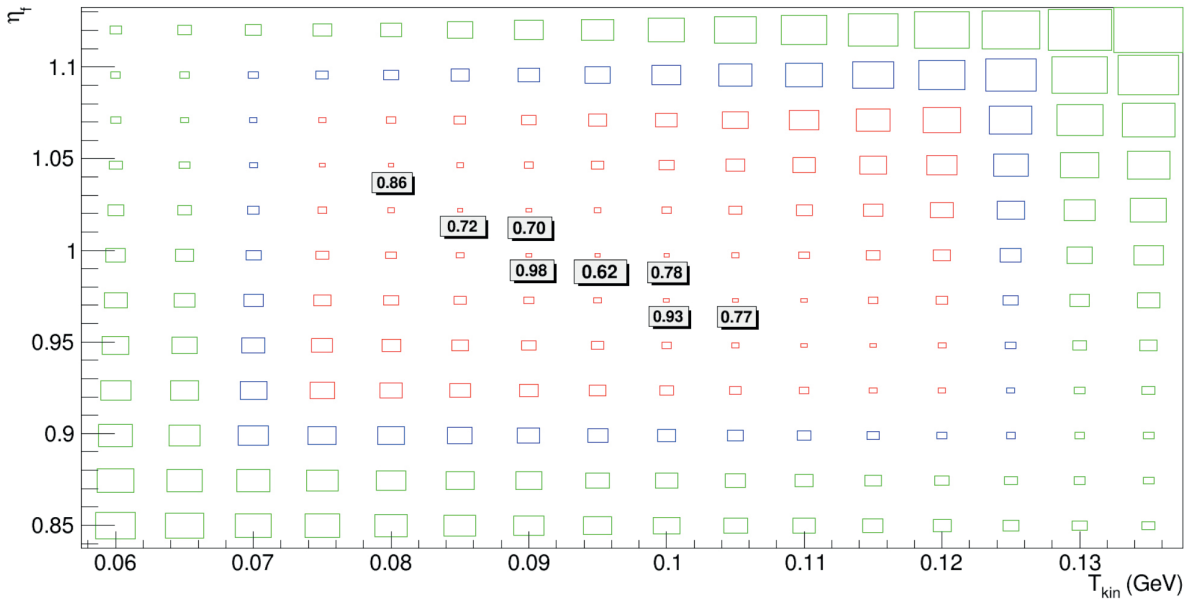

Fig. 1 χ^2 *DRAGON fit to the 0-5% of the most central ALICE data. The size of the boxes is proportional to the* χ^2 *value. The color of the boxes indicates the statistical size of the calculated spectra: green is based on 140 simulated events (collisions), blue on 1400 and red on 14 000 events*

hadron species including decays of unstable resonances is added. We fix the chemical freeze-out temperature for the purpose of this study at T_{ch} = 0.1656 GeV, baryochemical potential at μ_B = 0.002 GeV, strangeness potential[2] μ_S = 0.0069 GeV as dictated by the chemical composition of the produced hadrons. Then, T_{kin} and η_f are varied in order to find the best fit to the data which include p_T spectra of six hadron species: protons, antiprotons, charged pions (π^+,π^-), and charged kaons (K^+,K^-). The best fit is given by the minimum of the χ^2 distribution

$$\chi^2(T_{kin},\eta_f)=\sum_{i=1}^{6}\sum_{j=1}^{j_{max}}\frac{\left[N^{norm}_{DRAGON}(i,j,T_{kin},\eta_f)-N^{norm}_{ALICE}(i,j)\right]^2}{\sigma^{norm}_{ALICE}(i,j)^2}$$

The first sum runs over the six species i, the second sum over all p_T bins j (the maximum number of bins j_{max} = 42, 41, 36 for protons/antiprotons, pions and kaons respectively) with p_T from 0.3 to 4.6 GeV for protons/antiprotons, from 0.1 to 3.0 GeV for pions and from 0.2 to 3.0 GeV for kaons [2]. N_{DRAGON} (N_{ALICE}) gives the normalized numbers of hadrons of i-th species in the j-th bin for DRAGON and ALICE respectively, σ is the experimental error given by the combination of the statistical and systematic errors. Each of the six hadron spectra is normalized independently in order to match the total numbers of each species between DRAGON and ALICE.

2 Nonzero strangeness potential leads to unequal numbers of strange hadrons and antihadrons, such as K- and K+ (strange hadrons contain at least one strange quark which is one of six quarks in the Standard model of particle physics),

The resulting χ^2 divided by the number of degrees of freedom (N_{dof} = 232) from 0-5% most central Pb+Pb collisions (a central collision is one with the zero impact parameter between the two nuclei) are shown in Fig. 1 as a function of T_{kin} and η_f. The area of the boxes is proportional to the χ^2 value, the color of the boxes indicates the statistical size of the calculated spectra: green is based on 140 simulated events (collisions), blue on 1400 and red on 14 000 events. The minimum χ^2/N_{dof} value, 0.62, lies at T_{kin} = 0.095 GeV and η_f = 1.0.

The transverse momentum (p_T) spectra for the six hadron species simulated with DRAGON at the minimum and compared to 0-5% most central Pb+Pb experimental data are shown in Fig. 2. Fit results also for other centralities are summarized in Table 1.

Freeze-out temperatures and transverse expansion parameters from the fits to transverse momentum (p_T) spectra at different centralities based on 1400 simulated events Table 1

Centrality	T_{kin} [MeV]	η_f	χ^2/N_{dof}
0-5%	95	1	0.673
5-10%	95	1	0.764
10-20%	105	0.975	0.733
20-30%	120	0.925	0.881
30-40%	125	0.9	1.044
40-50%	145	0.825	1.411
50-60%	155	0.775	1.900

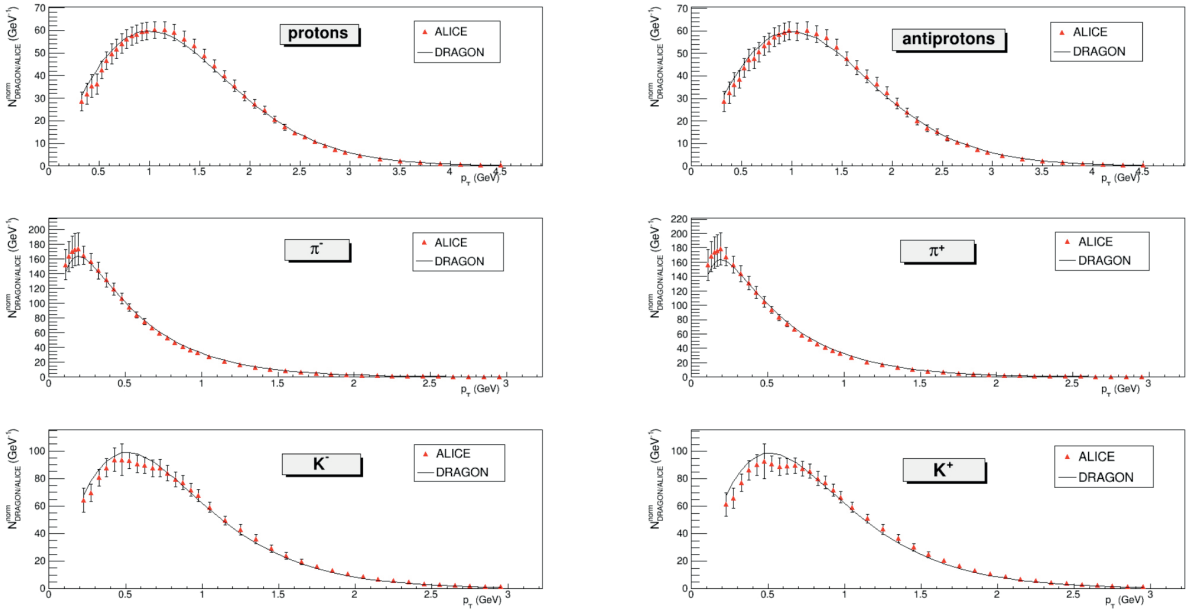

Fig. 2 The transverse momentum (p_T) spectra from central collisions for six hadron species calculated with DRAGON at the χ^2 minimum (solid line) and compared to 0-5% most central Pb+Pb experimental data from ALICE (red triangles)

To make a comparison with lower energy data from RHIC we repeated the fit with the 0-5% of the most central STAR data at the energy 62.4 GeV per nucleon pair [5] and found the minimum χ^2 value at T_{kin} = 0.085 GeV and η_f = 0.825. We observe that going from RHIC to the LHC energy both the freeze-out temperature and the transverse flow go up. This can be understood as a result of higher pressure which builds up at the LHC heavy ion collisions. Higher pressure leads to stronger transverse flow and stronger expansion also means that the interaction rate of hadrons in the fireball drops below the expansion rate earlier, at higher freeze-out temperature. ALICE has published similar results [2], however, our study properly accounts for all hadron species including resonance decays.

Acknowledgments

We would like to thank Mateusz Ploskon, ALICE Deputy Physics Coordinator, for supplying us with the ALICE p_T spectra. We would also like to acknowledge the support by APVV-0050-11 and VEGA 1/0457/12.

References

[1] AOKI, Y. et al.: *Phys. Lett.* B 643, 2006, 46.
[2] "Centrality Dependence of p, K, p Production in Pb–Pb Collisions at $\sqrt{s_{NN}}$ = 2.76 TeV", ALICE Collaboration, [arXiv:1303.0737 [hep-ex]].
[3] SCHNEDERMANN, E., SOLLFRANK, J., HEINZ, U.: *Phys. Rev.* C 48, 1993, 2462. [arXiv:nucl-th/9307020]; P. J. Siemens, J. O. Rasmussen, *Phys. Rev. Lett.,* 42, 1979, 880.
[4] TOMASIK, B.: *Comp. Phys. Commun*. 180, 2009, 1642- 1653.
[5] ABELEV, B. I. et al, STAR Collaboration, *Phys. Rev.* C 79 (2009) 034909.

Marian Janek - Beata Trpisova - Vladimir Petrovich Ladygin - Semen Mikhailovich Piyadin *

THE SELECTION OF THE dp BREAKUP EVENTS FROM d CH_2 REACTION AT 500 MeV

The simulations of dC and dCH_2 (CH_2 - polyethylene) reactions for different detector configurations were performed at 500 MeV of deuteron energy. We present method by means of which the signal from dp breakup reaction can be separated from the background that mainly comes from the carbon content of the target.

Keywords: *dp breakup, energy deposit, missing mass distribution, nucleon-nucleon correlations.*

1. Introduction

The results obtained at BNL [1], SLAC [2] and JLAB [3 and 4] clearly demonstrate that more than 90% of all nucleons with internal momenta k>300 MeV/c belong to 2N (2 nucleon) short range correlations; probability for a given proton with momenta 300 MeV/c < k < 600 MeV/c which belongs to pn correlation is ~18 times larger than for pp correlations; probability for a nucleon to have momentum k>300 MeV/c in medium nuclei is ~25% and 3N (3 nucleon) short range correlations are present in nuclei with a significant probability [5]. However, still many open questions persist and further investigations are required both from the experimental and theoretical sides. For instance, the experimental data on the spin structure of 2N (I=1) and 3N short range correlations are practically absent. The study of short range correlations can be realized via study of deuteron structure at large internal momenta of nucleons, ^{3}He structure, nuclei breakup reaction A(p, pp)X, A(p, pn)X, A(p, ppp)X etc. with the detection of few nucleons in the final state.

The great importance is the study of the spin effects in these reactions because the data on the spin structure of these correlations are scarce. Nuclotron allows to investigate the spin effects for multi-nucleon correlations in a wide energy range. The model of 2N and 3N correlations at low and intermediate energies (below pion threshold production) can be built from the boson-nucleon picture of strong interaction. During last several years a new generation of nucleon-nucleon potentials are built (Nijmegen, CD- Bonn, AV-18 etc.). These potentials reproduced the nucleon-nucleon scattering data up to 350 MeV with very good accuracy. But these potentials cannot reproduce triton binding energy (underbinding is 0.8 MeV for CD-Bonn potential), dp → dp elastic scattering and breakup reactions [6]. Incorporation of three nucleon forces (3NF), when the interaction depends on the quantum numbers of the all three nucleons, allows reproducing triton binding energy and unpolarized dp → dp elastic scattering and breakup data. The contribution of 3NF is found to be up to 30% in the vicinity of Sagara discrepancy for deuteron-proton elastic scattering at intermediate energies [7 and 8]. However, the use of different 3NF models in Faddeev calculations cannot reproduce polarization data intensively accumulated during last decade at different facilities [7 - 11].

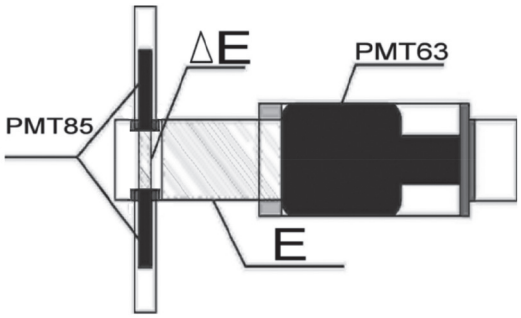

Fig. 1 Sketch view of ΔE-E detector

The dp breakup possesses rich phase space. The effects originating from the 3NFs can dominate in some regions of the phase space, the relativistic effects in other ones. Thus, to obtain data for a large region of the phase space it is desirable to get complementary information about the reaction mechanism and

* [1] Marian Janek, [1] Beata Trpisova, [2] Vladimir Petrovich Ladygin, [2] Semen Mikhailovich Piyadin
[1]Physics Dept., University of Zilina, Slovakia
[2]LHEP-JINR, 980 Dubna, Russian Federation
E-mail: janek@fyzika.uniza.sk

the structure of the objects involved in the dp breakup. Large discrepancies between experiment and theoretical calculations based on various NN and 3N potentials have also been found in case of the dp breakup measured at 130 MeV [12]. The main goal of this study is to present method for selection of dp breakup events. Obtained results will be used in the experimental deuteron spin structure program at the Nuclotron in Dubna.

2. Experiment and simulation

The dp breakup reaction is detected by the simultaneous registration of two protons by two detectors in coincidence. Deuteron energies range from 300 MeV up to 500 MeV. Eight ΔE-E scintillation detectors are used. Both scintillators are of a tube shape, the thin one of a height of 1 cm, the thick one of a 20 cm height, with the diameter of the cross section 8 cm and 10 cm, respectively. Two Photomultiplier tubes PMTs-85 are positioned opposite to each other at the outside cylindrical surface of the thin scintillator as shown in Fig. 1. The ΔE scintillator surface was polished in order to increase the area of the optical contact between the scintillator and the photocatode of the PMT-85. This scintillator is covered by white paper and digital dividers of high voltage are used for the PMT-85. At the free bottom of the E scintillator a photomultiplier tube PMT-63 is positioned. The E scintillator is also covered by white paper. The contact area of the two scintillators is covered by black paper in order to exclude the possibility of the transfer of light between them. The details of the ΔE–E detector construction can be found in [13]. Each detector is positioned at a distance of 99.6 cm from the target so that the angle whose vertex is the target subtended by the diameter of the thin scintillator is 4.6°.

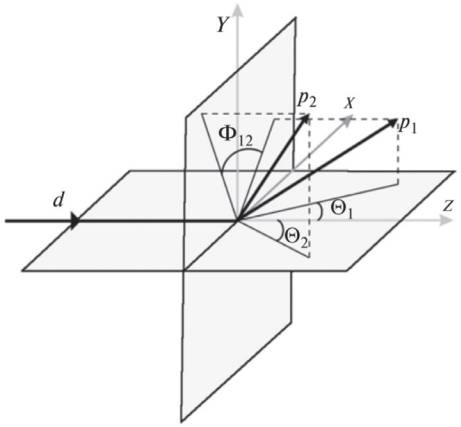

Fig. 2 Kinematic variables for the deuteron breakup reaction

Targets from carbon and CH_2 are enclosed in a spherical hull made from stainless steel with an external diameter of 160 mm and a thickness of 0.5 mm. To produce collisions of the deuteron with hydrogen, CH_2 target is used. When the CH_2 target is bombarded with deuterons, large background originates. Hence, ways must be found for selecting our signal events out of all detected events and this should be done for various detector configurations.

To accomplish this goal we performed computer modeling using the GEANT4 toolkit [14] with Liege intranuclear cascade model included. From simulation comes that when bombarding the CH_2 target with deuterons in the vast majority of cases the two detectors detect in one event two protons and very rarely other particles or more than two particles obviously mostly coming from the collisions of the deuterons with the carbon nuclei. The events represented by the collisions of deuterons with the carbon nuclei form the dp breakup background that we simulated by the collisions of the deuterons with a carbon target, i. e. by the dC events. Then by subtracting the dC events from the dCH_2 events the signal events can be selected.

Deuteron beam with energy of 500 MeV hits the target. The types of the outgoing particles, their energy and their scattering angle, i. e. the angle made by the trajectory of the outgoing particle and the direction of the deuteron beam, were recorded only if this angle is greater than 17°. The reason for this cut is that roughly for scattering angles smaller than 17° the collisions of the deuterons with the CH_2 target produce large background that is mainly due to the carbon content of the target. Energies deposited by particles in ΔE and E detector were also recorded. The longitudinal axes of scintillation detectors pass through the target and make angles that we designated Θ_1 and Θ_2 with the trajectory of the incoming deuterons. The angle between detectors in plane perpendicular to the direction of the deuteron beam is denoted by Φ_{12}. The three angles Φ_{12}, Θ_1 and Θ_2 (see Fig. 2) specify a detector configuration. The simulation was performed for 20 various detector configurations. They were selected according to experimental ones. Characteristicconfigurations for which we present our results are given in Table 1. As you can notice, the angles Θ_1 and Θ_2 appear as an interval of angles, which is due to the finite size of the detectors' cross section.

Detector configurations description — Table 1

Configuration	Θ_1	Θ_2	Φ_{12}
2 – Fig. 3a	22.400° - 27.000°	31.015° - 35.615°	40°
5 – Fig. 3b	22.400° - 27.000°	40.901° - 45.501°	180°
7 – Fig. 3c	22.400° - 27.000°	50.983° - 55.583°	140°
19 – Fig. 3d	31.015° - 35.615°	40.901° - 45.501°	130°

3. Results

To analyze our data we calculated the missing mass distribution of the two particles that hit the detectors in one event. We used as the particles' kinetic energy (incoming energy)

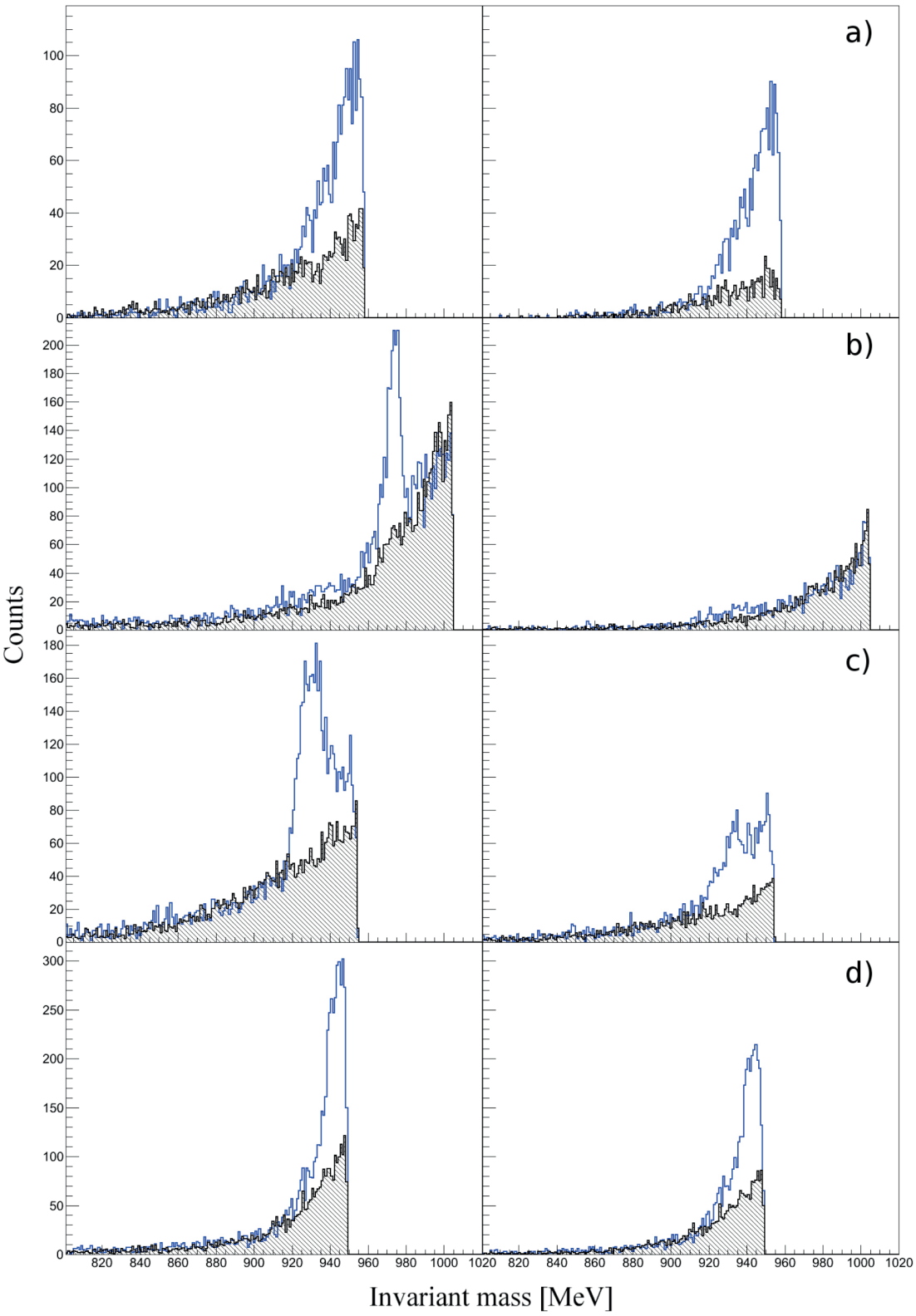

Fig. 3 Missing mass distribution of two charged particles obtained for CH2 (non-shaded spectra) and carbon (shaded spectra) target that were bombarded by deuterons of energy 500 MeV; the detector configurations are 2 (first row), 5 (second row) 7 (third row) and 19 (fourth row), respectively. First (second) column corresponds to the cut1 (cut2).

the energy deposited by them in the detectors and the mean value of the range of angles Θ_1 and Θ_2 for the relevant detector configuration as the directions of the particles momenta.

Two cuts were applied on missing mass distributions. The choice of energy ranges for ΔE and E detectors of these cuts were determined in the separate simulation in which protons with energies between 1 and 500 MeV hit the detector at various angles. First cut designated as "cut1" contains particles with deposited energy ΔE between 1 and 35 MeV and E less than 180 MeV. Cut1 contains also particles which not all their energy deposit in detector even if they passed along detectors main axis. It happens when particles have energy above 180 MeV due to insufficient length of the detector. Second cut designated as "cut2" contains particles with deposited energy ΔE between 5 and 35 MeV and E less than 180 MeV. The purpose of cut2 is to cut out mostly the particles which pass through the detector basically along its longitudinal direction and then leave it, thus depositing only a part of their kinetic energy there. However, in order not to suppress the signal significantly cut2 can contain a part of these particles. Hence the calculation of the missing mass for these particles does not give its correct value as well, which means that these events should also contribute to the background in the missing mass spectra. It will be shown below, however, that a part of this background are actually our signal events. Another contribution to the background is constituted by the events in which the particles registered by the detectors are not protons since in the calculation of the missing mass we assume that two protons are detected, i. e. we use the rest mass of protons in the missing mass formula. The main part of the background in the missing mass plots is due to the protons that come from the collision of the deuteron with the carbon nuclei.

Fig. 3 depicts the missing mass distribution of two charged particles registered by the detectors at deuteron energy of 500 MeV. The non-shaded spectra represent the dCH_2 simulations and the shaded ones the dC simulations. The dC spectra are normalized against the dCH_2 spectra according to the regions where only the carbon content is expected. Fig. 3 contains eight plots arranged in four rows and two columns. The rows correspond to the four detector configurations given in Table 1, the first column represents the spectra calculated using the cut1 events, in the second column are depicted spectra calculated using cut2 ones. The a), b) and d) spectra in Fig. 3 exhibit clear peaks at about 940 MeV, i. e. at the value of the rest mass of neutron.

From Fig. 3 we can see that the events corresponding to this peak are mostly our dp breakup events and calculating the missing mass is a good means of how to separate them from the rest of the events. The effect of using the cut2 selection of events is visible in Fig. 3 in all detector configurations. The calculation of the missing mass spectra for the cut1 case actually enabled us to localize in the spectra those events in which the energy of the incoming protons is larger than about 180 MeV. As can be seen, these events are shifted towards the right part of the spectra. Since GEANT4 gives the incoming energies of the particles, we could calculate the missing mass for these events with the correct value of their kinetic energy (that should be ideally whole deposited in the detectors) and we found that these events are also the dp breakup events, i. e. the signal events. Especially marked is the cut2 effect on the signal for detector configuration b) when a large part of the signal is cut out.

The main reason of the peak spreading in the missing mass spectra is connected with using in the calculation of the missing mass of a pair of charged particles instead of the actual value of the scattering angle of the particles hitting the detector the angle at which the detector is placed, i. e. the angle the longitudinal axis of the detector makes with the direction of the incoming deuterons. In this way we simulate the real experimental conditions at which the scattering angles of the detected particles will not be known. Other reasons of the peak spreading are associated with the detector response. The spherical hull affects the scattering angle and causes energy losses only at very low energies of scattered particles which are cut out by the ΔE and E coincidence condition.

Hence, we conclude that two methods of reconstructing the signal events are possible. The first one is based on the localization of the dp breakup events by means of the GEANT4 simulation that uses cut1 selections of events with the subsequent subtraction of the C spectra from the CH_2 spectra. The second one is calculating the CH_2 and C spectra using only the cut2 selection of events and subsequently applying the above described subtraction procedure. The spectra in the second row and second column in Fig. 3 shows that for this case the yield is low. One can see that the subtraction procedure can be used for selecting the signal events in the missing mass spectra but the yield varies with the detector configuration.

4. Conclusion

We present results of the GEANT4 simulations of the dp → ppn reaction at deuteron energy of 500 MeV for some configurations of two ΔE–E detectors. To separate the signal from the background we calculated the missing mass distributions of two charged particles assuming that these two particles are protons. The events that form the background of the missing mass spectra can be largely removed by means of the subtraction procedure, i. e. by simulating collisions of the deuterons with a target made from carbon and subsequent subtraction of the dC missing mass spectra from the dCH_2 ones.

Two variants of subtraction procedure were presented. First one uses cut1 which leads to results with higher statistics, but some part of signal is shifted to higher values (above 940 MeV) of the missing mass spectra. Second one uses cut2 which caused

lower statistics, but events are localized in the vicinity of the rest mass of neutron.

It was noted that the simulated missing mass spectra on CH_2 are normalized according to those of their regions where only carbon content is located. However, the normalization is questionable if the region with only the carbon content is very narrow, which can be also due to a large content of the misplaced dp breakup events, i. e. the signal events with the incorrect value of the missing mass. To conclude, our GEANT4 modeling suggests that the subtraction procedure may be a useful tool for separating the dp breakup events from the rest of the events originating in the deuteron collisions with the CH_2 target.

Acknowledgments

This work has been supported partly by the scientific cooperation program JINR-Slovak Republic in 2013 and by the Russian Foundation for Basic Research under grant no.13-02-00101a. Part of the calculations was performed on the Grid infrastructure, Slovak Infrastructure for High Performance Computing (ITMS 26210120002).

References

[1] PIASETZKY, E., SARGSIAN, M., FRANKFURT, L., STRIKMAN, M., WATSON, J. W.: *Phys.Rev.Lett.* 97, 162504, 2006
[2] FRANKFURT, L. L., STRIKMAN, M. I., DAY, D. B., SARGSIAN, M. M.: *Phys.Rev*. C48, 2451, 1993
[3] EGIYAN, K. SH. et al.: *Phys.Rev*. C68, 014313, 2003
[4] EGIYAN, K. S. et al., *Phys.Rev.Lett.* 96, 082501, 2006
[5] STRIKMAN, M. I.: Proc. of the VI. Int. Conf. on Perspectives in Hadronic Physics, 12-16 May 2008, Trieste, Italy; to be published in AIP Conf. Proc.
[6] GLOCKLE, W., WITALA, H., HUBER, D., KAMADA, H., GOLAK, J.: *Phys.Rep*. 274, 107, 1996
[7] SAKAMOTO, N. ET AL.: *Phys.Lett*. B367, 60, 1996
[8] SEKIGUCHI, K. et al., *Phys.Rev.* C65, 034003, 2002
[9] SEKIGUCHI, K. et al., *Phys.Rev.* C70, 014001, 2004
[10] HATANAKA, K., SHIMIZU, Y. et al.: *Phys.Rev.* C66, 044002, 2002
[11] ERMISCH, K. et al.: *Phys. Rev.* C68, 051001, 2003
[12] KISTRYN, S. et al.: *Phys. Rev.* C 68, 054004, 2003
[13] PIYADIN, S. M. et al.: *Physics of Particles and Nuclei Letters*, vol. 8, No. 2, pp. 107-113, 2011
[14] AGOSTINELLI, S. et al.: *Nucl.Instrum. Meth.* A, vol. 506, No. 3, pp. 250-303, 2003.

Jan Vittek - Branislav Ftorek *

ENERGY EFFICIENT SPEED AND POSITION CONTROL OF ELECTRIC DRIVES WITH PMSM

A new speed and position controller respecting principles of near-energy optimal control for the drives with permanent magnet synchronous motor are developed as a contribution to the energy saving and environmental protection. Two various approaches to the energy saving controller design are analysed. The first approach is strictly based on energy optimal control theory and derives analytical solutions of the control problem. The second approach develops approximated solution for the drive position controller when the optimal speed trajectory is modified to correspond to the triangular and trapezoidal profile. This approach enables not only to compare energy demands of the individual control system design but also to exploit near-energy optimal controller for any controlled industrial drive.

Keywords: *Energy optimal control, electric drives with PMSM, speed and position controller, pre-compensator.*

1. Introduction

The consumption of electric motor represents nearly half (46%) of global electricity consumption. Therefore, even small decrease of electric drives energy demands brought by efficient energy management, can result in significant energy savings with subsequent contribution to the protection of environment.

The main contribution of this paper is mathematical analysis of energy-optimal speed and position control of the drives with a *permanent magnet synchronous motor* (PMSM), taking into account stator copper losses and its possible extension towards controlled drives currently used in industry.

To complete these tasks the efficient exploitation of the time available for prescribed manoeuvre is suggested for speed controlled drives. For efficient position control a replacement of the parabolic speed profile required by analytical solution of energy optimal position control, with precisely defined trapezoidal one is proposed. Such approach enables to exploit currently used control techniques (*constant torque control and constant speed control*) and to extend principles of near-energy optimal control to any controlled drive with PMSM.

To get a practicable controller the influence of Coulomb friction and constant load torque on the stator current torque component is analyzed in two steps. Beside friction losses also copper losses of PMSM, which create more than 80% of total machine losses, are taking into account while the stator iron losses are neglected. As a result of analysis the useful algorithms suitable for numerical implementation, which also respect prescribed time for rest to rest manoeuvre, T_m are developed.

The verification of the efficient energy management of speed and position controlled electric drives is based on principles of *forced dynamics control* (FDC). FDC strategy exploits principles of feedback linearization [1]. Its capability to precisely follow pre-planned speed and position manoeuvre and compensate influence of load torque, which is taken into account during the planning of velocity profile, has been already experimentally verified. The proposed control structure comprises a generator of energy saving acceleration, speed and position profile, a zero dynamic lag pre-compensator and FDC position control loop. Designed near-energy optimal position control algorithm based on symmetrical trapezoidal speed profile decreases energy demand and respects prescribed time T_m for position manoeuvre.

Some significant progress on energy efficient speed control of electric drives has already been made. Model reference linear adaptive speed control of the drive with dc motor is exploited in [2] to drive output speed at any load to the maximum efficiency by controlling motor field current. A new energy saving control strategy for variable speed controlled parallel pumps based on sensorless flow rate estimation and pump operation analysis is described in [3].

Sheta et al developed minimum energy motion control systems respecting principles of optimal control theory for the drive with dc motor [4]. Similar approach was applied by Dodds et al, for the drives with PMSM [5]. Both control systems achieve

* [1] **Jan Vittek,** [2] **Branislav Ftorek**
[1]Department of Power Electrical Systems, Faculty of Electrical Engineering, University of Zilina, Slovakia
[2]Department of Applied Mathematics, Faculty of Mechanical Engineering, University of Zilina, Slovakia
E-mail: jan.vittek@fel.uniza.sk

minimization of input energy by decreasing the losses via exploitation of the drive's kinetic energy during motion decelerating phase with respect to the speed profile and the field current. Drawbacks of these strategies are assumptions of constant friction components dependent on environmental conditions.

Due to the fact that absolute optimization of energy loss during position control isn't the main goal of this paper, the symmetrical trapezoidal speed profile is chosen and modified to achieve lower energy expenditure for a specified manoeuvre time taking into account load torque as a function of the angular velocity.

2. Theoretical Background

Following differential equations describe dynamics of the rotor position, θ_r, speed ω_r, and motor torque, γ_e of the drive with PMSM:

$$\frac{d\theta_r}{dt} = \omega_r, \tag{1}$$

$$J_r \frac{d\omega_r}{dt} = \gamma_e - \gamma_L, \tag{2}$$

$$\frac{d\gamma_e}{dt} = \frac{-1}{T_S}\gamma_e - \frac{k_T^2}{L_S}\omega_r + \frac{k_T}{L_S}u_q, \tag{3}$$

where J_r is reduced moment of inertia to the shaft of PMSM, L_s and R_s are stator phase inductance and resistance respectively and stator time constant, T_s is defined as $T_s = L_s / R_s$.

For vector controlled PMSM constant linkage magnetic flux is achieved via condition, $i_{d\,dem} = 0$, where $i_{d\,dem}$ is magnetic flux component of the stator current [6]. In this case electrical torque of the motor can be expressed as:

$$\gamma_e = k_T i_q, \tag{4}$$

where $k_T = c\Psi_{PM}$ and $c = 3p/2$ where p is number of pol-pairs, Ψ_{PM} is linkage flux of permanent magnet and $i_q(t)$ is torque component of the stator current.

Exploiting state-space notation $\dot{x} = Ax + Bu$ the drive with PMSM can be described as:

$$\begin{bmatrix} \dot{\theta}_r \\ \dot{\omega}_r \\ \dot{\gamma}_e \\ \dot{\gamma}_L \end{bmatrix} = \begin{bmatrix} 0 & 1 & 0 & 0 \\ 0 & 0 & \frac{1}{J_r} & \frac{-1}{J_r} \\ 0 & \frac{k_T^2}{L_s} & \frac{-1}{T_s} & 0 \\ 0 & 0 & 0 & 0 \end{bmatrix} \begin{bmatrix} \theta_r \\ \omega_r \\ \gamma_e \\ \gamma_L \end{bmatrix} + \begin{bmatrix} 0 \\ 0 \\ \frac{k_T}{L_S} \\ 0 \end{bmatrix} u_q, \tag{5}$$

where the system described by (1) - (3) is completed with differential equation for constant load torque, $\dot{\gamma}_L = 0$.

The function of optimal energy controller is to transfer control system from its initial state to the demanded state (*demanded speed or position*) in such a way that energy performance index I is minimized [7 and 8]. This is achieved via energy optimal control algorithm, which determines optimal excitation of the system $u^*(\mathbf{x},t)$, in this case control variable, $u^*_q(\mathbf{x},t)$. Solution of the problem is obtained in two steps. The first step is formulation of the cost function, I_0, which describes minimization problem. The developed cost function is then completed with differential equations based on state space description of the control system. If the state-space description of the system has a form:

$$\dot{x}(t) = f[x(t), u(t)], \tag{6}$$

then function Φ defined as:

$$\phi(x, \dot{x}, u, t) = f(x, u, t) - \dot{x} = 0, \tag{7}$$

becomes the second part of the cost function after multiplication with Euler-Lagrange multipliers. The complete cost function I has a form:

$$I = L_0(x, u, t) + \lambda^T \phi(x, \dot{x}, u, t), \tag{8}$$

where L_0 is a function describing the minimization problem and λ represents Lagrange multipliers. Then:

$$I_0 = \int_{t_0}^{t_1} L_0(x, u, t)dt, \tag{9}$$

The solution of the problem requires calculation of Euler-Lagrange equations, which can be found via partial derivatives of the designed cost function I for individual variables of the control system state-space description [9] as follows:

$$\frac{\delta I}{\delta x} = \frac{d}{dt}\left(\frac{\delta I}{\delta \dot{x}}\right). \tag{10}$$

Analytical approach to this problem is explained further for energy minimized speed and position control of the drive with PMSM.

2. 1. Energy Optimal Speed Control

Energy consumption of the control system depends on minimization of copper losses given as:

$$I_0 = R_s \int i_q^2 dt. \tag{11}$$

If relations for PMSM torque γ_e is used, then minimization of copper losses for prescribed manoeuvre time T_m described as a function of the state-variable has a form:

$$I_0 = \frac{R_s}{k_T^2}\int_0^{T_m} \gamma_e^2 dt. \tag{12}$$

The complete cost function I_ω for stator losses minimization consists of (12), in which the state space description of rotor

speed and load torque multiplied by Lagrange multipliers is added:

$$I_\omega = \frac{R_s}{k_T^2}\gamma_e^2 + \lambda_1\left(J_r\dot{\omega}_r - \gamma_e + \gamma_L\right) + \lambda_2\dot{\gamma}_L \qquad (13)$$

and corresponding equations for individual Euler-Lagrange multipliers can be expressed as follows:

$$\frac{\delta I_\omega}{\delta\gamma_e} = \frac{d}{dt}\left(\frac{\delta I_\omega}{\delta\dot{\gamma}_e}\right),\ \frac{2R_s}{k_T^2}\gamma_e - \lambda_1 = 0, \qquad (14a,b)$$

$$\frac{\delta I_\omega}{\delta\gamma_L} = \frac{d}{dt}\left(\frac{\delta I_\omega}{\delta\dot{\gamma}_L}\right),\ \lambda_1 = \dot{\lambda}_2, \qquad (15a,b)$$

$$\frac{\delta I_\omega}{\delta\gamma_r} = \frac{d}{dt}\left(\frac{\delta I_\omega}{\delta\dot{\omega}_r}\right),\ J_r\dot{\lambda}_1 = 0. \qquad (16a,b)$$

Using (14b) Lagrange multiplier l_1 is expressed as:

$$\lambda_1 = \frac{2R_s}{k_T^2}\gamma_e. \qquad (17)$$

From (16b) for the same Lagrange multiplier l_1 is valid:

$$\lambda_1 = c_1. \qquad (18)$$

Exploiting (15b) and (18) multiplier l_2 is defined as:

$$\lambda_2 = c_1 t + c_2. \qquad (19)$$

Electrical motor torque can be expressed using (17) and (18):

$$\gamma_e = \frac{k_T^2}{2R_s}c_1. \qquad (20)$$

Derivative of rotor speed is expressed using (2) and (20):

$$\dot{\omega}_r = \frac{1}{J_r}\left(\frac{k_T^2}{2R_s}c_1 - \gamma_L\right). \qquad (21)$$

If (21) is integrated, then:

$$\omega_r = \frac{1}{J_r}\left(\frac{k_T^2}{2R_s}c_1 - \gamma_L\right)t + c_3. \qquad (22)$$

Constants c_1 and c_3 are calculated using boundary conditions as follows:

for t = 0 $\omega_r = \omega_0$ from which $c_3 = \omega_0$;

for t = T_m $\omega_r = \omega_{r\,dem}$ and c_1 is done as:

$$c_1 = \frac{2R_s}{k_T^2}\left(J_r\frac{\omega_{r\,dem} - \omega_0}{T_m} + \gamma_L\right). \qquad (23)$$

Using c_1 in relation (20) for electrical torque results in:

$$\gamma_e = J_r\frac{\omega_{r\,dem} - \omega_0}{T_m} + \gamma_L. \qquad (24)$$

Subsequently, the cost performance index is defined as:

$$I = \frac{R_s}{k_T^2}\int_0^{Tm}\gamma_e^2\,dt \qquad (25)$$

and for energy optimal speed control results in:

$$I = \frac{R_s}{k_T^2}T_m\left(J_r\varepsilon_r + \gamma_L\right)^2, \qquad (26)$$

where $\varepsilon_r = (\omega_{r\,dem} - \omega_0)/T_m$ is prescribed drive acceleration.

The conclusion for this paragraph of energy optimal speed controller can be formed as: The cost performance index is direct proportional to the prescribed angular acceleration of the drive and, therefore, the longer is prescribed manoeuvre time T_m for given change of the drive's velocity, the lower energy expenditures are required.

Results for energy optimal control of the drive speed are shown in Fig. 1. For manoeuvre time T_m=0,25 s and demanded speed, $\omega_{r\,dem}$ =100 rads^{-1} the individual time functions show: a) ideal drive acceleration and b) rotor angular speed.

2.2. Energy Optimal Position Control

In the case of drive's position control the complete cost function I_P for stator losses minimization consists of minimization problem description (12) completed with the state space description (*function* $\Phi(\mathbf{x}, \dot{\mathbf{x}}, u, t)$) for the rotor position and speed and load torque has a form:

$$I_p = \frac{R_s}{k_T^2}\gamma_e^2 + \lambda\left(J_r\dot{\omega}_r - \gamma_e + \gamma_L\right) + \lambda_2\left(\dot{\theta}_r - \omega_r\right) + \lambda_3\dot{\gamma}_L. \qquad (27)$$

Euler-Lagrange equations for the position control are:

$$\frac{\delta I_p}{\delta\gamma_e} = \frac{d}{dt}\left(\frac{\delta I_p}{\delta\dot{\gamma}_e}\right),\ \frac{2R_s}{k_T^2}\gamma_e - \lambda_1 = 0, \qquad (28a,b)$$

$$\frac{\delta I_P}{\delta\gamma_L} = \frac{d}{dt}\left(\frac{\delta I_P}{\delta\dot{\gamma}_L}\right),\ \lambda_1 = \dot{\lambda}_3, \qquad (29a,b)$$

$$\frac{\delta I_P}{\delta\gamma_r} = \frac{d}{dt}\left(\frac{\delta I_P}{\delta\dot{\omega}_r}\right),\ -\lambda_2 = J_r\dot{\lambda}_1, \qquad (30a,b)$$

$$\frac{\delta I_P}{\delta\theta_r} = \frac{d}{dt}\left(\frac{\delta I_P}{\delta\dot{\theta}_r}\right),\ \dot{\lambda}_2 = 0. \qquad (31a,b)$$

From (31b) is clear that multiplier λ_2 is constant:

$$\lambda_2 = c_1. \qquad (32)$$

Combining (30b) and (32) together for derivative of multiplier l_1 the following is valid:

$$\dot{\lambda}_1 = \frac{-c_1}{J_r}. \qquad (33)$$

Then multiplier λ_1 can be expressed as:

$$\lambda_1 = \frac{-c_1}{J_r} t + c_2 \tag{34}$$

And, finally from (29b), Lagrange multiplier λ_3 is:

$$\lambda_3 = \frac{-c_1}{J_r} \frac{t^2}{2} + c_2 t + c_3 . \tag{35}$$

If (28b) and (34) are combined together, then for electrical torque the following is valid:

$$\gamma_e = \frac{k_T^2}{2R_s}\left(c_2 - \frac{c_1}{J_r} t\right). \tag{36}$$

The constants c_1 and c_2 are again calculated using boundary conditions for motor torque, which can be expressed for constant torque as:

for t = 0 $\gamma_e = \gamma_0 + \gamma_L$ and or t = T_m $\gamma_e = -\gamma_0 + \gamma_L$,

which results in $c_2=(2R_s/k_T^2)(\gamma_0+\gamma_L)$ and $c_1=4R_s\gamma_0 J_r/(k_T^2 T_m)$. The required torque of PMSM has a general form:

$$\gamma_e = \gamma_0\left(1 - \frac{2}{T_m} t\right) + \gamma_L . \tag{37}$$

Derivative of rotor speed is expressed using (2) and (37):

$$J_r \frac{d\omega_r}{dt} = \gamma_0\left(1 - \frac{2}{T_m} t\right). \tag{38}$$

If (38) is integrated with regard to the initial condition $\omega_r(0)=0$ and then the rotor speed is expressed as:

$$\omega_r(t) = \frac{\gamma_0}{J_r}\left(t - \frac{t^2}{T_m}\right). \tag{39}$$

In a similar way, using (1) and $q_r(0)=0$ the rotor position is calculated as:

$$\theta_r(t) = \frac{\gamma_0}{J_r}\left(\frac{t^2}{2} - \frac{t^3}{3T_m}\right). \tag{40}$$

The value of initial motor torque γ_0, which completes all control parameters, is expressed via the condition that at the end of the manoeuvre time t=T_m the rotor position should achieve a demanded position $\theta_{r\,dem}$. The demanded value of initial motor torque is:

$$\gamma_0 = \frac{6J_r}{T_m^2}\theta_{r\,dem} . \tag{41}$$

The cost performance index defined by (25) for the rotor position control is equal:

$$I = \frac{R_s}{k_T^2}\left(\frac{12J_r^2}{T_m^3}\theta_{r\,dem}^2 + \gamma_L^2 T_m\right). \tag{42}$$

For the position control time function of consumed energy is:

$$E_C = \int_0^{\theta_{r\,dem}} \gamma_e d\theta_r = \theta_{r\,dem}\left[\gamma_0\left(1 - \frac{2}{T_m} t\right) + \gamma_L\right]. \tag{43}$$

The results for energy optimal control of the drive position are shown in Fig. 2. For manoeuvre time T_m=1 s and demanded position, $q_{r\,dem}$=10 rad individual time functions show: a) ideal drive acceleration, b) rotor speed, c) rotor angular position, which achieves a demanded position at T_m=1 s.

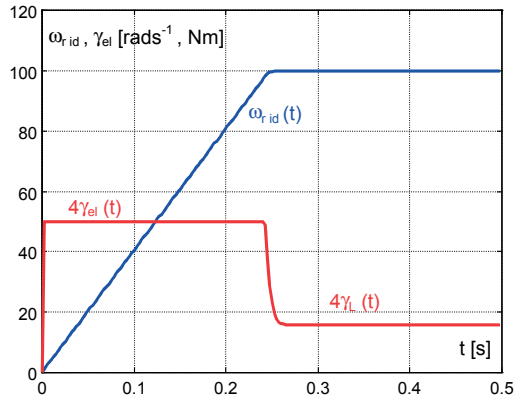

Fig. 1 Energy optimal speed control

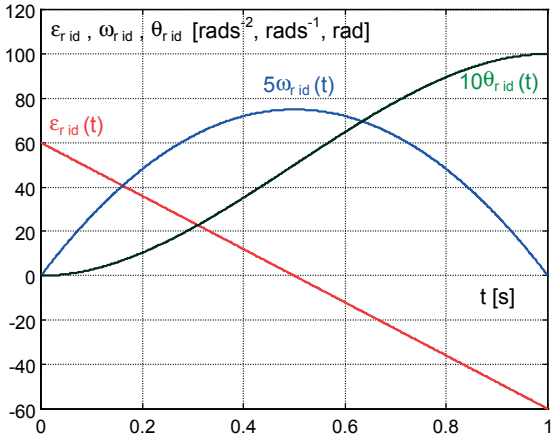

Fig. 2 Energy optimal position control

3. Position Control System Design

The individual approaches to energy efficient position control of electric drives differ mainly by description of velocity time profile. A controller for dynamical systems with energy optimization performances was proposed in [10].

A generation of three steps velocity function based on efficient binary search algorithm minimizing energy demands was proposed by Kim et al for a battery powered wheeled mobile

robot [11] in order to extend battery run time. A new objective function considering practical energy consumption was developed together with an efficient iterative search algorithm finding its numerical solution. Trapezoidal velocity function with constant acceleration, deceleration and cruising speed was used by Dodds for practicable system based on sliding mode control of the PMSM drive position [12]. Both papers report nearly 30 % less energy loss if compared with a conventional concept of control.

Minimization of the total dissipated energy for a position control system with reduction gear taking into account Coulomb and viscous friction was proposed by Zhu et al [13]. The optimal drive velocity and current functions are obtained as a function of the optimal zero crossing time. The comparison of the dc motor drive consumptions for optimized algorithm and trapezoidal velocity profile revealed energy savings of optimized algorithm, which were proportional to a moment of inertia.

3.1. Speed Profile Simplification

To avoid continues speed control during a position manoeuvre often the control on motor torque constant value with one switching in the middle of manoeuvre time is used to perform near-time optimal position control. Time functions for acceleration, speed and rotor position are shown in Fig. 3.

A more efficient energy saving solution for a near-energy optimal position control is proposed exploiting symmetrical trapezoidal function of rotor speed as shown in Fig. 4 together with other two control variables. In this case the control tasks are completed with control on constant torque during acceleration and deceleration intervals and control on constant cruising speed in the middle interval, which are the most common control techniques used in drive control.

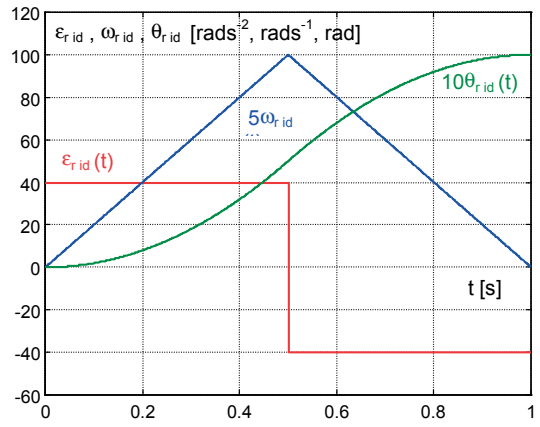

Fig. 3 Energy saving control, triangular speed profile

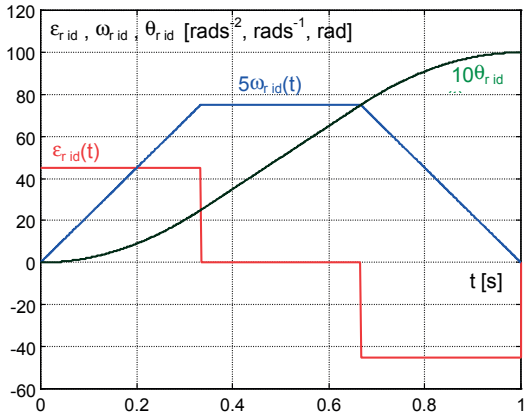

Fig. 4 Energy saving control, trapezoidal speed profile

Replacement of a continuously varying energy-optimal speed profile with symmetrical trapezoidal one was confirmed through analytical analysis of the Joule losses in stator winding and losses to cover Coulomb and viscous friction in [14]. Similar approach was applied to the drive with friction or load torque as a quadratic function of rotor speed [15]. Newton-Raphson search algorithm is exploited to find acceleration time with minimal energy expenditures.

The main goal of the position control system suitable for any described energy saving position control strategy is to track the best designed position, velocity and acceleration functions. The position control system shown in Fig. 6 contains an energy saving position generator, a zero dynamic lag pre-compensator and FDC based position control loop.

3.2. Forced Dynamics Speed Control

Speed control loop of the PMSM, which is designed using FDC, respects the vector control conditions [16 and 17]. Based on feedback linearization the rotor speed obeys (2) and the differential equation describing the closed loop dynamical behaviour has, therefore, linear first order dynamics (44) where T_ω is the prescribed time constant and $\omega_{r\,dem}$, is the demanded rotor speed:

$$\ddot{\theta}_r = \frac{1}{T_\omega}(\dot{\theta}_{rd} - \dot{\theta}_r). \tag{44}$$

Setting i_d=0 for vector control of the PMSM up to the nominal speed and equating the RHS of (2) and (44) yields the FDC speed control algorithm:

$$i_{d\,dem} = 0$$

and

$$i_{q\,dem} = \frac{1}{c\Psi_{PM}}\left[\frac{J}{T_\omega}(\dot{\theta}_{rd} - \dot{\theta}_r) + \hat{\Gamma}_L\right]. \tag{45}$$

Current components $i_d=i_{d\,dem}$ and $i_q=i_{q\,dem}$ are regarded as the control variables which means that the stator current equations are eliminated from the control system design. To estimate net load torque on the motor shaft the torque observer with filtering effect is used.

3.3. Forced Dynamics Position Control

For the design of a position control loop the FDC speed control loop is replaced by its ideal transfer function and completed with a kinematic integrator. Parameters of this loop are adjusted using Dodds's settling time formula [18]:

$$\frac{\theta_r(s)}{\theta'_{rd}(s)}=\left[\frac{1}{1+s\dfrac{T_{s\theta}}{1,5(1+n)}}\right]^n\Bigg|_{n=2}= \frac{1}{\dfrac{4T_{s\theta}^2}{81}s^2+\dfrac{4T_{s\theta}}{9}s+1}. \tag{46}$$

Converting (46) into time domain yields the second order differential equation for the rotor position:

$$\ddot{\theta}_r=\frac{81}{4T_{s\theta}^2}(\theta'_{rd}-\theta_r)-\frac{9}{T_{s\theta}}\dot{\theta}_r. \tag{47}$$

FDC law of the rotor angle is obtained by substituting (44) for LHS of (47) and solving it for the demanded rotor speed as a control variable $\dot{\theta}_{rd}$:

$$\dot{\theta}_{rd}=\left(1-\frac{9T_\omega}{T_{s\theta}}\right)\dot{\theta}_r+\frac{81T_\omega}{4T_{s\theta}^2}(\theta'_{rd}-\theta_r). \tag{48}$$

A block diagram for FDC of rotor position is shown in Fig. 5.

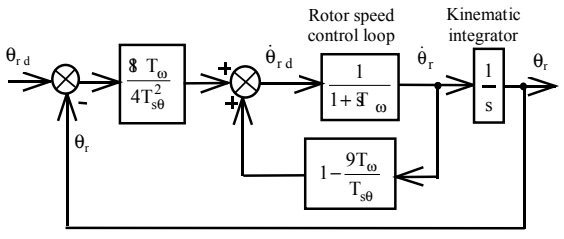

Fig. 5 Block diagram for FDC position control

3.4. Pre-compensator and Torque Observer

Closed loop dynamic of a position controller is prescribed by (46), therefore, the pre-compensator has then the inverse transfer function as follows:

$$F_{PC}(s)=\frac{\theta_{rd}(s)}{\theta_r(s)}=s^2\frac{4T_s^2}{81}+s\frac{4T_s}{9}+1. \tag{49}$$

Implementation of the pre-compensator to the overall energy saving position control block diagram is shown in Fig. 6. The design of observer was published in previous work and details can be found in [19].

4. Verification by Simulations

Energy demands of the designed energy-optimal control system and its two possible modifications as near-energy optimal control are investigated to observe their tracking abilities as well as energy expenditures.

4.1. Tracking Abilities Evaluation

All the simulations presented are carried out with zero initial state variables. A step position demand $\theta_{r\,dem}$=10 rad with prescribed manoeuvre time T_m = 0.25 s was applied to investigate response of the control system. The computational step of simulations is h=1e-4 s. PMSM parameters are listed in the Appendix.

Ideal state-variables produced by an energy saving profiles generator are shown in Fig. 7, in which time functions of speed and position responses of the drive for energy optimal and another two near-energy optimal control techniques can be seen. It's clear from subplot a) that the properly adjusted trapezoidal approximation of parabolic speed increase (*and decrease*) of energy-optimal control are very close and absolute error, $e_\omega(t)$ doesn't exceed 3 %. Also the magnitude of speed for both time functions is identical.

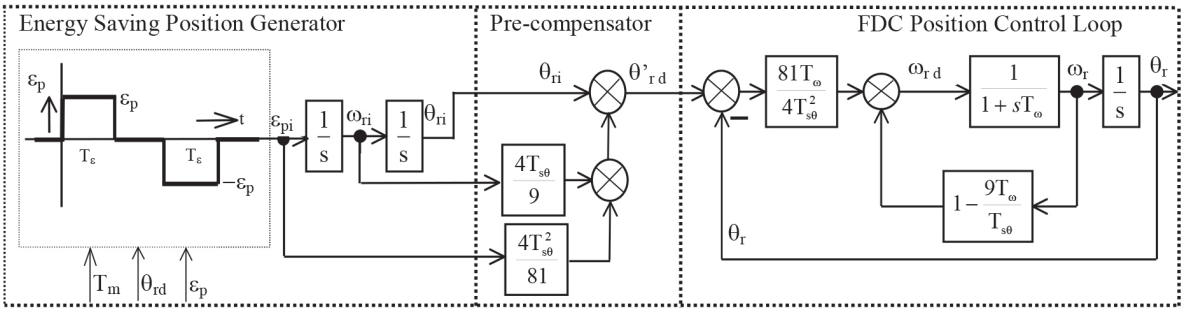

Fig. 6 Overall PMSM position control system block diagram for losses optimization

$$\omega_{p1,2} = \frac{3\theta_{rd}}{2T_m},\ \omega_{p3} = \frac{2\theta_{rd}}{T_m}. \tag{50}$$

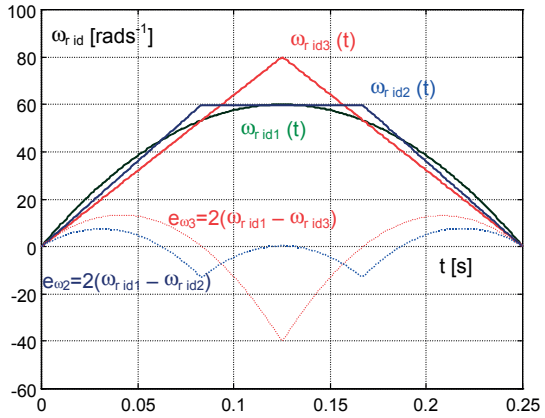

a) angular speed

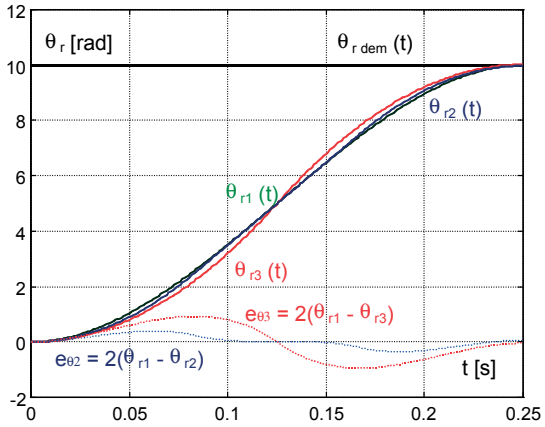

b) position response

Fig. 7 Ideal state-variables for energy optimal and near-energy optimal control

As it was observed from simulations tracking abilities of the designed overall control systems are capable to follow desired state variables with negligible dynamic lag.

4.2. Evaluation of Energy Consumption

Described energy saving control algorithms for PMSM were tested by simulation. Total energy consumption of the drive was evaluated as:

$$W_t = \frac{3}{2}\int_0^{T_m} (u_q i_q + u_d i_d)dt. \tag{51}$$

To check the correctness of energy computation, all output drive's energy components including energy of chokes and energy of rotational parts were summed in a good agreement with total input energy (51). Results of energy consumption evaluation are shown for idle running drive and drive loaded with nominal torque in Fig. 8. As Fig. 8 shows the total energy consumption for idle running and nominally loaded energy optimal controlled drive is $W_{t\,0}$ =188 Ws and $W_{t\,nom}$ =580 Ws respectively. These values were taken as a base for comparison of other two near-energy optimal control techniques.

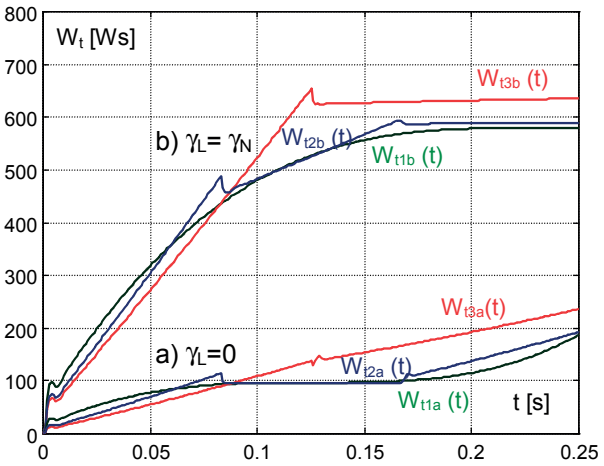

Fig. 8 Total energy consumption for prescribed position manoeuvre

Further observations show that the triangular speed profile is the most energy demanding. Its energy expenditures are by 25.8 % and 12.5 % higher for no-loaded and nominally loaded drive respectively.

On the contrary, the designed trapezoidal speed profile with respect to load conditions has only by 2.4 % and 2.7 % respectively higher energy demands if compared with the energy optimal control. It is necessary to note that energy expenditures are proportional to the moment of inertia, therefore the energy expenditures can differ for various moments of inertia.

5. Conclusion

A new energy saving speed and position controller respecting near-energy optimal control of PMSM were designed and verified by simulations.

Both control algorithms are based on losses minimization, therefore, their validity can be extended to any load with constant torque. Derived relations mathematically justify the choice of symmetrical trapezoidal speed profile selection for a position manoeuvre with prescribed position time.

The verification by simulations confirmed the lowest energy expenditures of the drive with energy-optimal control. Mutual

comparison of near-energy optimal position control with triangular and trapezoidal angular speed profiles has shown higher energy savings of the symmetrical trapezoidal angular speed profile..

Moreover, a developed energy saving position control system is practicable due to its simplicity and implementation ability exploiting the most common modes for controlled drives as control on constant torque and control on constant speed.

Acknowledgement

The authors wish to thank the Slovak Grant Agency VEGA for funding the project No.1/0355/11 'Optimal Control Techniques for Decreasing Losses of A.C. Drives'.

Appendix

Parameters of PMSM are: winding resistance, R_s=1.3 Ω, inductances, L_d=14.4 mH, L_q=16.3 mH, permanent magnet flux, Ψ_{PM}=0.13 Wb, number of pole pairs, p=5 and moment of inertia, J_r=0.005 kgm^2.

References

[1] ISIDORI, A.: *Nonlinear Control Systems*, London: Springer-Verlag Berlin, 2001. ISBN 3-5400-19916-3rd edition.

[2] GAJENDRAN, F., GEORGE S.: *A Simple Linear Adaptive Speed Control of Energy Efficient DC Drives.* Electric Machines and Drives, 1999. Intern. Conference IEMD '99, Seattle, WA, ISBN 0-7803-5293-9.

[3] VIHOLAINEN, J., TAMMINEN, J., ABONEN, T., AHOLA, J. et all: Energy-efficient Control Strategy for Variable Speed-driven Pumping System. *Springer, Energy Efficiency,* vol. 6, 2013, pp. 495-509.

[4] SHETA, M., AGARWAL, V. A., NATARAJ, V. S. P.: A New Energy Optimal Control Scheme for a Separately Excited DC Motor Based Incremental Motion. *Intern. J. of Automation and Computing*, vol. 6, No. 3, August 2006, pp. 267-276, ISSN 1476-8186.

[5] DODDS, S. J.: *Sliding Mode Vector Control of PMSM Drives with Minimum Energy Position Following*. Proc. of European power Electronic, Power Electronics and Motion Control, EPE-PEMC Conference, Poznan, 2008, pp. 2559-2566.

[6] FILKA, R., BALAZOVIC, P., DOBRUCKY, B.: A Sensorless PM Synchronous Motor Drive for Electric Washers, *Communications – Scientific Letters of the University of Zilina*, 2007, No. 1, pp. 24-32.

[7] WANG, Y., UEDA, K., BORTOFF, A. S.: *On the Optimal Trajectory Generation for Servomotors: A Hamiltonian Approach*. Proc. of the IEEE Conference on Decision and Control, 2012, pp. 7620-7625, ISSN: 0191-2216.

[8] BIVOL, I., VASILACHE, C.: The Application of Euler – Lagrange Method of Optimization for Electromechanical Motion Control. *The Annals of Dunarea de Joss University of Galati*, vol. 3, pp. 5-11, ISSN 1221-454X.

[9] GULDAN, V., MARCOKOVA, M.: Orthogonal Polynomials and Related Special Functions Applied in Geosciences and Engineering Computations. *Communications – Scientific Letters of the University of Zilina*, No. 1, 2010, pp. 12-15.

[10] FEDOR, P., PERDUKOVA, D.: *Energy Optimization of a Dynamic System Controller. Advances in Intelligent Systems and Computing*, vol. 189, AISC, 2013, pp. 361-369, **ISSN:** 21945357.

[11] KIM, C. H., KIM, B. K.: *Energy Saving 3-steps Velocity Control Algorithm for Battery-powered Wheeled Mobile Robot.* Proc. of 2005 IEEE Intern. Conference on Robotics and Automation, Barcelona, Spain 2005, pp. 2375-2380.

[12] DODDS, S. J., SOORIYAKUMAR, G., PERRYMAN, R.: Sliding Mode Minimum Energy Position Controller for Permanent Magnet Synchronous Motor Drives. *WSEAS Transactions on Systems and Control,* No. 4, vol. 3, April 2008, pp. 299-309. ISSN 1991-8763.

[13] ZHU, Y., ZHU, X., IZUMI, T., KANESAKA, M.: Optimal Velocity Function Minimizing Dissipated Energy Considering All Friction in a Position Control System. *J. of Robotics and Mechatronics,* vol. 10, Jan. 2007, pp. 97-105. ISSN 0915-3942.

[14] VITTEK, J., BRIS, P.: *Energy Saving Position Control Algorithms for PMSM Drives with Coulomb and Viscous Friction.* Proc. of 10th IEEE Intern. Conference on Control and Automation, Hangzhou, China, 2013. ISBN 978-1-4673-4706-8.

[15] VITTEK, J., BRIS, P., BIEL, Z., HRKEL, M.: *Energy Saving Position Control Algorithms for PMSM Drives with Quadratic Friction.* Proc. of IEEE Africon intern. conference on Control and Automation, Mauritius, 2013 pp. 1001-1006. ISBN 978-1-4673-5940-5

[16] LEONHARDT, W.: *Control of Electrical Drives.* Springer-Verlag, Berlin, 2001, ISBN 3-540-41820-2.

[17] BRANDTSTETTER, P., KRECEK, T.: *Speed and Current Control of Permanent Magnet Synchronous Motor Drive using IMC Controllers*. *Advances in Electrical and Computer Engineering*, No. 4, 2012, pp. 3-10, ISSN 1582-7445.

[18] DODDS, S. J.: *Settling Time Formulae for the Design of Control Systems with Linear Closed Loop Dynamics*. Proc. of the Intern. Conference AC&T - Advances in Computing and Technology, University of East London, 2007, pp. 31-39. ISSN 1350245X.

[19] VITTEK, J., DODDS, S. J.: *Forced Dynamics Control of Electric Drives,* EDIS Publishing Centre of Zilina University, Slovakia, 2003, available at http://www.kves. uniza.sk/ (*e-learning*).

Tomas Cakan - Vladimir Wieser - Andrej Tkac *

QoS ENHANCEMENT IN MANET BY DIRECTIONAL POWER CONTROL

In this paper, the 4-Way Directional Power Control with Recoil Loop (4WDPCRL) protocol for power control of directional antennas is presented. We propose the scheme with using of control packets (RTS/CTS/DATA/ACK) for exchanging information about node's transmitted energy. Whenever the frame is received, the appropriate power for transmitted frame is computed. This information is stored together with updated information about position of node to the table. If a new transmission occurs, the node sends packet with updated information about position and appropriate power. The simulation results show that the throughput and energy consumption of the proposed protocol was improved compared to IEEE 802.11 MAC protocol with omni-directional antenna and DMAC protocol with directional antenna.

Keywords: *MANET, directional antenna, power control, IEEE 802.11.*

1. Introduction

One of the main targets in designing mobile ad hoc networks (MANET) is how to enhance the network throughput while maintaining low energy consumption for packet processing and communications. One approach how to increase throughput is to use directional antenna. With directional antennas, a transmitter can concentrate most of its power towards the destination and reduce interference to nodes in the vicinity. This leads to extended communication range, increased spatial reuse and less interference to other ongoing transmissions. However, to control this antenna the effective directional MAC protocol is needed. A lot of researches are engaged to design an effective directional MAC protocol [1 and 2]. However, most of them assume transmitting signal without any power control mechanism. Although directional antenna and power control by themselves can improve spatial reuse considerably, only when both are employed simultaneously the full potential capacity is realized [3 - 6].

In this paper, we propose a new MAC protocol called 4-Way Directional Power Control with Recoil Loop (4WDPCRL). This protocol uses a directional virtual carrier sensing (DVCS) mechanism [7] to effectively control the directional antenna. Moreover, the power control mechanism is used. If a new transmission occurs, the node sends control packets (RTS, CTS, ACK) and DATA packets to exchange information about the transmission energy. Whenever the frame is received, the appropriate power for its transmission is computed. This information is stored together with updated angle of arrival (AoA) information about a position of node to the neighbor table. This table includes every node in the network with actual information about position and appropriate power. If a destination node doesn't receive a RTS packet, the source node sets value of transmitting power to maximal transmitting level to re-establish the connection. This leads to increased spatial reuse, less interference to other ongoing transmissions and saving the energy.

This paper is organized as follows. The proposed directional power control MAC protocol is presented in Section 2. In Section 3 the proposed protocol in more details is presented. Section 4 presents simulation environment and simulation results and section 5 provides the conclusion.

2. The Proposed Directional Power Control MAC Protocol

Interference Estimation Using Analytical Model

Preliminaries

A flat-top model of a directional antenna for determining the interference is shown in Fig. 1, where R denotes the maximal permitted transmission range of node A, θ is the beam width of the main lobe. This model is simplified, since the side lobes are not used [8].

* **Tomas Cakan, Vladimir Wieser, Andrej Tkac**
Department of Telecommunications and Multimedia, Faculty of Electrical Engineering, University of Zilina, Slovakia,
E-mail: vladimir.wieser@fel.uniza.sk

Two types of interference result from the application of directional antennas: *direct* and *indirect interference*. All nodes outside the main lobe (grid in Fig. 1) are considered to be direct interference and may turn their directional antennas in any direction. All nodes inside the main beam of A within range R (grey region in Fig. 1) are considered to be indirect interference since they will refrain from transmission in the direction of node A, and they will not cause any direct interference to node A. These nodes are free to be engaged in any communication toward other directions.

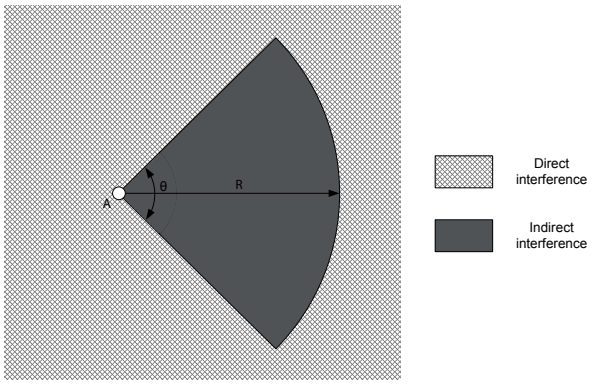

Fig. 1 Flat-top directional antenna interference region [1]

Directional interference model

Let P_t be the transmitted power, P_{th} receiver´s power threshold, h is the antenna height, α is the attenuation factor and G_m is gain of the main antenna lobe. Using a two-way propagation model, the exponential attenuation factor was set to 4. Then R is given by

$$R = \left(\frac{P_t G_m^2 h^2}{P_{th}} \right)^{\frac{1}{\alpha}}. \tag{1}$$

Those nodes which can directly interfere with A, may point their antenna to any direction with equal probability. As a result, the antenna gain of these nodes is a random variable given by G_1, i.e.

$$G_1 = \frac{\theta G_m}{2\pi}. \tag{2}$$

Now, we need to calculate the total amount of interference as perceived by node A. Consider the nodes inside the main beam of node A and at distances r and $r+dr$ from node A. Each node in this area is going to contribute to an interfering signal $I_1(r)$ and each node outside the main lobe of node A [r, $r+dr$] will contribute to an interfering signal $I_2(r)$. Values of $I_1(r)$ and $I_2(r)$ are given by

$$I_1(r) = \frac{P_t G_m h^2}{r^4}, r < R \tag{3}$$

$$I_2(r) = \frac{P_t G_m G_1 h^2}{r^4}, r > R \tag{4}$$

Therefore, the total interference for node A is given by

$$I_{total} = \rho\theta \left(\int_0^R I_1(r) r dr + \int_R^\infty I_2(r) r dr \right), \tag{5}$$

where ρ is the uniform active node density, determined by the number of active nodes in the whole network divided by the area of distribution of all nodes in the network (nodes per square meter).

If the node with which node A is communicating is located at distance d, then the signal-to-interference ratio (SIR) at A will be given by

$$SIR = \frac{(P_t h^2)/d^4}{I_{total}}. \tag{6}$$

Power Control Mechanism

For the correct reception of messages by 4-way handshake (RTS/CTS/DATA/ACK), it is needed that power of received packet must be higher than P_{th}, where P_{th} is the minimum power threshold required to receive the packet correctly.

$$\begin{cases} P_{r\_RTS} \geq P_{th} \\ P_{r\_CTS} \geq P_{th} \\ P_{r\_DATA} \geq P_{th} \\ P_{r\_ACK} \geq P_{th} \end{cases}, \tag{7}$$

where P_{r_RTS}, P_{r_CTS}, P_{r_DATA}, P_{r_ACK} are values of the received power of RTS, CTS, DATA and ACK packets. In NS-2 simulator the value $P_{th} = Rx_{threshold}$.

To calculate the effective transmission powers P_{t_CTS}, P_{t_DATA}, P_{t_ACK}, $P_{t\_F\_RTS}$, the following equations are used

$$P_{t\_CTS} = P_{t\_RTS} - (P_{r\_RTS} - P_{th}). \tag{8}$$

$$P_{t\_DATA} = P_{t\_CTS} - (P_{r\_CTS} - P_{th}). \tag{9}$$

$$P_{t\_ACK} = P_{t\_DATA} - (P_{r\_DATA} - P_{th}). \tag{10}$$

$$P_{t\_F\_RTS} = P_{t\_ACK} - (P_{r\_ACK} - P_{th}). \tag{11}$$

3. Four Way Directional Power Control with Recoil Loop

To explain the operation of the 4WDPCRL protocol, we use a simple scenario with only two nodes, where node A wants to send data to node B. The basic principle of the 4WDPCRL algorithm can be divided into the following five steps:

1. Step – Sending RTS packet

Node A first checks the information about the location of node B in the neighbor table. This information is estimated by using AoA or RSS (Received Signal Strength) mechanisms. However, this information is not obtained at the beginning of the transmission and, therefore, RTS packet is sent by using omni-directional antenna. Before node A will transmit the packet, it checks the information about value of transmission power for efficient packet transport to node B from previous transmission. This information is not obtained at the beginning, so RTS packet is sent by using the maximum power P_{max}. Information about transmission power $P_{t\_RTS}=P_{max}$ is encapsulated inside the RTS packet and also it is saved to the table. The flow graph of sending RTS packet is shown in Fig. 2.

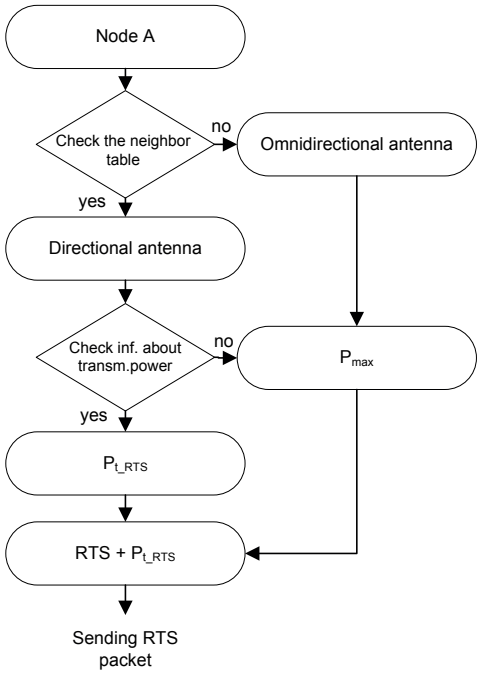

Fig. 2 Sending RTS packet

2. Step – Receiving RTS packet and sending CTS packet

Node B receives the RTS packet if the (7) condition is satisfied. If not, the packet is discarded. Node B records the information about the location of node A into the neighbor table, depending on fact which sector of the antenna received the maximum level of signal. Subsequently, the node B measures the value of received power P_{r_RTS}. Node also "knows" the value of which RTS packet was sent (value is encapsulated in the RTS packet). Based on information about P_{t_RTS} and P_{r_RTS}, node B computes the value of the effective transmitting power P_{t_CTS} for CTS packet by using (8). This value is encapsulated in the CTS packet and saved to the table. The node B then sends directional CTS packet using (8). The flow graph of receiving the RTS packet and sending CTS packet is shown in Fig. 3.

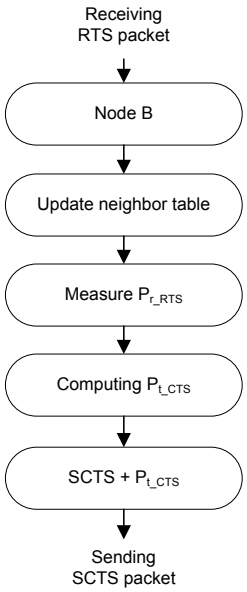

Fig. 3 Receiving RTS packet and sending CTS packet

3. Step - Receiving CTS packet and sending DATA packet

4. Step - Receiving DATA packet and sending ACK packet

Both steps are the same as the previous one, so only flow graphs are shown in Figs. 4 and 5.

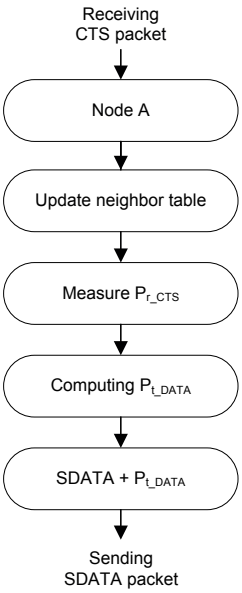

Fig. 4 Receiving CTS packet and sending DATA packet

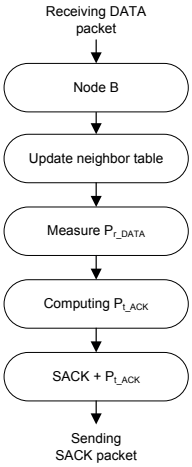

Fig. 5 Receiving DATA packet and sending ACK packet

5. Step - Receiving ACK packet and computing transmission power for future transmission

The first part of this step is the same as the previous ones. The second part is different - based on information about P_{t_ACK} and P_{r_ACK}, node B computes the value of the effective transmission power $P_{t\_F\_RTS}$ for future possible communication using (11). This information is stored in the table as the last known value of transmission power for node B. If the new transmission occurs to the same node (in this case to node B), the packet is transmitted with updated effective value of transmission power $P_{t\_F\_RTS}$ (11). This leads to loopback creation between the last and future transmission. If the destination node (B) doesn´t receive RTS packet when using the new transmission power value, the source node (A) automatically sets the output value $P_{t\_RTS} = P_{max}$ to restore the connectivity. The flow graph of receiving ACK packet and computing transmission power for future transmission is shown in Fig. 6.

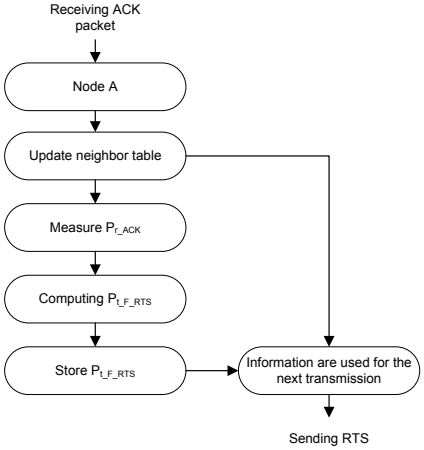

Fig. 6 Receiving ACK packet and computing transmission power for future transmission

4. Performance Evaluation

Simulation Setup

The NS-2 simulator was used to evaluate the performance of our proposed protocol scheme. We compared the proposed power control scheme with IEEE 802.11 MAC (omni-directional antenna) and D-MAC (directional antenna) schemes. The directional antenna is used as a switched beam antenna (divided to 12 antenna sectors) with a flat top radiation pattern. The simulation model consisted of 30 wireless nodes randomly placed in an area of 1000 x 1000 m. NS-2 mobility model was used, where nodes' speed was changed from 0 to 5 m/s with 1 m/s step. As a traffic model, 10 Constant Bit Rate (CBR) flows with the packet size of 512 bytes were used. The packets generation rate (number of packets per second) was randomly changed. Simulation parameters are summarized in Table 1.

Simulation parameters — Table 1

Parameter	Value	Parameter	Value
Test area	1000x1000 m	Antenna type	Omni-directional
MAC protocol	IEEE 802.11		Directional
	D-MAC	Directional beamwidth	30°
	4WDPCRL	Transmitter power	281.8 mW
Propagation model	Two ray ground	Rxthreshold	-89 dBm
Simulation time	200 s	Packet size	512 bytes
Initial energy	200 J	Traffic type	CBR (UDP)

As the routing function is not allowed, nodes that want to start communication with each other were located in their own communication range.

Results and Analysis

Figure 7 shows simulation results of average network throughput for 10 data flows, where speed of nodes was changed. The lowest value of average throughput for all speeds was achieved by using IEEE 802.11 MAC protocol with omni-directional antennas. For 0 m/s the proposed protocol enhanced throughput about 66.7% compared to IEEE 802.11 MAC protocol and for 5 m/s the enhancement was up to 58.4%. This enhancement in network throughput was achieved by increasing the number of simultaneous transmissions by minimization of interference.

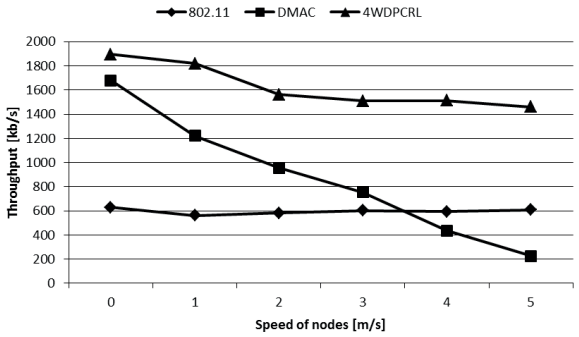

Fig. 7 Average values of throughput for different MAC algorithms and for 10 data flows.

Figure 8 shows the values of packet error rate (PER) for three different MAC protocols. From the results we can see that the best result was reached by 4WDPCRL protocol. This enhancement in PER is achieved by minimized interference.

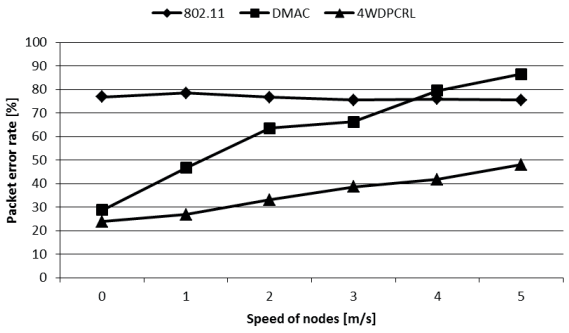

Fig. 8 Average values of packet error rate for different MAC algorithms and for 10 data flows

The average energy consumption per node is shown in Fig. 9. The results show that the highest values of energy consumption were reached with IEEE 802.11 MAC protocol. The best value was again achieved by using 4WDPCRL protocol. The enhancement in the energy consumption is achieved by integration of a power control scheme.

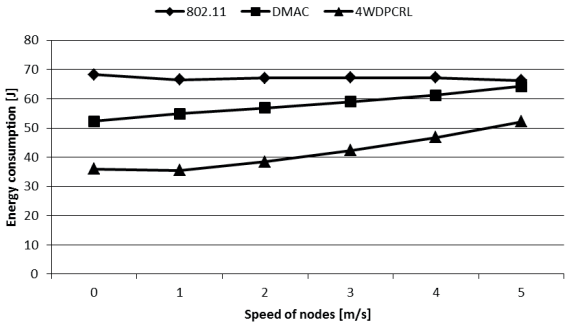

Fig. 9 Average values of energy consumption per node for different MAC algorithms and for 10 data flows

The average values of energy consumption of all nodes together are shown in Fig. 10. The results show that the highest value of energy consumption of all nodes was reached with IEEE 802.11 MAC protocol with omni-directional antennas, which was expected. More important improvement in energy consumption is in comparison of both directional MAC protocol schemes, where 4WDPCRL protocol outperforms DMAC protocol mainly in lower mobility. This enhancement in the energy consumption is achieved by integration of a power control scheme.

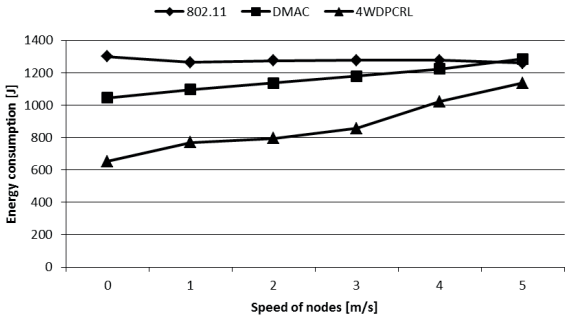

Fig. 10 Average values of energy consumption of all nodes for different MAC algorithms and for 10 data flows

5. Conclusions

In this paper, a new power controlled directional MAC protocol for MANET networks, named 4-Way Directional Power Control with Recoil Loop (4WDPCRL) was proposed. At the beginning of the transmission only the first RTS packet is transmitted omni directionally and with maximal power, other packets are sent directionally and with effective transmission power used. By using loopback, the interference at the start of the new transmission between the same nodes was optimized because both nodes had already included location information and information about effective transmitter power. This leads to

minimizing the interference, to improved spatial reuse and also to saving energy, which is very limited in MANET networks.

The rest of the paper gives the comparison of the proposed 4WDPCRL protocol with both widely used DMAC and IEEE 802.11 MAC protocols. On the basis of simulation results we can say that our proposed protocol outperforms both widely used IEEE 802.11MAC and DMAC protocols in chosen quality of service parameters - throughput and energy consumption.

Acknowledgment

This paper was supported by the Scientific Grant Agency VEGA in the project No. 1/0704/12.

References

[1] BASAGNI, S., CONTI, M., GIORDANO, S.: *Mobile Ad Hoc Networking.* New Jersey: A John Wiley & Sons, 2004, 459 p.

[2] TAY, M., CHUA, K. C.: A Capacity Analysis for the IEEE 802.11 MAC protocol, *J. of Wireless Networks*, vol. 7, No. 2, pp. 159-171, 2001.

[3] NASIPURI, A., YE, S., HIROMOTO, R.: *A MAC Protocol for Mobile Ad hoc Networks Using Directional Antennas,* Proc. of Wireless Communications and Networking Conference, Chicago, pp. 1214-1219, 2000.

[4] HUANG, Z., ZHANG, Z., RYU, B.: *Power Control for Directional Antenna-based Mobile Ad hoc Networks*, Proc. of the Intern. Conference on Wireless Communications and Mobile Computing (WiCOM 2006), Wuhan, pp. 917-922, 2006.

[5] NASIPURI, A., KAI, L., SAPPIDI, E.: *Power Consumption and Throughput in Mobile Ad Hoc Networks using Directional Antennas*, Proc. of 11th Intern. Conference on Computer Communications and Networks, Miami, pp. 620-626, 2002.

[6] XIAODONG, Z., JIANDONG, L., DONGFANG, Z.: *A Novel Power Control Multiple Access Protocol for Ad hoc Networks with Directional Antennas*, in Proc. of 20th Intern. Conference on Advanced Information Networking and Applications (AINA 2006), Vienna, pp. 18-20, 2006.

[7] CHOUDHURY, R., YANG, R. R., RAMANATHAN, R.: *Using Directional Antennas for Medium Access Control in Ad hoc Networks,* in Proc. of the 8th annual intern. Conference on Mobile Computing and Networking (MobiCom 2002), Atlanta, pp. 59-70, 2002.

[8] YI, S., PEI, Y., KALYANARAMAN, S.: *On the Capacity Improvement of Ad hoc Wireless Networks Using Directional Antennas*, in Proc. of Wireless Communications and Networking Conference (WCNC 2010), Sydney, pp. 1-6, 2010.

Monika Halamova – Tatiana Liptakova – Ayman Alaskari – Fabio Bolzoni *

INFLUENCE OF SURFACE STRUCTURE ON CORROSION BEHAVIOUR OF WELDED STAINLESS STEEL AISI 316L

The work deals with influence of surface structure on corrosion behaviour of austenitic stainless steel AISI 316L welded by TIG method without filler. Surfaces of the welded stainless steel were modified by mechanical treatment methods (grinding, garnet blasting, chemical method (pickling) and combination of both methods. Experimental procedures included the use of immersion and electrochemical tests where iron chloride ($FeCl_3$) and sodium chloride (NaCl) solutions were used as test electrolytes. The surfaces of the specimens were examined using light microscopy and scanning electron microscopy (SEM). Experimental results confirmed the significant influence of mechanical as well as chemical surface treatment on corrosion behaviour of the welded stainless steel AISI 316L in various chloride solutions.

Keywords: *Austenitic stainless steel, potentiodynamic test, corrosion properties, immersion test, surface treatment.*

1. Introduction

Austenitic stainless steel, in addition to its excellent corrosion resistance, mechanical properties (high ductility and high toughness) and weldability, is mainly used in environment that requires high reliability and durability of the material. These steels are sensitive to local corrosion attack such as pitting and intergranular corrosion in corrosive environments (e.g. with chlorides). Pitting resistance of stainless steel usually depends on many factors including the corrosive environment, chemical compositions and structure of the material. Corrosion resistance to local forms of corrosion is influenced by quality of the passive layer created by chemical reaction of stainless steel with oxygen at normal temperature. The protective ability is affected by metal structure, chemical composition (especially by the elements such as Cr, Mo, Ti, N) and also significantly by the surface treatment. By reducing carbon content in the stainless steel, carbide precipitation has less chance to occur during welding. Due to presence of molybdenum, AISI 316L austenitic stainless steel has good plasticity and high resistance against acids and deep local corrosion [1 - 7].

Durability, quality and long-term stability of engineering products are increasingly in demand. Welding of stainless steel can influence mechanical and corrosion properties. The size and character of the heat effect depends on chemical composition of stainless steel as well as welding parameters. AISI 316L stainless steels are widely used in components designed for high temperature applications. High temperature of welding process changes the steel structure by formation of carbides, various phases, ferrite and modification of grain size. A small amount of delta ferrite is necessary to avoid the problem of hot cracking during weld solidification. Properties of oxide layers on the surface are changed too [8 - 10]. Surface treatment of austenitic stainless steel has been a major interest of many industries and researchers. Surface conditions strongly affect the passive layer quality and, consequently, intensity and character of corrosion attack. Mechanical surface treatments are commonly used in industries and believed to have better mechanical properties and corrosion resistance. Chemical surface treatment (pickling) is believed to enhance the surface purity and also increases the corrosion resistance [11 - 13]. In many cases, it is acceptable to combine mechanical and chemical treatment.

The impact of surface treatments (mechanical, mechanical-chemical) of welded AISI 316L steels on corrosion resistance is presented in this paper. Corrosion behaviour of this steel under various chloride solutions was evaluated by immersion and electrochemical test. Optical microscopy and scanning electron microscopy were used to examine the surfaces.

2. Experimental material and surface treatment

The austenitic stainless steel of type AISI 316L was used as experimental material. The specimens were cut and prepared from

* [1]Monika Halamova, [1]Tatiana Liptakova, [2]Ayman Alaskari, [3]Fabio Bolzoni
[1]Department of Materials Engineering, Faculty of Mechanical Engineering, University of Zilina, SK, E.mail: monika.halamova@fstroj.uniza.sk
[2]Department of Mechanical Production Technology, P. O. Box: 42325 Shuwaikh 70654, Kuwait, College of Technological Studies
[3]Department of Chemistry, Materials and Chemical Engineering „Giulio Natta“, Politecnico di Milano, Milano, Italy

Chemical composition of the AISI 316L stainless steel Table 1

Element	Cr	Ni	Mo	Mn	C	Si	N	P	S	Fe
Content element [wt.%]	16.51	10.21	2.10	0.91	0.013	0.65	0.015	0.038	0.006	rest

the original sheet metal plate to dimension of 120 x 60 mm using laser cutting and then were welded by tungsten inert gas (TIG) method with no filler. Laser cutting was carried out at a pressure of 10 bar, cutting speed of 3700 mm.min^{-1} and power of 4 kW. The dimensions of the plate were selected to ensure the ease and homogeneity of the welding process. The chemical composition of the AISI 316L is listed in Table 1 where carbon content is quite low since very good weldability is required. The specimens were prepared for light microscopy in both transverse and longitudinal directions using wet grinding and etching in the solution of 10 ml of 40% HF, 30 ml of 65% HNO_3 and 20 ml glycerine.

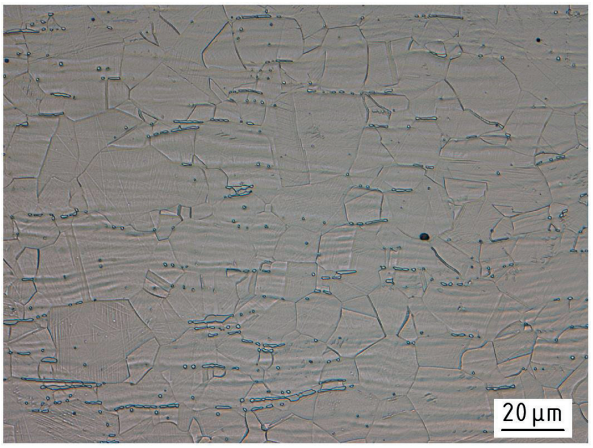

a) transverse

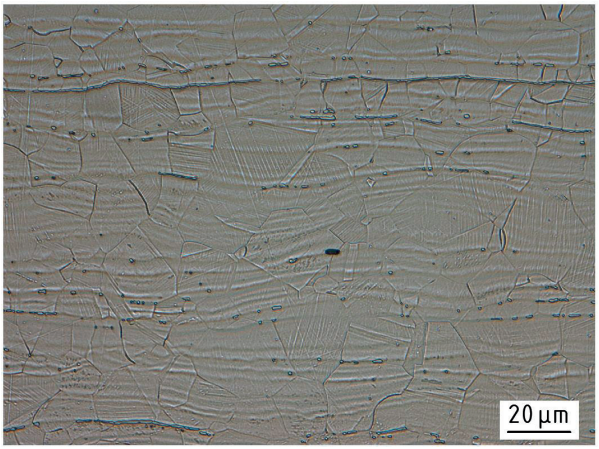

b) longitudinal

Fig. 1 The microstructure of the used AISI 316L stainless steel in different directions

Figure 1 shows the microstructure of the tested material in both directions, which is created by austenitic polyhedric grains with row deformation texture and deformation twins. In longitudinal section, deformation texture is very strong and there is present delta ferrite and inclusions.

All surfaces of the plates were degreased to ensure better weld quality. Then two plates were welded together using TIG method without filler. Welding parameters are shown in Table 2. During the welding process, argon gas was used for both sides (top and bottom) of the weld to provide a complete protection against oxidation of the welding area. Dimension of tested specimen was 50 x 25 mm with thickness 3 mm.

Welding parameters of the used TIG method without filler Table 2

Electrode diameter [mm]	Used current [A]	Argon flow [l/min]
1.6	92	7

Surfaces of the specimens were treated mechanically by grinding and garnet blasting. Initial surface grinding was performed to level up the surface of the welded area with base material. This was done by using surface grinding with Al_2O_3 belt with grit of 80. Then each specimen was ground by Al_2O_3 belt with grit of 180 for 3-4 minutes. This provided the welded surface with better surface finishing and better roughness. Blasting was performed on specimens with pressure of 6 bar and garnet abrasive grit of 80 (31 wt.% SiO_2, 21.6 wt.% Al_2O_3, 37 wt.% FeO, and 7.4 wt.% MgO). The blast pointed at 90 degree angle and lasted for about 60 seconds for each specimen. In addition, three specimens from each group (grinding, garnet blasting) were pickled for 30 minutes at temperature of 22 ± 2 °C in solution with composition 100 ml of 50% HNO_3, 5 ml of 38% HF, 395 ml of distilled H_2O. These specimens were cleaned and rinsed with distilled water and then left for sufficient time to dry out. All specimens were weighted to determine weight loss after corrosion test. The effects of different treated surfaces were investigated by scanning electron microscope (SEM) and the EDX chemical analysis.

3. Results and discussion

Surfaces of the specimens with different finishing were analysed with use of SEM on the JEOL JSM-7600F electron microscope (INCA Suite version 4.13 software). The tested surfaces in the weld locality were analysed and compared. In Fig. 2 there are shown the surfaces of welded joints after different

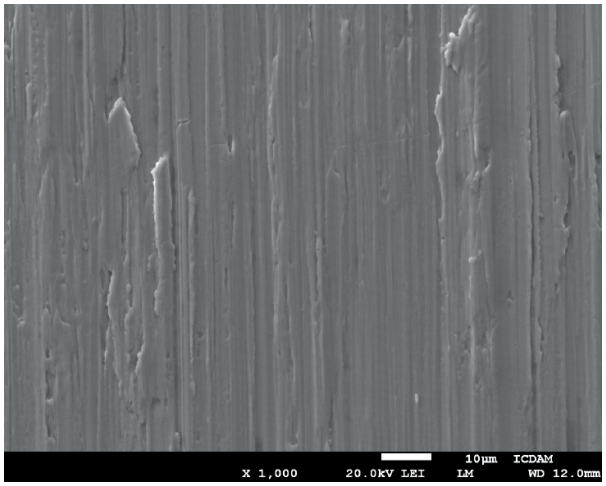

a) ground welded joint

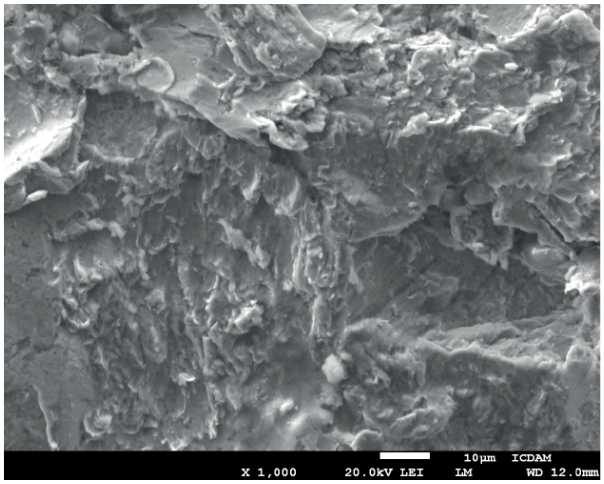

b) blasted welded joint

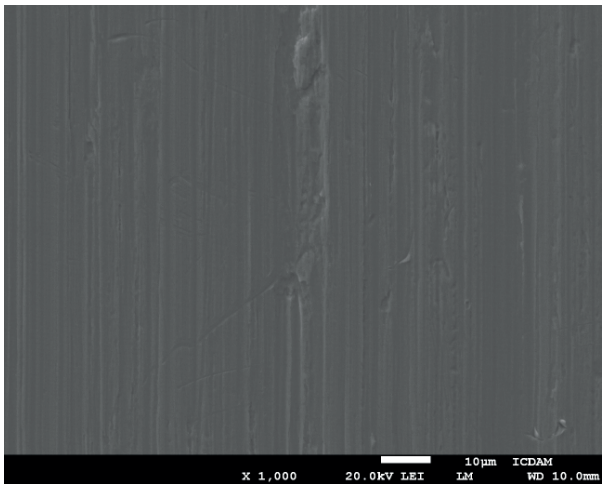

c) ground welded joint after pickling

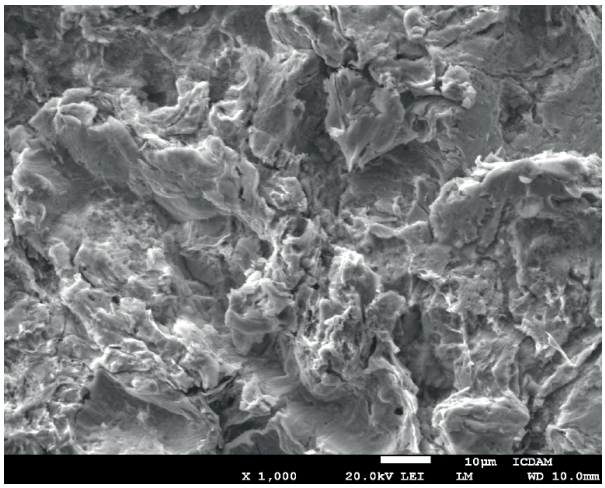

d) blasted welded joint after pickling

Fig. 2 SEM image of weld surfaces with mechanical (a, b) and mechanical-chemical (c, d) treatments

Chemical composition of the surfaces after various finishing Table 3

Surface treatment / Elements	Weight %			
	ground	ground + pickled	blasted	blasted + pickled
O	2.39	1.06	11	7.65
Mg	0	0	0.86	0.54
Al	0.53	0.42	1.62	1.46
Si	0.67	0.69	2.87	1.66
S	0.01	0.05	0.06	0.01
Ca	0	0	0.47	0.2
Cr	16.25	16.78	15.38	17.77
Fe	67.33	67.81	56.7	61.3
Ni	9.57	10	8.83	7.16
Mo	2.37	2.28	1.53	1.57
Mn	0.88	0.91	0.7	0.69

mechanical and mechanical-chemical finishing. The EDX chemical analysis was used to determine chemical composition of the surface. The differences in chemical composition between surfaces of welded metal finished by various treatments are shown in Table 3. By grinding the smooth and unite surface was achieved and pickling increased its purity. The surface roughness after blasting was high, pickling partially increased its purity, roughness and opened cracks.

Resistance to pitting corrosion of the AISI 316L welded specimens with various surface treatments (mechanical or mechanical-chemical) was tested. The immersion test was conducted using 6% $FeCl_3$ solution according to the standard ASTM G 48. The environment temperature during the test was 21 °C. After exposition in the test solution (72 hours) the specimens were removed from the immersion vessel, cleaned with distilled water and dried. Specimens were weighted on an analytical balance with the accuracy of 10^{-5} g and the corrosion rates were calculated. Results of immersion test are listed in Table 4.

Grinding surface after welding showed lower corrosion rate (Table 4a) in comparison with garnet blasted one. For the chemical treated surfaces in Table 4b the same trend of corrosion rates was observed. Chemical treatment (pickling) improved the corrosion resistance of ground specimens (increase by 14 %) when compared to specimens which were not treated chemically. Pickling increased purity and homogeneity of the surface which influenced quality of the passive layer and its better protection properties. In the case of specimens after garnet blasting, pickling negatively affected their corrosion resistance and the corrosion rate increased by about 43 %. The garnet blasting created a rougher surface, subsurface deformation. Oxidation products of welding and blasted particles were infiltrated into subsurface layers of steel. These phenomena escalated the corrosion process. Pickling partially removed blasting agents and oxides from surface and subsurface, but cracks created by peeling of material layers (caused by garnet blasting) were enlarged by pickling [14]. The roughness of the surface increased, thereby the real reaction area also increased. It supported reduction of the Fe^{+3} which is the main controlling process of corrosion. Also cracks are very sensitive places to corrosion attack because the access of oxygen into the cracks is more difficult and regeneration of passive layer is reduced. These circumstances affected negatively corrosion resistance of the AISI 316 L stainless steel.

Corrosion rates of the AISI 316L stainless steel in 6% $FeCl_3$ solution — Table 4

Type of surface treatment	Average weight losses [g]	Average corrosion rates [g×m^{-2}×h^{-1}]
grinding	0.28204	3.134
garnet blasting	0.39604	4.400
a) No chemical treatment		
grinding + pickling	0.23387	2.599
garnet blasting + pickling	0.56692	6.299
b) With chemical treatment		

Corrosion experiments realized by potentiodynamic polarization method were performed at 20 ± 2 °C in NaCl solution with concentration of Cl^- 100 ppm and pH = 7. The reference electrode was $Ag/AgCl/KCl_{satured}$. Set up of parameters: E_i (initial potential) was the same as E_{OC} (open circuit potential), E_f (final potential) was the same as E_i, max. current I_T = 1 mA, step height 10 mV/s.

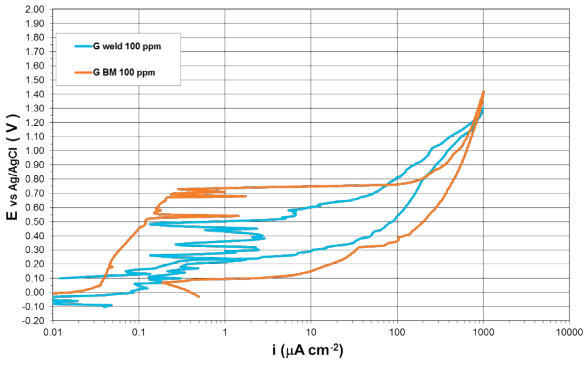

a)

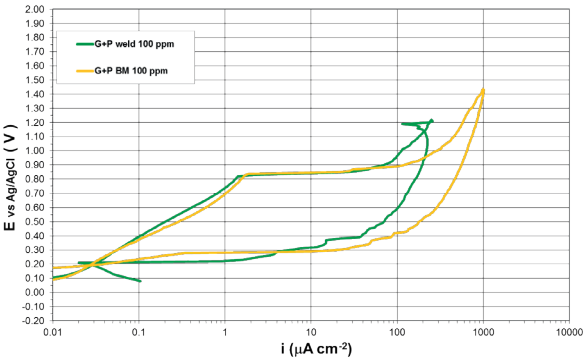

b)

Fig. 3 Comparison of electrochemical behaviour of a) ground (G) and b) ground + pickled (G+P) specimens in 100 ppm of Cl^- solutions for base material (BM) and weld

It is well known that potentiodynamic results depend on the scanning rate and immersion time before test. Potentiodynamic tests give qualitative information on electrochemical and corrosion properties of the investigated systems [15]. Figure 3 shows the trend of the cyclic potentiodynamic curves in the solution with 100 ppm of Cl^- for the specimens ground (G) and ground +

pickled (G + P). The treatment of pickling allowed a considerable improvement in localized corrosion. Electrochemical behaviour of garnet blasted (S) and garnet blasted + pickled (S + P) for base material and weld is in Fig. 4.

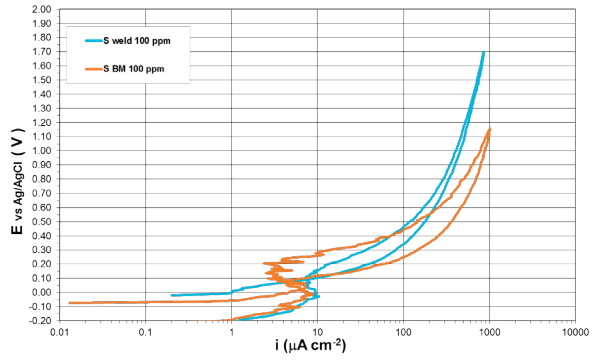

a)

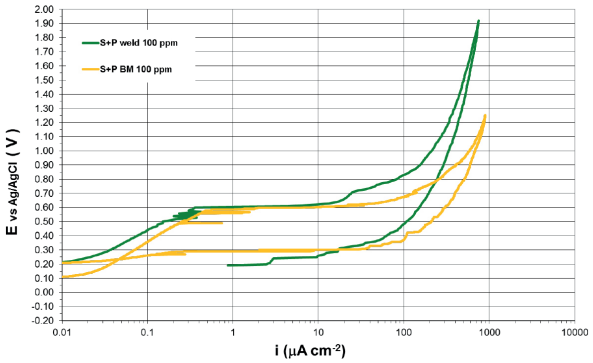

b)

Fig. 4 Comparison of electrochemical behaviour of a) garnet blasted (S) and b) garnet blasted + pickled (S+P) specimens in 100 ppm of Cl⁻ solutions for base material (BM) and weld

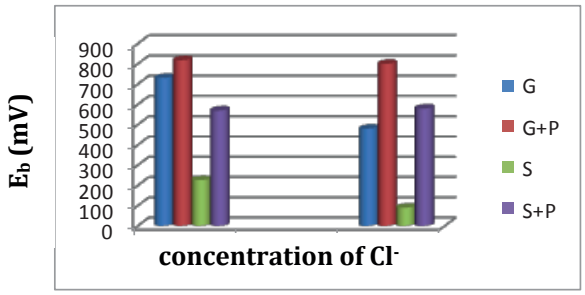

a) *b)*

Fig. 5 Comparison of breakdown potential (E_b) with various surface treatment for a) base material and b) weld in NaCl solution with Cl⁻ content 100 ppm

The graph (Fig. 5a) shows the values of breakdown potential (pitting potential) for base material in NaCl solution with Cl⁻ content 100 ppm. The specimens which were ground + pickled E_b = 818 mV had the highest breakdown potential for solution 100 ppm, then ground E_b = 730 mV, garnet blasted + pickled E_b = 569 mV. The garnet blasted specimens E_b = 226 mV had the lowest breakdown potential. The values of breakdown potential for weld are shown in graph in Fig. 5b. Weld with ground + pickled treatment had the highest breakdown potential E_b = 800 mV, then weld with garnet blasted + pickled treatment E_b = 579 mV. Weld with garnet blasted treatment E_b = 90 mV had the lowest value of breakdown potential. The breakdown potential value for ground treatment was E_b = 480 mV. Cyclic potentiodynamic test was used for evaluation of passive layer quality. Based on the results it is obvious that mechanically treated surface after pickling became more homogenous.

4. Conclusions

Based on the results of this experimental work it can be concluded:

1. The welded stainless steel AISI 316L treated by grinding has lower corrosion rate in comparison with garnet blasted (by about 25 %). Pickling of the ground surfaces slightly increases corrosion resistance according to results of the immersion corrosion test in the high redox potential solution. Pickling has a very positive influence on pitting corrosion characteristics of potentiodynamic experimental measurement. The surface purity achieved by pickling is reflected especially on the welds corrosion behaviour, than on the base material.
2. Based on the results of the immersion test the garnet blasting is an inappropriate method for surface treatment of the welded stainless steel AISI 316L since it accelerates corrosion in the environment with high redox potential. Blasting creates a rough surface with crevices and cracks where the aggressive solution stagnantes and the oxygen acces is restricted. Pickling even decreases corrosion resistance in this environment (by about 40 %). The surface purity of the garnet blasted specimens after pickling has positive influence according to potentiodynamic test where controlling process is metal anodic dissolution.

Acknowledgements

The research was supported by Scientific Grant Agency of Ministry of Education through VEGA grant No. 1/0066/11 and by European regional development fund and Slovak state budget by the project Research centre of University of Zilina, ITMS 26220220183. The authors thank for their support.

References

[1] SAHLAOUI, H., et al.: Effects of Ageing Conditions on the Precipitates Evolution, Chromium Depletion and Intergranular Corrosion Susceptibily of AISI 316L: Experimental and Modeling Results. *Materials Science and Engineering* A 372, p. 98-108, 2004.

[2] ALVAREZ-ARMAS, I.: Duplex Stainless Steels: Brief History and Some Recent Alloys. *Recent Patents on Mechanical Engineering* 1, p. 51-57, 2008

[3] SEDRIKS, A. J.: *The Corrosion Monograph Series. Corrosion of Stainless Steels.* A Wiley-Interscience Publication, 2nd ed. 1996.

[4] LIPTAKOVA, T.: *Pitting Corrosion* of Stainless Steels (in Slovak). Zilina : EDIS. ISBN 978-80-554-0083-9, 2009.

[5] LEFFLER, B.: *Stainless Steels and their Properties* [online]. [cit. 2012-29-11]. Available on the internet: http://www.hazmetal.com/f/kutu/1236776229.pdf, 2012.

[6] SZKLARSKA – SMIALOWSKA, Z.: *Pitting and Crevice Corrosion.* Texas: NACE International. Houston. Texas. 2005.

[7] BEDDOES, J., GORDEN PARR, J.: *Introduction to Stainless Steel*, ASM intern., 1999.

[8] DADFAR, M. et al.: Effect of TIG Welding on Corrosion Behavior of 316L Stainless Steel. *Materials Letters* 61 Elsevier, p 2343-2346, 2007.

[9] LIPPOLD, J. C., KOTECKI, D. J.: *Welding Metallurgy and Weldability of Stainless Steels.* John Wiley & Sons Inc, New Jersey. ISBN 0-471-47379-0, 2005.

[10] KOZUH, S., GOJIC, M., KOSEC, L.: The Effect of Annealing on Properties of AISI 316L Base and Weld Metals. *RMZ – Materials and Geoenvironment*, vol. 54, No. 3, p. 331-344, 2007.

[11] BEN RHOUMA, A. et al.: Effects of Surface Preparation on Pitting Resistance, Residual Stress, and Stress Corrosion Cracking in Austenitic Stainless Steels. *J. of Material Engineering and Performance* (ASM International), 10, pp. 507-514, 2001.

[12] ZATKALIKOVA, V., LIPTAKOVA, T.: Pitting Corrosion of Stainless Steel at the Various Surface Treatment. *Materials Engineering,* vol. 18, pp. 115-120., 2011.

[13] HALAMOVA, M., LIPTAKOVA, T., ALASKARI, A.: *Corrosion Resistance of AISI 316L Stainless Steel in Chloride Environment,* 30th Intern. Colloquium on Advanced Manufacturing and Repair Technologies in Vehicle Industry. Budapest : BME, 117-121, 2013

[14] LIPTAKOVA, T., FAJNOR, P., HALAMOVA, M.: *Effect of Surface Finishing on Local Corrosion of Ti-316 Stainless Steel*, 29th Danubia Adria Symposium on Advances in Experimental Mechanics, ISBN 978-86-7083-762-1, Belehrad 2012, 131-132, 2013.

[15] BOLZONI, F. et al.: *Electrochemical Characterization of Corrosion Resistant Alloys in Chloride Solutions.* Passivation of Metals and Semiconductors, and Properties of Thin Oxide Layers, 9th Intern. Symposium, Paris, 1st ed. Elsevier, Marcus, P. and Maurice, V., 2006.

Alaa Mohammed Abdul-Hadi - Olga Tarasyuk - Anatoliy Gorbenko - Vyacheslav Kharchenko - Thomas Hollstein *

THROUGHPUT ESTIMATION WITH REGARD TO AIRTIME CONSUMPTION UNFAIRNESS IN MIXED DATA RATE WI-FI NETWORKS

The paper discusses throughput unfairness inherent in the very nature of mixed data rate Wi-Fi networks employing random media access control technique CSMA/CA. This unfairness exhibits itself through the fact that slow clients consume more airtime to transfer a given amount of data, leaving less airtime for other clients. This decreases the overall network throughput and significantly degrades performance of high data rate clients. In the paper we propose mathematical models considering airtime unfairness and estimating wireless networks throughput depending on number of network connections and their data rates. These models show that all wireless clients have an equal throughput independently of data rates used by them. We verify our theoretical findings by running natural experiment and show that client's throughput approximates to the data rate of the slowest client.

Keywords: *Wireless networks, Wi-Fi, throughput, airtime consumption, unfairness.*

1. Introduction

Ethernet family of networks uses the CSMA/CD (Carrier Sense Multiple Access with Collision Detection) media access control technique, which provides random pseudo-fair access to the media for multiple users. This technique has been enhanced toward decreasing the probability of collision in wireless communications. This technique which is a core of IEEE 802.11 a/b/g/n Wi-Fi networks is called Carrier Sense Multiple Access with Collision Avoidance (CSMA/CA) [1].

In general case CSMA provides a random pseudo-fair multiply access to a wireless media that means a statistically equal number of chances that each computer gets to transfer its data frames over a shared media. For instance, if there are five computers connected to the same Fast Ethernet hub, the throughput available to the each computer can be roughly estimated as (*Throughput_MAX*)/(*the number of devices*), i.e. 100/5=20Mbps.

In contrast with the majority of network technologies worked over cables, the data rate used by Wi-Fi devices is not a constant value. Depending on signal strength (signal to noise ratio) a wireless access point (AP) and its clients, i.e. associated stations (STAs), are handshaking about the maximal possible transmitting/receiving data rate. The farther away a client is from the access point or from another client in case of Ad-hoc networks, the weaker a signal or the stronger a noise, the lower is the data rate.

802.11n devices, depending on the number of spatial streams and on the width of the wireless channel and guard interval, support rates from 6.5 Mbps up to 600 Mbps. Various data rates are represented by a Modulation and Coding Scheme (MCS) index value (1..31) which also defines modulation schemes and coding rates used.

The situation when different clients connected to the same AP (or sharing the same wireless channel in case of Ad-hoc communications) use different data rates is widespread. Slow clients occupy more airtime to transfer a frame of the same size, significantly degrading the performance of high-speed clients in the network. These facts significantly complicate estimation of the throughput available for a particular wireless client especially in case when all clients are busy transmitting and receiving data.

In this paper we focus on estimating throughput unfairness existing in wireless networks incorporating both low and high data rate clients. This is one of the most topical and yet not effectively resolved performance issues in mixed Wi-Fi networks occurred when high-speed 802.11n clients have to share 802.11n access points together with the legacy 802.11a/b/g clients [2]. Besides, this problem arises when one of the wireless clients is forced to reduce its data rate because of the weak strength of

* [1]Alaa Mohammed Abdul-Hadi, [1]Olga Tarasyuk, [1]Anatoliy Gorbenko, [1]Vyacheslav Kharchenko, [2]Thomas Hollstein
[1]Department of Computer Systems and Networks, National Aerospace University "KhAI", Kharkiv, Ukraine, E-mail: kharchenko@khai.edu
[2]Department of Computer Engineering, Tallinn University of Technology, Tallinn, Estonia

a signal (caused by the significant remoteness from the AP) or considerable noise level.

The paper introduces analytical models assessing existing unfairness towards high speed clients and overall throughput degradation as functions of a given divergence between clients' data rates in a mixed wireless network. Our theoretical findings have been verified by the practical throughput measurement.

There have been several studies of experimental measurement [3 and 4] and analytical estimation [5 and 6] of wireless networks throughput. These studies aim at analyzing Wi-Fi performance and understanding why the real throughput is significantly less than the advertised speed of wireless technologies (up to 54 Mbps for 802.11a/g and up to 600 Mbps for 802.11n).

Even though these works are important for understanding CSMA/CA performance overheads and uncovering the nature of the performance unfairness in mixed Wi-Fi networks, they do not provide a mathematical apparatus for its estimation.

The rest of the paper is organized as follows. In the next section we investigate a phenomenon of the airtime consumption unfairness arisen in mixed data rate wireless networks. Section 3 introduces analytical models quantifying existed unfairness and estimating wireless network throughput depending on the number of wireless clients and data rates they use. Finally, we verify our theoretical findings by running natural experiment and performing practical measurement, whose results are reported in Section 4, and conclude our work in section 5.

2. Airtime Consumption Unfairness

Slow clients consume more airtime to transfer a given amount of data, leaving less airtime for other clients. This decreases the overall network throughput and significantly degrades performance of high data rate clients.

Figure 1 helps in understanding the nature of this problem. It shows the simplified airtime distribution for the following scenarios:

1) there is only one high data rate client C_1 occupying the whole airtime;
2) there are two high data rate clients C_1 and C_2 sharing the wireless media and transferring frames of the same size with the same data rates ($V_1 = V_2$);
3) there are two clients C_1 and C_2 sharing a wireless media and transferring frames of the same size. The data rate V_2 of the second client is twice as less as the data rate V_1 of the first client ($V_2 = V_1 / 2$);
4) the data rate V_2 of the second client C_2 is three times less than the data rate V_1 of the first client C_1 ($V_2 = V_1 / 3$);
5) the data rate V_2 of the second client C_2 is five times less than the data rate V_1 of the first client C_1 ($V_2 = V_1 / 5$);
6) the data rate V_2 of the second client C_2 is eleven times less than the data rate V_1 of the first client C_1 ($V_2 = V_1 / 11$).

The inter-frame gap and the contention window can be neglected as their durations are much smaller than the frame transmission time. Besides, Fig. 1 assumes an alternate access to the media by different clients that is possible in theory but cannot be guaranteed in practice if CSMA/CA is used.

As it can be seen from Fig. 1, though the fast client could have sent more frames during the time the slow client spent sending only one, it still has to compete fairly for the wireless media on a frame-by-frame basis. Thus, the high data rate client spends more time waiting for the slow client to release the media than transmitting its own frames. This means that even a single client connected to the wireless network at a low data rate can dramatically slow down all of the high-speed clients.

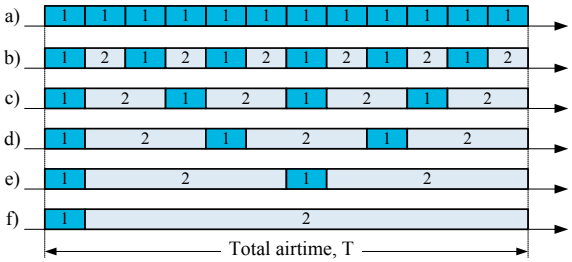

Fig. 1 CSMA/CA airtime distribution between two clients depending on their data rates

3. Throughput Estimation with Regard to Airtime Consumption Unfairness

If there is only one client connected to the wireless network at the data rate V_1 (see Fig. 1a) the volume of information that can be sent by this client during the given time T is equal to

$$N = V_1 \cdot T. \tag{1}$$

In case of two clients a portion of airtime T_1 utilized by a client connected at the data rate V_1 decreases inversely as the ratio between data rates (we assume that both clients transmit data using frames of the same MTU which is equal to 2.3 Kbytes in case of 802.11 wireless networks):

$$T_1 = T \cdot V_2 / (V_1 + V_2). \tag{2}$$

Thus, the volume of information that can be sent by the first client with the data rate V_1 during the time T_1 is equal to

$$N_1 = V_1 \cdot T_1 = T \cdot V_1 \cdot V_2 / (V_1 + V_2), \tag{3}$$

which actually has the same value for the second client too. This means that the effective throughput U_1 of the first client is K_1 times less compared to its data rate V_1:

$$U_1 = V_1/K_1, \quad (4)$$

where K_1 (a degradation coefficient) is equal to a ratio between N_1 and N_1':

$$K_1 = N/N_1 = (V_1 + V_2)/V_2. \quad (5)$$

Hence,

$$U_1 = V_1 \cdot V_2/(V_1 + V_2). \quad (6)$$

Using the same reasoning, the throughput U_2 of the second client is decreased by K_2 times as compared to its data rate V_2:

$$K_2 = (V_1 + V_2)/V_1, \quad (7)$$

$$U_2 = V_2/K_2 = V_2 \cdot V_1/(V_1 + V_2). \quad (8)$$

As it can be seen from (6) and (8) both clients get the same throughput though their data rates are different. We can also conclude that a faster client experiences much more significant throughput degradation while the throughput of the slow client is almost equal to its data rate.

Table 1 shows the differences between the degradation coefficients (K_1 and K_2) and the throughput depending on the data rates (V_1 and V_2) of two clients sharing the same wireless media. It is clear, that the random CSMA/CA access control technique significantly decreases effectiveness of the mixed Wi-Fi networks and is unfair towards clients with the higher data rate.

When two clients use the same data rates they share out network throughput equally as a half of their data rate (see the last row of Table 1). The bigger the difference between data rates used by clients, the lower the throughput they have and the closer it approximates to the data rate of the slowest client. For instance (see the first row of Table 1), when the first client is connected to a wireless network at 300 Mbps whereas the second one uses 15 Mbps connection a throughput available to both clients is equal to 14.3 Mbps.

By analogy with (1) – (6) a degradation coefficient K_1 in case of the three clients connected to the wireless network at data rates V_1, V_2 and V_3 can be estimated as

$$K_1 = \frac{V_2 \cdot V_3 + V_1 \cdot V_3 + V_1 \cdot V_2}{V_2 \cdot V_3}. \quad (9)$$

Hence, client throughput is equal to

$$U_1 = U_2 = U_3 = \frac{V_1 \cdot V_2 \cdot V_3}{V_2 \cdot V_3 + V_1 \cdot V_3 + V_1 \cdot V_2}. \quad (10)$$

Generalizing described particular cases we can get universal analytical equations which estimate maximal theoretical clients throughput and degradation factor in case of *n* clients sharing a wireless media at different data rates:

$$K_i = V_i \cdot \sum_{j=1}^{n} \frac{1}{V_j}, \quad (11)$$

$$U = U_i = \frac{\alpha}{\sum_{j=1}^{n} \frac{1}{V_j}}, \quad (12)$$

Throughput unfairness in mixed Wi-Fi networks — Table 1

MSC index		Data rate, Mbps		Degradation coefficient		Throughput, Mbps
MSC_1	MSC_2	V_1	V_2	K_1	K_2	$U_1 = U_2$
15	0	300	15	21.00	1.05	14.29
15	1	300	30	11.00	1.10	27.27
15	2	300	45	7.67	1.15	39.13
15	3	300	60	6.00	1.20	50.00
15	4	300	90	4.33	1.30	69.23
15	5	300	120	3.50	1.40	85.71
15	6	300	135	3.22	1.45	93.10
15	7	300	150	3.00	1.50	100.00
15	8	300	30	11.00	1.10	27.27
15	9	300	60	6.00	1.20	50.00
15	10	300	90	4.33	1.30	69.23
15	11	300	120	3.50	1.40	85.71
15	12	300	180	2.67	1.60	112.50
15	13	300	240	2.25	1.80	133.33
15	14	300	270	2.11	1.90	142.11
15	15	300	300	2.00	2.00	150.00

where α is OSI Level 7 throughput efficiency coefficient.

Many practical studies, e.g. [3 and 4], showed that a throughput practically achieved at the OSI Level-7 (or even Level-4) is substantially lower than the data rate at which a client is connected to the wireless network at level 1. It takes about 50% at best even in case of a single client connected to an access point and it gets worse when there are multiple clients sharing the same wireless network.

In [6] an efficiency coefficient α ($0 < \alpha \leq 1$) has been introduced to take into account such a decrease caused by many reasons including inter-frame gaps and CSMA/CA contention windows, numerous Wi-Fi control frames, collisions and retransmissions of corrupted frames. More detailed explanations of this phenomenon are given in [7], but they are out of the scope of this paper. Moreover, if a wireless network works in an Infrastructure mode every communication between wireless clients goes through the access point. This means that the same message goes over the air twice (from the source STA to the AP and then from the AP to the destination STA) and leaving only half of the available throughput. Thus, a value of the Level 7 throughput efficiency coefficient α can be roughly estimated using Table 2 taking into account different types of WLAN and communication.

Finally, the overall bandwidth of a wireless network incorporating n associated stations connected at different data rates can be estimated as:

$$U_{\Sigma} = \alpha \cdot n \cdot U_i = \frac{\alpha \cdot n}{\sum_{j=1}^{n} \frac{1}{V_j}}. \quad (13)$$

WLAN throughput degradation coefficient — Table 2

Service Set/Type of WLAN	Type of Communication	Throughput degradation coefficient α
IBSS/Ad-hoc	WLAN ⟷ WLAN	0.3 – 0.5
BSS/Infrastructure	WLAN ⟷ WLAN	0.15 – 0.25
	WLAN ⟷ LAN	0.3 – 0.5

4. Experimental Throughput Measurement

4.1 Method and Experimental Settings

The experiments that we report in this section use the configuration depicted in Fig. 2. It includes one desktop computer C connected directly to the 802.11n MIMO UniFi AP access point via 100 Mbps Fast Ethernet wired connection. Besides, we used two laptops (A and B) equipped with the Intel WiFi Link 6250 and Atheros AR9285 802.11n network adapters respectively. These laptops established network connections with the desktop computer C via the DAP-1360/E 802.11n access point. Each laptop supported one spatial downstream (1 x 2 : 1) using one 20-MHz-wide channel in the 2.4 GHz range. Both laptops were configured to simultaneously establish TCP connections with the desktop computer and to send 100 files of 1 MB size each in series.

At the beginning both laptops were placed close to AP so that were able to establish wireless connections at the maximal available data rates: 75.2 Mbps for A and 65 Mbps for B. This initial difference of the data rates is caused by the different guard intervals supported by Intel and Atheros adapters (400 ns and 800 ns). While a position of the laptop B was fixed during the whole experiment, the laptop A had been moved off the access point until its data rate decreased down to the minimal value (6.5 Mbps). Then it was moved back toward the access point (see Fig. 2).

To run this experiment and to measure network throughput and signal strength (RSSI) we used IxChariot tool which is the industry's leading test tool for simulating real-world applications and measuring system performance under realistic load conditions[1].

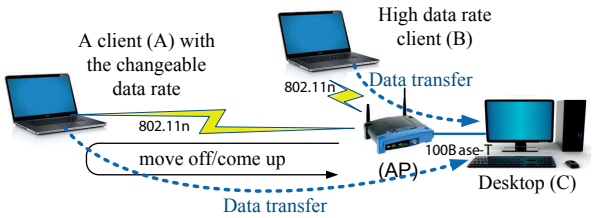

Fig. 2 Experimental configuration

4.2 Signal Strength and Throughput Measurement Results

As we can see in Fig. 3a the RSSI (Received Signal Strength Indication) measured by the laptop B was varying insignificantly during the whole observation time whereas the RSSI measured by the laptop A was decreasing when it was moving away from the access point and increasing back when it was coming up. As it also follows from Fig. 3a the receiver sensitivity of the laptop A was a bit better than one of the laptop B.

RSSI decrease caused reduction of the transmission data rate at the laptop A. As a result, its throughput went down as it is shown in Fig. 3b. At the same time we can see that the throughput of the laptop B went down too, though its data transfer rate remained constant during the whole experiment. This testifies to our theoretical findings about the throughput unfairness existing in mixed data rate Wi-Fi networks which is caused by the fact that slow clients consume more airtime to transfer a given amount of data leaving less for others.

However, we can see that throughput curves of the two clients are not exactly the same. This can be explained by the random nature of the CSMA/CA media access control technique and

1 http://www.ixchariot.com/products/datasheets/ixchariot.html

differences in hardware/software implementation of Intel and Atheros Wi-Fi adapters used by different clients.

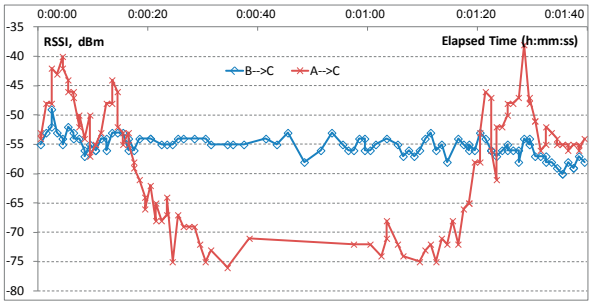

(a)

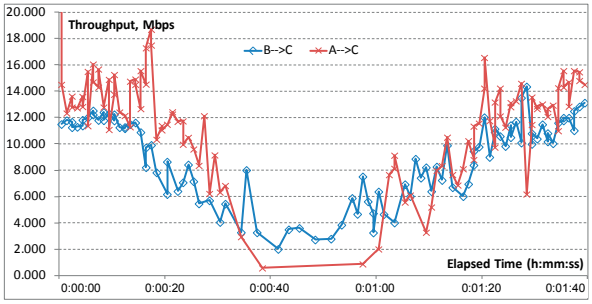

(b)

Fig. 3 Measurement results: received signal strength indication (a) and throughput (b)

4.3 Deviation Between the Theoretical and Experimental Results

With the purpose of estimating accuracy of the throughput analytical model (12) let us consider three time intervals observed during the experiment (see Fig. 3): [0:00:00 ... 0:00:10], [0:00:40 ... 0:00:50], and [0:01:30 ... 0:01:40].

During the first and the third time intervals clients A and B transferred data at their maximal data rates (75.2 Mbps for A and 65 Mbps for B). Thus, we can join these two intervals together (see Table 3). The average Client A's throughput measured during these time intervals was equal to 13.93 Mbps. The average Client B's throughput was a bit lower (11.7 Mbps). Using these data we were able to estimate the Level 7 efficiency coefficient α which in our experiments approximated to 0.373, which is in line with other studies [3 and 4].

During the second time interval we registered the maximal difference between data rates used by clients A and B (6.5 Mbps for A and 65 Mbps for B). At the same time their average throughput was equal to 1.62 Mbps (A) and 2.94 Mbps (B) respectively.

Client's maximal theoretical throughput estimated using (12) and assuming α=0.373 is equal to 12.66 Mbps for the first and the third time intervals. For the second time intervals it is equal to 2.19 Mbps. As it can be seen, the deviation between results obtained theoretically and those average values measured practically is less than 4% for the second time interval and 0.5% for the first and third intervals. Such a convergence between theoretical and experimental results approves accuracy of our analytical models proposed in section 3.

5. Conclusions

In general case CSMA/CA provides a random multiply access to a wireless media that means a statistically equal number of chances that each computer gets to transfer its data frames over a shared media. However, different wireless computers can use different data rates depending on the signal-to-noise ratio. This fact causes an unfairness as slow clients consume more airtime to transfer a given amount of data, leaving less airtime for other clients.

Deviation between the theoretical and experimental results — Table 3

Parameter	Time interval, h:mm:ss	
	[0:00:00 ... 0:00:10] [0:01:30 ... 0:01:40]	[0:00:40 ... 0:00:50]
Client A Data Rate	72.20	6.50
Client B Data Rate	65.00	65.00
Client A experimental throughput (average)	13.93	1.62
Client B experimental throughput (average)	11.70	2.94
Level 7 throughput degradation coefficient α	0.373	
Theoretical clients throughput estimated using (12) and assuming efficiency coefficient α = 0.373	12.76	2.20
Average clients experimental throughput	12.82	2.28
Deviation	0.44%	3.44%

At the same time, high data rate clients spent much more of air time just waiting for an access to the wireless media than transferring data. This decreases the overall network throughput and significantly degrades performance of high data rate clients. In the paper we investigate this phenomenon and propose mathematical models which estimate wireless connection throughput taking into account such unfairness occurred in mixed data rate Wi-Fi networks. We have shown both theoretically and experimentally that high data rate clients suffer much more from performance degradation than those connected at low data rate. Finally, all wireless clients have roughly the same throughput independently of data rates used by them. In the case when slow and high-speed clients are simultaneously sharing a wireless media their throughputs approximate to the data rate of the slowest client. Thus, CSMA/CA media access control technique needs to be improved in order to prevent wireless networks from performance degradation.

We have foreseen several approaches which can be used to deal with the throughput degradation caused by the airtime consumption unfairness. The first one is based on the frame aggregation that is an intrinsic part of the 802.11n standard. The idea is to allow high data rate clients to aggregate certain number of frames (depending on a ratio between data rates of different clients) to mitigate air time unfairness. Though, such a balanced frame aggregation can compensate the throughput unfairness caused by different client's data rates it does worsen the response time which is critical for many real time applications like VoIP, etc [8].

Another possible approach is to induce the CSMA/CA media access control algorithm to giving priority to the clients depending on their data rates. This can be done, for instance, through the dynamic adaptation of the size of the contention window [9] that seems to be more promising as it does not affect the response time. Thus, in our further work we are going to investigate this approach in more details and find out the correspondence between the clients data rate and the desired size of the contention window.

Acknowledgement

We are grateful to Harald Richter for his feedback on the earlier version of this work. The work is partially supported by the FP7 KhAI-ERA project.

References

[1] JUN, P.: A Wireless MAC Protocol with Collision Detection, *IEEE Transactions on Mobile Computing*, vol. 6, No. 12, pp. 1357-1369, 2007.

[2] *Impact of Legacy Devices on 802.11n Networks*, Airmagnet Inc. Whitpaper, 2008, 15 p.

[3] PACHECO DE CARVALHO, J. A. R., VEIGA, H., RIBEIRO PACHECO, C. F., REIS, A. D.: *Performance Evaluation of Wi-Fi IEEE 802.11 A,G WPA2 PTP Links: a Case Study*, Proc. World Congress on Engineering, 2012.

[4] KEMERLIS, V. P., STEFANIS, E. C., XYLOMENOS, G., POLYZOS, G. C.: *Throughput Unfairness in TCP over WiFi*, Proc. 3rd Annual Conference on Wireless on Demand Network Systems and Services, 2003, pp. 1-6.

[5] MALONE, D., DUFFY, K., LEITH, D.: Modeling the 802.11 Distributed Coordination Function in Nonsaturated Heterogeneous Conditions, *Networking, IEEE/ACM Trans. on* , vol.15, No.1, 2007, pp.159-172.

[6] MALONE, D., DUFFY, K., LEITH, D.: Modeling the 802.11 Distributed Coordination Function in Nonsaturated Heterogeneous Conditions, *IEEE/ACM Trans. on Networking*, vol.15, No.1, 2007, pp.159-172.

[7] XYLOMENOS, G., POLYZOS, G. C., MAHONEN P., SAARANEN, M.: TCP Performance Issues over Wireless Links, *IEEE Communications Magazine*, vol. 39, No. 4, 2001, pp. 52-58.

[8] CAMPS-MURA, D., GOMONYB, M. D., PEREZ-COSTAA, X., SALLENT-RIBESC, S.: Leveraging 802.11n frame aggregation to enhance QoS and power consumption in Wi-Fi networks, *Computer Networks*, vol. 56, No. 12, 2012, pp. 2896-2911.

[9] YOUNGMI, J., KESIDIS, G.: Distributed Contention Window Control for Selfish Users in IEEE 802.11 Wireless LANs, *IEEE J. on Selected Areas in Communications*, vol. 25, No. 6, 2007, pp. 1113 – 1123.

Radim Bris *

ASSESSMENT OF THE AVAILABILITY OF AN OFFSHORE INSTALLATION BY STOCHASTIC PETRI NET MODELING

The purpose of this article is to illustrate the combination of stochastic Petri nets and Monte Carlo simulation approach for the evaluation of the production availability of a multi-state, multi-output offshore installation with operational loops. The presented test case comprises a great number of the problems encountered when dealing with probabilistic studies. The reason for using Petri net modeling is that it provides the necessary flexibility to describe the complexity of the plant and the realistic aspects of system behavior, such as a degradation and standby of components, maintenance, etc. Different production levels of the system are assessed and evaluated from both reliability and production efficiency point of view. Four selected configurations of the system are analyzed to investigate how the production efficiency and average availability are influenced by applying a preventive maintenance and an additional cold standby of component.

Keywords: *Oil production, operational dependencies, production availability.*

1. Introduction

In many industries such as the power industry, chemical and oil ones, there is felt the need of realistic models to evaluate the availability of the multi-state and multi-output plants [1]. The complexity of the plant and of its maintenance and reconfiguration policies is such to render unfeasible its availability evaluation by analytical models. Production availability studies are more difficult to perform than classical reliability studies [2]. Combinatorial models as reliability block diagram, fault trees and reliability graphs are commonly used for system reliability and availability analysis. These models are not really adapted for production availability. Markov approach can be used to some extent but only for small systems. Thus the simulation method is employed when the analytical techniques have failed to provide a satisfactory mathematical model. The Monte Carlo simulation gives good results, but this simulation may be even very extensive if highly reliable and accurate results are required.

Petri nets [3] are a graphical paradigm for the formal description of the logical interactions among parts or of the flow of activities in complex systems. The growing importance of Petri nets (PNs) is related to their usefulness in the modeling and analysis of concurrent systems, distributed processing, work-flow systems, communication and control systems, all of whose dynamical behavior can be easily expressed as movement of tokens in PN. Stochastic Petri nets (SPNs) [4 and 5] represent an extension of the basic PNs obtained by addition timing and stochastic information. The advantages of PN for the modeling of systems are well-known [6]. The dynamic behavior of complex systems can be modeled by using only a few numbers of graphical elements. PNs are very flexible. It is possible to find a way to model almost any new constraint. The graphical aspect of PN allows us to design automatic or step by step hand simulators necessary for an efficient debugging of the models. The size of a PN model is linear with the number of components.

This paper tries to solve one test case [7] of the European thematic network SAFERELNET (EU project number GTC2-2000-33043) dealing with the dependability [8] of an industrial production process. This test case includes a great number of the difficulties encountered when dealing with probabilistic studies related to production processes. The complexity of the plant with the realistic conditions of the corrective and preventive maintenance policies and production priorities of the system render unfeasible an analytical approach. A Monte Carlo (MC) simulation approach for this test case was successfully applied in [9].

The research brings a continuation and extension of the original work in [10]. The paper deals with a PN model for the availability evaluation of a multi-state, multi-output offshore installation with operational loops. New extension is given by adding a new cold standby component which thoroughly modifies the basic SPN model both with and without the preventive maintenance.

* **Radim Bris**
Faculty of Electrical Engineering and Computer Science, VSB – Technical University of Ostrava, Czech Republic
E-mail: radim.bris@vsb.cz

2. System description and functioning

The test case represents the problem of an offshore installation in which different kinds of production processes are carried out. The installation is designed for the extraction of flow from a well and the following separation of the incoming flow in three different flows: gas, oil and water. The basic functions of the modeled system are shown in Fig. 1.

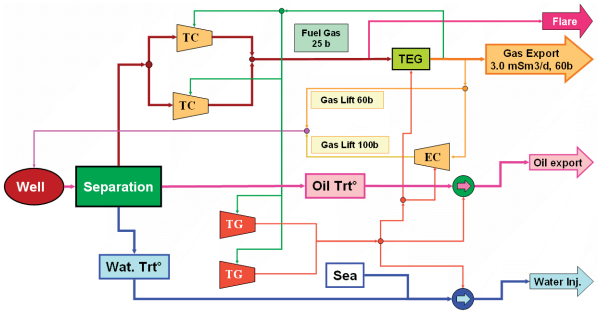

Fig. 1 Scheme of the offshore plant with three different flows: gas, oil and water

The oil coming from the well is separated by a separating unit into three different flows: gas, oil and water. The gas is compressed by two 50% capacity Turbo-Compressors (TCs), then dehydrated by a Tri-Ethylene Glycol (TEG) unit and then exported. The nominal capacity of the gas exported is $3.0 \cdot 10^6$ Sm^3/d at the pressure of 60 *bar*. A flare is used for safety purpose and to burn the gas when it cannot be exported, i.e. the gas is not compressed. After treatment, the oil is exported through a pumping unit. The pumping unit and the oil treatment system can process all the oil coming from the separation unit. The water separated by the separation unit is, after treatment, re-injected in addition with sea water in the field in order to maintain the pressure.

The maximum capacities of the components for the oil, gas and water production are shown in Table 1. In the typical production case the well can produce maximum 26500 m^3 of oil, $5.0 \cdot 10^6$ Sm^3 of gas, and 8000 m^3 of field water per day. The capacity of the separation unit limits these flows to $4.4 \cdot 10^6$ Sm^3 of gas, 23300 m^3 of oil and 7000 m^3 of water. Each TC is able to process at its maximum $2.2 \cdot 10^6$ Sm^3 of gas. The TEG unit is able to process $4.4 \cdot 10^6$ Sm^3 of gas at its maximum. Each TC uses $0.1 \cdot 10^6$ Sm^3 of "fuel-gas" and $1.0 \cdot 10^6$ Sm^3 of compressed gas is needed for "gas-lift ". Therefore, in the perfect case 23300 m^3 of "export oil" and $3.0 \cdot 10^6$ Sm^3 of "export gas" are produced. 7000 m^3 of field water is extracted which, after treatment, will be re-injected in the field or in the sea if the water injection is not available.

Most of the components need to be powered by electricity. Two 50% capacity electrical Turbo-Generators (TGs) are installed in order to provide electricity to the system. Each TG produces 13 *MW*. The electricity is used to power the TEG unit (consumes 6 *MW*), the Electro-Compressor (EC, *6 MW*), the oil pumping unit (7 *M*W) and water injection pumping unit (7 *MW*). In the system there is a loop because the gas produced by the TEG unit is used to produce, through the connection with the TGs, the electricity consumed by the TEG unit itself.

Turbo-compressors and turbo-generators are powered by "fuel gas". The fuel gas is taken from the export gas at the output of the TEG unit and then distributed to the two turbo-compressors and the two turbo-generators. Each of them consumes $0.1 \cdot 10^6$ Sm^3 per day. A second loop appears because compressed gas from the turbo-compressors is needed to produce fuel-gas and conversely fuel gas is needed to run the turbo-compressors.

The well is activated by using the so-called "gas-lift" that means the gas is taken from the TEG unit output then it is compressed by an electro-compressor (EC). Finally it is injected at bottom of the well in order to improve the production. When the EC fails, the gas lift is taken directly from the TEG unit output and injected at a lower pressure. The consumption is $1.0 \cdot 10^6$ Sm^3 of compressed gas for "gas-lift" per day and, therefore, the well has 3 levels of the production: the full production (gas-lift at a pressure of 100 *bars*) as is shown in Table 1; medium production of 80% of the maximum (60 *bars*); low production of 60% of the maximum (no gas lift). The failures of the well are not taken under consideration.

2.1 Component failures and repairs

In the proposed test case, only the failures of the TCs, TGs, EC and TEG are taken into account. All the other components are assumed to be in their faultless state. The TCs and TGs can be in three different states: **0** = As good as new; **1** = Degraded; **2** = Failed. The TEG and the EC can be in two states: **0** = As good as new; **2** = Failed.

The component is in the "Failed" state when a critical failure occurs. The critical failure is that which brings about immediate functionality loss of the component. The "Degraded" state is such that the component is still working but it has higher probability of going into the "Failed" state. Therefore, the corrective maintenance of the degraded failure can be delayed but, of course, at the end they must be repaired. In the model, we assume for simplicity that the times of the degradation and failure transitions are exponentially distributed with values of the rates shown in Table 2.

2.2 Production configurations

When a failure occurs, the system is reconfigured in order to minimize, firstly, the impact on the export oil production, and secondly, the impact on export gas production. It is supposed

that the impact on water injection does not matter. The different component failures have different effects on the three types of system production.

TEG failures. When the TEG is disabled, "Export Gas", "Gas-Lift" and "Fuel Gas" are lost. Therefore, the 2 TGs stop. The whole system is shutdown because it is not possible to use gas which has not been dehydrated.

EC failures. When the EC is lost, the "Gas-Lift" pressure is decreased (60 *bars*), therefore, the well production is reduced, too. At the end "Export Oil" and "Export Gas" are declined. "Fuel Gas" is maintained.

TCs failures. When one TC is broken, "Export Oil", "Water Injection", "Fuel Gas" and "Gas-Lift" are maintained. The two TGs are running. The non-compressed part of the gas is flared, therefore, the quantity of "Export Gas" is reduced. When both TCs are lost, all production (oil, gas, water) is stopped.

TGs failures. When one TG is damaged, the "Export Oil", "Export Gas", "Fuel Gas" and "Gas-Lift" are maintained. The EC and "Water Injection" are stopped due to lower level of electricity production. As a result of this situation the "Export Oil" and the "Export Gas" decrease because of lower production of the well due to the unavailability of the "Gas lift" high pressure. When both TGs are lost, all production is stopped because the TEG is not powered and it is not possible to use not dehydrated gas.

Maximum capacities of the components of the oil, gas and water production process — Table 1

Component	Oil m^3/d	Gas Sm^3/d	Water m^3/d
Well	26 500	$5.0 \cdot 10^6$	8000
Separator unit	23 300	$4.4 \cdot 10^6$	7000
Oil treatment	23 300	–	–
Pumping unit	23 300	–	7000
Water treatment	23 300	–	7000
TC	–	$2.2 \cdot 10^6$	–
TEG	–	$4.4 \cdot 10^6$	–

Failure and repair rates of the components — Table 2

Transition	Rate (1/hour)			
	TC	TG	EC	TEG
$0 \rightarrow 1$	$6.70 \cdot 10^{-4}$	$7.90 \cdot 10^{-4}$	–	–
$1 \rightarrow 2$	$2.12 \cdot 10^{-4}$	$1.86 \cdot 10^{-3}$	–	–
$0 \rightarrow 2$	$7.40 \cdot 10^{-4}$	$7.70 \cdot 10^{-4}$	$1.70 \cdot 10^{-4}$	$5.70 \cdot 10^{-5}$
$1 \rightarrow 0$	$3.30 \cdot 10^{-2}$	$3.20 \cdot 10^{-2}$	–	–
$2 \rightarrow 0$	$4.80 \cdot 10^{-2}$	$3.80 \cdot 10^{-2}$	$3.20 \cdot 10^{-2}$	$3.33 \cdot 10^{-1}$

2.3 Maintenance policy - corrective maintenance

There is available only a single maintenance team to perform repairs of components. Only one component at a time can be repaired. When more components fail simultaneously, the maintenance team starts to repair the component which has a higher repair priority and which is most important with respect to the system production. The repair priority of each component is dependent on the system state, as shown in Table 3. The repair levels of production components are defined in this way: *Utmost priority level (level 1*) pertains to failures leading immediately to the total loss of the process (TEG, both TGs, both TCs), *Medium priority level (level 2*) is used when only a part of the export oil is lost (single TC or EC failure), *Lower priority* level *(level 3*) includes the failures when no export oil is lost (single TG failure).

2.4 Maintenance policy – preventive maintenance

The TGs, TCs and EC are subordinated to the periodical preventive maintenance. It is supposed that the preventive maintenance is realized by a single team which is not the same as the corrective maintenance team. In order to keep up the production level as high as possible, no preventive maintenance operation can be started if the system is not in a perfect state of operation. Of course, when a preventive maintenance is in progress on one component, the other components can fail, then corresponding corrective maintenance is immediately started. Four different types of the preventive maintenance actions are considered. Each of them is characterized by a different frequency and different mean duration, see Table 4.

Repair priority levels of production components for the basic model — Table 3

Priority	Component	System conditions
1	TEG	–
1	TG	other TG failed
1	TC	other TC failed
2	EC	–
2	TC	other TC not failed
3	TG	other TG not failed

Preventive maintenance strategy — Table 4

Type of maintenance	Component	Period hours	Mean duration hours
1	TC, TG	2160	4
2	EC	2666	113
3	TC, TG	8760	120
4	TC, TG	43800	672

3. Stochastic Petri nets

A PN is a bipartite directed graph consisting of two kinds of nodes: places and transitions. In a graphical representation, the *places* are depicted by circles and the *transitions* by rectangles, see Fig. 2. The directed edges (*arcs*) connect places to transitions and transitions to places, never an arc from a place to a place or from a transition to a transition. The *tokens*, depicted by dots, are associated with places and the movement of these token represents the dynamic behavior of the system. The *marking* of a PN is the distribution of tokens in the set of places. Each marking defines a state of the system. A token in a given place indicates that the associated feature is active. The tokens move based on the *firing* of transitions. A transition is *enabled* to fire only if all its input places contain tokens. Upon firing, one token from each input place is removed and one token is deposited in each of the output places. It is important to note that the execution of a PN is non deterministic.

Formally, a PN is a four-tuple (P, T, I, O), where P is a finite set of places, T is a finite set of transitions, I is an input function and O is an output function. The input function I and the output function O define for each transition t_j the set of input places $I(t_j)$ and output places $O(t_j)$. If places can contain more than one token, the 4-tuple can be extended by the marking vector $m = (m_1, m_2, ..., m_i, ..., m_p)$, where m_i is the number of tokens in the place p_i.

SPN is an extension of the basic PN obtained by addition timing and stochastic information to the transitions. A firing rate is associated with each timed transition. Real process modeling requires the further extensions of the SPN framework. For our purpose it is advisable to add guards to some transitions (for example *Mess_TC* or *Mess_TG* in Fig. 2). A transition guard (so-called "message") is an annotation of a transition, which specifies additional requirements for enabling of a transition. A transition can only be enabled if the value of its guard is true.

The messages are very useful to synchronize the behavior of subnets which can work separately. The message received by transitions is indicated by a "question mark" ("?") and the message emitted by a transition is indicated by an "exclamation mark" ("!"). The same message can be both received and emitted by the same transition. When the component is in the state Failed and it is waiting for repair, the "repair" transition checks if a given condition is true. The message "?*RA*" is true when the team for the repair is available and false if the repair team is unavailable. The messages of some components are more complicated because logical operators (logical conjunction, logical sum and negation) can be used to formulate them.

The system (Fig. 1) is composed by four components (2 TGs and 2 TCs) that may be in 3 different states, and two components (TEG and EC) that may be in 2 states. The number of possible system configurations is then $3^4 \times 2^2 = 324$.

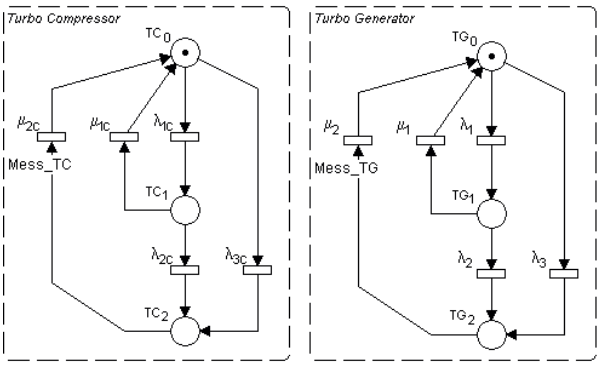

Fig. 2 SPN models of TCs and TGs components

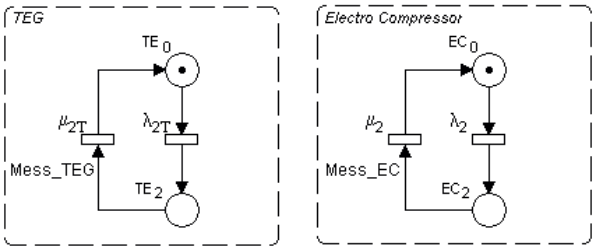

Fig. 3 SPN models of EC and TEG components

The SPN model is divided into smaller ones which represent sub-processes of the system. Figures 2-3 show a stochastic behavior of all considered system components expressed as single SPNs. The SPN model of the TC unit contains three places representing individual states in which this component can occur. The place TC_0 represents such case that the TC unit is in the state **0**. The place TC_1 represents the state **1** and the place TC_2 denotes the state **2**. Similarly it is applied for the TG unit. The system under consideration contains two TGs and two TCs - in following text they are marked as TGa, TGb and TCa, TCb. The TEG and EC units can be in two states so that their SPN models contain two places (Fig. 3). The actual state of the component is specified by the token position (a black dot). All transitions of these SPN models are exponential with failure or repair rates in Table 2 (marked here by Greek letters λ and μ.). To study the effect of the preventive maintenance and the effect of the cold standby the following four modifications of the plant have been taken into account:

Case A. The plant is operated without the preventive maintenance;

Case B. The components TG, TC and EC are preventively maintained with the predefined policy in Table 4;

Case C. The system is operated without the preventive maintenance, but the third TG is added to the system and it is normally used in a cold standby configuration;

Seven production levels with values of produced gas, oil and water Table 5

Production level	Oil m^3/d	Gas Sm^3/d	Water m^3/d	Failed components
0	23,300	$3.0 \cdot 10^6$	7000	–
1	23,300	$0.9 \cdot 10^6$	7000	$TCa \vee TCb$
2	21,200	$2.7 \cdot 10^6$	0	$TGa \vee TGb$
3	21,200	$1.0 \cdot 10^6$	0	$TGa \wedge TCa \vee TGa \wedge TCb \vee TGb \wedge TCa \vee TGb \wedge TCb$
4	21,200	$2.6 \cdot 10^6$	6400	EC
5	21,200	$0.9 \cdot 10^6$	6400	$EC \wedge TCa \vee EC \wedge TCb$
6	0	0	0	$TEG \vee TCa \wedge TCb \vee TGa \wedge TGb$

Case A - conditions for an activation of repairing transitions Table 6

Messages		Conditions
Mess_TEG	=	? RA
Mess_EC	=	? $(RA \wedge TE_0 \wedge (\neg(TCa_2 \wedge TCb_2) \vee \neg(TGa_2 \wedge TGb_2)))$
Mess_TGa	=	? $((RA \wedge TE_0 \wedge TGb_2) \vee (RA \wedge TE_0 \wedge EC_0 \wedge \neg(TCa_2 \vee TCb_2)))$
Mess_TGb	=	? $((RA \wedge TE_0 \wedge TGa_2) \vee (RA \wedge TE_0 \wedge EC_0 \wedge \neg(TCa_2 \vee TCb_2)))$
Mess_TCa	=	? $((RA \wedge TE_0 \wedge TCb_2) \vee (RA \wedge TE_0 \wedge EC_0 \wedge \neg(TGa_2 \wedge TGb_2)))$
Mess_TCb	=	? $((RA \wedge TE_0 \wedge TCa_2) \vee (RA \wedge TE_0 \wedge EC_0 \wedge \neg(TGa_2 \wedge TGb_2)))$

Case A - the definition of seven production levels Table 7

Level	Conditions
0	$\neg TCa_2 \wedge \neg TCb_2 \wedge \neg TGa_2 \wedge \neg TGb_2 \wedge \neg EC_2 \wedge \neg TE_2$
1	$(TCa_2 \vee TCb_2) \wedge \neg TGa_2 \wedge \neg TGb_2 \wedge \neg EC_2 \wedge \neg TE_2$
2	$\neg TCa_2 \wedge \neg TCb_2 \wedge (TGa_2 \vee TGb_2) \wedge \neg EC_2 \wedge \neg TE_2$
3	$((TCa_2 \wedge TGa_2) \vee (TGa_2 \wedge TCb_2) \vee (TCa_2 \wedge TGb_2) \vee (TGb_2 \wedge TCb_2)$
4	$\neg TCa_2 \wedge \neg TCb_2 \wedge \neg TGa_2 \wedge \neg TGb_2 \wedge EC_2 \wedge \neg TE_2$
5	$((TCa_2 \vee TCb_2) \wedge \neg TGa_2 \wedge \neg TGb_2 \wedge EC_2 \wedge \neg TE_2$
6	$(TCa_2 \wedge TCb_2) \vee (TGa_2 \wedge TGb_2) \vee TE_2$

Case D. The components TG, TC and EC are preventively maintained with predefined policy in Table 4 and the third TG is added to the system model as a cold standby.

Physical analysis of the system detected that the system produces 6 different quantities of gas and 3 different quantities of oil and water. From the combination of these productions, it turns out that the plant can be in 7 different levels of production, one full and 6 reduced production levels as shown in Table 5.

Case A - system without preventive maintenance

The basic SPN model of the considered system comprises 6 components (TGa, TGb, TCa, TCb, TEG, EC) using a common repair team (RA). The messages of all transitions representing individual component repairs are defined in Table 6. The definitions of production levels of the plant are demonstrated in Table 7 for this case. Each definition determines a condition having to be fulfilled in the PN model of the system in order to be said that the plant is in a given production level. The full production level 0 is defined as a state when no tokens are in the places TCa2, TCb2, TGa2, TGb2, EC2 and TE2. In the initial, nominal state of the system, all components are functional (the tokens are in the places TCa0, TCb0, TGa0, TGb0, EC0 and TE0) and the maintenance team is waiting (RA=1).

Cases B, C and D

The SPN model of Case A was extended and modified by proper parts ensuring both preventive maintenance of selected components (B), and adding the third TG used in a cold standby configuration (C), as well as combination of B, C (Case D). Detailed SPN models for all the cases are described in [11].

4. Numerical results and discussion

Basic calculations of average availabilities were performed by MOCA-RP software [12]. The software allows the construction of PNs with advanced graphic interface, the net validation by tokens game and the evaluation of some basic availability characteristics by Monte Carlo simulation. The number of MC trials used in all the calculations is 10^5. The numerical results of the average availability of each production level for all the simulated cases are reported in Table 8. The results are given for the mission time $5 \cdot 10^5$ hours. The expected values of gas, oil and water production for all the cases are demonstrated in Table 9.

Case A – system without preventive maintenance

Basic configuration of the plant includes only the corrective maintenance. A computing time was 2 minutes on Pentium4@3.40GHz. The system is highly available (92.4%) at the full production level 0.

Case B – system with preventive maintenance

The computing time increased to 35 minutes. The system is highly available (90.3%) at the full production level 0. Figure 4 brings comparison between cases A and B. It clearly shows how the average availability of different production levels increased, when the preventive maintenance is applied. On the other hand, Table 9 shows that the preventive maintenance slightly decreases the production.

Comparison of the availability of the production levels in the four cases simulated Table 8

Production level	Average availability			
	Case A	Case B	Case C	Case D
0	$9.24 \cdot 10^{-1}$	$9.03 \cdot 10^{-1}$	$9.64 \cdot 10^{-1}$	$9.43 \cdot 10^{-1}$
1	$2.75 \cdot 10^{-2}$	$3.88 \cdot 10^{-2}$	$2.96 \cdot 10^{-2}$	$4.13 \cdot 10^{-2}$
2	$4.05 \cdot 10^{-2}$	$4.89 \cdot 10^{-2}$	$7.13 \cdot 10^{-4}$	$7.78 \cdot 10^{-4}$
3	$2.22 \cdot 10^{-3}$	$2.59 \cdot 10^{-3}$	$7.78 \cdot 10^{-5}$	$8.62 \cdot 10^{-5}$
4	$4.46 \cdot 10^{-3}$	$4.44 \cdot 10^{-3}$	$4.87 \cdot 10^{-3}$	$4.84 \cdot 10^{-3}$
5	$3.33 \cdot 10^{-4}$	$3.59 \cdot 10^{-4}$	$3.79 \cdot 10^{-4}$	$4.08 \cdot 10^{-4}$
6	$9.17 \cdot 10^{-4}$	$1.01 \cdot 10^{-3}$	$3.99 \cdot 10^{-4}$	$5.01 \cdot 10^{-4}$

Case C– system without preventive maintenance and with standby

Computing time was 40 minutes. The system is highly available (96.4%) at the full production level 0. Table 9 demonstrates that the presence of standby TG maximizes the production.

Case D – system with preventive maintenance and with standby

The computing time increased to almost 1.5 hours. The plant is highly available (94.3%) at the full production level 0. Seeing Table 9 the plant production capacity of D (as well as B) appears reduced with respect to the case of no preventive maintenance of C (A). Comparing B and D we can see the effect of the cold standby component under preventive maintenance - the standby component decreases the probability of no production level 6 to half.

Expected values of the gas, oil and water production Table 9

Case	Oil km^3/d	Gas kSm^3/d	Water m^3/d
A	23.19	2921.35	6693.60
B	23.15	2891.74	6626.86
C	23.28	2934.29	6990.27
D	23.06	2880.70	6921.94

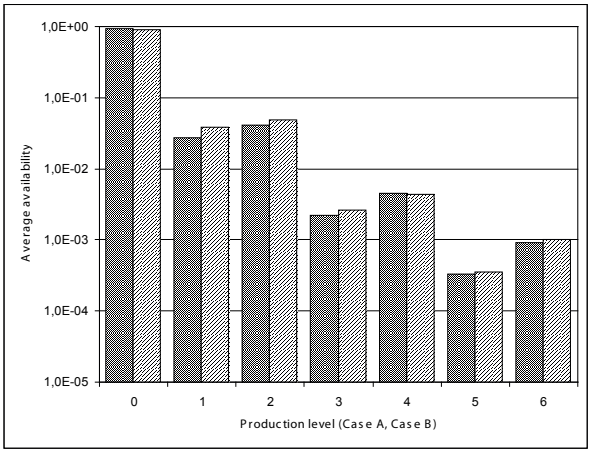

Fig. 4 Comparison of average plant availabilities over the mission time on the different production levels: case A and case B

5. Conclusions

This work focuses on the problem of the availability assessment of a multi-state, multi-output plant. A PN approach is used because it has proved to be an useful modeling tool for complex systems like offshore installation. One of PN advantages lies in the fact that they allow to integrate various deterministic and stochastic processes.

The numerical results presented in Section 4 are comparable with those published in [9] where the solution was based on minimal cut sets and MC simulation approach (only basic plant configuration, i.e. without extensions). On the basis of the results obtained from both these papers, the following conclusion may be formulated: both approaches may easily take into account very complex and realistic aspects of the system under consideration giving the comparable results.

Acknowledgement

This work was supported by the European Regional Development Fund in the IT4Innovations Centre of Excellence project (CZ.1.05/1.1.00/02.0070).

References

[1] LISNIANSKI, A., LEVITIN, G.: *Multi-State System Reliability. Assessment, Optimization, Applications.* World Scientific, 2003.

[2] TRIVEDI, K. S.: *Probability and Statistics with Reliability,* Queueing and Computer Science Applications. John Wiley & Sons, 2002.

[3] REISIG, W.: PETRI NETS: *An Introduction. EATCS, Monographs on Theoretical Computer Science*. Springer-Verlag, 1985.

[4] HAAS, P. J.: *Stochastic Petri Nets. Modelling, Stability, Simulation*. Springer-Verlag, 2002.

[5] MARSAN AJMONE, M., BALBO, G., CONTE, G., DONATELLI, S., FRANCESCHINIS, G.: *Modelling vith Generalized Stochastic Petri Nets*. John Wiley & Sons, 1995.

[6] GIRAULT, C., VALK, R. (Eds): *Petri Nets for Systems Engineering. A Guide to Modelling, Verification and Applications.* Springer-Verlag, 2001.

[7] SIGNORET, J. P., SAFERELNET: Production Availability Test Case Version 1. Document of TOTAL - DGEP/TDO/EXP/SRF 10-07, 2003.

[8] BERNARDI, S., BOBBIO, A., DONATELLI, S.: *Petri Nets and Dependability*. In: Lectures on Concurrency and Petri Nets, Reisig W. and Rozenberg G., Springer Verlag 2004; LNCS, Vol 3098: 125-79.

[9] ZIO, E., BARALDI, P., PATELLI, E.: Assessment of the Availability of an Offshore Installation by Monte Carlo Simulation. *Intern. J. of Pressure Vessels and Piping 2006*; 83(4):312–20.

[10] BRIS, R., KOCHANICKOVA, M.: *Stochastic Petri Net Approach to Production Availability and Maintenance Modelling of a Special Test Case*, Maintenance Modelling and Applications, Edited by John Andrews, Christophe Berenguer and Lisa Jackson, Chapter 10: Case Studies, pg 732-743, ISBN 978-82-515-0316-7, DNV 2011.

[11] BRIS, R.: Evaluation of the Production Availability of an Offshore Installation by Stochastic Petri Nets Modeling, Print ISBN: 978-1-4799-0923-0, DOI: 10.1109/DT.2013.6566303, pg 147 – 155, ©2013 IEEE, ISBN 978-1-4799-0922-3, IEEE Catalog Number CFP13CDT.

[12] Dessault Data Services. GRIF WorkShop-MOCA V12 Release 4.06.02 (2006). Software developed for TOTAL.

Michal Kvet - Karol Matiasko *

COLUMN LEVEL UNI-TEMPORAL DATA

The basic paradigm of conventional database systems is based on the current valid data processing. However, today's database systems should provide also management for historical and future valid data. Standard temporal model, using object level, stores the whole object data after the insert or update operation, although only some attributes changed their values. This paper deals with the principle of temporal data modelling based on the column level, not the whole object, describes the structure and principles of required methods, procedures, functions and triggers to provide functionality of the system. All designed and implemented solutions are compared with the existing solutions.

Keywords: *Conventional database, temporal database, column level temporal data, fully temporal model.*

1. Introduction

Database systems are one of the most important parts of the information technology. Almost certainly it can be said that a database system is the basic part, the root of any information system. The development of data processing has brought the need for modelling and accessing large structures based on the simplicity, reliability and speed of the system [1].

Most of the data in the database represent the current state, the data valid at this point. Properties and states of the objects evolve over the time, become invalid and are replaced by new ones. Once the state is changed, the corresponding data are updated in the database and it still contains only the current valid data. However, history management is very important in systems processing sensitive data; incorrect change would cause a great harm or in the systems requiring the possibility of restoring the previous states of the database. Therefore, it is necessary to store not only the current state, but also the previous states and progress. It can also help us to optimize processes or to make further decisions.

Historical data were saved using log files and archives in the recent past. Thus, the historical data could be obtained, but it is a complicated process, these data are in the raw form and handling them was difficult, lasted too much time. In addition, management requires quick and reliable access to data defined by any time point, but also getting information about the changes of the attributes in the future without significant time delays. However, the future valid data cannot be processed using mentioned methods at all.

The main disadvantage is the need of the administrator´s intervention (operation manager). An administrator must manage not only the running applications but also requirements for accessing historical backups. Decisions are based on historical data and the progress, so it was necessary to load historical backups to get the database snapshot at the historical time point. Operational decisions could not be based on the historical data because of the time consumption (sometimes even days to load all needed snapshots). In addition, the granularity of the data is still growing, so number of backup is above the acceptable level.

Nowadays, historical data management is easier than in the past, requires less processing time, but there is still need to make significant progress in temporal database processing research to create a complex module allowing to run existing applications without modifying source code and settings [2].

When managing temporal data, two aspects are considered to be most important. The aim is to provide the user easy and quickly manageable methods. The second criterion is the speed. We require the adequate processing time when managing historical and also future valid data. Last but not least, the requirement is based on the complex size of the database.

2. State of the art

Temporal databases define a new paradigm for selecting one or more rows based on the specified criteria, for projecting of one or more columns to the output sets and for joining the tables by

* **Michal Kvet, Karol Matiasko**
Department of Informatics, Faculty of Management Science and Informatics, University of Zilina, Slovakia
E-mail: Michal.Kvet@fri.uniza.sk

specifying relationship criteria. Rows with the different values of the primary key (*PK*) can represent one object at different times. Transactions for inserting, updating and deleting the rows must, therefore, specify not only the object itself, but also the processed period. If the valid time of the object is defined by a time interval, the transaction must include a time period - 2 time point values - begin and end timestamps (or other data structure based on the granularity, like the date). This means that the update query does not cause only update of existing data, but also insert of the new row based on the validity intervals [3, 4 and 5].

Row in a relational database table can be defined in three different ways using time (Fig. 1). *ID* is a unique identifier; *PK* refers to a primary key. *BD* and *ED1* is a pair of columns defining the beginning and end value of the period - validity, *BD2* and *ED2* defines the second time interval – transaction time. The first model does not use time for definition at all, it cannot provide management for non-current data in the main structure. This is a standard model used today, called the conventional model. The primary key is defined by the attribute *ID* (can be composite). All not key attributes in the table, regardless of their number, are merged into a common block called *data* [3, 4 and 6]. The uni-temporal system uses the composite primary key – object identifier and the time interval defining the validity state characterizing the row.

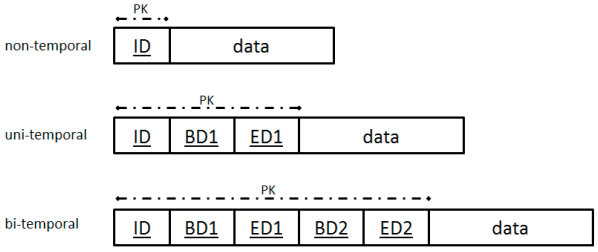

Fig. 1 Conventional and temporal table

This uni-temporal structure model thus allows defining the historical and also future valid data. However, the important factor for the time consumption and manipulation is the structure and its representation. Not all historical data are needed, if some attribute change monitoring is not important to us, we do not need to store it. In addition, a lot of duplicities are produced due to storing the whole rows, although only one attribute is going to be updated [4, 7 and 8].

Figure 2 shows the principle of data storing using the uni-temporal model. The interval is modelled using closed-open representation, which is, nowadays, the most often used method for time interval modelling. The other systems with open left side representation have problem with the definition of the begin validity time point. This method in comparison with the closed-closed representation does not have problem with changing granularity to smaller and does not need to update the table data to remove the undefined states. Ways of the modelling time intervals with the characteristics, features and principles for usage are described in [8].

ID	BD1	ED1	data
1	September 2012	September 2013	data1
2	January 2013	November 2014	data2
1	September 2013	December 2014	data11

Fig. 2 Uni-temporal table

The principle and importance of the bi-temporal data modelling is described in [8 and 9].

3. Uni-temporal model based on the begin time of the validity

Special type of uni-temporal system is a solution that contains only one time attribute that is part of the primary key. This

Tab_1_BD

ID	BD	data
1	Sep 2013	data
1	Dec 2013	data

1

Tab_1_BD_ED – *closed-closed interval*

ID	BD	ED	data
1	Sep 2013	Nov 2013	data
1	Dec 2013	*Dec 9999*	data

2

Tab_1_BD_ED – *closed-open interval*

ID	BD	ED	data
1	Sep 2013	Dec 2013	data
1	Dec 2013	*Dec 9999*	data

3

Fig. 3 Types of uni-temporal table modelling

means that any change of the corresponding object determines the validity of the prior state. The following Fig. 3 shows the representation of such a model, as well as corresponding standard uni-temporal system. The first part of the figure consists only of the definition of the begin time of the validity. The second one is a standard model with the closed-closed representation of the interval; the last consists of the model based on the closed-open representation.

The mentioned solution seems to be easy, but it does not address the fundamental problem of undefined states, the time intervals during which the state of the object is partially or completely undefined. We cannot easily replace the previous value with *NULL* value, because it can have special denotation. In addition, some attributes cannot have *NULL* value; it can be limited by the definition of the attribute column. The problem, however occurs, if even one attribute value is changed to the undefined state. The whole state of the object must be denoted as undefined or incorrect. It must be, therefore, possible to distinguish the condition of correctness and completeness of the object state. The easiest way is to delete this object from the database, because it cannot be referenced and even used for statistics and other manipulation. However, it would be necessary to remove the complete image of the object; the end date of the validity (new state determines the validity of the previous one) would be incorrect. If the state is no longer valid, history will not be stored. Thus, it will cause the temporal system degradation,. Object snapshots and images would disappear during the time. The question is easy, how to manage incorrect or incomplete states? Imagine the problem that only one attribute is unknown, for example, in industry caused by broken sensor or damaged cables.

One of the solutions is to add a flag representing the condition of the object state correctness. However, the problem is not solved completely. If one attribute value fails, the globalstate of the object is undefined. This is also the reason for defining the system based on the column level, where the whole state is a composition of the states of the temporal attributes.

4. Temporal column updating

Transformation of the conventional model to uni-temporal model on object level requires adding one or two attributes to extend the model with time validity. If there is a need to update the attribute, the whole state is modified and new one is inserted, thus, some attribute values are only copied to the new state because the values have not been changed. Moreover, some attributes do not need to be temporal, it is not necessary to monitor them or simply, they do not change their values over time. These values are still copied to the next image of the object. One of the solutions is based on a division of the original table. The first part contains non-temporal attributes, it is a classical conventional table, the second one is temporal, but it consists only of temporal columns – columns, which must be monitored and changes must be stored (Fig. 4). However, the problem is solved only partially, there is still problem with temporal columns which do not change their values in the time of update. This figure also shows the inefficiency of this system; if the number of temporal columns is high, the problem is more significant. Therefore, new system manipulating attributes not at object level must be developed.

Solution for temporal management should be universal, not only in terms of usability in practice, but also in terms of

ID	BD	$data_1$	$data_2$	...	$data_n$	non-temporal data
1	May 2012	A	B	C	X	data
1	Aug 2012	A_1	B	C	X	data
1	June 2013	A_1	B_1	C	X	data
1	Aug 2013	A_1	B_1	C_1	X_1	data

ID	BD	$data_1$	$data_2$	...	$data_n$
1	May 2012	A	B	C	X
1	Aug 2012	A_1	B	C	X
1	June 2013	A_1	B_1	C	X
1	Aug 2013	A_1	B_1	C_1	X_1

ID	non-temporal data
1	data
1	data
1	data
1	data

Fig. 4 Temporal table with non-temporal attributes

independence from the used database system. Creating new structures at the core level of the database system is, therefore, not appropriate. The basis of the proposed solution is to use existing resources and their combinations to create temporal solution. Moreover, it should be possible to be adapted into existing applications without the need of changing application programs.

The following Fig. 5 shows the developed and implemented structure. The existing program can continue to operate without any changes. The main part is to manage the table containing information about the changes of temporal columns. A column, whose changes need to be monitored, is temporal. If the value is changed, information about the update is stored in the developed

ID2	X	Y	Z
A	X_A	Y_A	Z_A
B	X_B	Y_B	Z_B
C	X_C	Y_C	Z_C

ID	Name	Surname	Street	Post_code	Birthdate
E	Ján	Veľký	Univerzitná	01026	1-1-1980
F	Anton	Liesko	Hlinská	12345	2-2-1968
G	Michal	Sused	Polná	97101	5-17-1993
H	Peter	Selko	Staničná	74523	1-26-1976

ID_change PK	ID_ previous_change	ID_tab NN	ID_orig NN	ID_column	ID_row	BD NN
1	NULL	1	A	NULL	NULL	11-1-2012
2	NULL	2	E	NULL	NULL	11-2-2012
3	NULL	2	F	NULL	NULL	11-3-2012
4	1	1	A	Z	11	11-4-2012
5	4	1	A	Z	12	11-5-2012
6	2	2	E	„street“	45	11-6-2012
7	6	2	E	„post_code“	37	11-7-2012
8	1	-1	A	NULL	NULL	11-8-2012
9	7	-2	E	NULL	NULL	11-9-2012

ID	Value
...	...
44	Školská
45	Mostná

ID	Value
...	...
36	34567
37	45678

ID	Value
...	...
11	Z_AA
12	Z_AAA

Fig. 5 Column level temporal system

temporal table and historical value is inserted into to the table containing historical values. Each temporal column has its own historical table.

The temporal table consists of the following attributes [7, 9 and 10] – see also Fig. 5:

- ID change
- *ID previous change* – references the last change of an object identified by *ID*. This attribute can also have *NULL* value which means the data have not been updated yet, so the data were inserted for the first time in past and are still current.
- *ID_tab* – references the table, record of which has been processed by DML statement (*INSERT*, *DELETE*, *UPDATE*).
- *ID_orig* - carries the information about the identifier of the row that has been changed.
- *ID_column*, *ID_row* – hold the referential information to the old value of attribute (if the DML statement was *UPDATE*). Only update statement of temporal column sets not null value.
- *BD* – the begin date of the new state of the object.

Figure 5 also shows the data representation and manipulation. The principles of the DML operations and related triggers source codes can be found in [7].

5. Future valid data definition

Data processing and data management valid in the future is also the requirement to the temporal system. Standard uni-temporal model does not have this problem; new data are inserted into the table which contains all the data about the objects during their life-cycle. The structure in Fig. 5 also allows managing future valid data. One of the easiest ways is based on the functionality *Job*, which allows you to plan data modelling operation to any time point in the future. It ensures the automatic update of the object state at defined time (*DBMS_SCHEDULER.CREATE_JOB*). Planning this event requires several parameters which are described in Fig. 6.

Create_job	
Job_name	Identifier of the job
Job_type	Type of the job (*plsql_block, stored_procedure, executable*)
Job_action	Statement
Start_date	Planned time to run the job
Repeat_interval	How often or when the job should be started
Enabled	The state of the job

Fig. 6 Job parameters

Information about the scheduled jobs is stored in the future table for each table consisting of one or more temporal columns. It has the same structure as the related conventional table, but it is extended by the operation (insert, delete, and update) and also by the identifier of the job. If the *Job* is executed, it provides deleting corresponding data from the future table, so this table contains only planned, but not executed jobs (Fig. 7).

Tab1_future			
job_name	Varchar2(10)	NN	(PK)
id_orig	Integer	NN	
operation	operation	NN	
x	Varchar2(30)		
y	Varchar2(30)		
z	Varchar2(30)		

Fig. 7 Structure of the future table

The method for executing the operation consists of the three parts (complete model is shown in Fig. 9):

- Productive table update *(insert, delete or update operation)* – Tab 1.
- *Insert into temporal_table* – it is provided using trigger.
- *Delete from the future table* – this table consists only of the planned, but not executed jobs.

However, there is much more principal complication of the future updates. The first problem is the process of dropping the related jobs if there is the incorrectly planned job – the values of the planned job are not correct, valid or simply, values do not correspond the future reality. Another problem is connected with the necessity of the jobs dropping based on the earlier update.. Suppose that there is a planned update of the object, but the system requires the earlier update (*T2*) of this object. The later planned (*T1*) job should be dropped. Another example is the need for replanning the job to another time.

7. Planned jobs management

Data about the planned *Jobs* can be found in the database system resources and tables. However, these data are raw and difficult to manipulate directly. Moreover, implemented system must dynamically react to any situation and request. Therefore, information about the planned jobs is stored in the related future tables (Figs. 7 and 9). Our implemented systems based on the column level were compared with each other and this presented model seems to be the most efficient [11]. Future table consists of the planned, but not executed jobs. However, planning the new job requires one more action, which has not been mentioned about yet, but it is expressed in Fig. 8. - the management of the jobs. If there is a request to change the object state (*insert*, *update*, *delete* operation), the system must search for any scheduled jobs based on this object. If there are some, the user is notified and must choose – retention or cancellation of the jobs - procedure ***drop_job_proc***.

```
create or replace procedure Job_proc(ID integer)
as
  cursor job_cur IS
    select job_name, id_orig, operation from Tab1_future where id_orig=ID;
    v_job_name varchar2(10);
begin
  open job_cur;
  loop
    fetch job_cur INTO v_job_name;
      if (job_cur%found) then drop_job_proc(v_job_name);
        else exit;
      end if;
  end loop;
end;
/
```

Fig. 8 Job management procedure

A complete structure of the fully temporal model can be seen in Fig. 9. The model consists of the classical non-temporal tables. Future data are stored in the future tables up to the execution or cancelling the process. The temporal table consists of the reference to historical values, so any state during the life-cycle can be reconstructed.

8. Experiments

The basis for the development of the new system is the performance compared with the existing systems to declare the characteristics, properties and limitations of the system. Our experiments and evaluations are based on the processing time, which, in our opinion, best represents the quality of the model. The second part contains the size of the model and related number of supplementary tables and structures. Figure 10 shows the experiment results based on the three models. The first model is the uni-temporal solution based on the object state management. The second one does not include the management for future valid data (Fig. 5). The last model is a complex fully temporal model with all the implemented structures and methods (Fig. 9).

ID2	X	Y	Z
A	X_A	Y_A	Z_A
B	X_B	Y_B	Z_B
C	X_C	Y_C	Z_C

Tab 1

ID2	Operation (I, U, D)	X	Y	Z	job_id
A	I	X_A	Y_A	Z_A	job_1
B	U	X_B	Y_B	Z_B	Job_2
C	D	X_C	Y_C	Z_C	Job_3

Tab 1 FUTURE

Temporal_table

ID_change PK	ID_ previous_change	ID_tab NN	ID_orig NN	ID_column	ID_row	BD NN
1	NULL	1	A	NULL	NULL	11-1-2012
2	NULL	2	E	NULL	NULL	11-2-2012
3	NULL	2	F	NULL	NULL	11-3-2012
4	1	1	A	Z	11	11-4-2012
5	4	1	A	Z	12	11-5-2012
6	2	2	E	„street“	45	11-6-2012
7	6	2	E	„post_code“	37	11-7-2012
8	1	-1	A	NULL	NULL	11-8-2012
9	7	-2	E	NULL	NULL	11-9-2012

ID	Value
...	...
44	Školská
45	Mostná

Fig. 9 Fully temporal model

	Uni-temporal system	Temporal table (historical data processing)	Temporal table (full – job info in future tables)
	MODEL 1	*MODEL 2*	*MODEL 3*
Type (level)	*Object*	*Column*	*Column*
Number of temporal columns	all	A <= all	A <= all
Number of conventional tables (containing temporal columns)	0	B	B
Number of temporal tables	B	1 (*developed*)	1 (*developed*)
Number of future tables	0	0	B
Number of historical tables	0	A	A
Size of the DB (kB)	41 235	18 093	18650
Time to get all actual data (current snapshot) (ms)	3921	931	931
Time to get all data during the life-cycle of one object (ms)	721	460	480

Fig. 10 Experiment results

The total number of records in the main structure is 100 000. The experiments were provided using the Oracle 11g database system. The experiment results can be divided into two categories which can be processed separately.

The first category evaluates temporal data. The second processed model deals with the temporal data, but only with historical data, which means, that there is no future table and possibility to manage these data using *Job*s. The third model can be considered as the extension of the second model using future valid data management.

The overall slowdown of the fully temporal structure (model 3) in comparison with model 2 is:

- **Size:** 3.08%.
- **Time to get current snapshot:** 0%.
- **Time to get all data during the life-cycle of one object:** 4.35%.

These results can be considered satisfactory. The increased requirement for the size of the structure is caused by the fully temporal system. The model 2 returns historical and current valid data, whereas the model 3 returns also future valid data.

The second category of experiments compares the temporal models based on the level. The first model is deals with the uni-temporal system on the object level. Each update causes the update of the whole object regardless of the number of the updated columns. All of the attributes in the application must be temporal. The model 3, which was developed by us, is based on the attribute – column level. Each state is, therefore, a merge of the data attribute values. Moreover, when some attribute data are not valid or are unknown, these columns are not processed, but the whole object can be considered valid or partially valid.

The overall acceleration of the developed system (model 3) in comparison with the standard uni-temporal system (model 1) is:

- **Size:** 54.77%.
- **Time to get current snapshot:** 76.25%.
- **Time to get all data during the life-cycle of one object:** 33.43%.

The developed system provides significantly better performance rate.

Overall results are influenced by the real number of temporal columns in comparison with the number of conventional attributes. However, in the most cases, it is not necessary to model systems with all temporal attributes..In the experiments, we used the system with one conventional and two temporal columns.

9. Conclusion

An object in the conventional database is represented by one row which expresses the current state of the object. However, developers nowadays require not only access to current valid data, but they also require having overview of properties, structures and values at any time point or time interval. Management of backups and log files is completely inappropriate, complicated and requires too much processing time. Temporal database brings possibilities and opportunities by adding time attributes limiting the validity and even transaction information. The aim is to store, monitor and evaluate information about all states of the objects during the life-cycle. Our system can store the information after the delete operation, if necessary.

Standard temporal database support is based on the object level; one row represents the whole state at a defined time point or time interval. However, our system is based on the column attribute level, the whole state is created by the grouping of the properties and states of the attributes. Critical factor for the new development is the processing time to get required reliable data. This paper deals with the principles and characteristics and describes implementation methods to provide the complex temporal data management. The developed system is compared with the existing structures based on the performance, the time to get required data as well as the size of the database and provides very good performance results.

Proposed methods and structure can be extended by the system processing transaction time.

The temporal data are usually large; the processing requires sophisticated access methods. In the future development, we will focus on the index structures creation, which should improve the performance of the model, too.

Acknowledgment

This publication is the result of the project implementation:

Centre of excellence for systems and services of intelligent transport II., ITMS 26220120050 supported by the Research & Development Operational Programme funded by the ERDF.

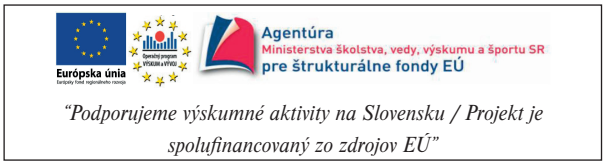

This work was partially supported by the project: ***Creating a new diagnostic algorithm for selected cancers***, ITMS project code: 26220220022 co-financed by the EU and the European Regional Development Fund.

The work is also supported by the project VEGA 1/1116/11 - ***Adaptive data distribution***.

References

[1] MATIASKO, K., VAJSOVA, M., ZABOVSKY, M., CHOCHLIK, M.: *Database systems*. EDIS, 2008. ISBN: 9788080708207

[2] DATE, C.: *Date on Database*. Apress, 2006. ISBN: 9781590597460

[3] JOHNSON, T., WEIS, R.: *Managing Time in Relational Databases.* Morgan Kaufmann, 2010. ISBN: 9780123750419

[4] SNODGRASS, R.: *Developing Time-Oriented Database Applications in SQL*. Morgan Kaufmann Publishers, San Francisco, 2000.

[5] KVET, M., LIESKOVSKY, A., MATIASKO, K.: *Uni-temporal and Bi-temporal Table*. IEEE Conference Digital Technologies 2013, Zilina, ISBN: 9781479909223.

[6] SNODGRASS, R.: *Developing Time-Oriented Database Applications in SQL*, Morgan Kaufmann, 1999. ISBN: 1558604367.

[7] KVET, M., MATIASKO, K.: *Temporal Data Management.* Conference IARIA ICCGI 2013, Nice, ISBN: 9781612082837

[8] KVET, M., LIESKOVSKY, A., MATIASKO, K.: *Temporal Data Modelling.* IEEE Conference ICCSE 2013, Colombo, 9781467344623

[9] KVET, M., MATIASKO, K.: *Conventional and Temporal Table – Temporal Table Model*. Conference ARSA, Zilina, 2012. ISBN: 9788055406060

[10] KVET, M., MATIASKO, K.: *Temporal Data Modeling – Future Valid Data Processing*. Conference DICTAP 2013, Ostrava, ISBN: 978989130609

[11] KVET, M., MATIASKO, K.: Management of Temporal System – Column Level. *Intern. J. of New Computer Architectures and their Applications*, vol. 3, No. 3, 2013. ISSN: 22209085.

Jaroslav Majernik - Jozef Zivcak *

INFLUENCE OF SINGLE WHOLE BODY VIBRATION TRAINING UNIT ON KINEMATICS OF HUMAN GAIT IN CHILDREN WITH NEUROLOGICAL DISORDERS

Utilisation of Whole body vibration (WBV) has been considered as a beneficial and powerful method to improve mobility and physical status of the patients during past decade. Benefits that were already published include enhanced muscular strength, power or bone density. However, there were also no significant effects reported in several clinical studies. The main aim of this pilot study was to investigate immediate effects of single WBV training unit on quality of gait kinematics in children patients suffering from neurological disorders. Five children (4.10 ± 1.75 years, 1 male and 4 females) were assessed before WBV exposure (10 minutes, 2 mm vertical vibrations, 30 Hz) and then 1 minute afterwards. Individual changes in gait parameters were analysed and the results indicated significant positive effects of WBV in two patients. Other two patients registered positive changes, but these changes were not statistically significant. One of the patients included in this pilot study registered worsening of gait symmetry.

Keywords: *Gait Analysis, whole-body vibration, rehabilitation.*

1. Introduction

Whole body vibration (WBV) represents a concept that was applied in several studies to confirm benefits for astronauts, athletes, and wellness of healthy population [1 - 3]. Positive results were obtained also in clinical studies in patients with various diseases [4 - 7]. WBV has been also studied for its dangerous effects on humans, especially when exposed as occupational vibration at high amplitudes and specific frequencies [8 - 10].

Recent clinical works suggest that low amplitude and low frequency of mechanical stimulation of the human body is a safe and effective way to exercise musculoskeletal structures [11]. The studies realized during past decade indicate that WBV may increase muscle strength, neuromuscular function, bone mass and mineral density [12], can be useful in improving physical capacity, cardiorespiratory functions, hormonal production, proprioception, and balance [13 - 14]. Despite of WBV positive effects presented in almost all related research studies, the authors interpret their results with caution. Also, the underlying mechanisms by which WBV enhance neuromuscular performance vary between studies and are still unclear. Inconsistency in presented results is caused by various training protocols and heterogeneity in study designs.

Because of both the positive and the negative effects of WBV on human body and its systems, it is important to consider all loading parameters that may affect WBV benefits. These parameters include type of vibration, frequency, amplitude, direction and exposure time, but also the position and activity of the subject on the WBV platform. The effect of vibration may be also tested using various modelling techniques [15 - 19].

The aim of this study was to investigate whether the single WBV session has any positive effects on gait kinematics in children patients. This was based on assumption that the WBV may stimulate muscle activation and that application of WBV will result in improvement of human gait quality.

2. Material and methods

A group of five children patients (age 4.10 ± 1.75 years, 1 male, 4 females) with hemiparesis or paraparesis of lower extremities were included in this pilot study. No of the patients had prior experience in WBV training. All patients and their parents or legal representatives were informed about the WBV training, tests to be realized and possible risks and benefits of the research. Prior to participation they gave written informed consent approved together with the study design by the local Ethics Committee.

All participants attended a familiarization session before the study was realized. No other physical treatment or intervention was realized at least 24 hour before WBV session. The anthropometric measures were also taken and registered in patients' experimental

* [1]Jaroslav Majernik, [2]Jozef Zivcak
[1]Department of Medical Informatics, Faculty of Medicine, Pavol Jozef Safarik University in Kosice, Slovakia, E-mail: jaroslav.majernik@upjs.sk
[2]Department of Biomedical Engineering and Measurement, Faculty of Mechanical Engineering, Technical University in Kosice, Slovakia

protocols. As for the aim of the study, the anthropometric characteristics of lower extremities were preferred, including thigh length (right: 21.80 ± 5.02 cm, left: 21.60 ± 4.88 cm), calf length (right: 23.80 ± 3.83 cm, left: 23.40 ± 3.63 cm) and foot length (right: 15.40 ± 0.89 cm, left: 15.20 ± 0.84 cm).

The experimental protocol was designed to discover potential immediate response of a single WBV training unit to the quality of gait kinematics in children patients. Training sessions were supervised by rehabilitation specialist and measurements as well as WBV sessions were conducted in the same thermally neutral room intended for physical training. All subjects did not engage in any therapeutic or rehabilitation procedures before testing.

The training session started with physical examination and short warming-up walk. Then, the patient's gait was captured and analysed before WBV exposure. Participants were asked to walk at their natural waking speed along the 6 m long path. After reaching the end point of the path, they were asked to turn back (180°), i.e. change the direction of gait, and to walk back to the starting point. Then, they turned back again and walked to the end point of the path, where the last turn back was realized and the patients finished walking in starting point of the path. In that sense, the subjects passed the length of walking path four times. WBV session followed one minute after this control gait was realized and captured. Here, each participant stood in static position on the vibration platform (VibroGym inSPORTline) with no shoes and socks and holding on the device handle. Erected posture with slightly bended knees was required during vibration test. The patients were asked to stop the training in the case of any pain responses to vibration. Duration of one WBV training unit was set to 10 minutes. Synchronous vertical stimulus with frequencies from 25 – 45 Hz and amplitude of 1 – 2 mm results in a significant increase in leg muscle activity as measured via electromyography. Therefore, the sinusoidal vertical vibration frequency was set to 30 Hz with amplitude of 2 mm. 1 minute rest interval followed after this WBV exposure. Then, the patient's gait was captured and analysed again.

Gait assessment was performed using our marker-free motion analysis system MAFRAN. Here, the patient's gait in sagittal plane is captured using any commercial video camera. Then, the raw record is used in the system to reconstruct motion trajectories of human body anatomical landmarks, i.e. the trajectories of all lower extremity joints and adjacent segments. These trajectories are consequently used to calculate other kinematical parameters for detailed description of patient's gait. Here analysed parameters include positions, velocities and accelerations of individual joints, hip flexion/extension, knee flexion/extension, and ankle plantar/dorsal flexion angles, gait cycle length, gait cycle time, gait cycle velocity, cadence (cycles per minute), stance phase and swing phase of the gait cycle.

All the parameters were analysed individually within the subject and then within the group of here included patients. The kinematical characteristics of the patients were evaluated as differences between right and left side. The hypothesis was based on assumption that these differences should be smaller after WBV training comparing values obtained before WBV training. Otherwise, the WBV will probably have no immediate benefits for gait kinematics. Statistical methods included descriptive statistics and Student's paired t-test and were used to ascertain specific and significant differences. The significance level was set to $P > 0.05$.

3. Results

All children patients accepted here realized WBV sessions very well. No one reported any pain or expressed any problems during WBV exposure. A first analysis was performed with anatomical joint angles of lower extremities in sagittal plane. Individually, no of the patients had the same curves of all tree

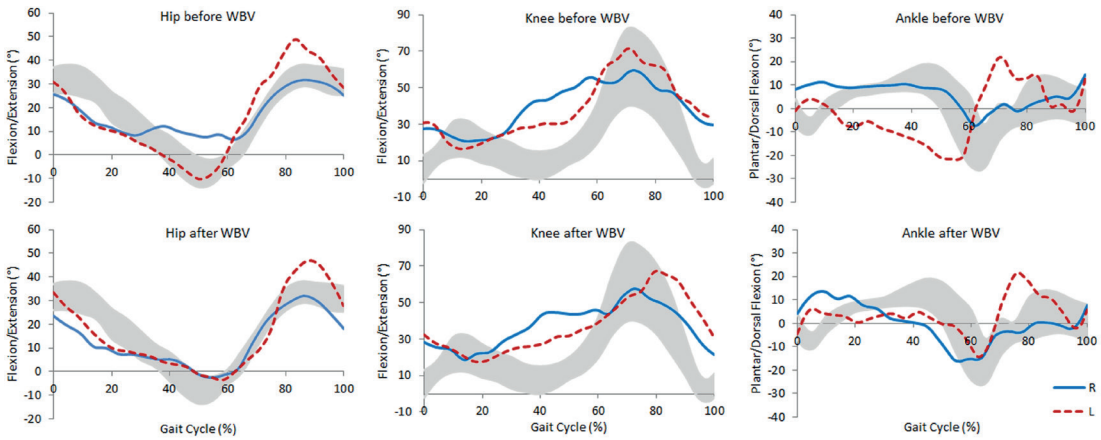

Fig. 1 Anatomical joint angles in 6 years old female patient with left paraparesis before and after WBV exposure (solid line – right leg, dashed line – left leg, greyed area – physiological gait values)

joints comparing before and after WBV values. At least one of the anatomical joint angles was changed either in positive or negative direction. An example of anatomical joint angles changes in 6 years old female patient with left paraparesis is shown in Fig. 1.

A paired t-test determined that the mean decrease of differences (M = -1.88, SD = 5.099, N = 51) was significantly greater than zero, t(50) = -2.63, two-tail p = 0.000 (95% CL = 1.434), providing evidence that the WBV was effective in reduction of differences between right and left hip flexion/extension angles. Knee flexion/extension angles of the same patient showed that the mean differences between right and left side before and after WBV were changed, but the mean decrease of differences (M = 2.17, SD = 8.213, N = 51) was not significantly greater than zero, t(50) = 1.89, two-tail p = 0.065 (95% CL = 2.310), providing evidence that the WBV was not effective in reduction of differences between right and left knee flexion/extension angle in this patient. The mean decrease of the right and the left side differences in ankle plantar/dorsal flexion angles of the same 6 years old female patient (M = 3.47, SD = 4.858, N = 51) was significantly greater than zero, t(50) = 5.10, two-tail p = 0.000 (95% CL = 1.366) provided evidence that the WBV was effective in reduction of differences between right and left ankle plantar/dorsal flexion angle.

Anatomical joint angles were analysed in all participants of this study in the same way. The summary of right and left side differences in anatomical joint angles in children patients showed that the most significant changes were registered in the ankle plantar/dorsal flexion angle (100.00%), followed by hip flexion/extension angle (80.00%) and knee flexion/extension angle (60.00 %). However, these significant changes include both the positive and the negative changes. The only significant positive changes were recognized in ankle plantar/dorsal flexion angle (80.00%), followed by the knee flexion/extension angle (60.00%) and hip flexion/extension angle (40.00%). Individually, there were two patients (40.00%) who had at least two significant positive changes of these kinematical parameters or they had no significant negative changes (subjects 1 and 4). Two patients (40.00%) had no beneficial improvements resulting from applied WBV exposure (subjects 2 and 3) and one (20.00%) of the children patients registered worsening because of no significantly positive or only significantly negative changes (subject 5).

The second analysis was performed in spatio-temporal parameters. Here, the symmetry of all characteristics was examined and summarized. The mean differences between right and left side and standard deviations of these parameters are listed in Table 1.

None of here analysed parameters had significantly either positive or negative changes. Nevertheless, some of the parameters had positive and another negative tendency. The positive trends were shown in decreasing differences between right and left side in gait cycle length (2.276 ± 9,837), velocity (0.008 ± 0.121) and cadence (0.416 ± 3.565). Gait cycle time remained almost unchanged (0.000 ± 0.057). Negative trends were registered in gait cycle phases (stance: -1.200 ± 3.626, swing -1.188 ± 3.630).

4. Conclusions

The effect of single WBV training unit was tested in the group of children patients with hemiparesis or paraparesis in lower extremities. The results of this pilot study proved that WBV influences kinematics of human gait. Significant improvements were also confirmed in some of the here analysed parameters. On the other hand, changes in anatomical joint angles and in spatio-temporal characteristics, even if not significant had both the positive and the negative trends. To confirm the long-term effect the individually planned training should be designed. First of all, this training should respect limitations given by patient's disease. Then, the amplitude, frequency, duration and repetition of WBV during training unit will be adopted to the particular patient. The usage of WBV in patients' therapy, especially in patients with neurological disorders, has to be managed by physicians to avoid serious injuries, physical harms and/or other health related damages.

Acknowledgements

Results presented in this work were obtained with the support of the national grant KEGA 005UPJS-4/2012.

Spatio-temporal characteristics of patients' gait obtained before and after WBV exposure (N=5) Table 1

	Pre	Post	Delta pre/post
GC length (cm)	8.560 ± 8.362	6.284 ± 4.595	2.276 ± 9,837
GC time (s)	0.088 ± 0.072	0.088 ± 0.018	0.000 ± 0.057
GC velocity (m/s)	0.112 ± 0.084	0.104 ± 0.043	0.008 ± 0.121
Cadence (GC/min)	7.258 ± 5.147	6.842 ± 2.945	0.416 ± 3.565
Stance phase (%)	2.784 ± 0.756	3.984 ± 2.983	-1.200 ± 3.626
Swing phase (%)	2.784 ± 0.756	3.972 ± 2.990	-1.188 ± 3.630

References

[1] CARDINALE, M., WAKELING, J.: Whole Body Vibration Exercise: Are Vibrations Good for You?", *Br J Sports Med*, 2005, vol. 39, pp. 585-589.

[2] PRISBY, R., D., LAFAGE-PROUST, M., MALAVAL, L., BELLI, A., VICO, L.: Effects of Whole Body Vibration on the Skeleton and other Organ Systems in Man and Animal Models: What we know and what we need to know, *Ageing Research Reviews*, vol. 7, 2008, pp. 319-329.

[3] MADOU, K. H., CRONIN, J. B.: The Effects of Whole Body Vibration on Physical and Physiological Capability in Special Populations, *Hong Kong Physiotherapy J.*, vol. 26, 2008, pp. 24-38.

[4] MILANESE, C., PISCITELLI, F., SIMONI, C., PUGLIARELLO, R., ZANCANARO, C.: Effects of Whole-body Vibration with or without Localized Radiofrequency on Anthropometry, Body Composition, and Motor Performance in Young Nonobese Women, *J. of Alternative and Complementary Medicine*, 2012, 18 (1), pp. 69-75.

[5] GLOECKL, R., HEINZELMANN, I., BAEUERLE, S., DAMM, E., SCHWEDHELM, A.-L., DIRIL, M., BUHROW, D., JERRENTRUP, A., KENN, K.: Effects of Whole Body Vibration in Patients with Chronic Obstructive Pulmonary Sisease - A Randomized Controlled Trial, *Resp. Medicine*, 2012, Vol. 106, pp. 75-83.

[6] Totosy de Zepetnek, J. O., Giangregorio, L. M., Craven, B. C., "Whole-body vibration as potential intervention for people with low bone mineral density and osteoporosis: A Review, *J. of Rehabilitation Research and Development*, vol. 46, No. 4, 2009, pp. 529-542.

[7] TORVINEN, S., KANNUS, P., SIEVANEN, H., JARVINEN, T. A. H., PASANEN, M., KONTULAINEN, S., JARVINEN, T. L. N., JARVINEN, M., OJA1, P., VUORI1, I.: Effect of Four-month Vertical Whole Body Vibration on Performance and Balance, *Medicine & Science in Sports & Exercise*, vol. 34, No. 9, 2002, pp. 1523-1528.

[8] SANTOS, B. R., LARIVIERE, CH., DELISLE, A., PLAMONDON, A., BOILEAU, P.-E., IMBEAU, D.: A Laboratory Study to Quantify the Biomechanical Responses to Whole-body Vibration: The Influence on Balance, Reflex response, Muscular activity and Fatigue, *Intern. J. of Industrial Ergonomics*, 38, 2008, pp. 626-639.

[9] MANI, R., MILOSAVLJEVIC, S., SULLIVAN, S. J.: The Effect of Occupational Whole-body Vibration on Standing Balance: A Systematic Review, *Int. J. of Industrial Ergonomics*, vol. 40, 2010, pp. 698-709.

[10] MAEDA, S., MANSFIELD, N. J, SHIBATA, N.: Evaluation of Subjective Responses to Whole-body Vibration Exposure: Effect of Frequency Content, Intern. J. of Industrial Ergonomics, vol. 38, 2008, pp. 509-515.

[11] ARTERO, E. G., ESPADA-FUENTES, J. C., ARGUELLES-CIENFUEGOS, J., ROMAN, A., GOMEZ-LOPEZ, P. J., GUTIERREZ, A.: Effect of Whole-body Vibration and Resistance Training on Knee Extensors Muscular Performance, European *J. of Applied Physiology*, 2012, 112 (4), pp. 1371-1378.

[12] SLATKOVSKA, L., ALIBHAI, S. M. H., BEYENE, J., HU, H., DEMARAS, A., CHEUNG, A. M.: Effect of 12 Months of Whole-body Vibration Therapy on Bone Density and Structure in Postmenopausal Women: A Randomized Trial, *Annals of Internal Medicine*, 2011, 155 (10), pp. 668-679.

[13] CLAERBOUT, M., GEBARA, B., ILSBROUKX, S., VERSCHUEREN, S., PEERS, K., VAN ASCH, P., FEYS, P.: Effects of 3 Weeks' Whole Body Vibration Training on Muscle Strength and Functional Mobility in Hospitalized Persons with Multiple Sclerosis, *Multiple Sclerosis*, 2012, 18 (4), pp. 498-505.

[14] PENHAKER, M., KASIK, V., HRVOLOVA, B.: Advanced Bilirubin Measurement by a Photometric Method, *Elektronika ir Elektrotechnika*, 2013, 19 (3), pp. 47-50.

[15] RAKHEJA, S., DONG, R. G., PATRA, S., BOILEAU, P.-E., MARCOTTE, P., WARREN, C.: Biodynamics of the Human Body under Whole-body Vibration: Synthesis of the Reported Data, *Intern. J. of Industrial Ergonomics*, 2010, vol. 40, pp. 710-732.

[16] MACUROVA, A., MACURA, D.: Jacobian of the Generalized C-hyperbolic Coordinates, *Intern. J. of Pure and Applied Mathematics*, 2009, 53 (4), pp. 563-569.

[17] PUSTKOVA, R., KUTALEK, F., PENHAKER, M., NOVAK, V.: *Measurement and Calculation of Cerebrospinal Fluid in Proportion to the Skull*, Proc. of 9th RoEduNet IEEE Intern. Conference, RoeduNet 2010, 2010, Article number 5541601, pp. 95-99.

[18] SAYENKO, D. G., MASANI, K., ALIZADEH-MEGHRAZI, M., POPOVIC, M. R., CRAVEN, B. C.: Acute Effects of Whole Body Vibration During Passive Standing on Soleus H-reflex in Subjects with and without Spinal Cord Injury, *Neuroscience Letters*, 482, 2010, pp. 66-70.

[19] ANDREJKOVA, J., SIMSIK, D., DOLNA, Z.: *An Experience from Testing an Ambient Intelligence, Devices for Household - Case Study*, SAMI 2010 - 8th Intern. Symposium on Applied Machine Intelligence and Informatics, Proc. 2010, Article number 5423717, pp. 283-286.

Sergey Stankevich - Vitaly Levashenko - Elena Zaitseva *

MULTISPECTRAL SATELLITE IMAGERY CLASSIFICATION USING A FUZZY DECISION TREE

A land cover classification system is very important nowadays for various remote sensing applications and many sectors of economy. Therefore, development of algorithms for multi- and hyperspectral imagery classification is an urgent task. In this paper we present a new efficient algorithm for multi- and hyperspectral imagery classification based on a fuzzy decision tree approach. Multispectral imagery spectral bands are used as fuzzy data source attributes and cumulative mutual information between them and the resulting fuzzy classification as a decision tree inducing criterion. The proposed algorithm ensures good classification accuracy.

Keywords: *Remote sensing, multispectral imagery classification, fuzzy decision trees, classification accuracy, spectral band selection.*

1. Introduction

A reliable land cover classification is the key data for a variety of remote sensing applications, such as natural resources prospecting, environmental management and geospatial planning [1]. The CORINE Land Cover (CLC) implementation over whole territory is a mandatory requirement for all countries of the European Union. In reality, land cover accuracy rarely achieves the commonly recommended 85% target [2].

In remote sensing image classification, useful information is determined by physical fields of landscape. Different classes have different spectral reflectance or self radiance. Multispectral imagery and hyperspectral imagery in particular provide more accurate registration of class spectra, which improves the accuracy of classification [3]. There are well known land cover classification methods. These methods are based on interpretation of multidimensional imagery by class identification features [4].

Modern satellite imagery processing includes different methods for supervised and unsupervised land cover classification. However, known algorithms developed during 1960s – 1980s on the basis of statistical or object-oriented paradigm do not provide the required classification accuracy without additional tweaks [5]. Such algorithms include the maximum likelihood (ML) classifier, k nearest neighbors (kNN) classifier, support vector machine (SVM), object-based image analysis (OBIA) [6].

The basic approach to classification of multispectral imagery is an optical signal in every pixel described as a discrete function $E(\lambda)$, $\lambda = 1, \ldots, m$ in a multidimensional spectral space $\Lambda = \{ \lambda \}$. It is obvious that the average classification accuracy of m-dimensional radiometric fields will increase asymptotically with the number of spectral samples m increment [7].

An important problem is the limited a priori knowledge of scene extrapolation to a detailed pixel-level classification. Usually it is performed by assigning a learning sample for each class. The classification theory requires a fundamental discriminability of classes in feature space, i. e., from a mathematical point of view, the probability density distribution should be a separable mixture of probability densities of the classes [8].

Known algorithms used in multispectral imagery classification evaluate some quantitative similarity of the current pixel with each of the defined classes. For classical statistical algorithms it is the class probability or the likelihood ratio, for other ones it is a more or less reasonable similarity measure [9].

Land surface remote imagery contains a significant fundamental stochasticity caused by variations in composition and material of objects observed, by temporal changes in imaging condition and radiation transfer environment and by sensor noises [10]. Therefore, a crisp data analysis for remote imagery classification is not always reasonable under such stochasticity. In some cases, better results can be obtained by fuzzy-logic processing.

This paper is structured as follows. Section 2 describes a fuzzy decision tree model implemented in remote sensing imagery classification. Section 3 presents two ways of processing algorithm for both multispectral (without dimensionality reduction) and hyperspectral imagery classification with the aforementioned model. Section 4 discusses preliminary results obtained from test

* [1]Sergey Stankevich, [2]Vitaly Levashenko, [2]Elena Zaitseva
[1]Scientific Centre for Aerospace Research of the Earth, Ukraine
[2]University of Zilina, Slovakia, E-mail: vitaly.levashenko@fri.uniza.sk

processing of actual multi- and hyperspectral satellite imagery. Section 5 presents conclusions drawn from this research.

2. Model

A fuzzy logic approach is quite suitable for multispectral imagery classification. A lot of fuzzy classification algorithms are commonly used in remote sensing, including fuzzy *c*-means (FCM), fuzzy *k* nearest neighbors (FNN), semi-supervised fuzzy cluster labeling (SFCL), and object-oriented fuzzy classifier (OOFC) [11]. However, all these algorithms are generalizations of the corresponding crisp statistical algorithms. These algorithms have inherited drawbacks in hyperspectral imagery classification. The major drawbacks include equalization of any quantitative estimations on high-dimensional data and computational instability.

In most cases of hyperspectral data processing, optimal selection of spectral bands is used. This reduces the strong information redundancy of hyperspectral imagery and enhances the overall informativity for the actual remote sensing application [12]. A fuzzy decision tree (FDT) is thus an ideal tool for hyperspectral data classification and simultaneous dimensionality reduction [13]. In terms of FDT, fuzzy data source attributes are spectral bands of a multispectral image, and an image classifying FDT is made using an information-theoretic approach. Up to now a simple unordered FDT is implemented in remote imagery classification. In this case, choice of the next fuzzy attribute depends on results of the previous attributes estimation [14 and 15].

The next spectral band B_{j+1} is selected for each branch of the FDT, providing the maximum amount of information about the target fuzzy classification $C = \{ C_i \}$, $i = 1, ..., n$, at minimal cost using the already known sequence of previous spectral bands B_j, $j = 1, ..., m$ estimates. The amount of such information $I(C; B_1, ..., B_m)$ is a cumulative mutual information between the resulting fuzzy attribute and the source ones. A number of spectral bands already selected can be used as the cost. The band selection criterion then takes the following form

$$\frac{I(C;B_1,...,B_m)}{m} \rightarrow \max. \quad (1)$$

Cumulative mutual information in (1) is calculated according to the rule [15]:

$$I(C; B_1, ..., B_m) = I(C) + I(B_1, ..., B_m) - I(C, B_1, ..., B_m), \quad (2)$$

where $I(C, B_1, ..., B_m)$ is cumulative joint information of fuzzy attributes which is expressed by the equation

$$I(B_1,...,B_m) = \log_2 m \times n - \log_2 \sum_{j=1}^{m} \prod_{k=1}^{w} \mu(B_1), \quad (3)$$

where $\mu_k(B_j)$ is the k-th value of the membership function of fuzzy attribute B_j, w is the number of possible values in a support set of B_j attribute.

For spectral bands attributes of multispectral imagery, the support set is just a gradation range of the registered signal in each band, usually uniform over the entire image. The defined (1) criterion provides a recurrent selection of the spectral band that contains the most information about the target classes. To avoid exhaustive search of all spectral bands, growth of the tree should be limited by pruning low-information branches.

3. Algorithm

Practical implementation of the proposed model in classification of remote sensing images should be performed in two ways. For a small number of spectral bands (multispectral image case), all of them are quite informative. For a sufficiently large number of spectral bands (hyperspectral image case) a fully-featured decision tree is built with branch pruning. A decision tree node is transformed into a leaf node, if the relative frequency of any solution alternative solution exceeds some a priori specified level β:

$$2^{-1(C|B_1,...,B_m)} \geq \beta, \quad (4)$$

where $I(C \mid B_1, ..., B_m)$ is cumulative conditional information of decision C with known values of fuzzy attributes $B_1, ..., B_m$. This variable can be calculated as

$$I(C \mid B_1, ..., B_m) = I(C, B_1, ..., B_m) - I(C), \quad (5)$$

where $I(C, B_1, ..., B_m)$ determined by the (3) and

$$I(C) = \log_2 m \times n - \log_2 \sum_{i=1}^{n} \mu(C_i).$$

An important stage of algorithm is to bring the source multispectral crisp data into fuzzy form required for FDT operations. In remote sensing, Gaussian distribution functions are usually used for this purpose [16], but in our research histogram-based membership functions in spectral bands were formed. The distributions obtained are smoothed by sliding Gaussian window. As to pixel fuzzification, it was carried out within the Gaussian-weighting two-dimensional window. This incorporates some positive properties of OBIA into the image classification result [17].

The computation takes into account the distribution of possible states of input fuzzy attributes with different membership degrees. A certain weighting factor, which is associated with tree branches up to the current leaf node, was assigned to each spectral band. Similarly, the output image classification contains the membership function values also for all allowable classes. To obtain a crisp (hard) classification, the class with the maximum value of the output membership function must be selected.

4. Results and discussion

The developed algorithm for remote sensing imagery classification using FDT was applied to test land cover classification on real satellite images. All data processing procedures have been coded and debugged with a Free Pascal compiler. All the source DN-data bands of satellite images calibrated through values of radiance at sensor are converted into land surface spectral reflectance to avoid the influence of solar irradiance and atmosphere.

a

b

c

Fig. 1 Sich-2/MSU multispectral satellite image classification
a – source color-composite (0.645, 0.835 and 0.555 μm bands) image, b – ML classification result, c – FDT classification result

The first type of processing (ranking bands only) was applied to the Sich-2/MSU multispectral 3-bands satellite image fragment (Crimea, Ukraine, November 8, 2011, see Fig. 1a). Supervised classification was performed using FDT. Also a conventional crisp classification using the ML method was carried out as reference. The outputs are shown in Fig. 1b and 1c.

A full-featured processing (a limited FDT with branch pruning) was done over the EO-1/Hyperion hyperspectral 220-bands satellite image fragment (Kiev suburb, Ukraine, March 17, 2012, see Fig. 3a). In the source full-band hyperspectral image, 78 of 220 spectral bands with a better signal-to-noise ratio were preselected for further analysis. A fuzzy decision tree was formed in the first stage of the algorithm, as shown in Fig. 2.

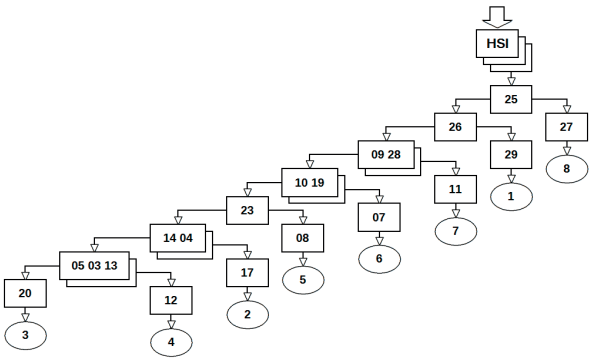

Fig. 2 Fuzzy decision tree for a test hyperspectral satellite image classification

In Fig. 2, decision nodes with codes of evaluating spectral bands are presented as rectangles, and leaf nodes with class numbers are presented as ovals. It is clear that another decision tree will be induced for another hyperspectral image (HSI) or for other classes composition.

The result of the FDT supervised classification is given in Fig. 3c. A spectral angle mapper (SAM) classification was used as a reference (see Fig. 3b) because the generic ML classifier is inoperable over high-dimensional data due to covariance matrices singularization.

Analysis of the classification results leads us to conclude that the FDT algorithm provides a better classification in general. In the Sich-2/MSU multispectral image, arable lands are classified more accurately, sand and concrete are discriminated better, but water surface is identified with less confidence. Even if ground-based validation of test images is not carried out, visual assessment using high-resolution imagery can roughly estimate classification accuracy of 75% for the ML algorithm and 80% for the FDT one. In SAM-based classification of the EO-1/Hyperion hyperspectral test image, a substantial percentage of the land cover was incorrectly classified as water. Correct classification was not observed in the vicinity of high spectral reflectance areas (snow). Artificial cover was falsely detected among deep woodlands, etc. A classification accuracy was estimated as 65% for the SAM algorithm and as 75% for the FDT algorithm. In

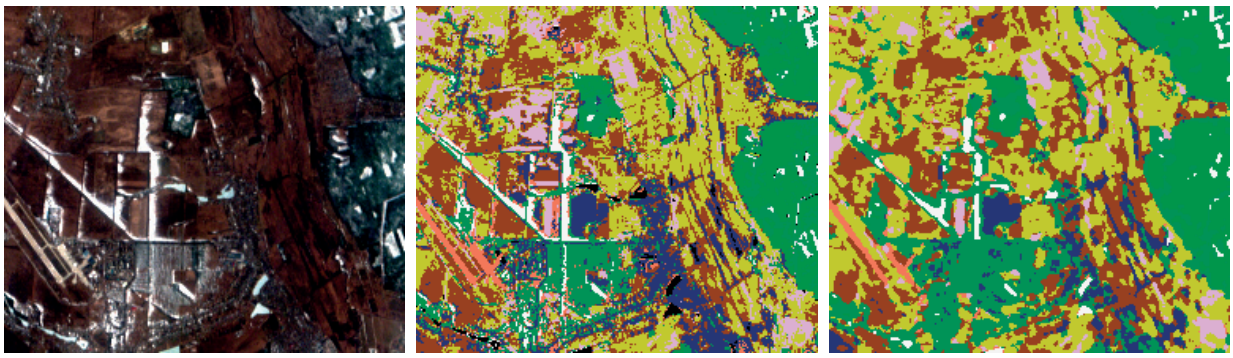

a *b* *c*

Fig. 3 EO-1/Hyperion hyperspectral satellite image classification
a – source color-composite (793, 671 and 579 nm bands) image, b – SAM classification result, c – FDT classification result

addition, the number of spectral bands selected for processing was reduced from 78 to 20, which would significantly cut down computation costs without any degradation in classification accuracy. A decrease in classification accuracy in comparison with a multispectral image can be most likely explained by low spatial resolution of the hyperspectral image. No serious misclassification effect intrinsically inherent in the traditional pixel-based classification has been found in the FDT-classified images.

5. Conclusions

A new algorithm for remote sensing multi- and hyperspectral imagery classification based on a fuzzy decision tree approach has been developed. In some cases, this algorithm provides more exact classification accuracy than traditional ones, approximately by 5-10%. In addition, a significant reduction of data dimensionality (more than 3.5-fold) for hyperspectral imagery processing is ensured by informative spectral bands selection using branch pruning of the decision tree. A proper and productive reduction in data dimensionality is very important for large-scale high-performance practical analysis of remote sensing hyperspectral imagery. The results obtained are supported preliminary by experiments in test processing and analysis of actual multi- and hyperspectral satellite imagery.

The problem of achieving the required performance of the developed algorithms and demonstration software modules has not been solved yet. This can be seen in problems with difficult processing of large-size imagery. Moreover, positive results obtained previously must be validated through in situ observations.

We look forward to continue our joint research in improving models for FDT-based remote sensing image classification, in particular by implementation of more sophisticated decision strategies and new remote sensing application-oriented informativity metrics entering into the algorithms.

Acknowledgements

This research was supported by the Slovak Academic Information Agency under the National Scholarship Programme of the Slovak Republic approved by the Government of the Slovak Republic. The authors would like to thank the Faculty of Management Science and Informatics of the University of Zilina for the opportunity to carry out this study and for the constructive discussion on the results obtained.

References

[1] *Multispectral Remote Sensing in Nature Management (in Ukrainian).* LYALKO V.I., POPOV M. O. (Eds). Naukova Dumka, 2006.
[2] BRODSKY, L., BUSHUEV, E., VOLOSHIN, V., KOZLOVA, A., PARSHINA, O., POPOV, M., SABLINA, V., SAKHATSKY, A., SIROTENKO, A., SOUKUP, T., STANKEVICH, S., TARARIKO, A.: The INTAS Project for the Elaboration of Automated Technology of Land Cover Classification: The Scientific Problems, Main Results and Prospects (in Russian). *Space Science and Technology*, 2009, 15(2):36-48.
[3] LU, D., WENG, Q.: A survey of Image Classification Methods and Techniques for Improving Classification Performance. *Intern. J. of Remote Sensing,* 2007, 28(5):823-870.

[4] DUDA, T., CANTY, M.: Unsupervised Classification of Satellite Imagery: Choosing a Good Algorithm. *Intern. J. of Remote Sensing*, 2002, 23(11):2193-2212.
[5] POPOV, M.A., STANKEVICH, S. A., SAKHATSKY, A. I., KOZLOVA, A. A.: *Multispectral Imagery Normalized Band-difference Indexes for Land Cover Classification.* Proc. of Digital Earth Summit on Geoinformatics (DE'08): Tools for Global Change Research, Potsdam, 2008:333-338.
[6] TSO, B., MATHER, P. M.: Classification Methods for Remotely Sensed Data. Taylor & Francis, 2004.
[7] HO, T. K., BAIRD, H. S.: Large-scale Simulation Studies in Image Pattern Recognition. *IEEE Transactions on Pattern Analysis and Machine Intelligence*, 1997, 19(10):1067-1079.
[8] FUKUNAGA, K.: *Introduction to Statistical Pattern Recognition.* Academic Press, 1990.
[9] CHA, S.-H.: Comprehensive Survey on Distance/similarity Measures between Probability Density Functions. *Intern. J. of Mathematical Models and Methods in Applied Sciences*, 2007, 1(4):300-307.
[10] WOODCOCK, C. E.: *Uncertainty in Remote Sensing, in Uncertainty Remote Sensing and GIS*. FOODY G.M., ATKINSON P.M. (Eds). John Wiley, 2006:19-24.
[11] CHEN, W., JI, M.: *Comparative Analysis of Fuzzy Approaches to Remote Sensing Image Classification*. Proc. of 7th Intern. Conference on Fuzzy Systems and Knowledge Discovery (FSKD'10), Yantai, 2010:537-541.
[12] STANKEVICH, S. A.: *Quantitative Estimation of Hyperspectral Imagery Informativity for the Remote Sensing Applications (in Ukrainian).* Proc. of NAS of Ukraine, 2006, 10:53-58.
[13] LEVASHENKO, V., ZAITSEVA, E., PUURONEN, S.: *Fuzzy Classifier Based on Fuzzy Decision Tree.* Proc. of the IEEE Intern. Conference Computer as a Tool (Eurocon'07), Warsaw, 2007:823-827.
[14] LEVASHENKO, V., ZAITSEVA, E.: *Fuzzy Decision Trees in Medical Decision Making Support System*. Proc. of the IEEE Federated Conference on Computer Science and Information Systems (FedCSIS), Szczecin, 2012, 213-219.
[15] STANKEVICH, S., LEVASHENKO, V., ZAITSEVA. E.: *Fuzzy Decision Tree Model Adaptation to Multi- and Hyperspectral Imagery Supervised Classification.* Proc. of the IEEE Intern. Conference on Digital Technologies, Zilina, 2013, 198-202.
[16] NEDELJKOVIC, I.: *Image Classification Based on Fuzzy Logic.* The Intern. Archives of the Photogrammetry, Remote Sensing and Spatial Information Sciences, 2004, 34(XXX):83-88.
[17] GOMEZ, D., MONTERO, J.: Fuzzy Sets in Remote Sensing Classification. *Soft Computing*, 2008, 12(3):243-249.

Jozef Kostolny - Miroslav Kvassay - Stefan Kovalik *

RELIABILITY ANALYSIS OF NONCOHERENT SYSTEMS BY LOGICAL DIFFERENTIAL CALCULUS AND BINARY DECISION DIAGRAMS

Reliability is the important characteristic of systems. Most of the systems consist of more than one component. Moreover, modern systems are very complex and they include a lot of components. Therefore, effective methods have to be developed for analysis of these systems. The techniques that have been already considered for this purpose are the Binary Decision Diagrams and the Logical Differential Calculus. However, these methods have been considered only for the coherent systems. In this paper, their use in the reliability analysis of the noncoherent systems is considered.

Keywords: *Noncoherent system, binary decision diagram, direct partial logic derivative, importance analysis, strucutral importance measure.*

1. Introduction

Reliability is one of the basic characteristics of many real systems. During the last decades, there has raised the necessity of reliability analysis of very complex systems [1]. These systems contain a huge amount of components and so there exist some difficulties in analyzing of these systems. One of possible ways to decide this problem is to use special methods and algorithms for processing of large dimension data. Authors of the paper [2] considered for reliability analysis of systems such approach that is named as the Binary Decision Diagram (BDD). The BDD has been developed for the effective representation of the Boolean functions [3], but they can be also used for the structure function [4], which is used in the reliability analysis to express the correlation between the states of the system components and the state of the whole system.

The suitability of using the BDD for the representation of the structure function results from the fact that the definition of the structure function is formally equivalent with the definition of the Boolean function [5]. This fact allows using the tools for the analyzing of the Boolean functions. The Logical Differential Calculus is one of the techniques that can be also used in the special part of the reliability analysis, which is known as the Importance Analysis [4]. The principal goal of this part of the reliability analysis is to identify the components of the system that are more critical for the proper functioning of the analyzed system [6]. For this purpose, there exist some measures that are known as Importance Measures.

The most attention in the reliability is addressed to the coherent systems, which are characterized by the fact that the failure of the system can be caused only by the failure of the system component, i.e. not by the repair of the component. However, there exist some real systems that do not meet this assumption [7]. These systems are known as the noncoherent systems. Some techniques for the evaluation of the reliability and for the Importance Analysis of these systems have been considered in papers [8 - 11]. In this paper, the new techniques for the analysis of noncoherent systems using the BDD and the Logical Differential Calculus are suggested.

This paper has the following structure. The section II contains the concept of the system structure function and noncoherent systems, the usefulness of the Logical Differential Calculus in the reliability analysis and the use of the BDD for the representation of the structure function. In the section III, the evaluation of the system reliability of the noncoherent system is considered using the BDD. Finally, the ideas of the Importance Analysis of the noncoherent systems are presented in the section IV. Using the Logical Differential Calculus, the universal definition of the Structural Importance Measure for the noncoherent system and

* **Jozef Kostolny, Miroslav Kvassay, Stefan Kovalik**
Department of Informatics, Faculty of Management Science and Informatics, University of Zilina, Slovakia
E-mail: jozef.kostolny@fri.uniza.sk

the algorithm for its calculation from the BDD of the structure function is developed in this section too.

2. Mathematical Background

A. The Structure Function

Consider the system of n components. Every component can be in one of two states: failed (it is 0) and functional (it is 1). The state of the whole system depends on the states of its components. Define the state of the i-th system component as x_i, for $i = 1,..., n$. Then, the system state can be described mathematically by the structure function [5]:

$$\phi(x_1, x_2, ..., x_n) = \phi(\boldsymbol{x}) : \{0,1\}^n \to \{0,1\}, \quad (1)$$

where $\boldsymbol{x} = (x_1,..., x_n)$ denotes the vector of states of the system components. The structure function describes the topological dependencies between individual components and therefore, it can be used only for the system reliability analysis from the topological point of view. The reliabilities of individual components must be known to analyze the real (not only topological) reliability of the whole system. Because of that, every component is characterized by probabilities of functional and failed state:

$$p_i = \Pr\{x_i = 1\}, q_i = \Pr\{x_i = 0\}, p_i + q_1 = 1, \quad i = 1, 2, ..., n. \quad (2)$$

The probability p_i represents the reliability of component i, while the probability q_i represents its unreliability.

B. Coherent and Noncoherent Systems

According to the properties of the structure function (1), there exist two different types of systems: coherent and noncoherent systems. The coherent system has the following properties [5]:

(i) every component is relevant; i.e. for every component there exist at least one situation, in which the change of the component state results in the change of the system state:

$$\forall i \in \{1, 2, ..., n\} \exists (1_i, \boldsymbol{x}) : \phi(1_i, \boldsymbol{x}) \neq \phi(0_i, \boldsymbol{x}),$$

where $(a_i, \boldsymbol{x}) = (x_1, x_2,..., a_i,..., x_n)$, for $a \in [0, 1]$,

(ii) the structure function is non-decreasing; i.e. the failure of any functional component must not cause the repair of the failed system and the repair of any failed component must not result into the repair of the system:

$$\forall i \in \{1, 2, ..., n\} \forall (1_i, \boldsymbol{x}) : \phi(1_i, \boldsymbol{x}) \neq \phi(0_i, \boldsymbol{x}).$$

The noncoherent system does not meet at least one of the assumptions (i) and (ii). Specially, if only assumption (i) is not satisfied, then the system is identified as a monotone or semicoherent system [12].

Most of the systems that are studied in reliability engineering are coherent. However, there exist some real systems that do not satisfy the property (i) or (ii). The typical systems, which are noncoherent, because they do not meet the assumption (ii), are k-to-l-out-of-n systems, which real examples in multiprocessor and transportation systems are given in paper [7]. These systems are functional if and only if at least k but not more than l components are working. Other examples of the noncoherent systems have been presented in papers [8] and [10], in which the reliability of liquid-level control-system and gas-detection system has been analyzed.

C. The Logical Differential Calculus in the Reliability Analysis

The formal definition of the structure function (1) is identical with the definition of the Boolean function. Therefore, the tools of the Boolean logic and Boolean algebra can be used for the reliability analysis, based on the structure function. One of such tools is the Logical Differential Calculus [13], which allows the investigation of the change of the value of the Boolean function caused by the change of the value of the Boolean variable. In the reliability engineering, the structure function and the system components are used instead of the Boolean function and the Boolean variables. Therefore, the Logical Differential Calculus can be used for the analysis of the influence of the change of the system component state on the system state. The application of this technique for the coherent systems is considered in paper [5].

The Direct Partial Logic Derivative (DPLD) is the tool of the Logical Differential Calculus, which can be used in the reliability analysis [5]. The DPLD $\partial\phi(j \to \bar{j})/\partial x_i(a \to \bar{a})$ of a Boolean function $\partial\phi(\boldsymbol{x})$ of n variables with respect to variable x_i reflects the fact of changing the function from j to $\bar{j}$ when the value of variable x_i changes from a to $\bar{a}$ [5]:

$$\partial\phi(j \to \bar{j})/\partial x_i(a \to \bar{a}) = \{\phi(a_i, \boldsymbol{x}) \sim j\} \wedge \{\phi(\bar{a}_i, \boldsymbol{x}) \sim \bar{j}\}, \quad (3)$$

where $a, j \in \{0, 1\}$ and ~ is the symbol of the equivalence operation.

The definition (3) implies that there exist 4 different DPLDs for one variable, which have the following properties [5]:

$$\partial\phi(1 \to 0)/\partial x_i(1 \to 0) = \partial\phi(0 \to 1)/\partial x_i(0 \to 1), \quad (4)$$

$$\partial\phi(1 \to 0)/\partial x_i(1 \to 0) = \partial\phi(0 \to 1)/\partial x_i(1 \to 0). \quad (5)$$

In the reliability analysis, the DPLDs $\partial\phi(1 \to 0)/\partial x_i(1 \to 0)$ and $\partial\phi(0 \to 1)/\partial x_i(1 \to 0)$ model the influence of the component's failure on the system state, while the DPLDs $\partial\phi(0 \to 1)/\partial x_i(0 \to 1)$ and $\partial\phi(1 \to 0)/\partial x_i(0 \to 1)$ model the consequence of the component's repair. Therefore, the DPLDs

permit to determine boundary states, i.e. situations, in which the failure or repair of the component results in the change of the system state.

The property (ii) of the coherent system implies that the coherent system meets the following assumption [5]:

$$\partial\phi(1 \to 0)/\partial x_i(1 \to 0) = 0$$
$$\text{and } \partial\phi(0 \to 1)/\partial x_i(0 \to 1) = 0.$$

The consequence of this assumption is that only two DPLDs have to be considered in the case of the analysis of the coherent system. However, the noncoherent systems do not satisfy this assumption and, therefore, all DPLDs have to be analyzed.

D. The Binary Decision Diagram for the Representation of the Structure Function

The structure function can be represented in several ways, for example, algebraically (the expression in the terms of the Boolean algebra), tabular (the decision table) and graphically. The BDD is one of graphic forms that are very common [2]. The BDD allows implementation of new algorithms for reliability quantification that are efficient in terms of computational time and accuracy [2].

The construction of the BDD is based on a disjoint decomposition of the Boolean function, which is known as the Shannon expansion [3]. In the terms of the structure function (1), this expansion can be defined as:

$$\phi(\boldsymbol{x}) = x_i\phi(1_i,\boldsymbol{x}) \vee \overline{x}_i\phi(0_i,\boldsymbol{x}). \tag{6}$$

The BDD is a directed acyclic graph for representation of the Boolean function. It has two sink nodes, labeled by 0 and 1, which represent two different values (false and true) of the Boolean function. Each non-sink node is labeled with some variable of the Boolean function and has two outgoing edges, labeled by 0 and 1, which represent the possible values (false and true) of the variable. The BDD has just one source node, which has the same properties as other non-sink nodes. All paths from the source node to the 0-sink node represent all variables assignments, for which the Boolean function has false value and all paths from the source node to the 1-sink node represent all situations, for which the function is true [3].

In the terms of the reliability analysis, the sink nodes of the BDD present the possible states of the system (failure and functioning). The non-sink node represents a system component. The 0-edge, which leaves the non-sink node, agrees with the fail of the component, while the 1-edge represents the operation state of the component [2]. A path from the source node to the 0-sink node coincide with one or more situations, in which the system is failed, and a path to the 1-sink represent one or more cases, in which the system is operational.

For example, consider the liquid-level control-system (Fig. 1), which is studied in papers [8] and [10]. This system consists of three relevant components: the pump, the level controller and the level sensor. Also, there are two components, which are irrelevant from the point of view of the reliability analysis: the vessel and the control valve, which never fails. This system is defined in paper [8]: "*The pump feeds liquid to the vessel. If the liquid level in the vessel exceeds a specified level, the level sensor sends to the level controller the signal "liquid level in the vessel is high." Upon receiving the signal, the level controller sends a command to the control valve to increase the output flow. The system failure is defined as the situation, when the liquid level in the vessel is higher than specified. The following assumptions are taken:*

1. *The pump feeds either normal* (x_1 = 1)*, or too much liquid* (x_1 = 0).
2. *The level sensor is functional* (x_3 = 1)*, or it generates a spurious signal indicating that "liquid level in the vessel is low" even if the liquid level is actually not low* (x_3= 0).
3. *The level controller either fails to respond to any signal from the level sensor (no action is taken by the control valve)* (x_2 = 0)*, or responds correctly to the signal from the level sensor (the correct control command is sent to the control valve)* (x_2 = 1)*."*

The structure function of this system is defined as follows:

$$\phi(\boldsymbol{x}) = (x_1 \wedge x_2) \vee (x_2 \wedge x_3) \vee (x_1 \wedge \overline{x}_3). \tag{8}$$

The values of the unreliability of the system components are in Table 1 and the BDD of this system is presented in Fig. 1.

The unreliability of the system components — Table 1

Component	q_i
x_1	$9.90099\text{x}10^{-3}$
x_2	$7.40740\text{x}10^{-2}$
x_3	$1.52534\text{x}10^{-1}$

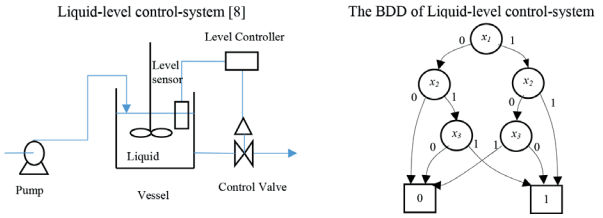

Fig. 1 Liquid-level control-system and its BDD

3. The System Reliability

The system reliability is defined with respect to the structure function (1) as the probability, that system is functional [5]:

$$R = \Pr\{\phi(\boldsymbol{x}) = 1\}. \tag{7}$$

According to this methodology, the system unreliability is defined as follows [5]:

$$F = \Pr\{\phi(\boldsymbol{x}) = 0\} = 1 - R. \tag{8}$$

The definitions of the system reliability (7) and the system unreliability (8) can be used in the case of the coherent system as well as in the case of the noncoherent system, because they relate only with the system states regardless of the properties of the structure function.

Now, consider the system, which structural function is defined using the BDD. According to the interpretation of the BDD in the reliability engineering, which is described in the section 2.D, the system reliability (7) and the system unreliability (8) can be defined by the BDDs, which are interpreted as sub-diagrams of the BDD of the structure function.

For example, consider the BDD of the liquid-level control-system from Fig. 1. The system unreliability can be studied and computed using the first BDD in Fig. 2, while the system reliability can be calculated using the second BDD in Fig. 2.

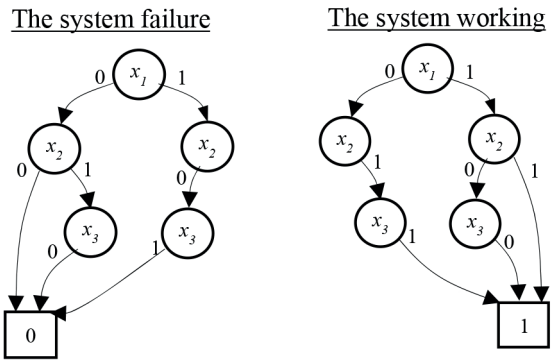

Fig. 2 The failure and working of liquid-level control-system

The reliability of the studied system can be calculated using the second BDD from Fig. 2 as:

$R = q_1p_2p_3 + p_1q_2q_3 + p_1p_2 = 9.925888\text{x}10^{-1}$.

The unreliability of the system can be calculated using the first BDD from Fig. 2 as:

$F = q_1q_2 + q_1p_2q_3 + p_1q_2p_3 = 7.411204\text{x}10^{-3}$,

or using the definition (8) as:

$F = 1 - R = 7.411204\text{x}10^{-3}$.

4. Importance Analysis

The system reliability (7) and unreliability (8) are the global characteristics of the analyzed system. However, they have no information value about the importance of individual components for the system. There exist other measures that are used for this purpose. The part of the reliability analysis that studies the influence of individual components on the reliability of the system is known as the Importance Analysis [6]. The Importance Analysis uses some special measures to identify those components, which have the most influence on the function of the system. These measures are known as the Importance Measures (IM).

Most of the IMs have been developed for the analysis of coherent systems. One of possible approaches for calculation of the IMs for the noncoherent system has been considered in paper [9]. Another development of methods for the Importance Analysis of noncoherent systems has been proposed in works [10] and [11], where authors suggested new approach for computation of some IMs for noncoherent systems that included three steps:

1. quantify the influence of the component's failure on the system reliability,
2. quantify the influence of the component's repair on the system reliability,
3. compute the overall influence of the component on the system reliability as the sum of values that have been obtained in steps 1 and 2.

However, some techniques that are considered in papers [10] and [11] cannot be used when the structure function of the noncoherent systems is defined by the BDD. Therefore, another approach for the computation of the IMs is considered in the next part.

A. The Structural Importance Measure for the Non-coherent System

The Structural Importance Measure (SIM) is one of the simplest measures of the Importance Analysis. It focuses only on the topological aspects of the system. According to [14], this measure determines the proportion of working states of the system in which the working of the component makes the difference between the system failure and its working:

$$SIM_i = \frac{\rho_i}{2^{n-1}}, \tag{9}$$

where ρ_i is the number of situations when the change of the component's state results in the failure of the system. In the case of the coherent system, this number can be obtained as the number of nonzero elements of the DPLD $\partial\phi(1 \to 0)/\partial x_i$ $(1 \to 0)$ [5]. However, in the case of the noncoherent system, also the repair of the system component can cause the failure of the system. Therefore, the number of nonzero elements of the DPLD $\partial\phi(1 \to 0)/\partial x_i(0 \to 1)$ has to be also considered. So, the SIM for the noncoherent system can be computed as follows:

$$SIM_i = \frac{\rho(\partial\phi(1 \to 0)/\partial x_i(1 \to 0))}{2^{n-1}} + \frac{\rho(\partial\phi(1 \to 0)/\partial x_i(1 \to 0))}{2^{n-1}}, \tag{10}$$

where ρ(.) is the function that returns the number of nonzero elements of its argument.

The first term in (10) quantifies the consequence of the component's failure on the system functioning, while the second one quantifies the result of the repair of the component on the system functioning. Equation (10) fully agrees with the approach, proposed in paper [10], and moreover it is not fixed to the form, in which the structure function is expressed.

B. Calculation of the Direct Partial Logic Derivatives from the Binary Decision Diagram

Consider that the structure function of the system has the form of the BDD. To compute the SIM (10), the nonzero elements of the DPLDs $\partial\phi(1 \rightarrow 0)/\partial x_i(1 \rightarrow 0)$ and $\partial\phi(1 \rightarrow 0)/\partial x_i(0 \rightarrow 1)$ have to be calculated. Some algorithms for this task have been proposed in paper [15]. The algorithms locate two sets of paths in the BDD which satisfy the conditions (3) for the calculation of the DPLD. In the case of the computation of the DPLD $\partial\phi(j \rightarrow \bar{j})/\partial x_i(a \rightarrow \bar{a})$, the first set consists of the paths that satisfy the condition $\phi(\bar{a}_i, \boldsymbol{x}) = \bar{j}$, i.e. the paths from the source node to the $\bar{j}$-sink node which go through only the $\bar{a}$-edge of the non-sink nodes presented the i-th component. The second set includes paths for the condition $\phi(a_i, \boldsymbol{x}) = j$. The comparison of these sets permits to determine paths in the BDD that conform to non-zero values of the DPLD $\partial\phi(j \rightarrow \bar{j})/\partial x_i(a \rightarrow \bar{a})$.

There have been considered some modifications of these algorithms in the paper [4]. These modifications have allowed obtaining two new algorithms. Both new algorithms have identical basic principle. They find the paths from the source node to the sink node that satisfy the conditions (3) for the calculation of the DPLDs. These paths are stored in the special structure that is named as the "Tree of paths" [4].

The first algorithm for calculation of the DPLD $\partial\phi(j \rightarrow \bar{j})/\partial x_i(a \rightarrow \bar{a})$ includes three steps:

1. calculate the "Tree of paths" for the condition $\phi(\bar{a}_i, \boldsymbol{x}) = \bar{j}$,
2. calculate the "Tree of paths" for the condition $\phi(a_i, \boldsymbol{x}) = j$,
3. calculate the intersection of the "Trees of paths" from steps 1 and 2.

In the second algorithm only two steps are performed:

4. calculate the "Tree of paths" for the condition $\phi(\bar{a}_i, \boldsymbol{x}) = \bar{j}$,
5. check which paths from the "Tree of paths" exist in the sub-diagram of the BDD that fulfill the condition $\phi(a_i, \boldsymbol{x}) = j$.

For example, consider the calculation of the DPLDs from the BDD depicted in Fig. 1 using the first algorithm. In Fig. 3, there is shown its work in the case of the calculation of the DPLDs $\partial\phi(1 \rightarrow 0)/\partial x_3(1 \rightarrow 0)$ and $\partial\phi(1 \rightarrow 0)/\partial x_3(0 \rightarrow 1)$. The second algorithm is very similar to the first one and its work is closely described in paper [4].

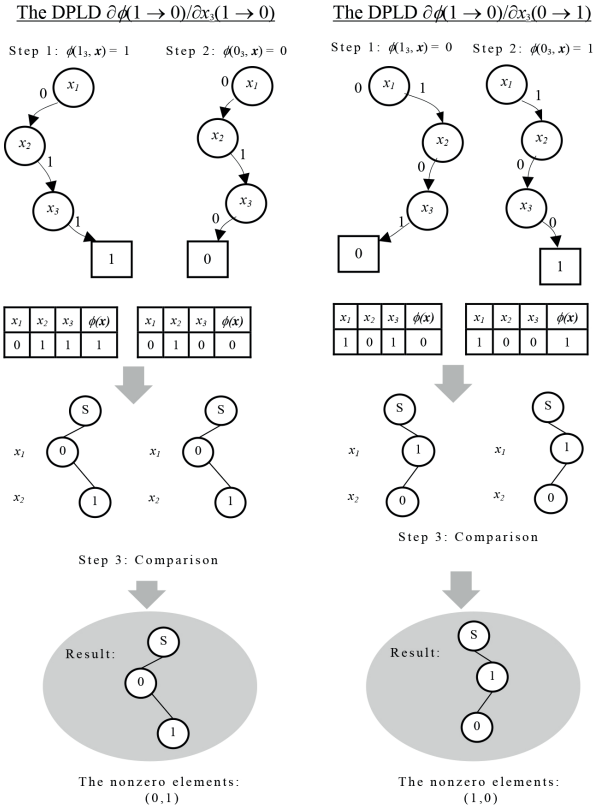

Fig. 3 The first algorithm for the calculation of DPLDs for the third component of liquid-level control-system

C. The Structural Importance Measures for the Liquid--Level Control-System

Consider the system in Fig. 1. The nonzero elements of DPLDs $\partial\phi(1 \rightarrow 0)/\partial x_i(1 \rightarrow 0)$ and $\partial\phi(1 \rightarrow 0)/\partial x_i(0 \rightarrow 1)$, for i = 1,2,3, have to be found to calculate the SIMs of its components according to (10). These nonzero elements can be found using some algorithm from the previous section (Table 2). When the nonzero elements of individual DPLDs are known, their count can be determined (Table 2). Finally, the SIMs (10) can be computed (Table 2). It is clear from Table 2 that all components of the system from Fig. 1 have the same value of the SIM and, therefore, there exists no component, which has dominant influence on the system reliability from the topological point of view.

The nonzero elements of the DPLDs and the SIMs of individual components Table 2

Component	DPLD	Nonzero elements of DPLD	Number of nonzero elements of DPLD	SIM
x_1	$\partial\phi(1\to0)/\partial x_1(1\to0)$	(0,0) (1,0)	2	0.5
	$\partial\phi(1\to0)/\partial x_1(0\to1)$	–	0	
x_2	$\partial\phi(1\to0)/\partial x_2(1\to0)$	(0,1) (1,1)	2	0.5
	$\partial\phi(1\to0)/\partial x_2(0\to1)$	–	0	
x_3	$\partial\phi(1\to0)/\partial x_3(1\to0)$	(0,1)	1	0.5
	$\partial\phi(1\to0)/\partial x_3(0\to1)$	(1,0)	1	

5. Conclusion

Some of the modern challenges of the reliability analysis are the analysis of large systems, which contain a lot of interconnected components, and the research of the noncoherent systems which have some properties that have not been considered in the classical approaches of the reliability analysis. The BDD is an efficient tool for the representation of the Boolean functions. The Boolean function can be interpreted as two-valued function. Also the structure function, that defines the structure of the analyzed system, is two valued function. Therefore, the BDD can be used for the effective representation of the structure function. The usefulness of this tool in the reliability analysis of coherent systems has been presented in papers [2] and [4], where the calculations of the system reliability and IMs have been considered.

In this paper the reliability analysis of noncoherent systems is considered. It is shown that the BDD can also be used for the representation of these systems and that the BDD can be used for the evaluation of the reliability and the unreliability of the noncoherent system.

The Importance Analysis of the noncoherent system is considered in the last section of this paper. The definition of the SIM is proposed using the DPLDs. This definition is consistent with the approach which has been suggested in work [10], but moreover, it does not depend on the form of the structure function. Also, the algorithm for the calculation of the SIM for the noncoherent system from the BDD is proposed. The algorithm is based on the procedures for the calculation of the DPLD from the BDD which have been suggested in paper [4].

References

[1] ZIO, E.: Reliability Engineering: Old Problems and New Challenges, *Reliability Engineering & System Safety*, vol. 94, No. 2, pp. 125-141, 2009.

[2] CHANG, Y., AMARI, S.: Computing System Failure Frequencies and Reliability Importance Measures using OBDD, *IEEE Transactions on Computers*, vol. 53, No. 1, pp. 54-68, 2004.

[3] BRYANT, R. E.: Graph-Based Algorithms for Boolean Function Manipulation, *IEEE Transactions on Computers*, vol. C-35, No. 8, pp. 677-691, 1986.

[4] KOSTOLNY, J., KVASSAY, M., KOVALIK, S.: *Analysis of System Reliability by Logical Differential Calculus and Decision Diagrams,* Intern. Conference on Digital Technologies (DT), 2013, pp. 170-175.

[5] ZAITSEVA E. N., LEVASHENKO, V. G.: Importance Analysis by Logical Differential Calculus, *Automation and Remote Control*, vol. 74, No. 2, pp. 171-182, 2013.

[6] KUO, W., ZHU, X.: *Importance Measures in Reliability, Risk, and Optimization*. Chichester, John Wiley & Sons, Ltd, 2012.

[7] UPADHYAYA, S. J., PHAM, H.: Analvsis of Noncoherent Systems and an Architecture for the Computation of the System Reliability, *IEEE Transactions on Computers*, vol. 42, No. 4, pp. 484-493, 1993.

[8] INAGAKI, T., HENLEY, E. J.: Probabilistic Evaluation of Prime Implicants and Top-events for Non-coherent Systems, *IEEE Transactions on Reliability*, vol. 3, No. 5, pp. 361-367, 1980.

[9] JACKSON, P. S.: On the s-importance of Elements and Prime Implicants of Non-coherent Systems, *IEEE Transactions on Reliability,* vol. R-32, No. 1, pp. 21-25, 1983.

[10] ANDREWS, J. D., BEESON, S.: Birnbaum's Measure of Component Importance for Noncoherent Systems, *IEEE Transactions on Reliability*, vol. 52, No. 2, pp. 213-219, 2003.
[11] BEESON, S. , ANDREWS, J. D.: Importance Measures for Non-coherent-system Analysis, *IEEE Transactions on Reliability*, vol. 52, No. 3, pp. 301-310, 2003.
[12] KUO, W., ZHU, X.: Relations and Generalizations of Importance Measures in Reliability, *IEEE Transactions on Reliability*, vol. 61, No. 3, pp. 659-674, 2012.
[13] AKERS, S. B., Jr.: On a Theory of Boolean Functions, *J. of the Society for Industrial and Applied Mathematics*, vol. 7, No. 4, p. 487, 1959.
[14] ARMSTRONG, M. J.: Reliability-importance and Dual failure-mode Components, *IEEE Transactions on Reliability*, vol. 46, No. 2, pp. 212-221, 1997.
[15] ZAITSEVA, E., LEVASHENKO, V.: Multiple-Valued Logic Mathematical Approaches for Multi-state System Reliability Analysis, *J. of Applied Logic*, vol. 11, No. 3, pp. 350-362, 2013.

Miroslava Mrvova - Peter Pocta *

A QUALITY ESTIMATION OF SYNTHESIZED SPEECH TRANSMITTED OVER IP NETWORKS

A design of the parametric models estimating a quality of synthesized speech transmitted through IP networks is presented in this paper. A Genetic Programming and Random Neural Network as machine learning techniques were deployed to design the models. A set of the quality-affecting parameters was used as an input to the designed parametric estimation models in order to estimate a quality of synthesized speech transmitted over IP networks (VoIP environment). The performance results obtained for the designed parametric estimation models have validated both genetic programming and random neural network as powerful techniques, delivering good accuracy and generalization ability; this makes them perspective candidates for quality estimation of this type of speech in the corresponding environment. The developed parametric models can be helpful for network operators and service providers in a planning phase or early-development stage of telecommunication services based on synthesized speech.

Keywords: *Genetic programming, random neural network, speech quality estimation, synthesized speech, packet loss, speech codec.*

1. Introduction

A speech quality assessment process is useful for network operators and service providers to evaluate the quality of voice services offered by current telecommunication networks. The speech quality assessment can be performed either from the subjective or objective point of view. The traditional way how to assess speech quality is called subjective testing. In principle, subjective testing is based on a large enough group of human subjects, who listen to given samples and assign an opinion score on a scale ranging from 1 "bad quality" to 5 "excellent quality" (i.e. MOS (Mean Opinion Scale) scale). This approach is impractical in real conditions, because of the number of subjects, that have to participate in a test, time-consumption, high costs, etc.

In contrast to subjective testing, the objective testing employs a computer program or mathematical model to approximate an average user behavior associated with a perception of speech quality. There are two kinds of objective testing. Firstly, the intrusive models (e.g. ITU-T PESQ) are characterized by comparing two types of signals. They evaluate the quality of a degraded (output) speech signal by comparing it with a corresponding reference (input) speech signal. These methods are very accurate but not suitable for monitoring real-time traffic in telecommunication networks. Secondly, non-intrusive models can be classified into two groups, namely signal-based and parametric. Signal-based non-intrusive models are based (as the name implies) on a speech signal and do not use the reference speech sample in comparison to the intrusive models. A hidden reference speech sample is created internally and compared to degraded signal deploying similar approaches as used in the intrusive models. On the other hand, parametric non-intrusive models are based on estimating the quality of speech transmission using input parameters characterizing this transmission from a quality point of view [1] and [2].

Parametric models based on machine learning techniques, such as a neural network or genetic programming, are considered as a novel approach of speech quality estimation. This approach has become popular because of its high correlation with a human perception and relatively easy implementation. Moreover, it is able to offer a real-time and continuous evaluation of the speech quality in comparison with the intrusive and non-intrusive signal-based methods.

In recent years, the interest in a synthesized speech (speech generated by computer) has grown extremely. Up to now, synthesized speech has reached a quality level which allows it to become a part of modern daily life [3]. Furthermore, voice-based telecommunication services are on decline. In order to make some of voice-based services more economically effective, informational services involving call center operators have been replaced by services based on the synthesized speech. Although,

* **Miroslava Mrvova, Peter Pocta**
Department of Telecommunications and Multimedia, Faculty of Electrical Engineering, University of Zilina, Slovakia,
E-mail: miroslava.mrvova@fel.uniza.sk

the services based on this kind of speech are broadly used, there is no parametric model designed for estimating a speech quality of these services. Such a model could be helpful for network operators and service providers implementing them in a planning phase or early-development stage of telecommunication services based on synthesized speech.

In this article, novel parametric non-intrusive models estimating the quality of synthesized speech transmitted through IP networks are addressed. These models make use of two different biologically inspired machine learning techniques, namely Genetic Programming (GP) and Random Neural Network (RNN). The decision to deploy these two approaches in this study was mostly motivated by very promising results obtained by GP and RNN for very similar tasks as here, see for instance [4 and 5]. It should be noted here that GP employs an evolutionary process inspired by Darwinian evolution to automatically derive mathematical model (function) from initial parameters; it requires only minimal assumptions about a structure of solution and it provides promising results in terms of accuracy and computational efficiency [4]. On the other hand, RNN consists of neurons, which interact with each other by exchanging excitatory and inhibitory signals in a network, similar to a biological neural network. Each state of neuron is characterized by a neuron potential as a non-negative integer value, which yields to a more detailed state representation. The positive potential means that neuron is in an excited state, sending excitatory and inhibitory signals at random intervals to other neurons or outside of the network. It was found in [5] that a well trained RNN model is able to give reasonable results even for parameter values outside the range defined in training phase, i.e. it provides a good extrapolating ability. In other words and contrary to ANN models, RNN has also good ability to generalize for new inputs. More detailed information about GP and RNN can be found in [6 - 9].

The rest of the paper is organized as follows: In Sections 2 and 3, the experimental setup and results (a performance of the designed parametric models for predicting the speech quality of synthesized speech impaired by packet loss and coding) are presented and discussed respectively. Finally, Section 4 concludes the paper and suggests a future work.

2. Experimental setting

The GP and RNN are approaches, which employ supervised learning, i.e. they require values of inputs together with values of their relevant outputs in a training process. In general, their main task is to learn the numerical or logical relationship between input and actual output parameters during the training process. Due to a fact that the aim of this article is to design parametric model estimating a quality of synthesized speech in a VoIP environment, following parameters were considered as input parameters:

- a quality-affecting parameters representing an impact of IP networks, i.e. parameters characterizing packet loss process: unconditional loss probability (ulp) and conditional loss probability (clp)),
- other quality-affecting parameters, like speech codec type and a type of synthesized speech signal.

The input parameters defined above were used together with their corresponding MOS values expressing the speech quality ranging from 1 “bad quality” to 5 “excellent quality” (actual output parameter). GP and RNN were fed with the above mentioned parameters in order to provide the MOS values as a function of parameters typical for IP networks. Fig. 1 shows a diagram of the designed parametric estimation model.

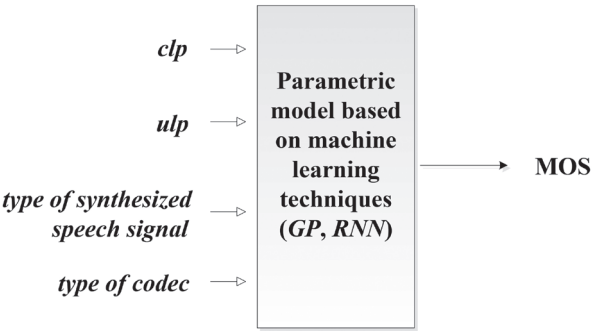

Fig. 1 A diagram of the designed parametric estimation model

A. Database creation

4320 speech samples representing different conditions affecting the speech quality were recorded and assessed for the purpose of this research. At the beginning, the speech samples with a length of 12 seconds were synthesized by two state-of-the-art Slovak synthesizers, namely Diphone synthesizer (Kempelen 1.6 [10]) and Unit-selection synthesizer (Kempelen 2.1 [10]). Subsequently, these synthesized speech samples were coded by three different encoding schemes, namely ITU-T G.729AB [11], ITU-T G.711 [12] and iLBC [13]. After a transmission of the particular speech signals through the IP network, where we simulated different packet loss situations, their speech quality scores were predicted by ITU-T P.862 PESQ (Perceptual Evaluation of Speech Quality) [14]. The decision to use PESQ model (an objective model designed for predicting a quality of naturally-produced speech) as a predictor of speech quality was based on the experiments carried out in [15 - 17], which have proven that PESQ is able to provide accurate predictions of the quality of synthesized speech impaired by the impairments used in this study. For example, the correlation coefficient reported in [15] was above 0.9.

Regarding the packet loss situations, we have concentrated on parameters, which precisely capture all aspects of a packet loss process, namely conditional loss probability (as an indicator of packet loss burstiness, denoted as clp) and unconditional loss

probability (as an indicator of packet loss rate, denoted as ulp). In fact, we simulated different values of clp: 0% (theoretically) - Bernoulli loss model (modeling independent losses), 70% and 80% - Gilbert loss model (modeling dependent losses) and of ulp: 0%, 1.5%, 3%, 5%, 10% and 15%. By using these 4320 synthesized speech samples, 108 average speech quality scores (6 ulp x 3 clp x 2 types of synthesized speech signals x 3 types of codec) called configurations were formed.

B. Design of parametric models

The 108 average configurations served to create two databases needed for the purpose of designing parametric models. The first one (denoted as D1) had a knowledge of an overall range of the configurations during a training process, whereas the second one (denoted as D2) did not cover any boundary condition during a training process.

In order to acquire a relation between input and output, 90 configurations (from overall number of 108 configurations) were employed during a training process. In order to verify a performance of the designed parametric estimation models, remaining 18 configurations (common ratio of 80:20) were used during a testing process.

i. Training process of GP-based parametric model

GPlab (Matlab toolbox for a genetic programming developed by Sara Silva [18]) was used for a computational purpose in this research. Some of the GPlab parameters and their values used in the simulations are listed in Table 1. Regarding other parameters, we used default values defined in the GPlab.

The initial population size consisted of 1000 individuals with an initial maximum depth of each tree equals to 6. Ramped half-and-half method was chosen to generate initial population, because it generates trees with a wide variety of sizes and shapes in a ratio of 50:50; which means 50% of identical trees (with the same initial maximum tree depth for all branches) and 50% of different trees (with the different tree depth for all branches considering initial maximum tree depth). Selection of parents needed for a recombination was performed according to a lexicographic parsimony pressure tournament, which prefers shorter individuals to longer ones when their fitness is identical. This strategy helps to reduce a production of complicated individuals and consequently a code growth. A standard tree crossover and mutation were used with probabilities adjusted to equal value. The reproduction rate was set to 0.1. It means that each selected parent has 10% chance of being copied to a next generation without modifications in a tree structure [19]. The maximum tree depth in the case of a creation of offspring by genetic operators was set to 32. New populations were composed of newly-generated offspring only, i.e. replace survival. A function set was defined according to the following studies [4, 16 and 20]. Due to a stochastic nature of the genetic programming, it is required to execute several runs of GP to obtain statistically stable and reliable results. For that reason, 5 independent runs for each database were performed. It would be noted that each run spanned 30 generations with 1000 individuals.

Values of the GP parameters used in the simulations Table 1

GP Parameters	Defined values
Initial population size	1000 individuals
Initial tree depth	6
Initialization of population	Ramped half-and-half method
Selection	Lexicographic parsimony pressure tournament
Genetic operators	crossover; mutation; reproduction
Operator probabilities	0.5, 0.5; 0.1
Survival	Replace
Function set	plus, minus, times, divide, sqrt, power, log, log10, log2, sin, cos
Terminal set	X1, X2, X3, X4 - inputs
Fitness	the sum of the absolute values of the differences between obtained and actual outputs

ii.Training process of RNN-based parametric model

RNNSIM v.2 developed by Abdelbaki [21] was used to implement RNN in MATLAB. We applied two different RNN feed-forward architectures (without circuit in the layers, i.e. signal cannot return back to neuron which has already visited) in a design process of the estimation model. Figure 2 depicts RNN architectures used in our research, namely 3-layer architecture with one hidden layer and 9 neurons on that layer and 4-layer architecture with 5 and 4 hidden neurons situated in two hidden layers respectively. The decision to use these architectures with the corresponding configurations (e.g. number of hidden layers and nodes per hidden layer) was based on other experiment run by the authors and published in [22], where the selected architectures and their particular configurations have achieved the best performance from all investigated conditions. Gradient descent method was used as a learning algorithm because of its simplicity and strong generalization capability even for small training data sets. Due to a stochastic nature of the random neural network, five simulations were conducted for each network architecture and training database in order to obtain statistically stable and reliable results.

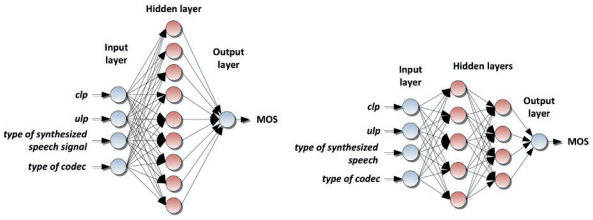

Fig. 2 Architectures of RNN used in the simulations

C. Design of parametric model - testing process

As already mentioned above, the randomly chosen 18 testing configurations (naturally not used in a training process) were used to verify a performance of the designed parametric estimation models during a testing process. The MOS values provided by these models (ranging from 1 "bad quality" to 5 "excellent quality") were compared with the actual MOS values predicted by the PESQ model. On the basis of this comparison, the performance of the designed parametric estimation models was quantified in terms of the Pearson correlation coefficient R, the respective root mean square error RMSE and epsilon-insensitive root mean square error RMSE* as defined in [23].

3. Experimental results

A. Experimental results for GP-based parametric model

As already stated above, five simulations (runs) were conducted for each database. Each simulation spanned 30 generations with 1000 individuals. The estimated MOS values provided by the designed parametric model within a testing phase were compared with the MOS values predicted by PESQ. The best results selected from all realized simulations according to the root mean square error and epsilon-insensitive root mean square error are presented in Table 2. A comparison of actual (predicted by PESQ model) and MOS values estimated by the designed parametric model based on GP approach for both used databases (D1 and D2) is depicted in Figs. 3 and 4, respectively.

The performance results presented in Table 2 obtained for the designed parametric model confirmed very good accuracy provided by GP approach, which is proven by very high values of Pearson correlation coefficient (94% and higher) and very low values of root mean square error (0.104MOS) and epsilon-insensitive root mean square error (0.052MOS). Surprisingly, the performance results are comparable with the results obtained in our previous study [24], where we trained the designed GP-based parametric models separately for each of the three speech codecs (ITU-T G.729AB, ITU-T G.711 and iLBC) involved in this study using smaller training databases (30 configurations). On the basis of this fact, we can conclude that a bigger training database did not help to improve an accuracy of the parametric model based on the GP approach.

Chosen best-of-run individuals — Table 2

Database	D1	D2
R [%]	94.37	98.22
RMSE	0.1106	0.1037
*RMSE **	0.0517	0.0560

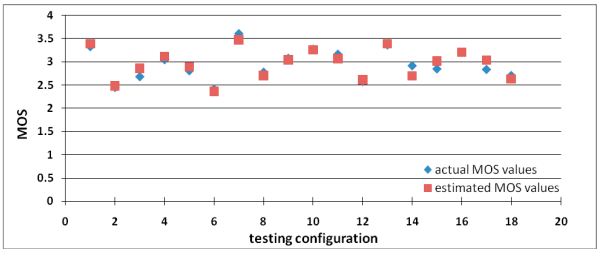

Fig. 3 The actual and estimated MOS values obtained for D1 database and GP approach

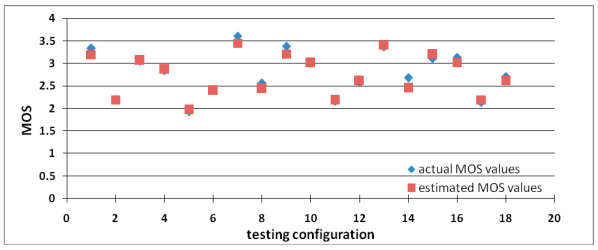

Fig. 4 The actual and estimated MOS values obtained for D2 database and GP approach

B. Experimental results for RNN-based parametric model

Similar to the GP approach, five simulations were conducted for two network architectures of RNN and two experimental databases. The estimated MOS values provided by the designed parametric model were compared with the MOS values predicted by PESQ. The best results selected from all realized simulations according to the root mean square error and epsilon-insensitive root mean square error are presented in Table 3. A comparison of the actual (predicted by PESQ model) and MOS values estimated by the designed parametric model based on RNN for both databases (D1 and D2) are depicted in Figs. 5 and 6, respectively.

The performance results presented in Table 3 also confirmed very high estimation accuracy. Comparing the individual network architectures, 3-layer RNN with 9 hidden neurons seems to provide more accurate results than a 4-layer RNN. This fact is confirmed by lower values of root mean square error and epsilon-insensitive root mean square error. As expected, a higher number of the configurations in a training database provides more accurate estimations in comparison with the estimations obtained in [25] for the RNN-based parametric model designed for speech codec G.729AB (using smaller training database (30

configurations)). It should be noted here that an expansion of the training database was only useful for the RNN-based parametric model. In other words, as can be seen in a previous subsection, a size of the training database did not influence an accuracy of the parametric model based on the GP approach.

Chosen best simulations Table 3

Database/ *RNN* architecture	D1		D2	
	4_9_1	4_5_4_1	4_9_1	4_5_4_1
R [%]	93.99	94.10	98.58	97.84
RMSE	0.1204	0.1278	0.1072	0.1169
*RMSE **	0.0507	0.0521	0.0510	0.0599

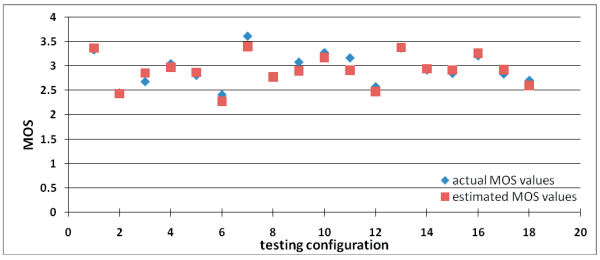

Fig. 5 The actual and estimated MOS values obtained for D1 database and 3-layer RNN architecture (4_9_1)

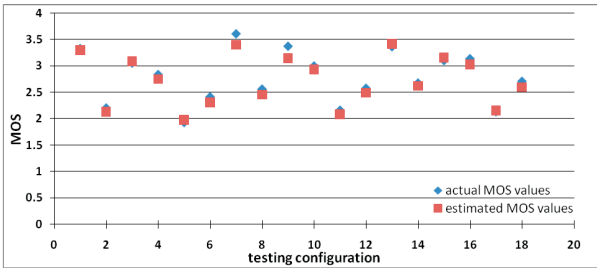

Fig. 6 The actual and estimated MOS values obtained for D2 database and 3-layer RNN architecture (4_9_1)

In addition to a relatively very high accuracy of both designed parametric quality estimation models based on the machine learning techniques, the performance results even confirmed their good generalization ability for new inputs not included in a training process. Comparing both databases (D1 and D2) for both approaches (GP and RNN), the latter one provides (in some cases) a bit more accurate results (except for RMSE* values). It is necessary to note that the D1 database had a knowledge of an overall range of the configurations during the training process, whereas the D2 database did not cover any boundary condition during the training process. This can be explained by a fact that a discovered function by the GP approach and curve characterizing relationship between the perceived quality of the synthesized speech and quality-affecting parameters learned by the RNN are well-defined even beyond the specified interval. In fact, the designed parametric models are able to provide good results even outside the area defined in the training process.

4. Conclusion

In this article, we presented the novel parametric models for a non-intrusive estimation of the speech quality based on biologically inspired machine learning techniques, like a Genetic Programming (GP) and Random Neural Network (RNN). It is worth reiterating that the designed parametric models estimate the quality of synthesized speech transmitted over IP networks (VoIP environment). Therefore, the quality-affecting parameters characterizing packet loss process, speech codec type and a type of synthesized speech signal were considered as an input to the designed parametric estimation models. Outputs of the designed parametric models represent estimated MOS values (ranging from 1 “bad quality” to 5 “excellent quality”). When comparing the performance results obtained for the designed parametric models with the predictions provided by PESQ model, we can conclude that the designed parametric models represent promising candidates for estimating the quality of synthesized speech transmitted over IP networks. Furthermore, the designed parametric models are computationally very efficient and useful for real-time speech quality estimation. The developed parametric models can be helpful for network operators and service providers in a planning phase or early-development stage of telecommunication services based on synthesized speech. Finally, as a performance of both designed parametric models is roughly the same in terms of all monitored performance indicators, we leave up to the intended users to decide, which one of them, they will deploy in their implementations.

Future work will focus on an optimization of the complexity of the function defined by GP approach, as the function has been found very complex.

Acknowledgement

This contribution is the result of the project implementation: Centre of excellence for systems and services of intelligent transport II., ITMS 26220120050 supported by the Research & Development Operational Programme funded by the ERDF.

„Podporujeme vyskumne aktivity na Slovensku/Projekt je spolufinancovany zo zdrojov EU.”

References

[1] DE RANGO, F., TROPEA, M., FAZIO, P., MARANO, S.: Overview on VoIP: Subjective and Objective Measurement Methods, *IJCSNS Intern. J. of Computer Science and Network Security*, vol.6, No.1B, 2006.

[2] MAHDI, A. E., PICOVICI, D.: Advances in Voice Quality Measurement in Modern Telecommunications, *Digital Signal Processing* 19 (2009), pp.79-103.

[3] MOELLER, S.: *Quality of Telephone-based Spoken Dialogue Systems,* Springer, New York, 2005, ISBN 0-387-23190-0.

[4] RAJA, A., ATIF AZAD, R. M., FLANAGAN, C., RYAN, C.: A Methodology for Deriving VoIP Equipment Impairment Factors for a mixed NB/WB Context, *IEEE Transactions on Multimedia*, vol.10, No. 6, 2008.

[5] RUBINO, G., VARELA, M.: *A New Approach for the Prediction of End-to-end Performance of Multimedia Streams*, Proc. of the First Intern. Conference on the Quantitative Evaluation of Systems (QEST'04), 2004.

[6] KOZA, J. R.: *Genetic Programming: On the Programming of Computers by Means of Natural Selection,* A Bradford book, 1998, ISBN 2-262-11170-5.

[7] POLI, R., LANGDON, W. B., MCPHEE, N. F., KOZA, J. R.: *A Field Guide to Genetic Programming,* 2008, Published via http://dces.essex.ac.uk/staff/rpoli/gp-field-guide/A_Field_Guide_to_Genetic_Programming.pdf. .

[8] ABDELBAKI, H. E.: *Random Neural Network Simulator* (RNNSIM v. 2), for use with MATLAB, September 1999, online: http://www.cs.ucf.edu/~ahossam/rnnsimv2/rnnsimv 2.pdf.

[9] GELENBE, E.: Random Neural Networks with negative and positive Signals and Product Form Solution, *Neural Computation* 1 (4), 1989, pp. 502-510.

[10] DARJAA, S., RUSKO, M., TRNKA, M.: *Three Generations of Speech Synthesis Systems in Slovakia,* Proc. of XI Intern. Conference Speech and Computer (SPECOM 2006), Sankt Peterburg, 2006, pp. 297-302, ISBN 5-7452-0074-X.

[11] ITU-T Rec. G.729: *Coding of Speech at 8 kbit/s using Conjugate-Structure Algebraic-Code-Exited Linear Prediction (CS-ACELP)*, Intern. Telecommunication Union, Geneva (Switzerland), 2007.

[12] ITU-T Rec. G.711: *Pulse Code Modulation (PCM) of Voice Frequencies*, Intern. Telecommunication Union, Geneva, 1988.

[13] IETF RFC 3951: *Internet Low Bit Rate Codec (iLBC)*, Internet Engineering Task Force, 2004.

[14] ITU-T P.862: *Perceptual Evaluation of Speech Quality (PESQ): An Objective Method for End-to-end Speech Quality Assessment of Narrow-band Telephone Networks and Speech Codecs,* Intern. Telecommunications Union, Geneva, 2001.

[15] POCTA, P., HOLUB, J.: Predicting the Quality of Synthesized and Natural Speech Impaired by Packet Loss and Coding Using PESQ and P.563 Models, *Acta Acustica united with Acustica*, vol. 97, No. 5, pp. 852-868, 2011, ISSN 1610-1928.

[16] RAJA, A., ATIF AZAD, R. M., FLANAGAN, C., PICOVICI, D., RYAN, C.: *Non-Intrusive Quality Evaluation of VoIP Using Genetic Programming,* Bio-Inspired Models of Network, Information and Computing Systems, 2006, pp.1-8.

[17] BASTERRECH, S., RUBINO, G., VARELA, M.: *Single-sided Real-time PESQ Score Estimation*, Proc. of Measurement of Speech, Audio, and Video Quality in Networks (MESAQIN'09), Prague, 2009.

[18] SILVA, S.**:** GPLAB: *A Genetic Programming Toolbox for MATLAB,* Published via http://gplab.sourceforge.net/download.html.

[19] VANNESCHI, L., CASTELLI, M., SILVA, S.: *Measuring Bloat, Overfitting and Functional Complexity in Genetic Programming*, GECCO 2010, pp. 877-884.

[20] RAJA, A., ATIF AZAD, R. M., FLANAGAN, C., RYAN, C.: *Real-Time, Non-intrusive Evaluation of VoIP,* EuroGP'07, LNCS, vol. 4445, Springer, Heidelberg 2007, pp. 217-228.

[21] ABDELBAKI, H. E.: *Random Neural Network Simulator* (RNNSIM v. 2), 1999, online: http://www.cs.ucf.edu/~ahossam/rnnsim.

[22] MRVOVA, M.: *Quality Estimation of Synthesized Speech Signals Transmitted through a Telecommunication Channel*, Ph.D. thesis (available only in Slovak), University of Zilina, 2013.

[23] ITU-T Rec. P.1401: *Methods, Metrics and Procedures for Statistical Evaluation, Qualification and Comparison of Objective Quality Prediction Models,* Intern. Telecommunication Union , Geneva, 2012.

[24] MRVOVA, M., POCTA, P.: Novel Parameter-based Models Estimating Quality of Synthesized Speech Transmitted over IP Network Based on Genetic Programming Approach, *Microwave and Radio Electronics Week,* 2013, Pardubice, pp. 361-366, ISBN 978-1-4673-5517-9.

[25] MRVOVA, M.: *Novel Parameter-based Model Estimating Quality of Synthesized Speech Transmitted over IP Network Based on Different RNN Architectures*, 10th European Conference of Young Research and Scientific Workers TRANSCOM 2013, 2013, Zilina, Slovakia, pp. 81-84, ISBN: 978-80-554-0692-3.

COMMUNICATIONS – Scientific Letters of the University of Zilina
Writer's Guidelines

1. Submitted papers must be unpublished and must not be currently under review for any other publication.
2. Submitted manuscripts should not exceed 8 pages including figures and graphs (in Microsoft WORD – format A4, Times Roman size 12, page margins 2.5 cm).
3. Manuscripts written in good English must include abstract and keywords also written in English. The abstract should not exceed 10 lines.
4. Submission should be sent: By e-mail – as an attachment – to one of the following addresses: komunikacie@uniza.sk or holesa@uniza.sk (or on CD to the following address: Zilinska univerzita, OVaV – Komunikacie, Univerzitna 1, SK-10 26 Zilina, Slovakia).
5. Uncommon abbreviations must be defined the first time they are used in the text.
6. Figures, graphs and diagrams, if not processed in Microsoft WORD, must be sent in electronic form (as JPG, GIF, TIF, TTF or BMP files) or drawn in high contrast on white paper. Photographs for publication must be either contrastive or on a slide.
7. The numbered reference citation within text should be enclosed in square brackets. The reference list should appear at the end of the article (in compliance with ISO 690).
8. The numbered references (in square brackets), figures, tables and graphs must be also included in text – in numerical order.
9. The author's exact mailing address, full names, E-mail address, telephone or fax number, the name and address of the organization and workplace (also written in English) must be enclosed.
10. The editorial board will assess the submitted paper in its following session. If the manuscript is accepted for publication, it will be sent to peer review and language correction. After reviewing and incorporating the editor's comments, the final draft (before printing) will be sent to authors for final review and minor adjustments
11. Submission deadlines are: September 30, December 31, March 31 and June 30.

COMMUNICATIONS

SCIENTIFIC LETTERS OF THE UNIVERSITY OF ZILINA
VOLUME 16

Address of the editorial office:
Zilinská univerzita
Office for Science and Research
(OVaV)
Univerzitna 1
SK 010 26 Zilina
Slovakia

E-mail: komunikacie@uniza.sk

Each paper was reviewed by two reviewers.

Journal is excerpted in Compendex and Scopus.

It is published by the University of Zilina in
EDIS – Publishing Institution of Zilina University
Registered No: EV 3672/09
ISSN 1335-4205

Published quarterly

Single issues of the journal can be found on:
http://www.uniza.sk/komunikacie

ICO 00397 563
February 2014